Forschungszentrum Karlsruhe
Technik und Umwelt

Wissenschaftliche Berichte
FZKA 5846

Physico-Chemical Behavior of Zircaloy Fuel Rod Cladding Tubes During LWR Severe Accident Reflood

Part I:
Experimental results of single rod quench experiments

P. Hofmann, V. Noack

Institut für Materialforschung
Projekt Nukleare Sicherheitsforschung

Part II:
Modelling of quench phenomena

M. S. Veshchunov, A. V. Berdyshev,
A. V. Boldyrev L. V. Matweev, A. V. Palagin,
V. E. Shestak

Nuclear Safety Institute,
Russian Academy of Science, Moscow

Mai 1997

Forschungszentrum Karlsruhe
Technik und Umwelt

Wissenschaftliche Berichte
FZKA 5846

Physico-Chemical Behavior of Zircaloy Fuel Rod Cladding Tubes During LWR Severe Accident Reflood

Part I: Experimental results of single rod quench experiments

P. Hofmann, V. Noack

Institut für Materialforschung
Projekt Nukleare Sicherheitsforschung

Part II: Modelling of quench phenomena

M. S. Veshchunov, A. V. Berdyshev, A. V. Boldyrev
L. V. Matweev, A. V. Palagin, V. E. Shestak

Nuclear Safety Institute, Russian Academy of Science, Moscow

Forschungszentrum Karlsruhe GmbH, Karlsruhe
1997

Summary

An important accident management measure for controlling severe accident transients in LWRs is the injection of water to cool the degrading core. Quenching is considered a worst-case scenario regarding hydrogen generation rates which should not exceed safety-critical values.

A series of separate-effects tests is being carried out on Zircaloy PWR fuel rod cladding to study the enhanced oxidation which can occur on quenching. In these tests, performed in the QUENCH rig, single tube specimens are heated by induction to a high temperature and then quenched by water or rapidly cooled down by steam injection. The main objectives of the program are:

- the provision of an extensive experimental database for the development of detailed mechanistic quench models,
- the examination of the physico-chemical behavior of overheated fuel elements (core) under different flooding conditions,
- to provide an improved understanding of the effects of water addition at different stages of a degraded core,
- the determination of a cladding failure criteria; exposure of new metallic surfaces to steam which results in renewed temperature escalation and hydrogen production, and
- the determination of the hydrogen source term.

The cladding tubes temperatures at onset of quenching have been varied between 1000 and 1600°C and the extent of preoxidation between 0 and 300 µm ZrO_2. The simulated flooding rate was 1,5 cm/s and the alternative steam injection rate about 2 g/s. The hydrogen generation is correlated with the conditions of the specimen before and after the test. (Part I).

The essential physico-chemical processes occurring during quenching of fuel rods are analytically considered: a) heat exchange, b) oxidation of Zircaloy by steam and c) the mechanical behavior of the cladding tubes. A new combined numerical QUENCH module was elaborated by coupling of the heat exchange module THERM, the oxidation module PROF and the mechanical deformation module CROX: the models are presented; the results of the calculations are compared with the available experimental data (Part II).

Physikalisch-chemisches Verhalten von Zircaloy Brannstab-Hüllrohren beim Wiederfluten eines LWR während eines schweren Störfalles

Eine der wichtigsten Notfallschutzmaßnahmen zur Beherrschung eines schweren Störfalls in Leichtwasserreaktoren ist die Wiederherstellung der Kühlung des teilzerstörten Reaktorkerns durch Einspeisen von Wasser. Wiederfluten wird jedoch auch als ein Störfallszenario mit besonders hoher Wasserstofffreisetzungsrate in das Containment angesehen, bei dem sicherheitsrelevante Werte nicht überschritten werden sollen.

Um die verstärkte Oxidation von Zircaloy während des Wiederflutens zu untersuchen, wird im Forschungszentrum Karlsruhe eine Reihe von Einzeleffekt-Experimenten mit Zircaloy-Hüllrohren durchgeführt. In diesen Experimenten werden einzelne Rohrproben durch induktive Beheizung auf hohe Temperaturen gebracht und dann mit Wasser oder Dampf abgeschreckt. Die vorrangigen Ziele des Programms sind:

- Bereitstellung einer experimentellen Datenbasis für die Entwicklung detaillierter, mechanistischer Modelle.
- Untersuchung des physikalisch-chemischen Verhaltens überhitzter Brennstäbe bei verschiedenen Flutbedingungen.
- Ein besseres Verständnis der Phänomene beim Fluten von Reaktorkernen mit unterschiedlichem Ausmaß der Schädigung.
- Bestimmung eines Hüllrohrversagenskriteriums; durch Hüllrohrversagen werden neue metallische Oberflächen dem Dampf ausgesetzt, was zu verstärkter Oxidation und Wasserstofferzeugung führt.
- Bestimmung des Wasserstoffquellterms im Containment.

Besonders intensiv wurden der Einfluß der Hüllrohrtemperatur und der Einfluss des Ausmaßes der Voroxidation untersucht. Die Proben wurden von Temperaturen zwischen 1000 und 1600 °C mit Oxidschichtdicken zwischen 0 und 300 µm ZrO_2 abgeschreckt. Die simulierte Flutrate betrug 1,5 cm/s, bei Versuchen mit Abkühlung von Dampf wurde ein Dampfmassenstrom von 2 g/s gewählt. Der Einfluss der verschiedenen Anfangsbedingungen auf die gemessene Wasserstofffreisetzung wurde untersucht und mit dem Zustand der Proben korreliert (Teil 1).

Folgende wesentliche physikalisch-chemische Prozesse beim Wiederfluten wurden modelliert: a) Wärmeübertragung, b) Oxidation von Zircaloy in Dampf, c) das mechanische Verhalten der Hüllrohre. Ein neues numerisches QUENCH-Modul wurde durch die Kopplung des Wärmeübertragungsmoduls THERM, des Oxidationsmoduls PROF und des Moduls für mechanisches Hüllrohrverhalten CROX entwickelt. Die Modelle werden vorgestellt, Ergebnisse von Berechnungen werden im Teil 2 des Berichts mit den experimentellen Ergebnissen verglichen.

Part I: Experimental results of single rod quench experiments

P. Hofmann, V. Noack

Institut für Materialforschung

Projekt Nukleare Sicherheitsforschung

Contents

1. Introduction

An important accident management measure for controlling severe accident transients in light water reactors is the injection of water to cool the degrading core. Analysis of the TMI-2 accident and the results of out-of-pile and in-pile experiments (CORA, LOFT, Phebus, PBF) have shown that the quenching of a partially degraded fuel bundle or of a whole core by water injection could cause renewed oxidation of fuel rods leading to reheating of the rods, a sharp increase in hydrogen production and the intensified release of volatile fission products. Quenching is considered a worst-case accident scenario regarding hydrogen release rates to the containment. For in- and ex-vessel hydrogen management measures one has to prove that hydrogen release rates do not exceed safety-critical values for the power plant.

The increased hydrogen production during quenching cannot be determined by the available Zircaloy/steam oxidation correlations. For example, none of the codes participating in the OECD International Standard Problem 31, the blind calculation of the CORA-13 quench experiment, was able to calculate the experimentally observed quench peak, as can be seen in Fig. 1 /1/.

The current understanding is that water entering the overheated bundle (core) and the generated steam cause a rapid cooldown resulting in a thermal shock in the oxygen-embrittled material, generating new metallic surfaces by cracking and fragmentation of the cladding. Reaction of the steam with the metallic components of the newly-formed surfaces is believed to lead to local temperature escalation and rapid hydrogen generation because of the exothermic Zircaloy-steam reaction. Metallic Zircaloy can absorb a part of the hydrogen, whereas the solubility of hydrogen in zirconia is very low. The uptake of hydrogen in Zircaloy and its additional release during oxidation of the metal possibly influences the kinetics of hydrogen release. In most of the present Severe-Fuel-Damage code systems, the quench behavior is not considered or only treated by simplified user-specified criteria which are not verified by experimental data. An extensive separate-effects experimental database is required as a basis for model improvement and development, as indicated in /2/.

2. Experimental program

In case of flooding of a four-meter high reactor core, the fuel rods experience different cooling mechanisms (see Fig. 2). The upper part of the rods will be cooled convectively by steam generated in the lower part of the bundle. Closer to the quench front, intensified cooling by a mixture of steam and water droplets occurs. The high temperature of the rods prevents the rewetting of the outer surface of the cladding in the film boiling region. The transition from film boiling to nucleate boiling, where rewetting of the outer cladding surface occurs, is accompanied by a strong increase of the heat transfer coefficient. There has been the assumption that the fast cooldown at onset of nucleate boiling could induce stresses resulting in the formation of cracks in the oxide layer of the cladding. Finally, the rods are cooled by convection in water.

Another source of stresses which may result in the formation of cracks in the cladding accompanied by enhanced oxidation шы phase transitions in the material during cooldown. The zirconium-oxygen phase diagram is depicted in the upper part of Fig. 3. It is known from literature /3/, that particularly the transition from the tetragonal to the monoclinic oxide at about 1200 °C is accompanied by a jump in the thermal strain, as can be seen in the lower part of Fig. 3. Also the transition of metallic β-Zircaloy to metallic α-Zircaloy generates stresses in the cladding, as well as radial temperature gradients during fast cooldown.

The Forschungszentrum Karlsruhe has started a program to investigate the generation of new metallic surfaces in Zircaloy cladding tubes and their influence on oxidation and hydrogen generation. A small-scale test rig was designed and built in which it is possible to quench short Zircaloy fuel rod segments by water and steam (see table 1). The experiments are mainly focused on the investigation of mechanisms generating new metallic surfaces during reflooding by cracking and fragmentation of the oxygen-embrittled cladding and on the resulting hydrogen generation. The principal investigated experimental parameters are the extent of preoxidation and the temperature of the tube before cooldown. The experiments are supported by theoretical works at the Institut für Materialforschung III at the Forschungszentrum Karlsruhe, a group of scientists of the Russian Academy of Sciences (see part two of this report) and by AEA Technology (United Kingdom). The objective of the investigations is the development of physically-based models for the generation of new metallic surfaces during quenching and their impact on the hydrogen generation.

The design of the QUENCH rig is shown in Fig. 4. The Zircaloy test specimen used in most of the tests is a cylindrical sample of standard Siemens/KWU Zircaloy-4 fuel rod cladding tube with a length of 150 mm, an outer diameter of 10.75 mm and a wall thickness of 0.725 mm filled with high density ZrO_2 pellets with an outer diameter of 9.1 mm. The specimen is suspended by a thin Zircaloy capillary tube inside a quartz tube. Heating is provided by an induction coil around the section of the quartz tube enclosing the specimen. Power is supplied to this coil from a 20 kW oscillator, at a frequency of up to 700 kHz, which induces surface currents in the metal with consequent Joule heating. The QUENCH rig allows quenching by water or rapid cooldown by steam. A valve ensures that no water vapor reaches the specimen before the start of the quench process. The quench water is contained in a quartz cylinder which is moved up inside the outer quartz tube at a predetermined rate (0.3 - 3 cm/s). The heating of the specimen is terminated as soon as the water level in the quench cylinder reaches 25 mm elevation of the specimen. The water level in the quench tube is kept constant by simultaneously raising a large balance tank, which is connected to the quench tube. The water in the balance tank can be heated and is continuously circulated through the quench cylinder. Steam flow rates up to 2 g/s are used in the experiments with rapid steam cooling. The inductive heating of the specimen is terminated at the onset of rapid cooldown by steam.

The test matrix is shown in Fig. 5 together with a scheme of the test conduct. Test series with specimens without preoxidation, with oxide scales of 100 µm and 300 µm ZrO_2 thickness and specimen temperatures of 1200 °C, 1400 °C and 1600 °C before cooldown have been performed. The specimens were quenched by water or rapidly cooled by steam. Experiments with water quenching have been performed under the same conditions a second time to determine how reproducible the results are. Be-

cause of the high radiative heat losses in the QUENCH rig, none of the tests conducted have resulted in significant temperature excursion occurring during quenching such as had been observed for example in the quenched (flooded) CORA-bundle tests /4, 5/. The specimen is mounted in the QUENCH rig and heated to 1400 °C in an argon-oxygen atmosphere (see Fig. 5). It is then kept at this temperature until the desired oxide scale thickness is reached. Afterwards argon-oxygen is replaced by argon and the specimen is heated or cooled to the desired initial temperature. The water temperature before quench amounts to 90 °C and the flooding rate to 1.5 cm/s in experiments with water quenching. Experiments with rapid cooldown by steam have been performed with a steam inlet temperature of 140 °C and a steam flow rate of about 2 g/s. The temperature of the Zircaloy tube is measured by three thermocouples attached to its outer surface. The transient temperatures of the outlet gas/steam mixture and of the quench water (water-quenching) or the steam flow rate (rapid steam-cooling) are also measured. A video camera is used to record the behavior and movement of the quench front. After passing a condenser the hydrogen content of the outlet gas is determined by two methods. A Caldos device determines the hydrogen concentration of the outlet gas by measurement of the electrical conductivity of the argon-hydrogen mixture. The outlet gas is also sampled at a predetermined rate for mass spectrometer measurements.

3. Temperature measurement

Temperatures of the outer surface of the cladding are recorded at 28 mm, 75 mm and 122 mm elevation, referred to the lower end of the specimen. The temperature of the specimen has a substantial impact on the generation of mechanical stresses in the material and on the oxidation kinetics. The accuracy of temperature measurement has to be taken into account if one uses the experimental results for modeling. Therefore, temperature measurement is discussed here in detail.

Pt/Rh thermocouples have been used in the experiments in the QUENCH rig. The legs of the thermocouples are connected by a small pearl formed by welding. The pearl represents the hot junction. One has to keep in mind that temperature curves always represent the temperature of the hot junction. In tests without preoxidation a rhenium foil with a thickness of 150 μm and an area of 3□3 mm is spot welded on the outer surface of the specimen. The thermocouple pearl is then spot welded on the foil. Rhenium prevents the eutectic interaction of Zircaloy with the thermocouple materials. This arrangement guaranties a close contact between thermocouple and specimen, but it cannot be used in an oxidizing atmosphere. The rhenium foil would also oxidize, thus allowing the chemical interaction of the material of the thermocouple with Zircaloy. Therefore, in this case a preoxidized ring (outer diameter 11.8 mm, 0.8 mm thick) of Zircaloy is used to fix the thermocouple pearl on the outer surface of the slightly preoxidized ($\leq$ 10 μm ZrO_2) specimen, as can be seen in Fig.6. The ring has a conical slope on its inner side to press the thermocouple on the surface. The thin oxide layers prevent the chemical interaction between the cladding and the thermocouple. A small gap between the ring and the tube specimen forms at the position, where the thermocouple is pressed on the specimen.

A number of tests with spot welded thermocouples and thermocouples fixed by a ring have been performed to determine the reliability of the applied methods of temperature measurement. Fig. 7 represents the temperature measurement with both

methods of thermocouple attachment applied in the center of an empty specimen, quenched from 1000 °C. The temperature curves coincide down to the temperature of about 750 °C. Then the thermocouple readings deviate strongly. Our explanation for this behavior is, that the ring acts as a cooling fin thus shifting the transition from film boiling to nucleate boiling to higher temperatures in the vicinity of the ring. In the film boiling regime the steam film insulates the specimen from the water, reducing the heat transfer. With decreasing temperature of the specimen the steam film becomes thinner. The rewetting of the ring starts, if the surface of the specimen is still in the film boiling regime. Rewetting or nucleate boiling is accompanied by enhanced heat removal. Therefore, the temperature in the vicinity of the ring is lower than at other axial positions of the specimen if the recorded temperature falls below 800 °C. Regarding enhanced oxidation and hydrogen generation the interesting temperature range is above 800 °C, and for that range temperature measurement with thermocouples fixed by a Zircaloy ring can be applied. However, one should keep in mind that the temperature measurements below 800 °C underestimate the real surface temperature in the case of preoxidized specimens and quenching by water.

4. Experimental results

Temperature curves of central thermocouples and pertinent hydrogen concentrations in the outlet gas are represented in Fig. 8 through Fig. 13 for experiments with water quenching and rapid steam cooling, respectively. The time scales in Fig. 8 to Fig. 13 are referred to the termination of the inductive heating, i.e. for experiments with water quenching zero seconds correspond to that moment, where the water level in the quench cylinder reaches 25 mm elevation of the specimen. For experiments with steam cooling zero time corresponds to the onset of the steam cooling.

No significant temperature excursion during quenching occurred such as had been observed for example in the quenched (flooded) CORA-bundle tests /4, 5/. This absence of any temperature escalation is believed to be due to the high radiative heat losses in the QUENCH rig. The temperature curves for different degrees of preoxidation are very similar at temperatures above 800 °C for both steam cooled and water quenched experiments, thus proving the reproducibility of the experiments. The steep temperature drop in case of preoxidized specimen if the temperatures fall below 800 °C is based on the method of temperature measurement and does not reflect the real surface temperature of the specimen, as discussed in the last paragraph. Transition from film boiling to nucleate boiling occurs at 400 °C. Therefore, new metallic surfaces forming due to stresses generated by the rapid cooldown at transition to nucleate boiling cannot contribute to hydrogen generation.

The time-dependent hydrogen content in the outlet gas presented in Fig. 8 through Fig. 13 has been measured with a mass spectrometer. The gas samples were taken at the gas outlet after the steam condenser. The transport of the gas through the condenser and the gas pipe results in a delay between hydrogen release by the specimen and hydrogen measurement. The dependency of hydrogen release on the various experimental boundary conditions will be discussed later in this section.

The mechanical behavior of the cladding tube depends on the initial oxide scale thickness and the tube temperature at the onset of quench. Results regarding test series with water quenching are summarized in table 2. Table 3 presents the me-

chanical behavior of specimens rapidly cooled by steam. Specimens with 300 µm thick oxide scales are generally very brittle. Some specimens fragmented during handling after the experiments, others even in the facility (see table 2). Large cracks, penetrating the oxide layer and metal substrate, can be observed in water-quenched and steam-cooled specimens with a 300 µm thick oxide layer (Fig. 14). Metallographic examinations show that most of the metallic Zircaloy is converted into the brittle oxygen-stabilized α-Zr(O). The surfaces of the cracks are partially oxidized, as can be seen in Fig. 14. This indicates that the cracks have already formed at high temperatures and that they therefore contribute to the hydrogen generation. Zirconia changes its crystal structure from tetragonal to monoclinic at about 1200 °C during cooldown. This phase transition is accompanied by a volume increase, thus generating mechanical stresses in the oxide /3/. The crack formation at specimen temperature of about 1200 °C was also directly observed during an experiment with slowly reduced inductive heating and slow cooldown. This observation confirms that the cracks are generated at high temperatures because of the phase transition. The formation of the cracks is more pronounced if the quench is initiated from low temperatures (1200 °C compared to 1600 °C), as can be seen in Fig. 15 and Fig. 16. The number of cracks penetrating the oxide and metal increases with decreasing temperature of the specimen before cooldown, in experiments with water quenching as well as in experiments with cooldown by steam. Fig. 17 shows the result of an attempt to visualize cracks penetrating oxide and cladding by filling segments of the cladding with an acetone soaked cotton wool. The „acetone“ tracks on the right side of Fig. 17 indicate the pattern of cracks penetrating the cladding. These through-wall cracks can enable double-sided cladding oxidation and by this enhanced hydrogen generation. A number of small cracks on the surface of the specimen can be observed besides the large cracks. Fig. 18 shows the typical pattern of a cladding with a 300 µm thick oxide scale. The large cracks are accompanied by a number of small cracks aligned close together. Additional small cracks are distributed with larger distances to each other. Fig. 19 shows the surface of such a cladding at higher magnification. Cracks of different sizes form, not necessarily penetrating the whole cladding wall. But these cracks penetrate into the oxide layer at least partially, thus reducing the effective oxide scale thickness for the diffusion of oxygen to the metal. Therefore, also the small cracks can contribute to enhanced oxidation under reflood conditions.

Fig. 20 exhibits a cladding with a 300 µm thick oxide scale after cooldown by radiation, i.e., without cooling by steam or water, from four different azimuthal directions. The cladding is very brittle. Also without the additional cooling by steam or water, respectively, a lot of cracks formed. Moreover, a specimen with the same extent of preoxidation and a reduced cooldown rate of 1.5 K/s due to subsequent heating showed a similar crack pattern. This may be an indication that the crack formation is not necessarily dependent on high cooldown rates.

At specimens with 100 µm thick oxide scales cracks can mainly be found in the oxygen stabilized α-layer (Fig. 21). At this extent of preoxidation two to three macroscopic cracks penetrating the whole cladding wall have been observed, however only for water quenched and steam cooled specimens with an initial temperature of 1600°C (see table 3). The surfaces of the cracks were not oxidized and did apparently not contribute to hydrogen generation. Local spalling of the oxide layer on the phase boundary between oxide and metal occurred at some of the water quenched specimens with an 100 µm thick oxide scale, but not in experiments with rapid steam

cooling (see Fig. 22). However, the observed spalling seems not to be reproducible. The spalled surface amounted always only to less than 1% of the total surface of the cladding. The newly formed metallic surface was not oxidized and did probably not contributed to hydrogen generation.

The radiative heat losses in the QUENCH rig prevent the increase of the specimen temperature due to exothermic oxidation. Therefore, the oxidation rates and the total amounts of released hydrogen are low. Fig. 23 shows the comparison of the released hydrogen masses in the test series with water quenching and steam cooling, respectively. The experiments releasing the largest masses of hydrogen were performed at high temperatures and low preoxidation, as one should expect if diffusion-controlled oxidation is the governing process. The relatively high amount of hydrogen released in tests with 100 µm thick oxide scales and an initial temperature of 1600 °C is possibly based on the dissolution of zirconia during the two minutes before cooldown where the specimen is under pure argon (see Fig.5). The oxide layer can be reduced during this phase of the experiment to ZrO_{2-x} because of the diffusion of oxygen into metallic Zircaloy. The oxidation of substoichiometric zirconia during cooldown by steam or water may then result in the relatively high amounts of released hydrogen. The impact of crack formation on hydrogen release can be seen in specimens with 300 µm thick oxide scales and 1200 °C or 1400 °C specimen temperature at onset of cooldown. From the description of the oxidation by diffusion, i.e., without taking into account the influence of cracks, one should expect an exponential increase of hydrogen release with increasing temperature of the specimens and an exponential decrease of hydrogen release with increasing thickness of the oxide scale, as can be seen for specimens without preoxidation or with 100 µm thick oxide scales and for the specimens cooled down from 1600 °C, respectively. However, specimens with an initial temperature of 1200 °C and 300 µm thick oxide scales release more hydrogen than specimens with the same initial temperature and 100 µm thick oxide scales. The total amount of hydrogen released by specimen cooled down from 1400 °C is similar for specimens with 100 and 300 µm thick oxide scales in case of water quenching and steam cooling, respectively. This proves that the oxidation of crack surfaces contributes to the total amount of the released hydrogen. In an environment with lower heat losses, as in the core of a nuclear reactor, the additional oxidation on crack surfaces could increase the specimen temperature thus leading to a further enhanced oxidation.

Zircaloy has considerable hydrogen storage potential at elevated temperatures, whereas the solubility of hydrogen in zirconia is very low. The uptake of hydrogen in metallic Zircaloy and its release during oxidation and cool down can affect the kinetics of hydrogen release during a severe accident. Hydrogen, absorbed in the metal in steam-starved regions of a reactor core can be released additionally on subsequent oxidation. Due to the preoxidation with an argon-oxygen mixture in the QUENCH-rig, the total amount of generated hydrogen during quenching or steam cooling consists of the released hydrogen and the hydrogen stored in the specimen. The hydrogen concentration of one sample of every specimen was therefore determined by the extraction method after the experiment. It was then assumed that the hydrogen concentration measured in the sample is the average hydrogen concentration of the specimen. The total amount of hydrogen stored in the specimens was determined with this concentration. Because of the unknown uncertainties of this procedure, the final results should be considered as semi-quantitative information. The

results for water-quenched and steam-cooled specimens are depicted in Fig. 24. It is known from literature that zirconia acts as a diffusion barrier isolating the hydrogen from the metal. This is in accordance to the low hydrogen content of specimens with 100 μm ZrO_2 preoxidation, which had intact oxide scales. The contribution of crack formation on the hydrogen uptake can be seen on specimens with 300 μm thick oxide layers in steam-cooled and water-quenched experiments. Hydrogen absorption by metallic Zircaloy during preoxidation in steam should alter the hydrogen absorption and release in the quench phase. Consequently, in future experiments preoxidation of the specimens will be performed in steam instead of in an argon-oxygen mixture. Cooldown rates are higher in the QUENCH rig than the expected cooldown rates in a reactor in case of a severe accident with flooding. Experiments with subsequent heating are planned to simulate adequate cooldown rates.

Some of the typical thermohydraulic boundary conditions during quenching of a reactor core can only be simulated by large-scale bundle tests. An experimental facility, which allows the quenching of bundle simulators under nearly adiabatic conditions is under construction at Forschungszentrum Karlsruhe. The first bundle quench experiment will be performed in 1997.

5. Summary and conclusions

A series of separate-effects tests on Zircaloy PWR fuel rod cladding segments is being carried out to study the generation of new metallic surfaces by cracking and fragmentation of the oxygen-embrittled cladding during quenching. It is assumed that the newly formed surfaces result in enhanced oxidation and hydrogen generation during quenching as observed in the TMI-2 accident and in several integral tests.

The tube specimen of a length of 150 mm, filled with ZrO_2 pellets, is suspended inside a quartz tube which is surrounded by an induction heating coil. Preoxidation of the Zircaloy tube specimen (0 - 300 μm ZrO_2 layer thickness) is executed at 1400 °C in an argon/oxygen gas mixture in the QUENCH rig immediately before quenching. The specimen is quenched from 1000 to 1600 °C by water (30 or 90 °C) or rapidly cooled-down by steam, respectively. The simulated flooding rate was 1.5 cm/s in all experiments; in the case of high speed steam quenching about 2 g/s steam of 150 °C has been injected. The temperature of the specimen and the hydrogen generation are continuously recorded during the quench tests.

The mechanical behavior of the cladding tubes depends on the quench temperature, the quench medium and the extent of preoxidation. Through-wall crack formation can be observed in all water or steam quenched specimens with 300 μm thick oxide layers. Crack formation is more pronounced at lower specimen temperatures before quenching. The surfaces of the cracks in the remaining metallic part of the cladding tubes are oxidized and contribute to hydrogen generation. The generation of additional hydrogen because of crack formation can also be seen in the measured total amounts of released hydrogen in the off-gas. Water-quenched specimens with 100 μm thick ZrO_2 layers can show localized spalling of the ZrO_2 scale. An influence of the local spalling on hydrogen generation can not be seen. Steam quenched specimens show no local spalling of the oxide layer at all.

The uptake of hydrogen in Zircaloy and its additional release during oxidation of the metal and during the cool down period can influence the kinetics of hydrogen release and has therefore to be studied quantitatively in more detail. Crack formation in the oxide and partially in the metal increases the total amount of hydrogen stored in the specimens. However, hydrogen absorption by metallic Zircaloy during pre-oxidation in steam could alter the hydrogen absorption and release in the quench phase.

Further activities are directed at the investigation of critical oxide layer thicknesses and critical cooldown rates (for quenching by steam only) which result in cracking of the tube specimen. The influence of the mode of preoxidation (argon oxygen mixture compared to steam) on the extend of hydrogen uptake and release shall also be determined. It is foreseen to measure the crack length per surface unit to support the modeling of the observed phenomena.

6. Acknowledgment

The authors thank Dr. T. Haste of AEA Technology, Winfrith, for valuable discussions and for his thorough and critical review of this paper.

We would also like to thank Mr. H. Metzger for the preparation of the specimens, the conduct of the experiments and for the metallographic preparation and examination of the specimens as well as Mr. J. Burbach for the SEM examinations.

The work was partly funded by the European Union in the framework of the Nuclear Fission Safety Program “Investigation of Core Degradation” under contract number FI4S-CT95-0013.

7. References

/1/ M. Firnhaber, K. Trambauer, S. Hagen, P. Hofmann, „ISP-31 OECD/NEA-CSNI International Standard Problem, CORA-13 Experiment on Severe Fuel Damage“, NEA/CSNI/R (93) 17, GRS-106, KfK 5287, 1993

/2/ T. J. Haste, B. Adroguer, N. Aksan, C. M. Allison, S. Hagen, P. Hofmann and V. Noack, “Degraded Core Quench: A Status Report”, NEA/CSNI/R(96)/4, OECD/ SD(97)5, 1997

/3/ C. M. Allison et. all., ”MATPRO-A Library of Materials Properties for Light-Water-Reactor Accident Analysis”, NUREG/CR-6150, 1994

/4/ S. Hagen, P. Hofmann, V. Noack, G. Schanz, G. Schumacher and L. Sepold, ”Results of SFD Experiment CORA-13 (OECD International Standard Problem 31)”, KfK 5054, February 1993

/5/ S. Hagen, P. Hofmann, V. Noack, G. Schanz, G. Schumacher and L. Sepold, „Comparison of the Quench Experiments CORA-12, CORA-13, CORA-17“, FZKA 5679, August 1996

QUENCH-rig

Specimen temperature	1000 - 1600 °C
Water temperature	30 - 90 °C
Flooding rate	0.3 - 3 cm/s
Steam flow rate	< 2g/s
Extent of preoxidation	< 350 µm ZrO_2 scale thickness

Specimen:

Rod length	150 mm
Cladding thickness	0.725 mm
Cladding outside diameter	10.75 mm
Cladding material	Zircaloy-4
Pellet outer diameter	9.1 mm
Pellet material	dense ZrO_2, MgO stabilized (no phase transformation)

Quartz cylinder

Outer diameter	44 mm
Inner diameter	40.5 mm

Quench cylinder (quartz)

Outer diameter	34 mm
Inner diameter	30.5 mm
Length	215 mm

Table 1: Design characteristics of the QUENCH rig

Test	Temp. Before quenching °C	Oxide layer µm	α-Zry layer µm	β-Zry µm	Water temp. °C	Quench rate cm/s	Hydrogen[1] Caldos/ Spectrometer mg	Weight gain[2] mg/%	Increase of length mm	∅ increase max. mm	macroscopic post-test appearance of the specimen
19105_1	1000	not yet investigated			90	1.5	2.9/-	25	-	0.01	no cracks in and no spalling of ZrO_2 layer; specimen surface black shining
18105_1	1000	115 115 115	150 160 160	rest rest rest	90	1.5	0./-	1.04/ 3.7	1.1	0.14	specimen mechanically still very stable, no cracks in and no spalling of ZrO_2 layer; cracks only in the α-Zr(O) layer
13105_1	1000	285 255 265	rest rest rest	- - -	90	1.5	2.4/-	fragmentation of the specimen in the facility		-	specimen very brittle; ZrO_2 layer splits locally at the tin layer; partial spalling of ZrO_2 layer; cracks in radial direction penetrating the cladding wall (ZrO_2 layer and metal); no oxidation of crack surfaces
24085_1	1200	upper pos. 5 central pos. 5.5 lower pos. 7.5	4 45 5	rest rest rest	90	1.5	3.2/-	56	0.35	0.02	no cracks in and no spalling of ZrO_2 layer; specimen surface black shining
20066_1	1200	0*			90	1.5	5.7/5.2				no metallographic investigation; no cracks in and no spalling of ZrO_2 layer; specimen surface black shining
04066_1	1200	100*			90	1.5	1.1/1.0	960/3.6	1.0		no metallographic investigation; no cracks in and no spalling of ZrO_2 layer; specimen surface gray

* oxide scale thickness estimated from the duration of preoxidation

Table 2: Experiments with quenching by water

Test	Temp. Before quenching °C	Oxide layer µm	α-Zry layer µm	β-Zry µm	Water temp. °C	Quench rate cm/s	Hydrogen[1] Caldos/ Spectrometer mg	Weight gain[2] mg/%	Increase of length mm	∅ increase max. mm	macroscopic post-test appearance of the specimen
06075_1	1200	120 120 120	160 190 195	rest rest rest	90	1.5	1.4/-	1130/4	1.1	0.13	specimen mechanically still stable; cracks only in the α-Zr(O) layer; local spalling of ZrO_2 layer (about 12 mm^2) 36 mm from the lower end of the specimen
25095_1	1200	300 265 280	rest rest rest	- - -	90	1.5	2.2/-	2504/9	0.9	0.54	specimen very brittle; macroscopic cracks in axial and circumferential direction penetrating the cladding wall (ZrO_2 layer and metal), surfaces of the cracks and inner surface of the cladding oxidized; ZrO_2 layer splits locally at the tin layer; local spalling of ZrO_2 layer (about 50 mm^2) 15-24 mm from the lower end of the specimen
30056_1	1200	300*			90	1.5	-/2.0	specimen broken during handling after the experiment		0.6	no metallographic investigation; specimen very brittle; macroscopic cracks in axial and circumferential direction, cracks partially penetrating the cladding wall (ZrO_2 layer and metal)
28085_1	1400	7.5 10 13	12 11 12	rest rest rest	90	1.5	7.7/-	123/ 0.44	0.5	0.05	specimen surface black shining, no cracks; local flaking of a thin ZrO_2 layer 15 - 20 mm from the lower end of the specimen
21066_1	1400	0*			90	1.5	9.5/9.1	100/ 0.36	0.3	0.06	no metallographic investigation; no cracks in and no spalling of ZrO_2 layer; specimen surface black shining

* oxide scale thickness estimated from the duration of preoxidation

Table 2: Experiments with quenching by water

Test	Temp. Before quenching °C	Oxide layer µm	α-Zry layer µm	β-Zry µm	Water temp. °C	Quench rate cm/s	Hydrogen[1] Caldos/ Spectrometer mg	Weight gain[2] mg/%	Increase of length mm	∅ increase max. mm	macroscopic post-test appearance of the specimen
05075_1	1400	100 100 100	200 220 200	rest rest rest	90	1.5	3.6/-	1012/ 3.74	0.85	0.2	specimen mechanically still stable, cracks only in the α-Zr(O), local layer spalling of oxide layer (about 15 mm^2) 95 mm from the lower end of the specimen; a thin ZrO_2 layer of 5 - 6 µm thickness was locally lifted off
29056_1	1400	100*			90	1.5	3.0/2.8	1012/ 3.74	0.95	0.14	no metallographic investigation, specimen mechanically still stable, some small cracks (only visible in the microscope) at 30 to 35 mm from the lower end of the specimen
12075_1	1400	280 320 310	rest rest rest	- - -	90	1.5	4.0/-	specimen fragmented during handling after the experiment		0.4	specimen mechanically very brittle; macroscopic cracks penetrating the ZrO_2 layer and the cladding wall; crack surfaces oxidized
05066_1	1400	300*			90	1.5	2.8/2.3	-	0.6		no metallographic investigation; specimen mechanically very brittle; cracks at 30 to 120 mm from the lower end of the specimen
31085_1	1600	14 16 30	24 24 30	rest rest rest	90	1.5	13.6/-	320/ 1.09	0.35	0.08	specimen surface black shining; no cracks in the ZrO_2 layer, some cracks in the α–Zr(O) layer; local flaking of the ZrO_2 layer 2-12 mm from the lower end of the specimen, possibly due to welding during pre-test preparation

* oxide scale thickness estimated from the duration of preoxidation

Table 2: Experiments with quenching by water

Test	Temp. Before quenching °C	Oxide layer µm	α-Zry layer µm	β-Zry µm	Water temp. °C	Quench rate cm/s	Hydrogen[1] Caldos/ Spectrometer mg	Weight gain[2] mg/%	Increase of length mm	∅ increase max. mm	macroscopic post-test appearance of the specimen
24066_1	1600	0*			90	1.5	39.5/41.5	-	0.9		no metallographic investigation; no cracks in and no spalling of ZrO_2 layer; specimen surface black shining
10075_1	1600	110 115 110	210 210 200	rest rest rest	90	1.5	14.8/-	1190/ 4.28	1.0	0.23	3 cracks penetrating the cladding wall, crack surfaces not oxidized; a lot of cracks in α-Zr(O), partially penetrating also β-Zry; local spalling of oxide layer (about 33 mm^2) 50-62 mm from the lower end of the specimen
31056_1	1600	100*			90	1.5	20.9/21.4	1013/ 3.77	1.45		no metallographic investigation; one 40 mm long crack can be seen in the microscope, local spalling of oxide layer (about 20 mm^2) 20-30 mm from the lower end of the specimen
27095_1	1600	300 310 260	rest rest partially still β-Zr		90	1.5	7.7/-	specimen fragmented during handling after the experiment		0.25	specimen very brittle; macroscopic cracks in axial and circumferential direction penetrating the ZrO_2 layer and the cladding wall. surfaces of the cracks partially oxidized
19066_1	1600	300*			90	1.5	5.9/5.7	specimen broken during handling after the experiment			no metallographic investigation; specimen very brittle, a number of cracks can be found
11075_1	1600	340 340 360	rest rest rest	- - -	90	1.5	9.3/-	specimen fragmented during handling after the experiment		0.3	specimen very brittle, comparable with specimen 27095_1

* oxide scale thickness estimated from the duration of preoxidation

Table 2: Experiments with quenching by water

Test	Temp. before quenching °C	Oxide layer µm	α-Zry layer µm	β-Zry layer µm	Steam flow rate g/s	Hydrogen[1] Caldos/ Spectro-meter mg	Weight gain[2] mg/%	Increase of length mm	∅ Increase max. mm	Macroscopic post-test appearance of the specimen
16046_3	1200	6 6 5	5 5 4	rest	1.75-2	9.5/9.5	0.047/ 0.17	0.5	0.02	no cracks in and no spalling of ZrO_2 layer, specimen surface black shining
16046_1	1200	100 105 100	150 165 170	rest	1.75-2	2.0/0.9	0.94/ 3.28	1.05	0.12	no cracks in and no spalling of ZrO_2 layer, cracks only in the α-Zr(O) layer; specimen still mechanically stable
27036_1	1200	250 270 275	400-500 400-500 rest	-	1.5-1.75	4.3/4.0	specimen fragmented during handling after the experiment		0.6	specimen extremely brittle; macroscopic cracks in axial and circumferential direction penetrating the ZrO_2 layer and the cladding wall; surfaces of the cracks oxidized
16046_2	1400	11 11 11	12 12 12	rest	1.75-2	14.3/14.6	0.11/ 0.42	0.15	0.04	no cracks in and no spalling of ZrO_2 layer, specimen surface black shining
25036_1	1400	85 90 90	190 210 220	rest	1.5-1.75	-/3.0	0.92/ 3.3	0.9	0.1	no cracks and no spalling of ZrO_2 layer, cracks only in the α-Zr(O) layer; specimen still mechanically stable
25036_2	1400	240 290 290	450 rest rest	- - -	1.5-1.75	4.3/4.9	-	2.0	0.33	specimen extremely brittle, macroscopic cracks in axial and circumferential direction penetrating the ZrO_2 layer and the cladding wall; surfaces of the cracks partially oxidized

Table 3: Experiments with cooldown by steam

Test	Temp. before quenching °C	Oxide layer µm	α-Zry layer µm	β-Zry layer µm	Steam flow rate g/s	Hydrogen[1] Caldos/ Spectro-meter mg	Weight gain[2] mg/%	Increase of length mm	∅ Increase max. mm	Macroscopic post-test appearance of the specimen
16046_4	1600	24 29 28	25 28 27	rest	1.75-2	38.0/39.0	0.25/ 0.93	0.35	0.05	no cracks in and no spalling of the ZrO_2 layer; specimen surface black shining
26036_1	1600	95 95 95	200 220 210	rest	1.5-1.75	15.1/15.4	0.99/ 3.55	1.3	0.20	no spalling of the ZrO_2 layer, specimen mechanically still stable; two cracks penetrating the ZrO_2 layer and the cladding wall, crack surfaces not oxidized, other cracks only in the α-Zr(O) layer
26036_2	1600	230 290 280	450 rest rest	rest - -	1.5-1.75	4.2/3.8	-	0.9	0.21	specimen very brittle; about six cracks in circumferential direction penetrating the ZrO_2 layer and the cladding wall, crack surfaces not oxidized

Table 3: continued

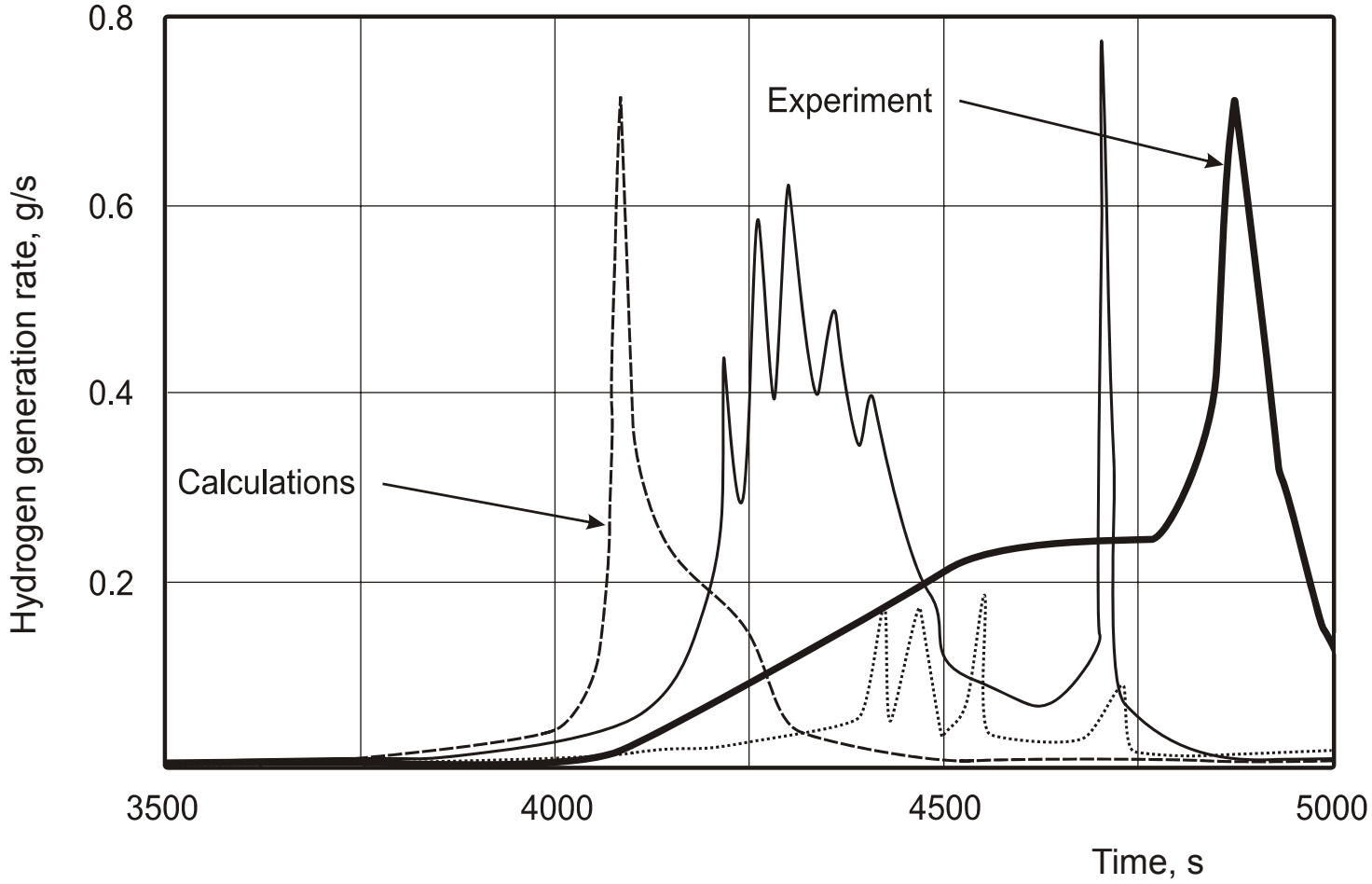

Fig. 1: Hydrogen generation rate (bundle and shroud) in the experiment CORA-13; Comparison of measurement with various calculations

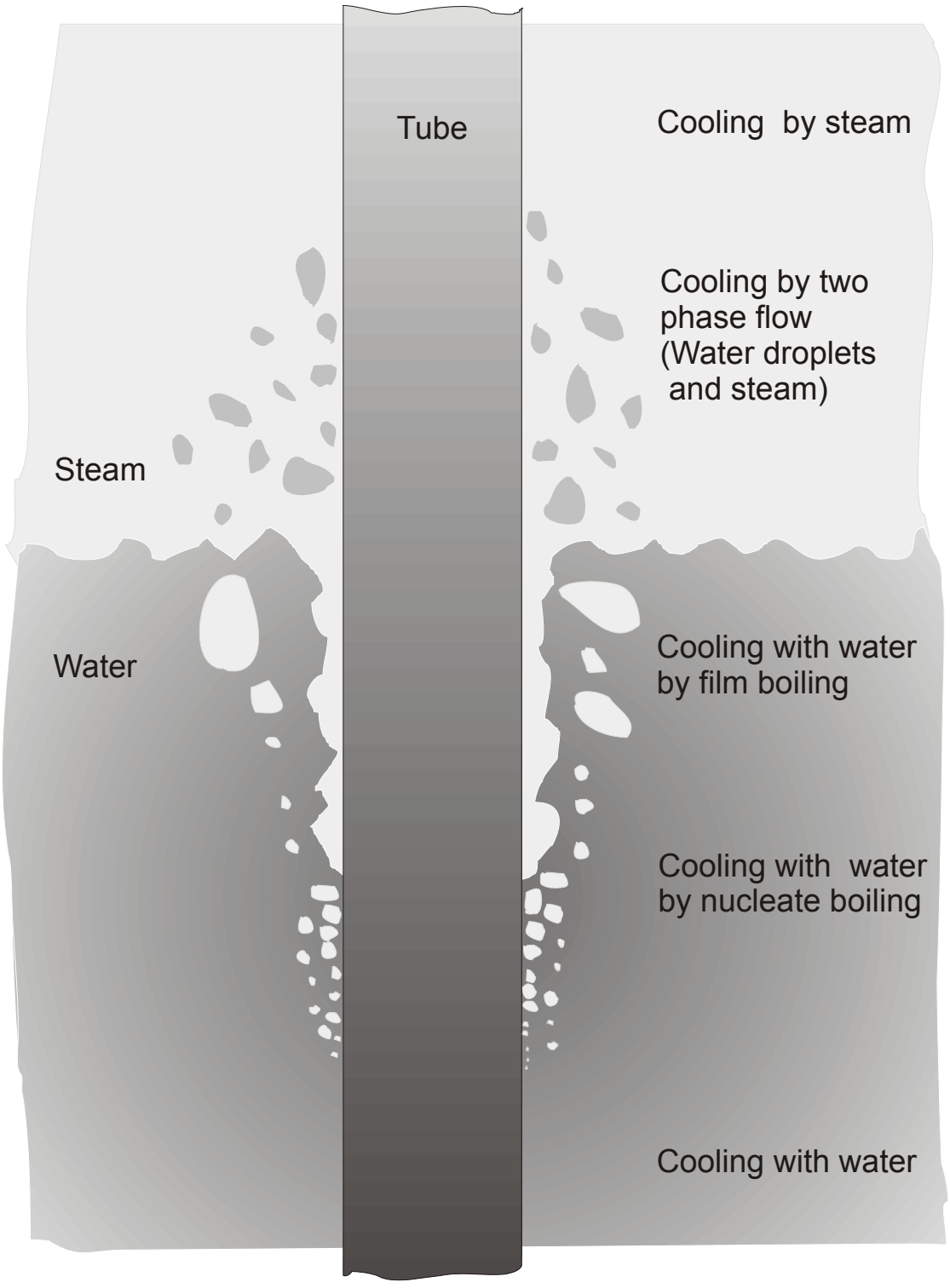

Fig. 2: Different cooling mechanisms during quenching

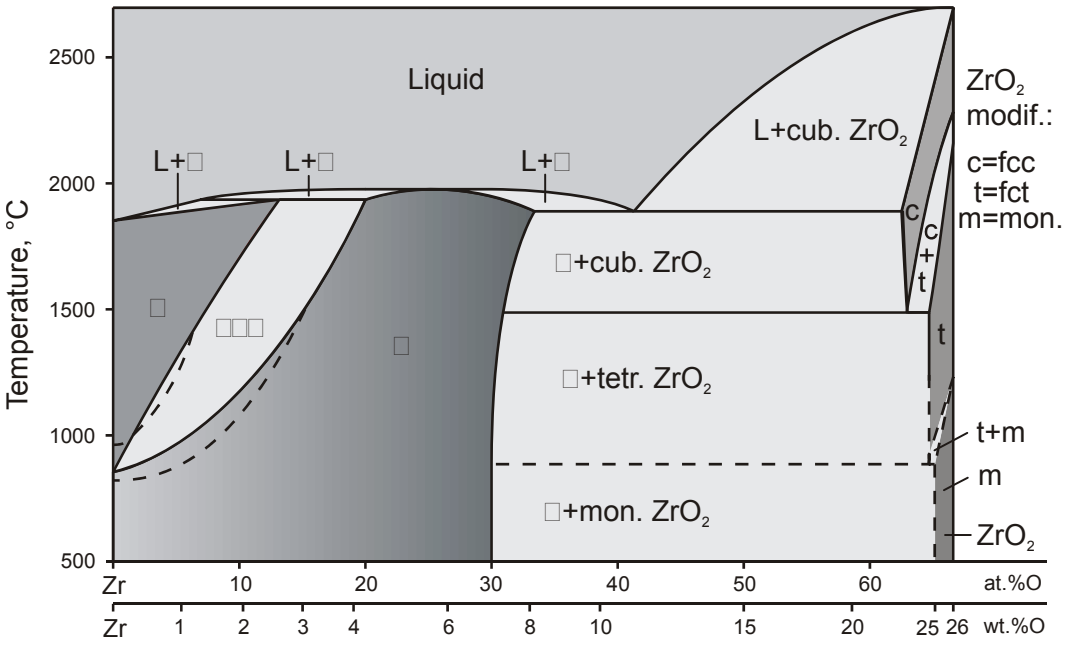

Zirconium-oxygen phase diagram*

*According to Gebhard et al. and Ruh et al. Modification for Zircaloy (□□□) field after Kassner et al.

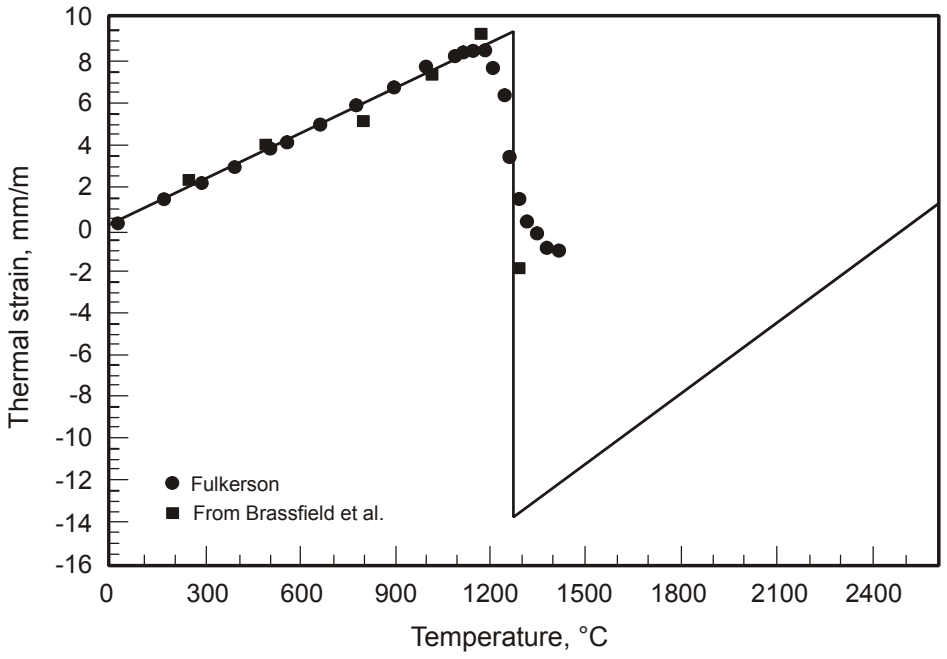

Zircaloy oxide thermal strain data*

* According to NUREG/CR-6150, Volume IV

Fig. 3: ZrO_2 monoclinic-tetragonal phase transition results in a discontinuous strain at about 1200 °C

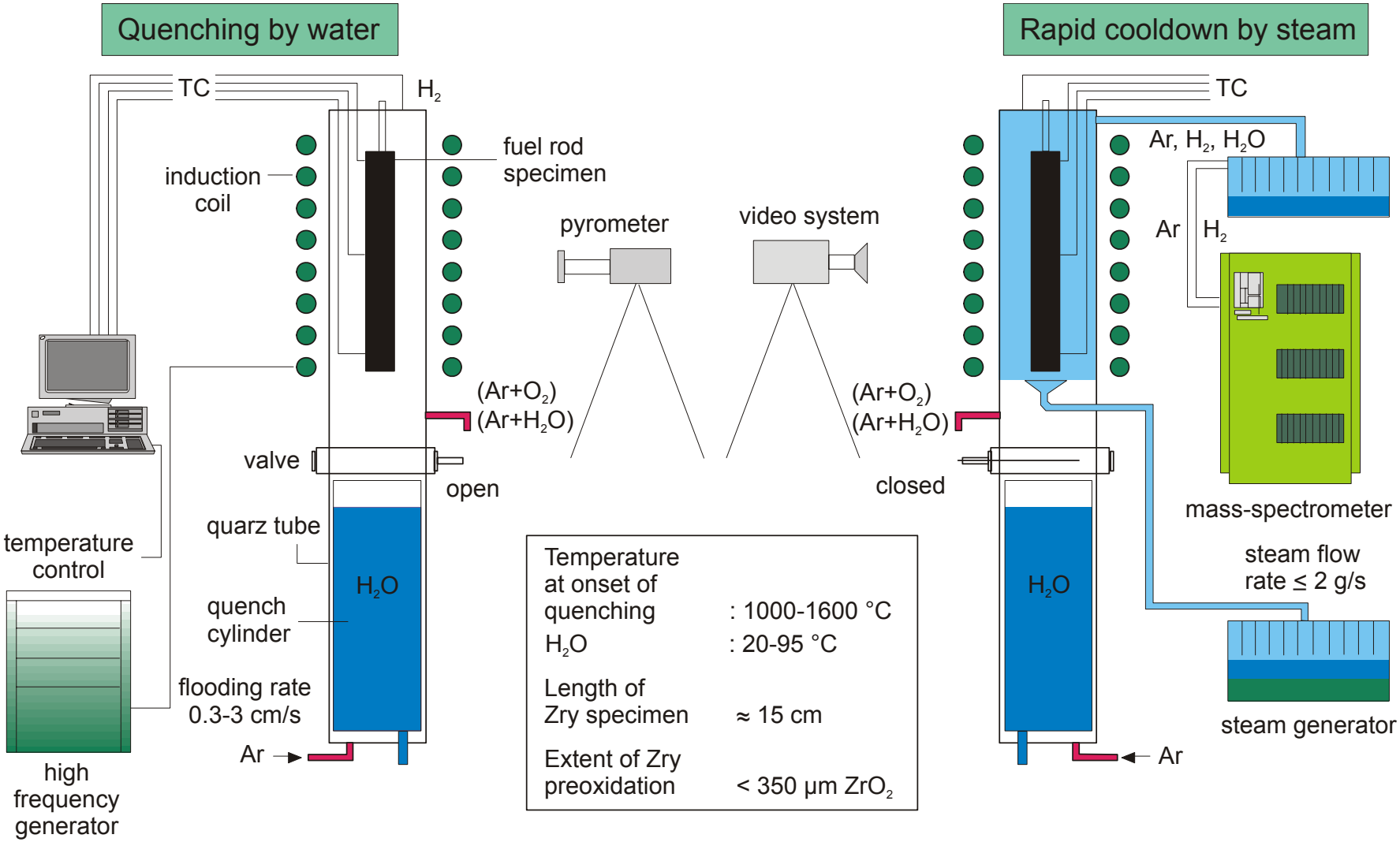

Fig. 4: Quench apparatus simulating flooding conditions of a degraded LWR core

- 19 -

Test Matrix

Test conditions:
Specimen filled with ZrO_2 pellets

Quenching by water
Initial Water Temperature: 90 °C
Flooding rate: 1.5 cm/s

Quenching by steam
mass flow rate: 2 g/s

Temperature, °C / Oxide layer, μm	1200	1400	1600
0	×	×	×
100	×	×	×
300	×	×	×

Test conduct

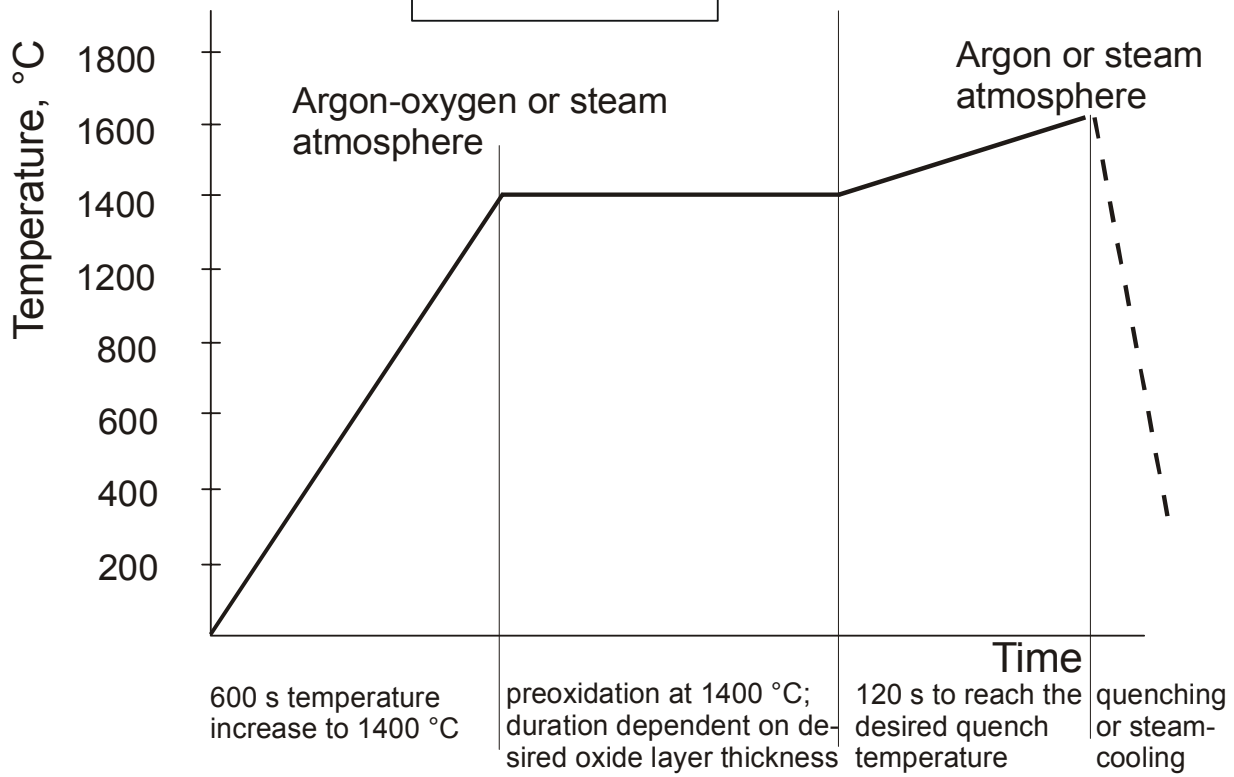

Fig. 5: Test conditions and test conduct

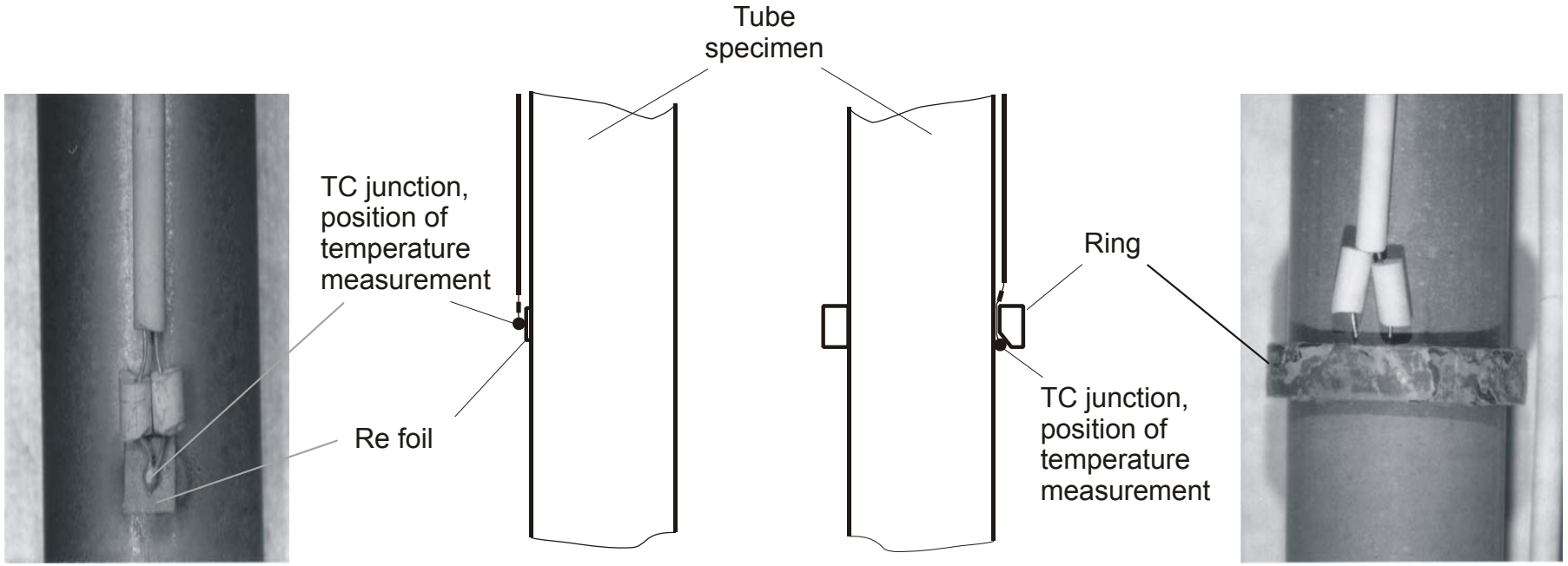

Spot welded TC
(no preoxidation)

TC fixed by a Zircaloy ring
(preoxidation)

Fig. 6: Temperature measurement methods in the QUENCH rig

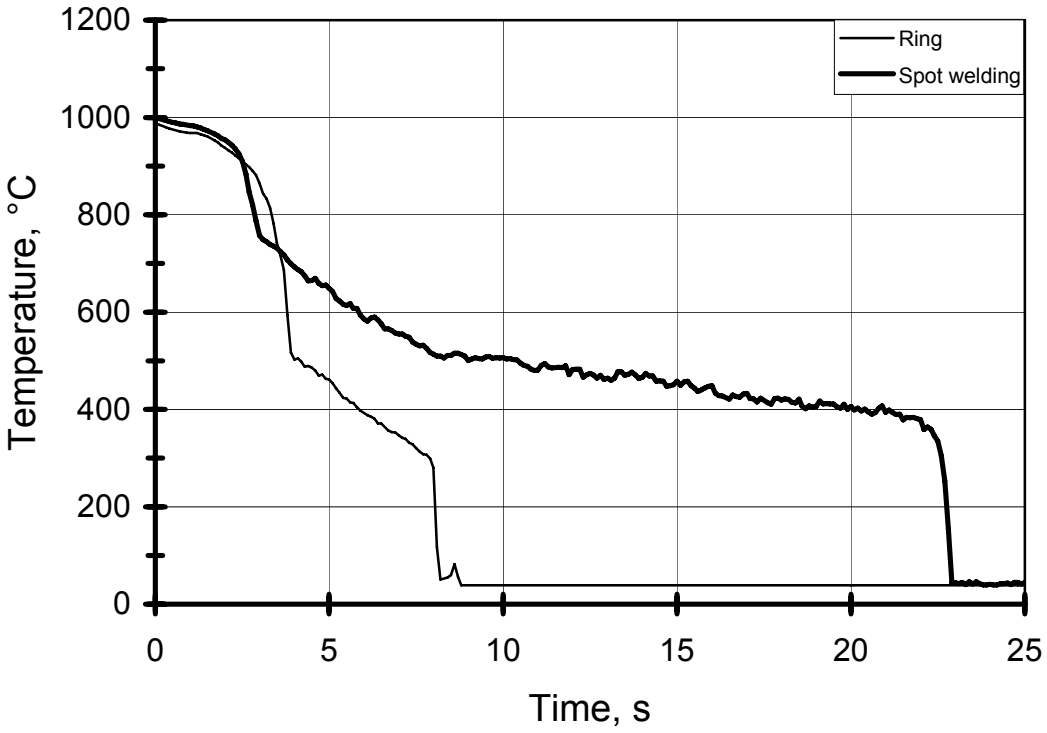

Fig. 7: Impact of thermocouple attachment on temperature measurement during water-quenching

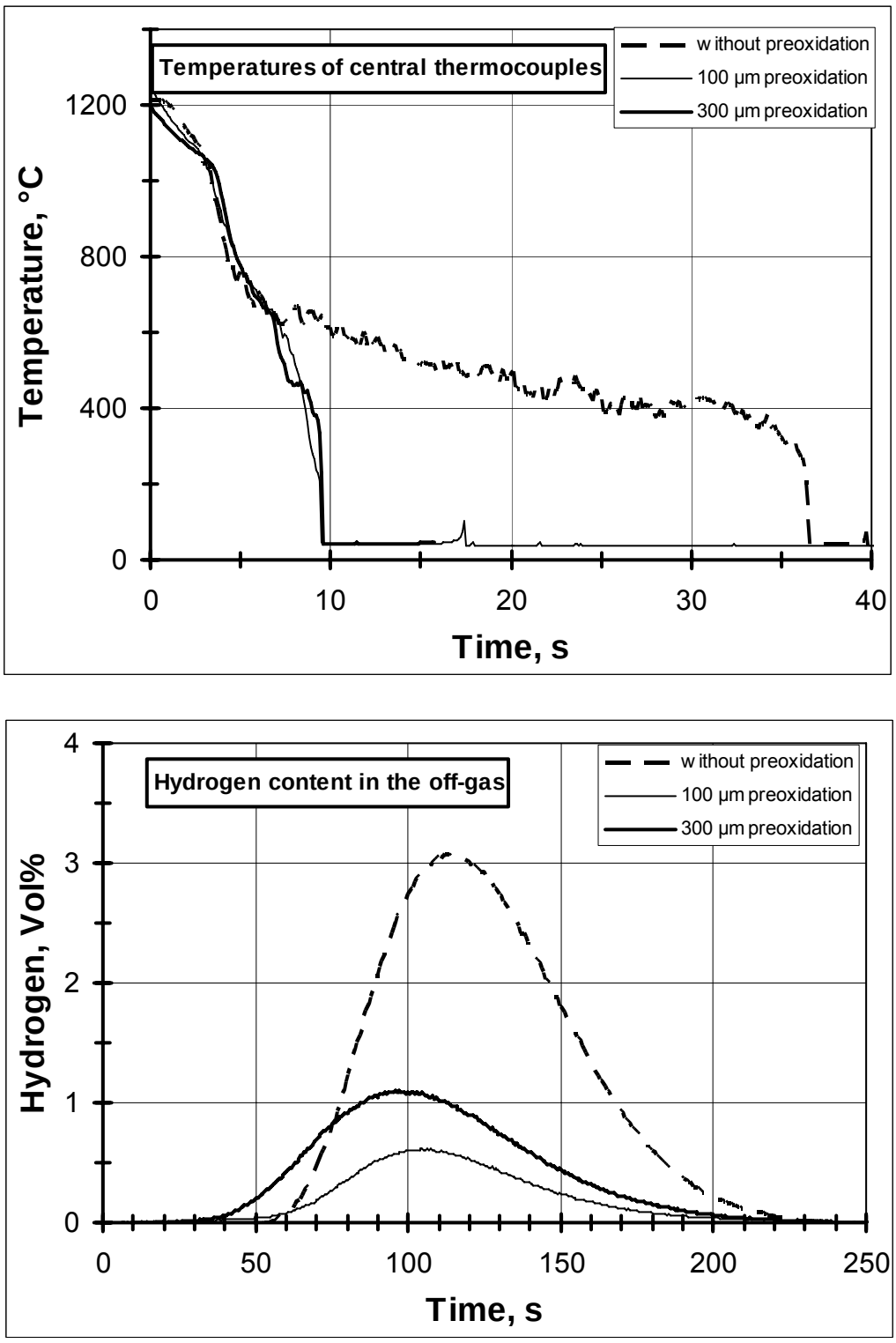

Fig. 8. Temperature history of central thermocouples and corresponding hydrogen release, water-quenching from 1200°C

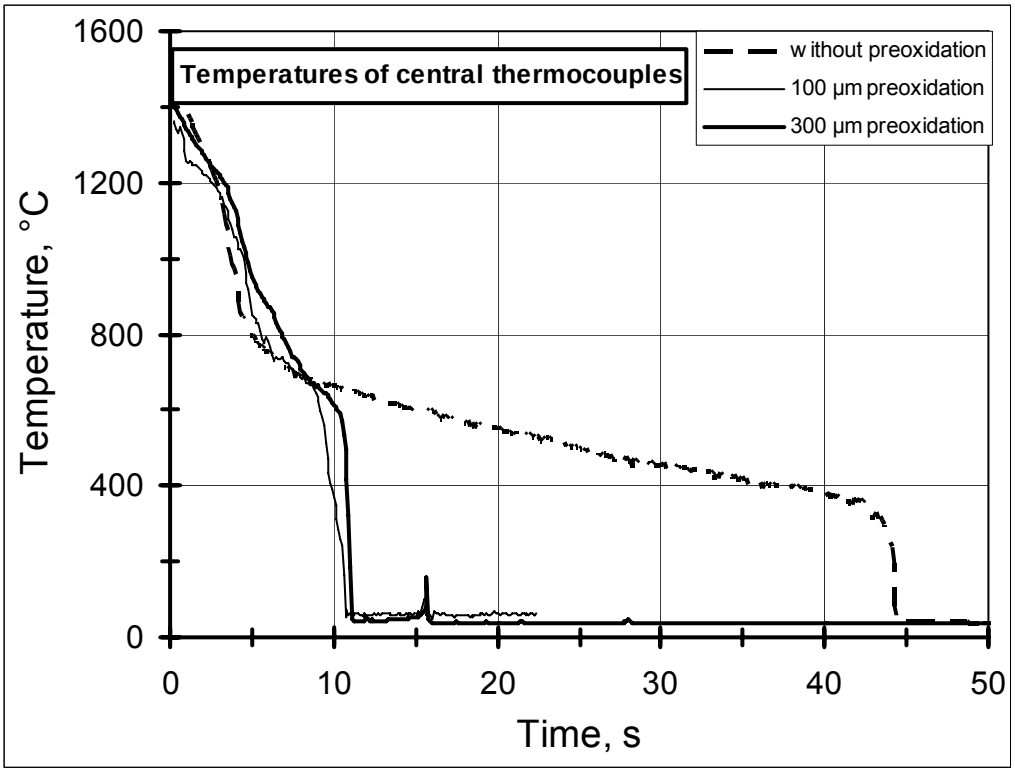

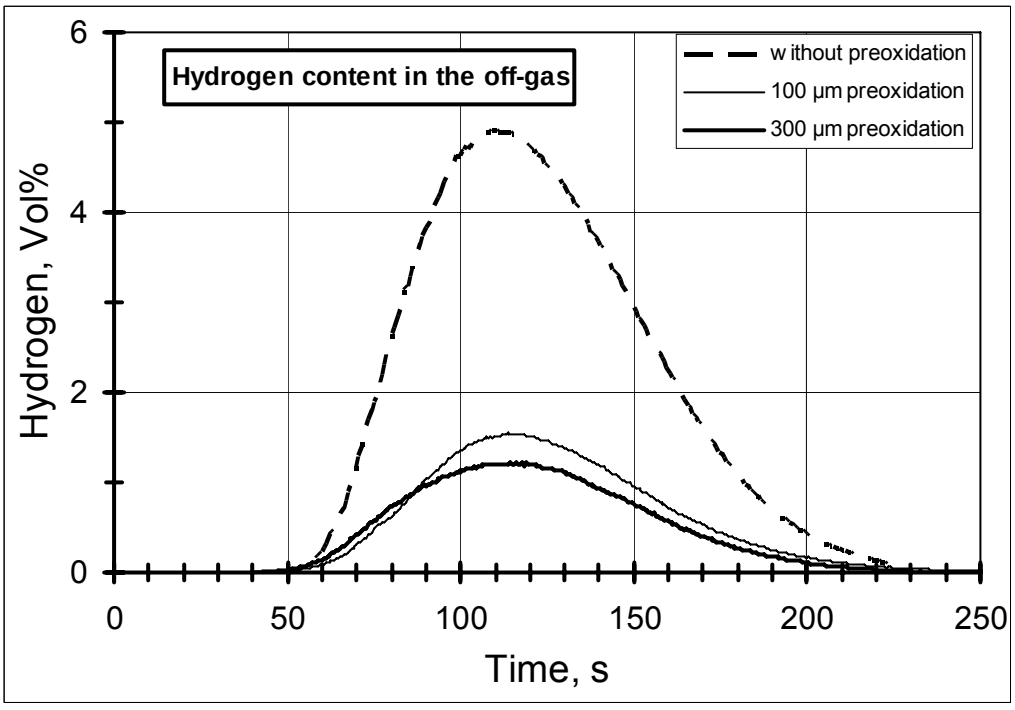

Fig. 9. Temperature history of central thermocouples and corresponding hydrogen release, water-quenching from 1400°C

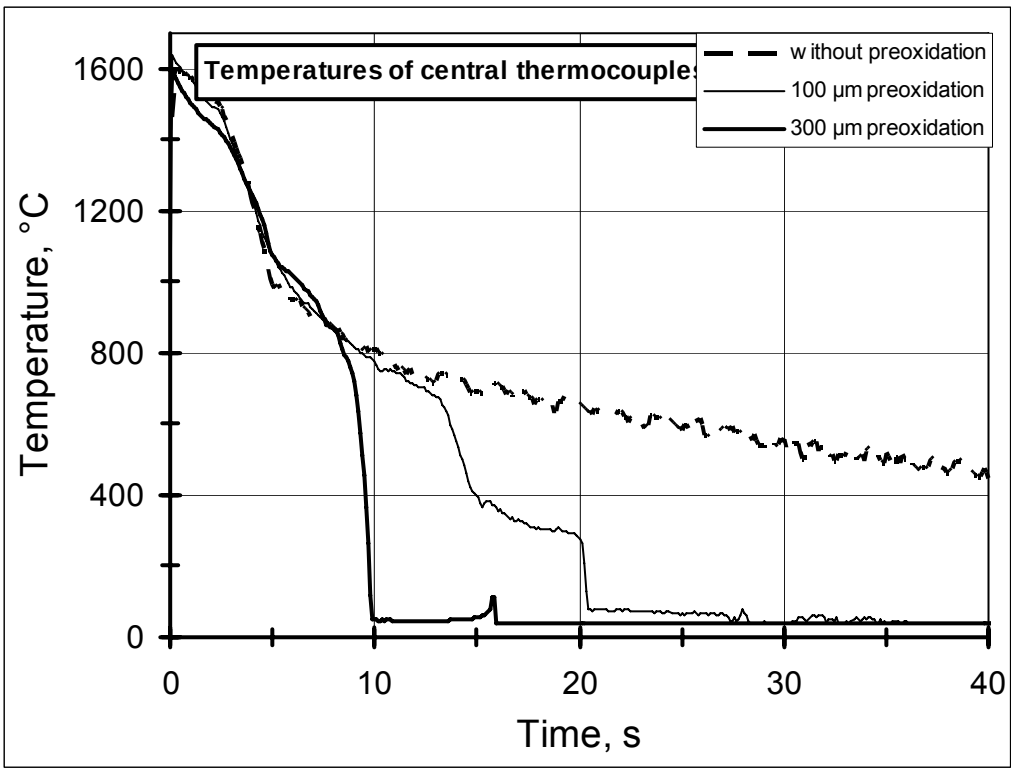

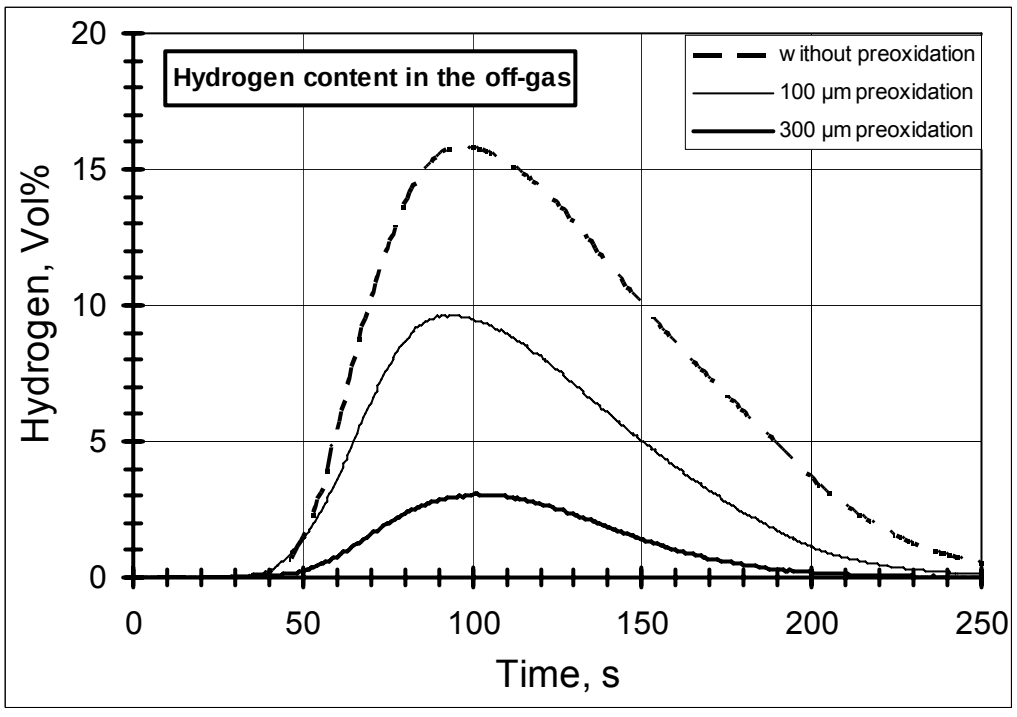

Fig. 10. Temperature history of central thermocouples and corresponding hydrogen release, water-quenching from 1600°C

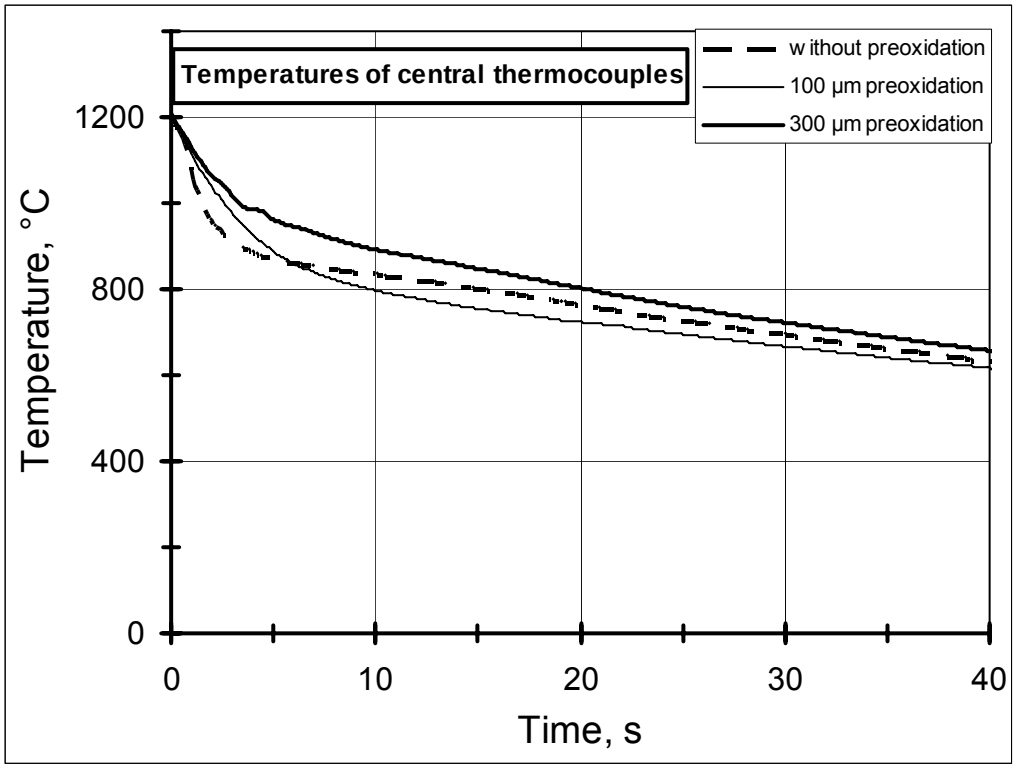

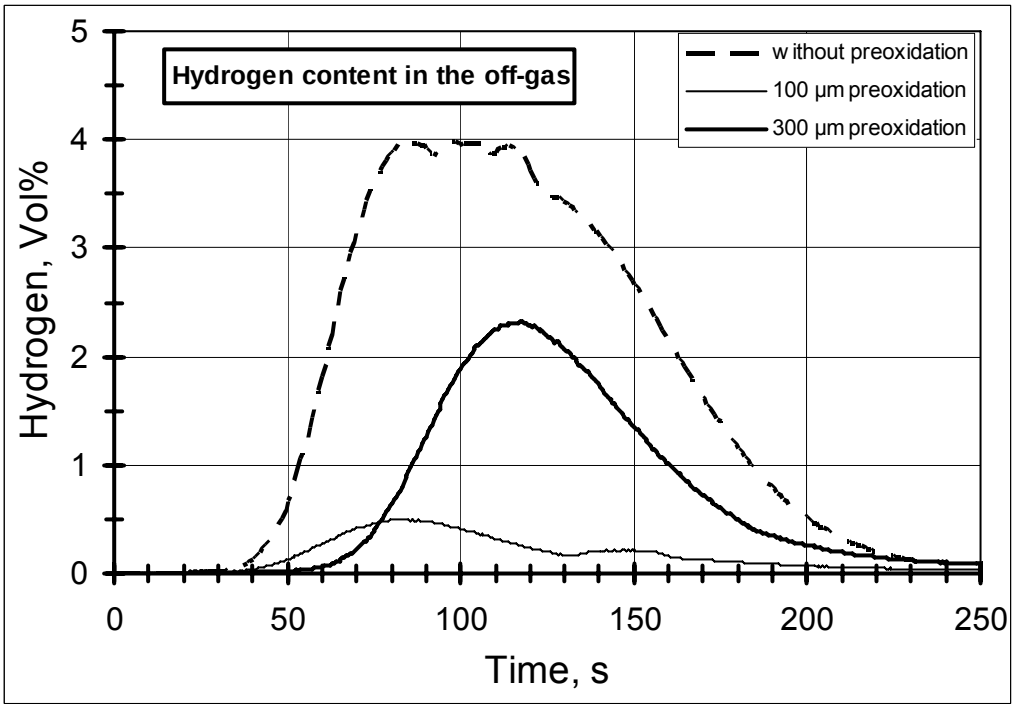

Fig. 11. Temperature history of central thermocouples and corresponding hydrogen release, steam-quenching from 1200°C

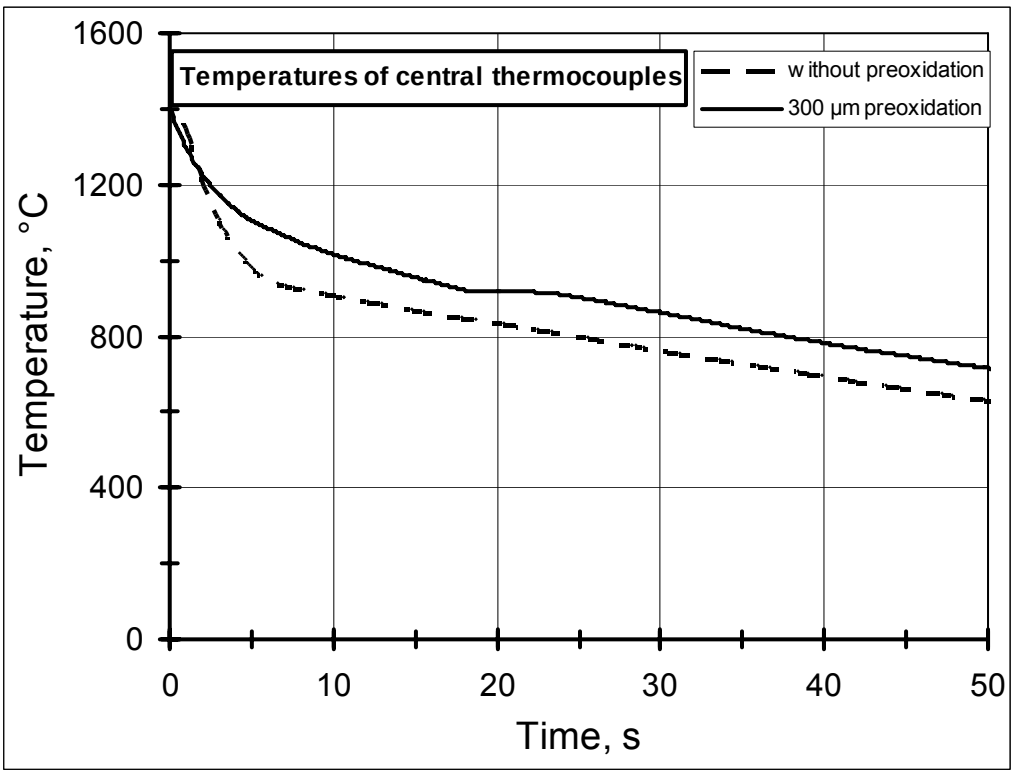

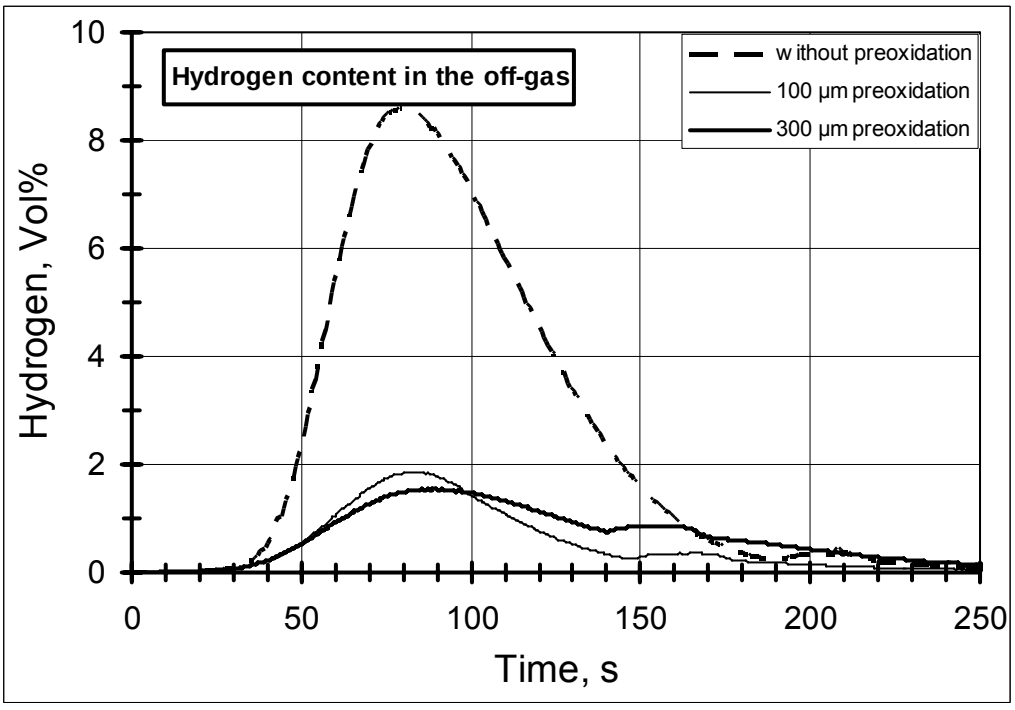

Fig. 12. Temperature history of central thermocouples and corresponding hydrogen release, steam-quenching from 1400°C

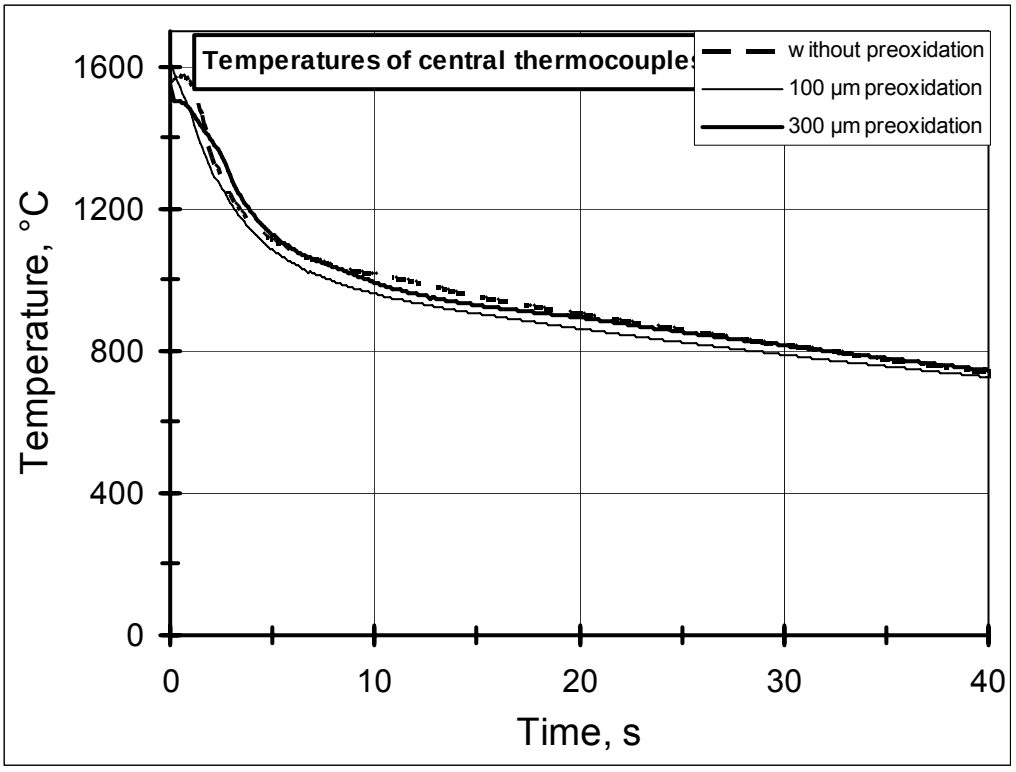

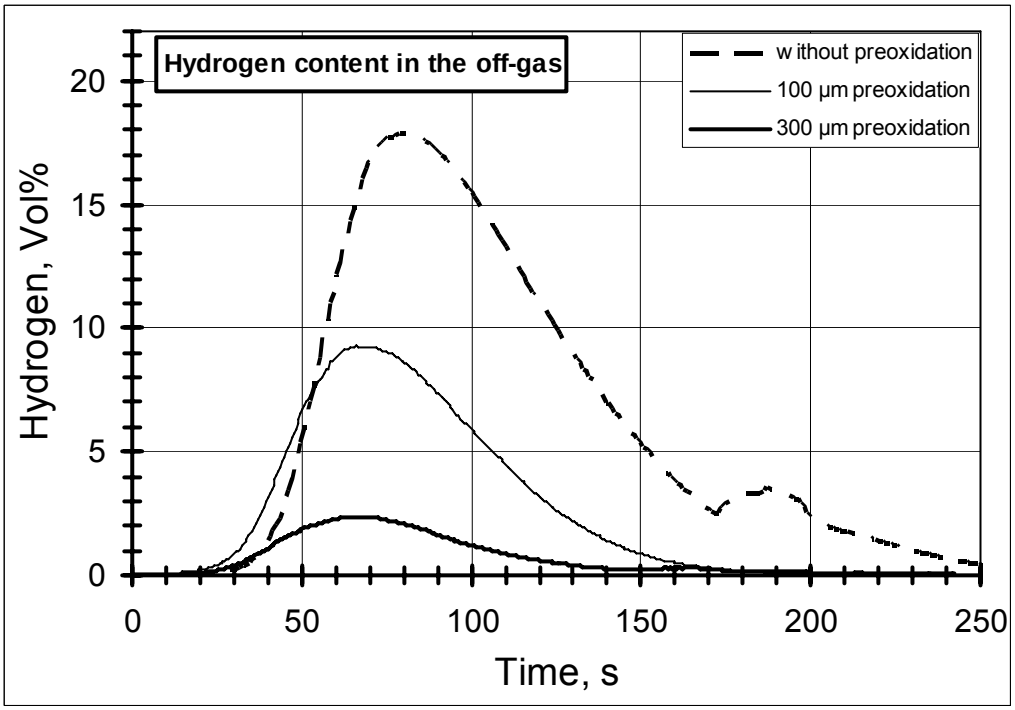

Fig. 13. Temperature history of central thermocouples and corresponding hydrogen release, steam-quenching from 1600°C

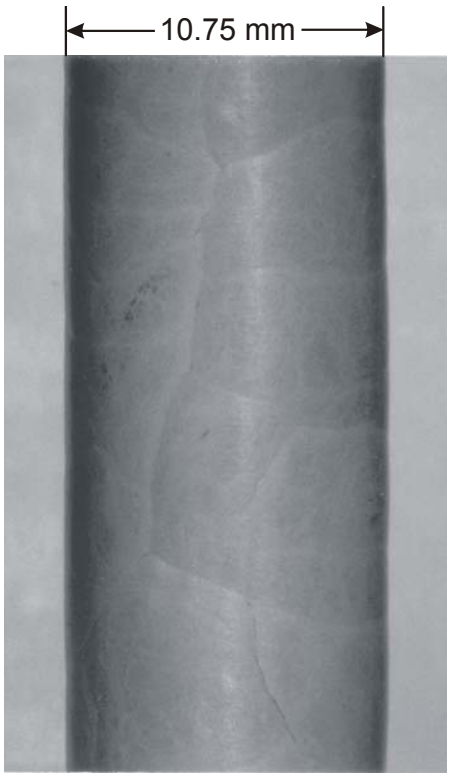

formation of
macroscopic cracks

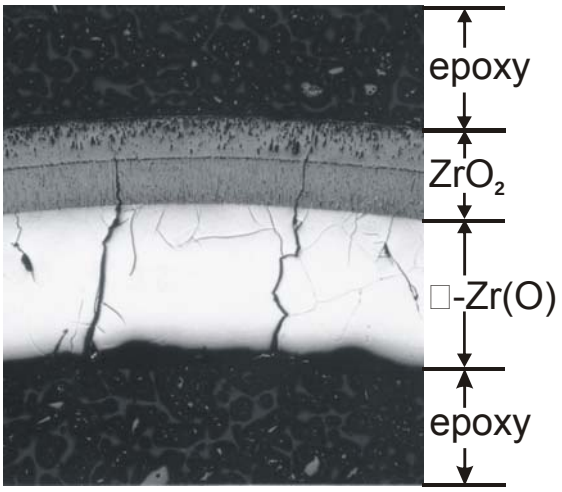

cracks penetrating oxide and metal

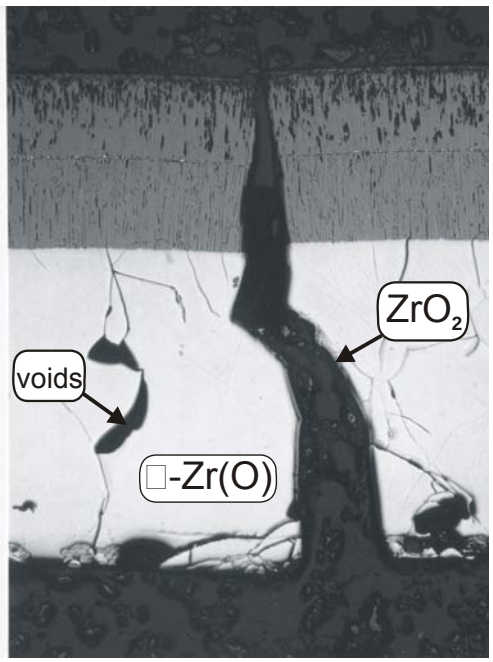

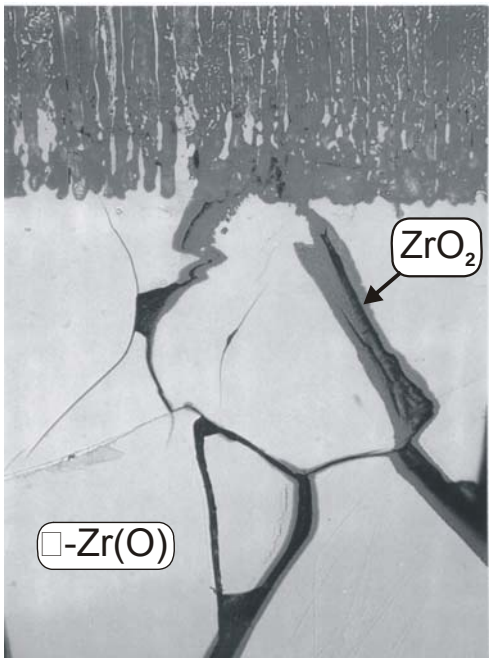

metallic surfaces of cracks oxidized during quenching

Fig. 14: Generation of cladding through-wall cracks;
300 µm preoxidation

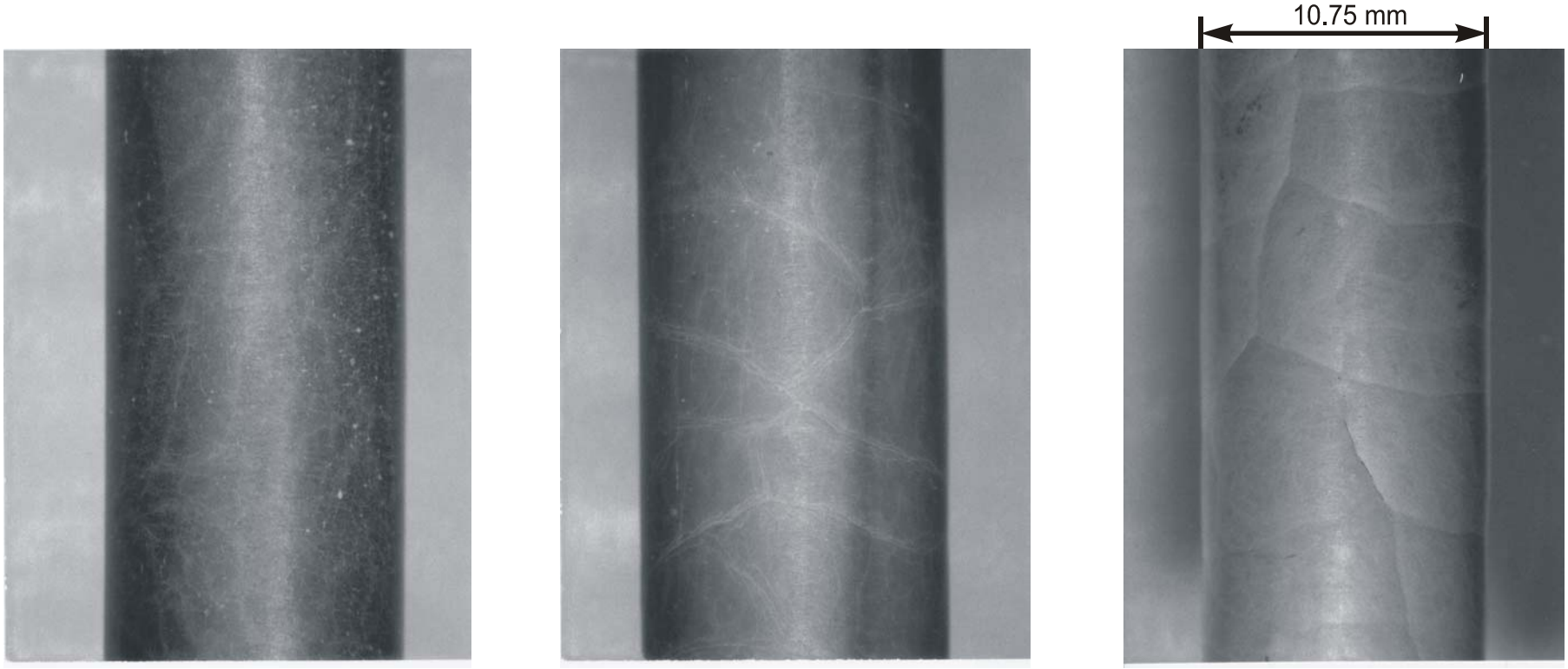

1600 °C 1400 °C 1200 °C

temperature at onset of quenching

Fig. 15: Crack formation in Zircaloy cladding after quenching by water; 300 µm preoxidation

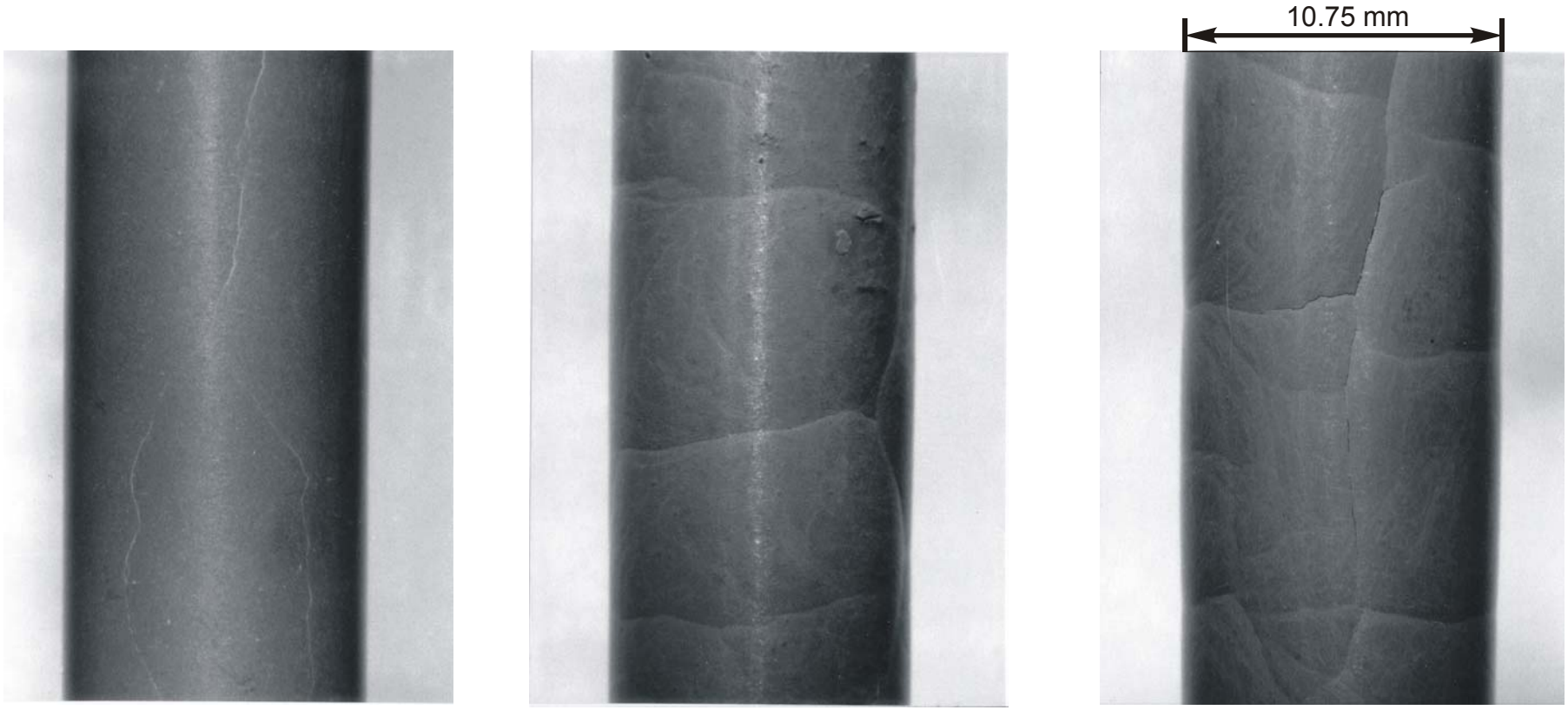

1600 °C 1400 °C 1200 °C

temperature at onset of quenching

Fig. 16: Crack formation in Zircaloy cladding after rapid cooldown by steam; 300 µm preoxidation

quenching from 1600 °C

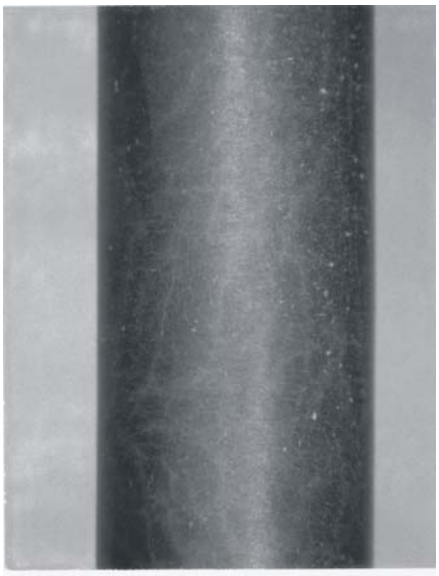

without visualisation

with visualisation

quenching from 1400 °C

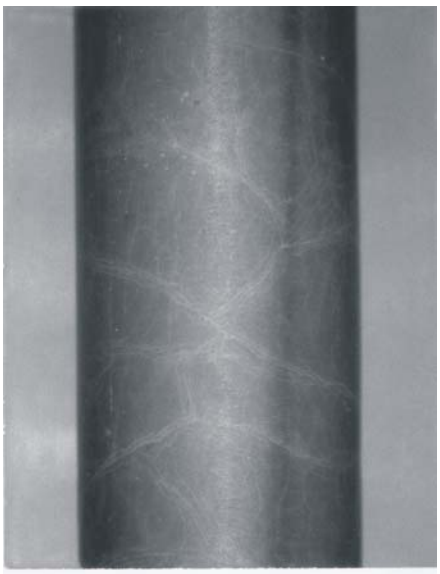

without visualisation

with visualisation

300 µm preoxidation

Fig. 17: Zircaloy cladding after quenching by water; visualisation of cracks

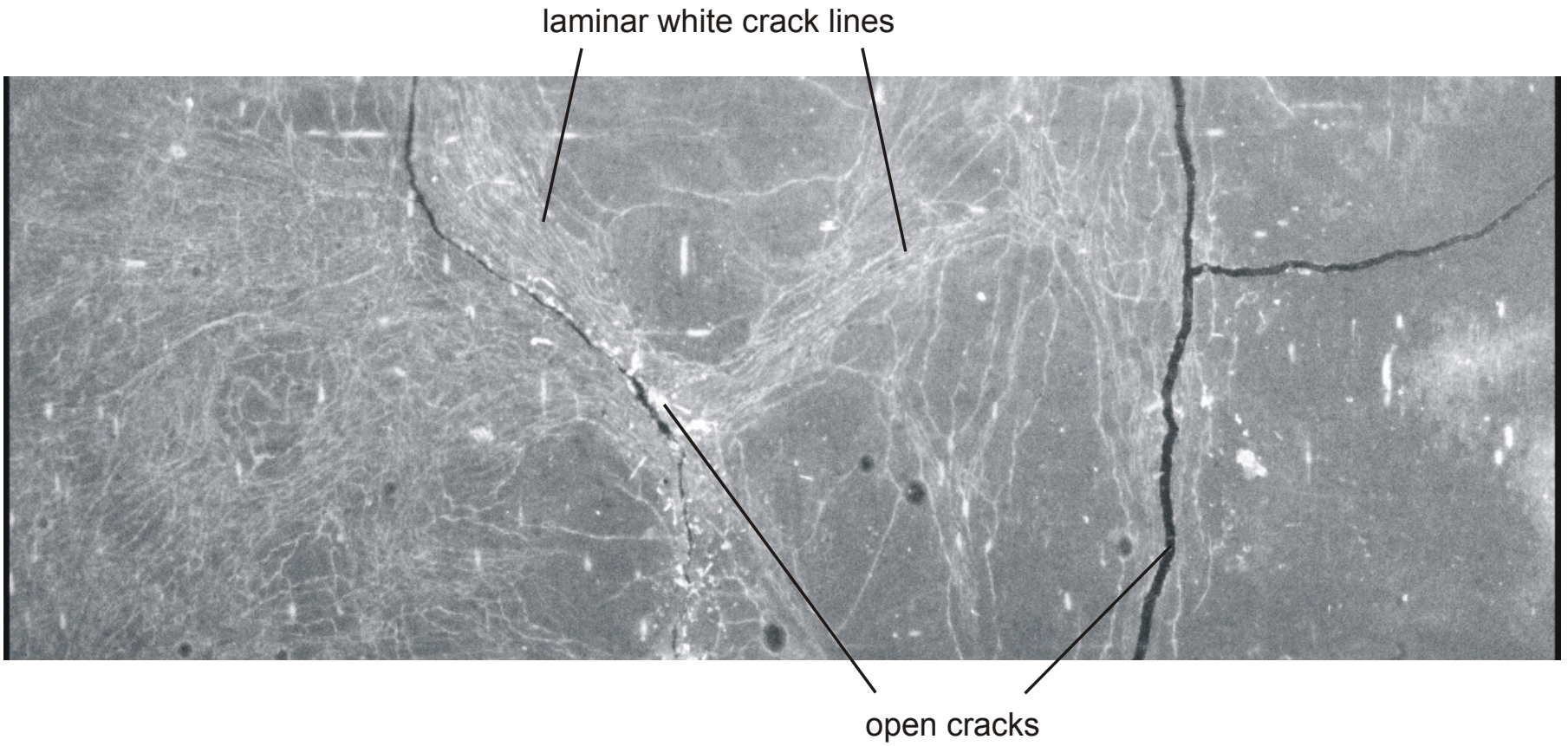

Fig. 18: Oxidized and cracked Zircaloy surface;
(1400 °C, 300 µm oxide layer)

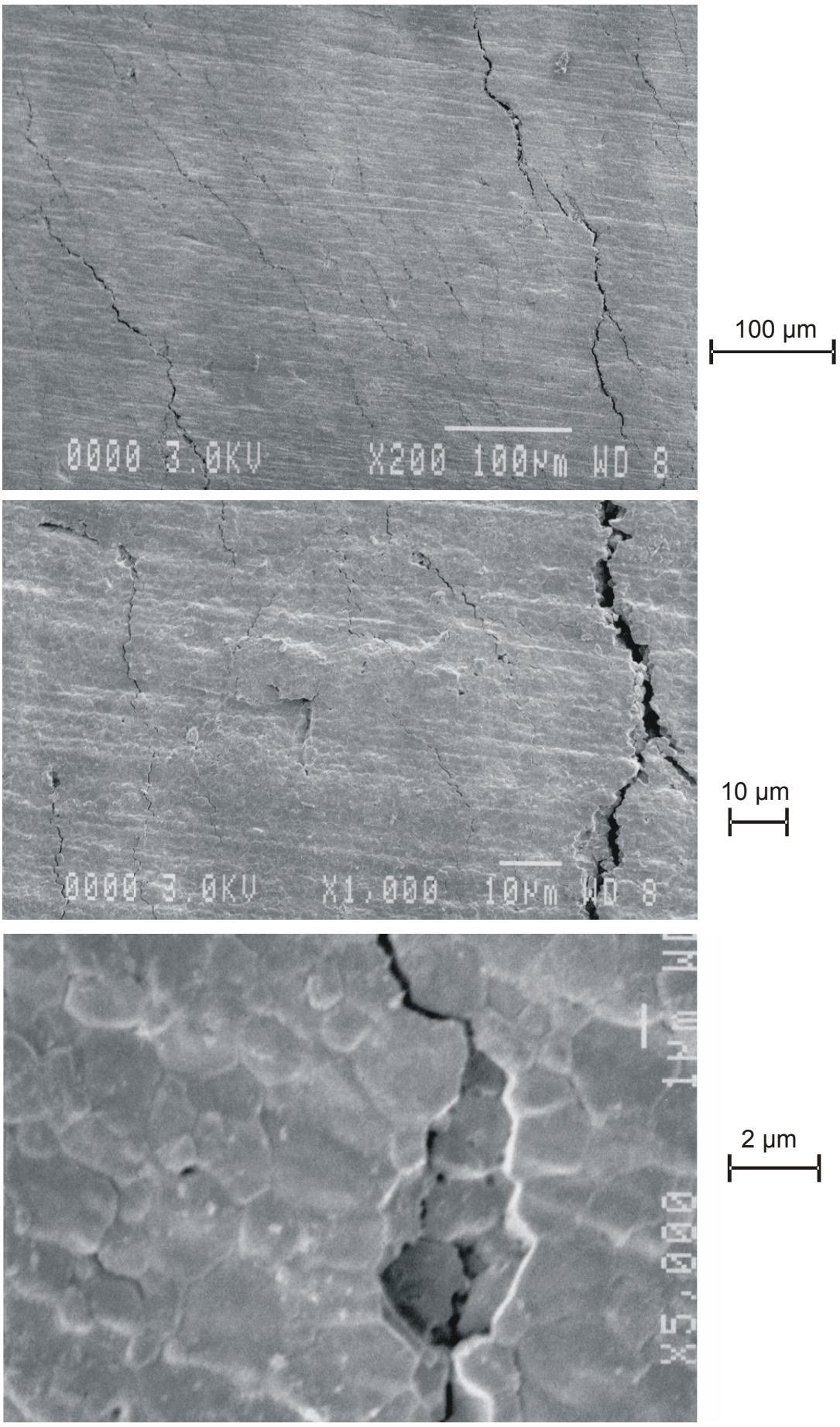

Fig. 19: Micro cracks in quench experiments

preoxidation: 300 □m
initial temperature: 1200 °C

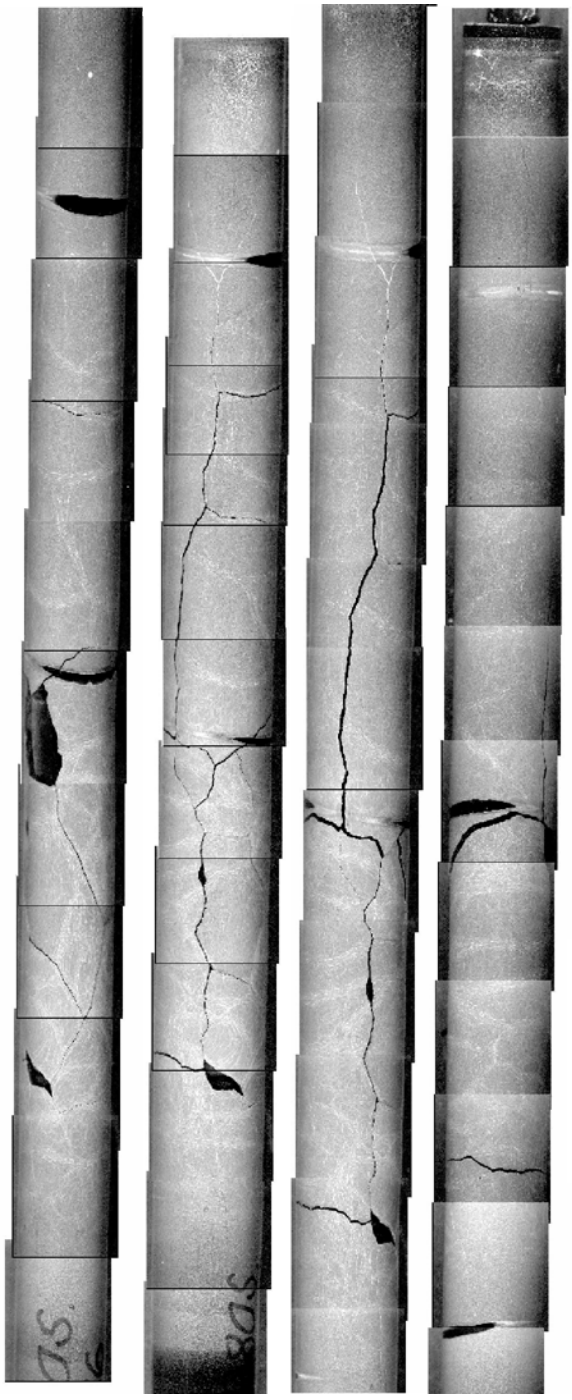

(four views of one specimen)

Fig. 20: Crack formation during cooldown by radiation

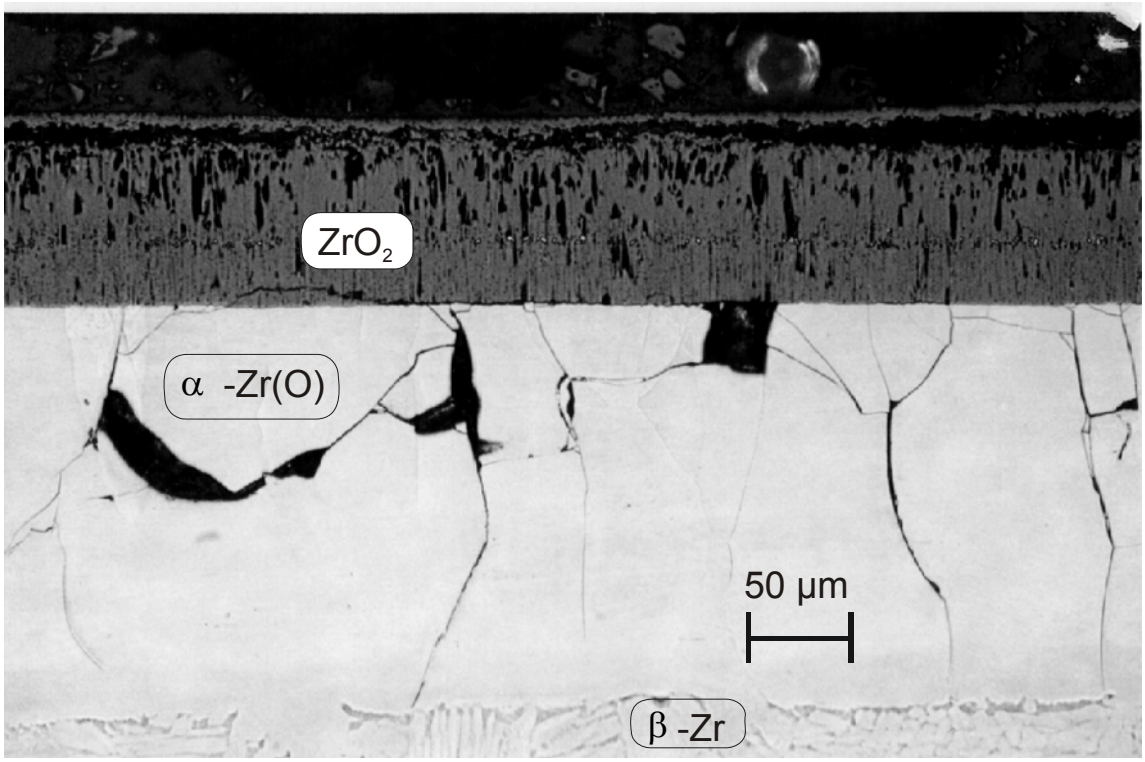

Fig. 21: 100 µm thick oxide scales;
cracks in the α -Zr(O) layer

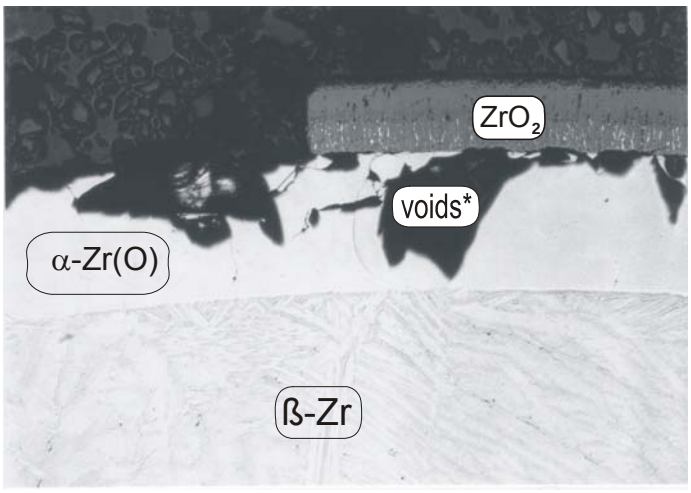

100 µm

*) material removed during metallographic preparation

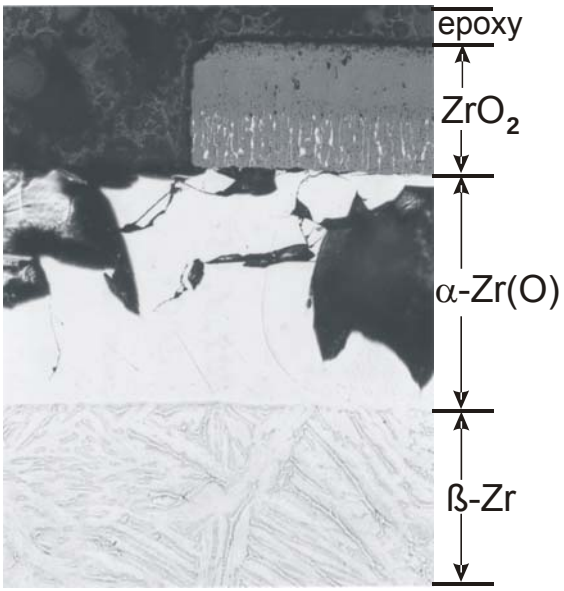

100 µm

quench temperature: 1600 °C
preoxidation: 100 µm

Fig. 22: Local spalling of oxide layer by water quenching

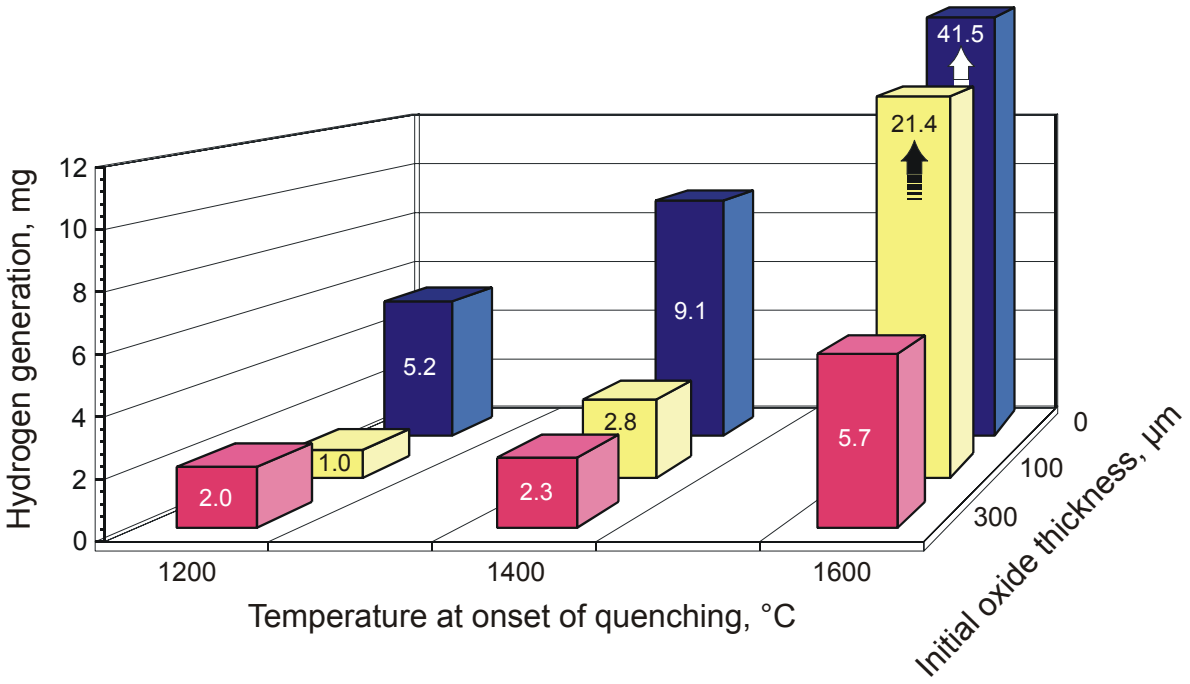

Water quenched specimens

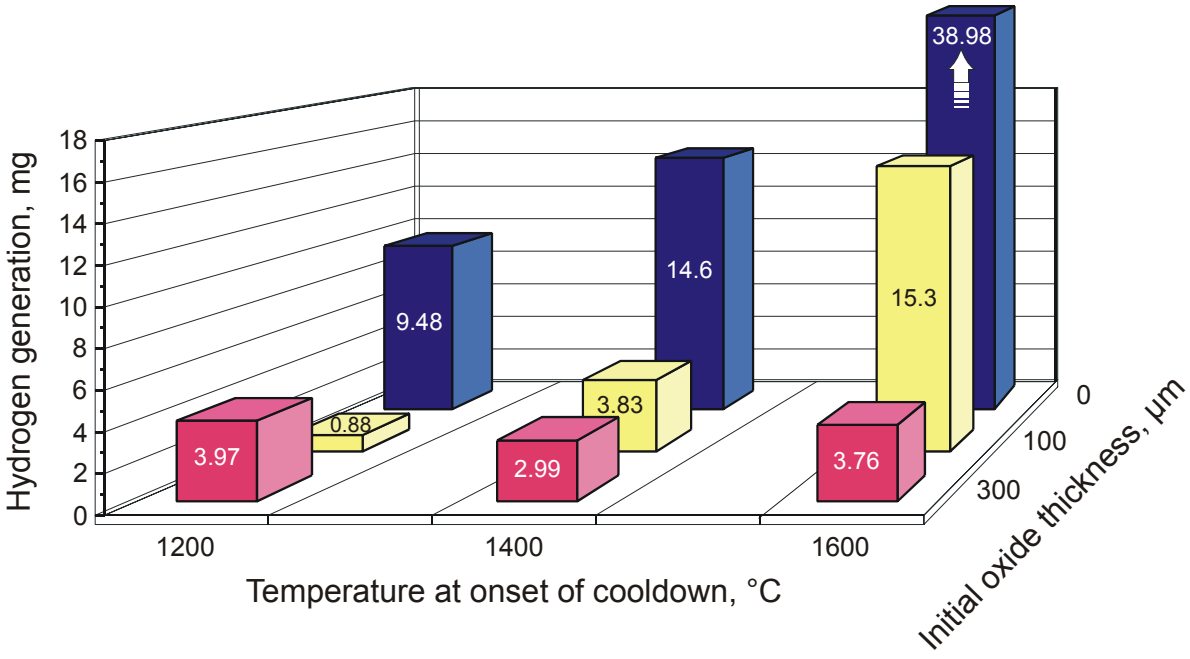

Specimens cooled down by steam

Fig. 23: Total amount of released hydrogen

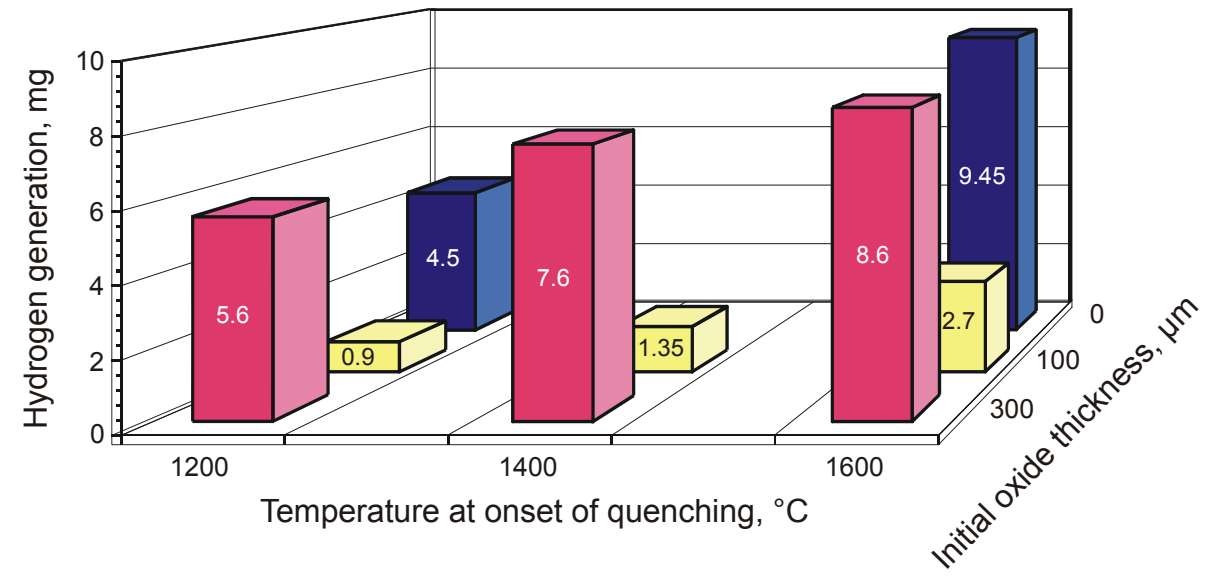

Water quenched specimens

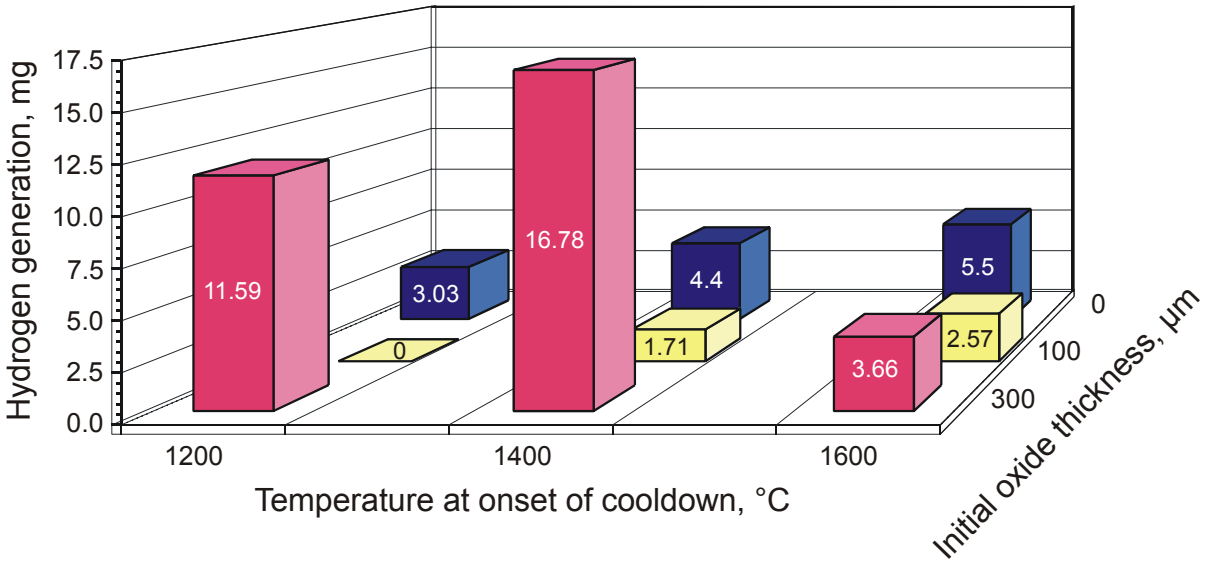

Specimens cooled down by steam

Fig. 24: Total amount of hydrogen stored in the specimens

Part II: Modelling of quench phenomena

M. S. Veshchunov, A. V. Berdyshev, A. V. Boldyrev
L. V. Matweev, A. V. Palagin, V. E. Shestak

Nuclear Safety Institute, Russian Academy of Science, Moscow

Contents:

Abstract

The reflooding of LWR core during severe accident may lead to the cooling down and cessation or to the temperature escalation and further development of the accident. That will depend on several important parameters, characterizing the core state and the way of the reflooding. Appropriate understanding of the complex core reflooding phenomena is necessary for the prediction of the system evolution.

In order to describe the results of the FZK quench experiments the main processes taking place during fuel rod bundle reflooding are considered: heat exchange, oxidation of Zr, mechanical behaviour of the cladding.

New combined numerical QUENCH module was elaborated by coupling of the heat exchange module THERM, oxidation module PROF and mechanical deformation module CROX.

The results of the calculations are compared with the available experimental data.

Introduction

The reflooding of LWR core during severe accident may lead to the cooling down and cessation of the accident or to the temperature escalation and further development of the accident. That will depend on several important parameters, characterizing the core state and the way of the reflooding. Appropriate understanding of the complex core reflooding phenomena is necessary for the prediction of the system evolution.

In order to describe the results of the FZK quench experiments the main processes taking place during fuel rod bundle reflooding are considered: heat exchange, oxidation of Zr, mechanical behaviour of the cladding. New combined numerical QUENCH module was elaborated by coupling of the heat exchange module THERM, oxidation module PROF and mechanical deformation module CROX.

The description of the heat exchange process requires simultaneous solution of two problems: heat conduction problem inside the solid body (fuel rod) and heat convection problem in the surrounding two phase water-steam media. For the solution of the heat conduction problem the finite differences numerical scheme with adaptive grid is used in the present work. The non-stationary four-region thermo-hydraulic model based on the conservation laws describes the heat convection process. The description of the heat exchange model and the comparison of the THERM calculation results with the experimental data are given in the Chapter I.

Zr oxidation leads to the heat release and hydrogen generation and affects the mechanical properties of the cladding. For the adequate description of this process the statistical analysis of available experimental data on oxidation is carried out, and the universal correlation dependencies for oxidation kinetic parameters (diffusion coefficients in various phases of oxidizing Zry) in the temperature interval 1000-1825 C are derived. The obtained correlations are used in the oxidation PROF module. The statistical procedure and the results obtained are described in the Chapter II.

The influence of the $\beta \rightarrow \alpha$ phase transformation of Zircaloy and tetragonal-to-monoclinic phase transformation of the oxide as well as the additional stresses generated by the temperature gradients on the stress state of the oxidized cladding, crack formation and spalling are investigated by the mechanical deformation module CROX and compared with the available experimental data in the Chapter III.

The mutual work of the oxidation module PROF and mechanical deformation module CROX - simulation of the oxide cracking influence on the oxidation kinetics under the conditions of cladding deformation and the comparison with the results of some small-scale experiments are described in the Chapter IV.

The combined QUENCH module (the result of coupling of THERM, PROF and CROX modules) allows to describe self-consistently the mutual interaction of all the phenomena involved in the quenching process. The set of the QUENCH module calculations and the comparison with the available experimental data are presented in the Chapter V.

I. Quench phenomena modelling: heat exchange problem

Introduction

Quenching can be defined as the sudden cooling of an object caused by reflooding (immersing it in a cooling liquid). The good understanding of the heat transfer mechanisms during reflooding of nuclear reactor cores at postulated LOCA accident is of great importance.

Generally, the description of quench phenomena requires simultaneous solution of two problems: (i) heat conduction problem inside the solid body (fuel rod) and (ii) heat convection problem in the surrounding two phase water-steam media. In the earlier investigations reviewed in [1,2,3,4] several heat conduction models for the uniform rod (lump, one-dimensional, two-dimensional and three-dimensional) based on the different simplifying assumptions were obtained. The most important of these simplifying assumptions concerned the heat exchange rate with surrounding media. The connection between the surface temperature and the heat flow to the liquid (boiling curve) was approximated by a combination of step, linear and (or) exponential functions. This approach made it possible to consider the heat exchange problem analytically in a stationary approximation, but both the description of the surrounding water-steam media and the heat conduction process (uniform rod) was oversimplified.

The fuel rod simulators used in the current FZK experiments have multi-layered structure with the gap between the pellets and the cladding. This structure affects sufficiently the heat exchange as compared with the uniform rod. For the adequate solution of the heat conduction problem the finite differences numerical scheme is used in the present work. The heat conduction model takes into account: different thermal properties of the different layers and spatial distribution of the heat sources (due to Zr oxidation and possible residual heat release). The adaptive grid accounts for the layers thicknesses axial variation due to phase transition and thermal expansion, and for the sharp axial temperature gradients in the quench region. In more details this model will be described below in the “Heat conduction model description” section of the present chapter.

As for the heat convection during reflooding, it has received much investigation, both theoretical and experimental. The flow pattern of the water-steam mixture and the heat exchange during reflooding depend on several important parameters: initial water temperature (subcooling), initial wall temperature (overheating), flooding rate, pressure, geometry of the channel (length, width), thermal properties of the solid body (heat conductivity, heat capacity), the working fluid. Depending on these parameters, different flow regimes with different heat transfer rates were realized and investigated.

At relatively low flooding rates, when the wall temperature is too high for the liquid to rewet, the liquid column is formed downstream from the axially progressing quench front (QF), separated from the hot wall by a thin steam film. This flow regime is often called an Inverted Annular Film Boiling (IAFB) and it takes place in the current FZK experiments. The details of the heat transfer process during stationary film boiling as well as the quazi-stationary IAFB motion and flow regime transitions were studied in different works.

The Bromley equation [5] for the variation of the heat transfer coefficient along the film was obtained for a laminar steam layer and a saturated liquid pool. Some empirical correlations [6] and modifications [7] were proposed to take into account the effects of subcooling and flow rate. Hsu and Westwater [8] considered the turbulent steam layer with a laminar sublayer and improved the predictions of the Bromley model.

In the work [9] the effect of the liquid flow rate on the film boiling heat transfer coefficient was investigated experimentally using 6×6 heated rod bundle. The experiments parameters were: the pressure 1.6-3.1 bar, typical subcooling 30-0 K, flooding rate 2-30 cm/s, initial wall temperature 970-900 K.

In the work [10] the reflooding in the annular channel typical to small research reactors was investigated experimentally. The experimental parameters were: subcooling 70-40 K, flooding rate 1.8 - 9.0 cm/s, initial wall temperature 850-670 K. The obtained data were used to assist the theoretical consideration of the heat flow, rewetting temperature and vapour film thickness at the vicinity of the quench front.

Film boiling models have been also developed in [11, 12, 13,14] with the main attention paid to the turbulent motion in the steam film and interfacial interactions. In the work [15] the turbulent boundary layer analysis was applied to the problem and the expressions for the phases radial and axial velocity distributions were derived. However, the effects of the phase change on the temperature and velocity distributions was neglected. The results obtained were tested on the experimental data using Freon R-113 as a working fluid.

The two-fluid hydrodynamic "6-equation" approach for the quazi-stationary description of the IAFB motion was formulated in [16] and developed in [17]. Six equations represented the mass, momentum and energy conservation laws for water and steam, averaged over the radial coordinate. The model predictions were compared with the results of the single tube reflooding experiments [18, 19], at that the wall temperature was considered as an input parameter. In this set of the experiments the pressure range was 1-3 bar, typical subcooling 30-70 K, flooding rate 17-2.5 cm/s, initial wall temperature 1033-588 K.

With certain modifications this model was considered in [20]. In this work the model [17] was generalised to make it applicable to both tubes and bundles of different geometry (square and triangular lattices). The other modifications concerned the interaction between two phases on the interface and its influence on the heat and momentum transfer. The new factors accounting for the enhancement of the momentum and heat transfer due to interfacial disturbances and turbulence were introduced. The comparison of the model predictions with the experimental data [18 ,19, 21, 22] was carried out. In this set of the experiments the pressure range was 1-4.4 bar, subcooling 0-30 K, flooding rate 3-50 cm/s, initial wall temperature 573-1273 K.

In several works briefly reviewed in [15] the transitions from the IAFB to so-called Dispersed Flow (DF) and Inverted Slug Flow (ISF) were observed and investigated. In these works mainly the cryogenic fluids: liquid hydrogen [23], liquid nitrogen [24], freon R-113 [15, 25, 26], or water-gas mixtures [27] were used. This fact makes questionable the application of the obtained results to the current FZK quench experiments analysis.

The last statement holds true for all the above mentioned papers. The results obtained in these works can not be applied directly for the description of the current FZK quench experiments due to the following reasons:

- The quenching process in the current FZK quench experiments is essentially non-stationary, transient, in contrast to the ordinary quazi-stationary approximation.

- The typical overheats in the experiments [18, 19, 21, 22] used for the verification of the 6-equation models in the mentioned above works [17, 20] (650-200 K) as well as in the other experiments with tubes and rod bundles [9, 10] were too small as compared with the current experiments overheat (1100-1500 K).

These large overheats in the current experiments seem to change qualitatively the flow pattern. The new region which is defined as Droplets-Splashes (DS) region occurs downstream from the IAFB one. This region is formed by the water droplets and splashes ejected from the IAFB region. The axial size of the DS region increases with the initial overheat increase. Thus, there may exist four water-steam regions at a time: Bubble Boiling region (BB) upstream from the QF; IAFB, DS and, finally Pure Steam (PS) regions downstream from the QF, at increasing elevations.

The heat transfer in the DS region is very intensive, and it is just this fact which makes the DS region so important for the description of the rod segment cooling down. The heat transfer coefficient in the IAFB region at high overheats may also be different from the usually used [17, 20] values due to the intensive disturbances at the water-steam interface.

Another important peculiarity of the high overheat experiments is the non-stationary motion of the interregion boundaries. Since the heat transfer coefficients are different in the different regions, the prediction of the interregion boundaries locations is very important for the calculation of the surface temperature evolution.

From the above discussion one can formulate the general requirements for the quench model. The model suitable for the description of the current FZK experiments with the fuel rod segments and the future ones with the rod bundle should be able to:

- consider the simultaneous occurrence of several water-steam regions (BB, IAFB, DS, PS) at different elevations,

- calculate self-consistently the non-stationary motion of interregion boundaries,

- calculate the heat transfer coefficients for different regions in the wide overheats range.

The model for the description of non-stationary reflooding which fit these requirements will be rather complex. It will contain partial differential equations and a lot of closure relations, some of which are undefined or unknown in the parameters range of interest. For the first moment, it is necessary to develop a simplified model in order to determine the separate closure relations from the comparison with the single rod experimental data. The ordinary way to do that is to omit the time derivatives and consider a stationary situation [17, 20].

However, as it was emphasised above, the current FZK experiments are essentially non-stationary, and can not be adequately described by quazi-stationary model. The appropriate simplified model should account for the non-stationary motion of the interregion boundaries. Such simplified heat exchange model will be described in the next Section.

It should be noted, that successful application of the simplified model to the analysis of the current experiments (see below) may be partially explained by the fact that such important parameters of the system as pressure, reflooding rate and subcooling were constant in the analysed experiments. The possibility of the adequate accounting for the effect of these parameters by the simplified model in the case of the rod bundle reflooding is questionable. That is why the development of the detailed two-fluid heat exchange model (with making use of the results obtained with simplified one) for the analysis of the future FZK experiments is very desirable.

Heat convection model description

1. Bubble Boiling Region

In the Bubble Boiling Region at low overheats (less than 30-170 K), where the nucleate boiling and transition to the film boiling take place, the heat flow from the fuel rod to the water-steam media is determined by a kind of the boiling curve modified for the description of a vertical rod reflooding .

2. The Inverted Annular Film Boiling Region

The Inverted Annular Film boiling Region consists mainly of water. The upper boundary of the IAFB region $l_1(t)$ is some function of time which will be determined below. The heat flow from the fuel rod in this region is given by the sum of the heat flow due to radiation and the film boiling heat flow:

$$q_1 = \varepsilon_1 \sigma T_r^{\,4} + q_b \tag{1}$$

The value of the film boiling heat flow depends on the thickness of the steam film $\delta_s(z)$ and the steam velocity $U_{s1}(z)$ averaged over the steam film thickness.

The thickness of the steam film is not self-consistently determined in the present heat convection model. The following simple relation for the approximation of the steam film thickness:

$$\delta_s(z) = \delta_{s0}\left(\frac{z}{z_0}\right)^b, \tag{2}$$

was choosen because it gives $\delta_s = 0$ at $z = 0$ (the rewetting point) and represents the slow dependence of the steam film thickness on the elevation (at the small values of *b*), observed in the various experiments (in FZK experiments as well). The steam film thickness parameters are initially defined as $\delta_{s0} = 0.3$ cm, $z_0 = 1$ cm, $b = 0.25$; later these parameters will be determined on the basis of the experimental data analysis.

The steam is assumed to be in the equilibrium with the water in both IAFB and DS regions. The later means that all the heat released in these regions goes into the water evaporation (but not steam heating), and the temperature of the steam is equal here to the saturation temperature ($T_s = 373$ K).

The averaged steam velocity in the IAFB region is given by [28]

$$U_{s1}(z) = \frac{1}{\rho_s r_*}\int_0^z \frac{q_1(x)}{\delta_s(x)}dx, \tag{3}$$

where ρ_s is steam density, and r_* is the latent heat of vaporisation (with possible account for water subcooling). The IAFB region Reynolds number is based on the values (2) and (3):

$$\mathrm{Re}_1(z) = \frac{\rho_s U_{s1}(z)\delta_s(z)}{\eta_s}. \tag{4}$$

The boiling heat flow $q_b(T_r)$ in the region of high overheats is approximated by the following expression:

$$q_b(T_r, z) = C_1 \,\mathrm{Re}_1^{\alpha_1}(z)\frac{\kappa}{\delta_s(z)}(T_r - T_s). \tag{5}$$

Parameters C_1 and α_1 should be determined from the comparison with the experimental data.

3. The Droplets-Splashes Region

The Droplets-Splashes region consists of steam and water jets and droplets splashed out from the IAFB region. The DS region is located between two elevations: $l_1(t) < z < l_2(t)$. The upper boundary of the DS region $l_2(t)$ will be determined below. The heat flow from the fuel rod to the water-steam media in the II region is given by the sum of the heat flow due to radiation, heat flow to steam and heat flow to water jets and droplets:

$$q_2 = \varepsilon_2 \sigma T_r^{\,4} + q_{s2} + q_{w2}. \tag{6}$$

The steam velocity in the II region is given by

$$U_{s2}(z) = \frac{2R_1}{R_2^2 - R_1^2}\left(U_{s1}^*\delta_s^* + \frac{1}{\rho_s r(1-\beta)}\int_{l_1(t)}^{z} q_2(x)dx\right). \tag{7}$$

Here R_1 and R_2 are the external radius of the rod and internal radius of the cylinder, respectively; U_{s1}^* and δ_s^* are the steam velocity and the steam film thickness on the boundary between the IAFB and the DS regions (at $z = l_1(t)$):

$$U_{s1}^* = \frac{1}{\rho_s r_*}\int_0^{l_1(t)} \frac{q_1(x)}{\delta_s(x)}dx, \tag{8}$$

$$\delta_s^* = \delta_{s0}\left(\frac{l_1(t)}{z_0}\right)^b; \tag{9}$$

$(1-\beta)$ is the void fraction in the DS region. The DS region Reynolds number is based on the value (7):

$$\mathrm{Re}_2(z) = \frac{\rho_s U_{s2}(z)(R_2 - R_1)\sqrt{1-\beta}}{\eta_s}. \tag{10}$$

Heat flow to steam in the second region is given by the expression [29]:

$$q_{s2}(T_r, z) = C_2 \, \mathrm{Pr}_s^{\,0.4} \, \mathrm{Re}_2^{0.8}(z) \frac{k}{(R_2 - R_1)} (T_r - T_s) \tag{11}$$

(Pr_v is the steam Prandtl number).

Calculation of the heat flow to the water drops and jets in the DS region requires detailed physical modelling. This problem may be divided into two parts: (i) calculation of the heat flow rate to a single drop (jet) from the hot rod upon knowing drop (jet) volume and velocity and (ii) calculation of the drops (jets) volumes and velocities distribution upon knowing steam velocity at the boundary between the IAFB and DS regions. Essentially irregular nature of the water swashing in the DS region complicates the problem.

At the present moment, the simple relation is used for the description of the heat flow to the water drops and jets:

$$q_{w2} = C_q \beta^a q_{cont} . \tag{12}$$

Here q_{cont} is the averaged heat flow to a drop (jet) during its contact with the rod (this value should be determined from the solution of the mentioned above problem (i)), and C_q is an empirical constant. The value β^a accounts for the water fraction in the DS region.

4. The Pure Steam Region

The Pure Steam region is located above the elevation $z = l_2(t)$. The heat flow from the fuel rod in the PS region is given by the sum of the heat flow due to radiation and the heat flow to steam:

$$q_3 = \varepsilon_3 \sigma T_r^{\,4} + q_{s3} . \tag{13}$$

The steam velocity in the PS region is assumed to be equal to that at the boundary between the DS and the PS regions (i.e. at $z = l_2(t)$):

$$U_{s2}^*(z) = \frac{2R_1}{R_2^2 - R_1^2} \left(U_{s1}^* \delta_s^* + \frac{1}{\rho_s r (1-\beta)} \int_{l_1(t)}^{l_2(t)} q_2(x) dx \right) . \tag{14}$$

The estimations show, that the steam is only insignificantly heated in the PS region (several degrees) because of its high velocity (several meters per sec). That is why steam velocity and properties are considered as uniform along the PS region.

The Reynolds number is based on the value (14):

$$\mathrm{Re}_3(z) = \frac{\rho_s U_{s2}^*(z)(R_2 - R_1)}{\eta_s} . \tag{15}$$

Heat flow to steam in the PS region is given by the expression [29]:

$$q_{s2}(T_r, z) = 0.023 \,\mathrm{Pr}_s^{\,0.4}\, \mathrm{Re}_3^{0.8}(z) \frac{\kappa}{2(R_2 - R_1)} \left[1 - \frac{0.45}{2.45 + \mathrm{Pr}} \left(\frac{R_1}{R_2} \right)^{0.6} \right] (T_r - T_s) . \qquad (16)$$

5. Interregion boundaries

The upper boundary of the DS region $l_2(t)$ is determined by the maximal flight height of a drop splashed out from the I region. Here it is assumed that the main reason of the water splashing out is the interaction with the steam flow at the boundary between the IAFB and DS regions. During this interaction a part of the steam momentum is transferred to the water, and then due to the cumulative effect to a small part of water (drop) which get relatively high velocity U_d:

$$U_d \propto Cu \frac{\rho_s}{\rho_w} U_{s1}^* . \qquad (17)$$

Here *Cu* is the cumulative coefficient. The maximal flight height is then given by $U_d^2 / 2g$, and the value of $l_2(t)$ is

$$l_2(t) = l_1(t) + \frac{(Cu)^2}{2g} \left(\frac{\rho_s}{\rho_w} \right)^2 U_{s1}^{*\,2} . \qquad (18)$$

The average mass flow from the IAFB to the DS region in the form of drops is given by

$$J = \beta \rho_w U_d = \beta Cu \rho_s U_{s1}^* . \qquad (19)$$

Some part of water is evaporated during the drop's flight through the DS region. The average volume of evaporated liquid in the DS region during the time period Δt is estimated as

$$\Delta V = 2\pi R_1 \frac{1}{r \rho_w} \int_{l_1(t)}^{l_2(t)} q_2(x) dx \cdot \Delta t . \qquad (20)$$

The motion of the upper boundary of the IAFB region is described by the following differential equation derived from the mass balance equation:

$$\frac{dl_1(t)}{dt} = u_{cool} - u_2 - u_3 + u_4 . \qquad (21)$$

The first term in the right side of eq. (21) corresponds to the flooding rate. The second term

$$u_2 = \frac{2R_1 \delta_s^*}{R_2^2 - R_1^2} \frac{\rho_s}{\rho_w} U_{s1}^* \qquad (22)$$

describes the mass flow from the IAFB to the DS region in the form of steam, the third term

$$u_3 = \frac{2R_1}{R_2^2 - R_1^2} \frac{1}{r\rho_w} \int_{l_1(t)}^{l_2(t)} q_2(x)dx \tag{23}$$

describes the mass flow from the IAFB to the DS region in the form of drops. The last term

$$u_4 = 2\pi R_1(\rho_w - \rho_s) \frac{d}{dt} \int_0^{l_1(t)} \delta_s(x)dx \tag{24}$$

accounts for the steam film thickness variations.

The obtained system of equations describes the heat exchange of the fuel rod with the surrounding water-steam media and provides the boundary condition for the heat conduction problem inside the fuel rod. The obtained system of equations contains several undefined parameters, which should be considered as the empirical ones. These parameters will be determined on the basis of the validation of the heat exchange module against experimental data.

Heat conduction model description

1. Problem definition, main equations

An object under consideration is a layered oxidized tube element filled by pellets. Each layer of a tube consists of the one of the following materials: zirconium; oxygen stabilized alpha-zirconium; zirconium oxide. The order of the layers may be arbitrary. Number of layers is not limited and varies according to oxidation model from one (empty nonoxidized tube) to five (double side oxidation). The material of the pellet is zirconium oxide or uranium dioxide. The pellet and the cladding are considered as a system of layers, where pellet is the inside layer. Temperature evolution in the layered rod is simulated using an assumption of axially symmetrical boundary conditions. The main cooling processes are: the radiation heat transfer; the heat exchange with boiling water and with steam flow.

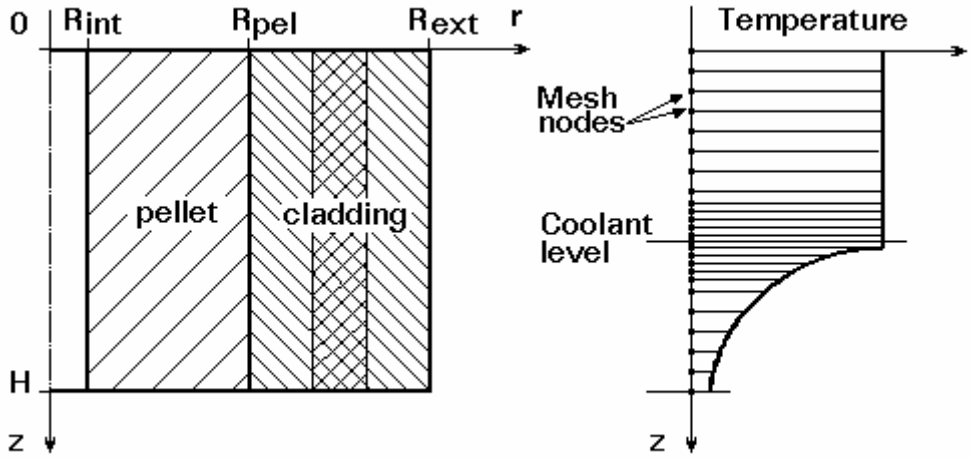

Fig.A. Structure of layered rod element.

The heat conduction equation for the two dimensional temperature distribution in cylindrical coordinates system is

$$c(T,r)\,\rho(T,r)\frac{\partial T}{\partial t}=\frac{1}{r}\frac{\partial}{\partial r}\left(r\,\lambda(T,r)\frac{\partial T}{\partial r}\right)+\frac{\partial}{\partial z}\left(\lambda(T,r)\frac{\partial T}{\partial z}\right)+f, \qquad (25)$$
$$\left(R_{\text{int}}\le r\le R_{\text{ext}},\ 0\le z\le H\right),$$

where t - time, $T(r,z,t)$- temperature, $c(T,r)$- specific heat capacity, $\rho(T,r)$- density, $\lambda(T,r)$- thermal conductivity, $f(r,z,t)$- heat source density R_{int}- internal radius of the pellet (or of the first layer if there is no pellet), R_{ext}- external radius of the cladding, H- height of the cladding element.

Boundary conditions on the surfaces of the rod are formulated for heat flows densities

$$\left(\lambda(T,r)\frac{\partial T}{\partial r}\right)_{r=R_{int}} = -q_{int}(z,t), \tag{26}$$

$$\left(\lambda(T,r)\frac{\partial T}{\partial r}\right)_{r=R_{ext}} = -q_{\text{ext}}(z,t), \tag{27}$$

$$\left(\lambda(T,r)\frac{\partial T}{\partial z}\right)_{z=0} = -q_{\text{up}}(r,t), \tag{28}$$

$$\left(\lambda(T,r)\frac{\partial T}{\partial z}\right)_{z=H} = -q_{\text{low}}(r,t), \tag{29}$$

where $q_{\text{int}}(z,t)$, $q_{\text{ext}}(z,t)$, $q_{\text{up}}(r,t)$, $q_{\text{low}}(r,t)$- heat flows densities trough the internal, external, upper and lower surfaces of the rod accordingly.

Properties of materials are functions of temperature and change discontinuously on the layers interfaces. Heat flows through the boundary surfaces in common case are functions of temperature on them. Heat flows for internal, upper and lower surfaces in most cases are equal to zero. Boundary condition for upper faces of the layers may be defined by specifying the value of temperature on them.

If a gap between the pellet and the cladding exists, the total heat flow through the gap is modelled as a sum of the radiation heat flow and the conduction heat flow:

$$q_{gap}(z,t) = q_{rad}(z,t) + q_{cond}(z,t).$$

The radiation heat flow from the pellet to the cladding is given by:

$$q_{gap}(z,t) = \frac{\sigma\left(T_{pel}^4(z,t) - T_{clad}^4(z,t)\right)}{\frac{1}{\varepsilon_{pel}} + \left(\frac{1}{\varepsilon_{clad}} - 1\right)\frac{R_{pel}}{R_{clad}}}, \tag{30}$$

and the heat flow due to conduction is given by the expression:

$$q_{cond}(z,t) = \lambda_{ar}\frac{T_{pet}(z,t) - T_{clad}(z,t)}{R_{clad}(z,t) - R_{pel}(z,t)}. \tag{31}$$

Here, $T_{pel}(z,t)$ and $T_{clad}(z,t)$ are the temperatures of the pellet outer surface and the cladding inner surface, respectively; $R_{pel}(z,t)$ and $R_{clad}(z,t)$ are the pellet outer radius and the cladding inner radius, these last two values are calculated by the mechanical deformation module; ε_{pel} and ε_{clad} are the emissivities of the corresponding materials; σ is Stefan-Boltzmann constant, λ_{ar} is the argon heat conductivity. Taking into account very small values of the gap thickness and the gap heat capacity, the quazi-

stationary approximation (2) for the conduction heat flow through the gap appears to be rather satisfactory one.

It is assumed that an oxidation reaction heat is generated at the interface between alpha-zirconium and zirconium oxide.

2. The numerical scheme

A finite difference implicit method is used for the temperature distribution calculation. The layers are divided into a different number of nodes. Spatial step in radial direction is constant inside one material. The differential equation for heat conduction is converted to the following difference equation

$$c_{ij}^{(n+1)}\rho_{ij}^{(n+1)}\left(T_{ij}^{(n+1)}-T_{ij}^{(n)}\right)\frac{1}{\Delta t}=a_{ij}\left(T_{i-1,j}^{(n+1)}-T_{ij}^{(n+1)}\right)-a_{i+1,j}\left(T_{ij}^{(n+1)}-T_{i+1,j}^{(n+1)}\right)+$$
$$+b_{ij}\left(T_{i,j-1}^{(n+1)}-T_{ij}^{(n+1)}\right)-b_{i,j+1}\left(T_{ij}^{(n+1)}-T_{i,j+1}^{(n+1)}\right)+f_{ij}^{(n+1)}, \qquad (32)$$
$$\left(i=2\ldots N_z-1,\quad j=2\ldots N_r-1\right),$$

where z_i - axial coordinates of mesh nodes $(i=1\ldots N_z)$, r_j - radial coordinates of mesh nodes $(j=1\ldots N_r)$, Δt - time step, t_n - time at the end of previous time step, $t_{n+1}=t_n+\Delta t$.

The coefficients in difference equation are equal to

$$a_{ij}=\frac{\frac{1}{2}\left(\lambda_{ij}^{(n+1)}+\lambda_{i-1,j}^{(n+1)}\right)}{\Delta z_i\,\Delta z_i^c}, \qquad (33)$$

$$a_{i+1,j}=\frac{\frac{1}{2}\left(\lambda_{ij}^{(n+1)}+\lambda_{i+1,j}^{(n+1)}\right)}{\Delta z_{i+1}\,\Delta z_i^c}, \qquad (34)$$

$$b_{ij}=\frac{\frac{1}{2}\left(\lambda_{ij}^{(n+1)}+\lambda_{i,j-1}^{(n+1)}\right)\frac{1}{2}\left(r_j+r_{j-1}\right)}{\Delta r_j\,\Delta S_j}, \qquad (35)$$

$$b_{i,j+1}=\frac{\frac{1}{2}\left(\lambda_{ij}^{(n+1)}+\lambda_{i,j+1}^{(n+1)}\right)\frac{1}{2}\left(r_j+r_{j+1}\right)}{\Delta r_{j+1}\,\Delta S_j}, \qquad (36)$$
$$\left(i=2\ldots N_z-1,\ j=2\ldots N_r-1\right),$$

where $\Delta r_j=r_j-r_{j-1}$, $\Delta z_i=z_i-z_{i-1}$,

$$\Delta r_j^c=\frac{1}{2}\left(r_{j+1}-r_{j-1}\right),\ \Delta z_i^c=\frac{1}{2}\left(z_{i+1}-z_{i-1}\right),$$
$$\Delta S_j=\frac{1}{2}\left(\frac{1}{2}\left(r_j+r_{j+1}\right)+\frac{1}{2}\left(r_j+r_{j-1}\right)\right)\Delta r_j^c.$$

Temperature derivatives in the equations for the boundary conditions may be approximated using three neighboring nodes near the boundaries of the rod:

$$\lambda_{i,1}^{(n+1)}\left(\frac{2\Delta r_2^c}{\Delta r_2\Delta r_3}\left(T_{i,2}^{(n+1)}-T_{i,1}^{(n+1)}\right)-\frac{\Delta r_2}{2\Delta r_2^c\Delta r_3}\left(T_{i,3}^{(n+1)}-T_{i,1}^{(n+1)}\right)\right)=-q_{\text{int},i}^{(n+1)}, \quad (37)$$

$$\lambda_{i,N_r}^{(n+1)}\left(\frac{2\Delta r_{N_r-1}^c}{\Delta r_{N_r}\Delta r_{N_r-1}}\left(T_{i,N_r}^{(n+1)}-T_{i,N_r-1}^{(n+1)}\right)-\frac{\Delta r_{N_r}}{2\Delta r_{N_r-1}^c\Delta r_{N_r-1}}\left(T_{i,N_r}^{(n+1)}-T_{i,N_r-2}^{(n+1)}\right)\right)=-q_{\text{ext},i}^{(n+1)}; \quad (38)$$

$$\lambda_{1,j}^{(n+1)}\left(\frac{2\Delta z_2^c}{\Delta z_2\Delta z_3}\left(T_{2,j}^{(n+1)}-T_{1,j}^{(n+1)}\right)-\frac{\Delta z_2}{2\Delta z_2^c\Delta z_3}\left(T_{3,j}^{(n+1)}-T_{1,j}^{(n+1)}\right)\right)=-q_{\text{up},j}^{(n+1)}, \quad (39)$$

$$\lambda_{N_z,j}^{(n+1)}\left(\frac{2\Delta z_{N_z-1}^c}{\Delta z_{N_z}\Delta z_{N_z-1}}\left(T_{N_z,j}^{(n+1)}-T_{N_z-1,j}^{(n+1)}\right)-\frac{\Delta z_{N_z}}{2\Delta z_{N_z-1}^c\Delta z_{N_z-1}}\left(T_{N_z,j}^{(n+1)}-T_{N_z-2,j}^{(n+1)}\right)\right)=-q_{\text{low},j}^{(n+1)}, \quad (40)$$

$$\left(j=2\ldots N_r-1\right),\left(i=1\ldots N_z\right).$$

Finite difference approximation for the heat conduction equation and the boundary conditions form the system of equations with nonlinear coefficients, which can be solved by iteration method.

Heat flow through the outer surface varies sharply in the mesh nodes close to the coolant level. For better evaluation of the axial temperature change the spatial step size is reduced in this region. Such step decreasing allows to use lesser number of nodes in comparison with the uniform mesh size. The region of small spatial steps moves simultaneously with the coolant level motion.

The difference equation for the mesh nodes on the layers interfaces has the same form as for inside one, but the coefficients are modified in the following way:

$$\hat{a}_{ij}=\left(a_{ij}^{-}\Delta S_j^{-}+a_{ij}^{+}\Delta S_j^{+}\right)\frac{1}{\Delta S_j}, \quad (41)$$

$$\hat{a}_{i+1,j}=\left(a_{i+1,j}^{-}\Delta S_j^{-}+a_{i+1,j}^{+}\Delta S_j^{+}\right)\frac{1}{\Delta S_j}, \quad (42)$$

$$\left(\hat{c}\,\hat{\rho}\right)_{ij}=\left(c_{ij}^{-}\rho_{ij}^{-}\Delta S_j^{-}+c_{ij}^{+}\rho_{ij}^{+}\Delta S_j^{+}\right)\frac{1}{\Delta S_j}, \quad (43)$$

$$\hat{f}_{ij}=\left(f_{ij}^{-}\Delta S_j^{-}+f_{ij}^{+}\Delta S_j^{+}\right)\frac{1}{\Delta S_j}, \quad (44)$$

$$\hat{b}_{ij}=b_{ij}^{-},$$
$$\hat{b}_{i,j+1}=b_{i,j+1}^{+}, \quad (45)$$

$$\Delta S_j^{-}=\tfrac{1}{2}\left(r_j+\tfrac{1}{2}\left(r_j+r_{j-1}\right)\right)\tfrac{1}{2}\Delta r_j,\ \Delta S_j^{+}=\tfrac{1}{2}\left(r_j+\tfrac{1}{2}\left(r_j+r_{j+1}\right)\right)\tfrac{1}{2}\Delta r_{j+1},$$

where the terms with the minus superscripts are the coefficients, properties and heat sources of the material to the left of the interface, and the terms with the plus superscripts are for the material to the right of the interface. Coefficients $a_{ij}^{-}, a_{i+1,j}^{-}, a_{ij}^{+}, a_{i+1,j}^{+}, b_{ij}^{-}, b_{i,j+1}^{+}$ are determined by the equations (33)-(36).

When pellet is separated from cladding by a gap, gap is an additional layer. The heat transfer through this layer is determined by the current values of the pellet and the cadding radii and temperatures in accordance with the relations (30)-(31). Only one node in the radial direction belongs to the gap layer. In this case

$$a^{+}_{i\,j} = a^{+}_{i+1,\,j} = b^{+}_{i,\,j+1} = 0,\ \Delta S_j = \Delta S^{-}_j$$

for the pellet outer surface nodes,

$$a^{-}_{i\,j} = a^{-}_{i+1,\,j} = b^{-}_{i\,j} = 0,\ \Delta S_j = \Delta S^{+}_j$$

for the cladding inner surface nodes.

Radiation and covective heat flows through the gap are converted into the volume heat sources for the pellet and cladding corresponding surface's nodes.

3. The main features of the heat conduction numerical module

The heat conduction numerical module consists of the three calculation procedures:

1. The iteration procedure for the solution of the system of linear equations;

2. The iteration procedure for the determination of nonlinear coefficients of the system of equations;

3. Adaptable time step process for the determination of value of internal time step.

Flow chart of the main subroutine of the heat conduction module for the temperature distribution calculation during one global time step is shown on Fig. B.

The basic features of the code are:

1. The number of layers is not limited;

2. A gap between the pellet and the cladding is taken into account;

3. The boundary conditions are time dependent;

4. The material properties are input to the program as temperature dependent functions [30];

5. All the materials properties are located in the separate subroutines.

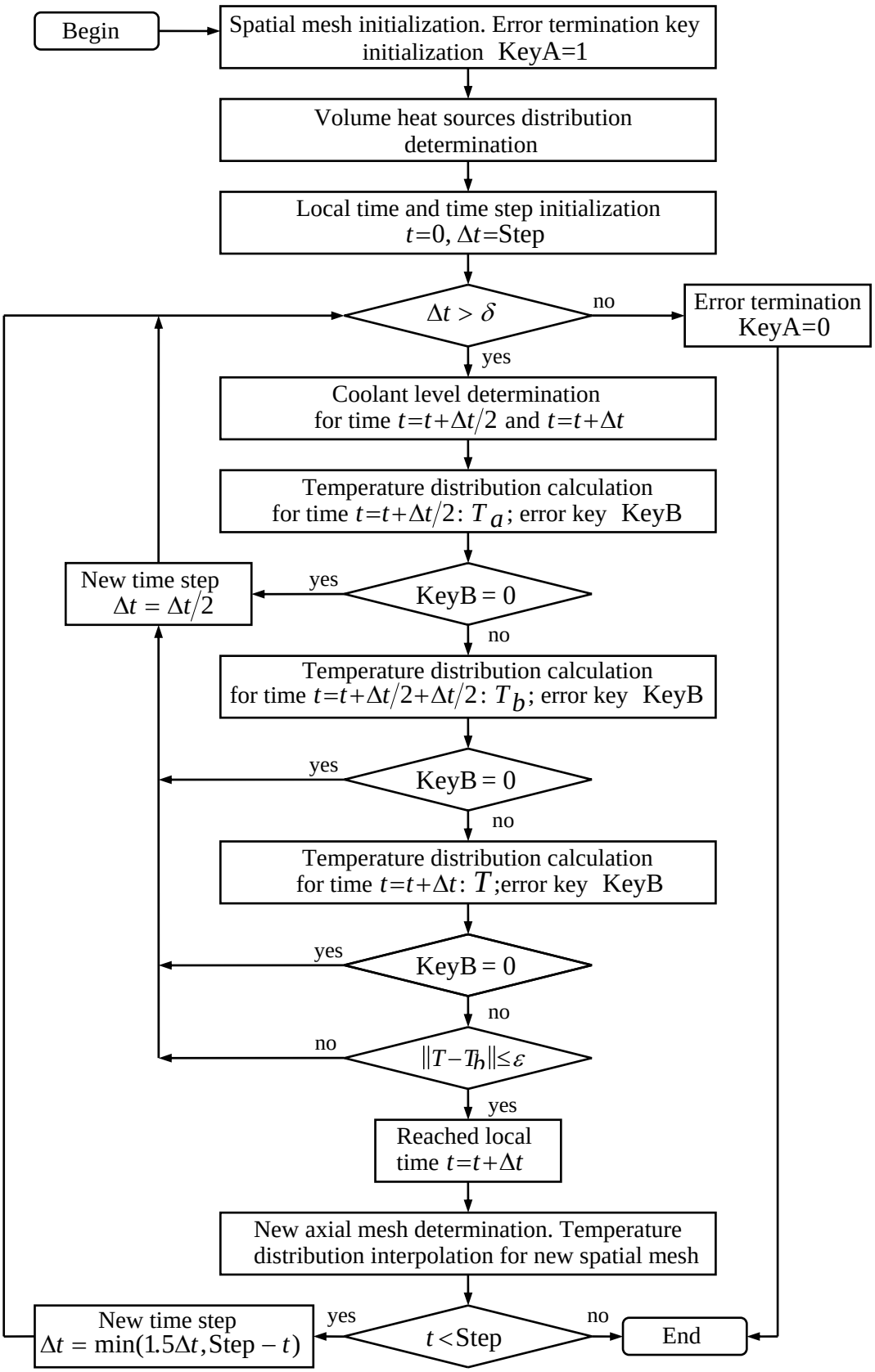

Fig.B. Flowchart of the main subroutine of the heat conduction module.

Pre-heating stage

At the pre-heating stage the temperature distribution inside the fuel rod is determined by the balance of the heat release in the metal layer due to induction and heat flow from the rod outer surface due to radiation. In a stationary case, the heat conduction problem inside the rod can be investigated analytically.

Consider a rod which consists of 3 layers: a pellet, Zr cladding and external ZrO2 layer with external radii r_1, r_2 and r_3, and heat conductivities λ_1, λ_2 and λ_3, respectively. Heat generation rate inside the metal layer is equal to q. It should be noted that in a stationary case the presence of a gap between the pellet and the cladding does not affect the temperature distribution. The heat conduction equations for the different layers are:

pellet: $$\lambda_1\left(\frac{\partial^2 T_1}{\partial r^2}+\frac{1}{r}\frac{\partial T_1}{\partial r}\right)=0, \qquad r_1 > r > 0; \tag{46}$$

Zr layer: $$\lambda_2\left(\frac{\partial^2 T_2}{\partial r^2}+\frac{1}{r}\frac{\partial T_2}{\partial r}\right)+q=0, \qquad r_2 > r > r_1; \tag{47}$$

oxide layer: $$\lambda_3\left(\frac{\partial^2 T_3}{\partial r^2}+\frac{1}{r}\frac{\partial T_3}{\partial r}\right)=0, \qquad r_3 > r > r_2; \tag{48}$$

The solution of the above problem is given by:

$$T_1(r)=Const=T_{in}, \tag{49}$$

$$T_2(r)=T_{in}-\frac{1}{4}\frac{q}{\lambda_2}r_1^2\left[\left(\frac{r}{r_1}\right)^2-1-2\,ln\left(\frac{r}{r_1}\right)\right], \tag{50}$$

$$T_3(r)=T_{in}-\frac{1}{2}q\frac{r_1^2}{\lambda_2}\left\{\left[\left(\frac{r_2}{r_1}\right)^2-1\right]\left(\frac{\lambda_2}{\lambda_3}ln\left(\frac{r}{r_2}\right)+\frac{1}{2}\right)-ln\left(\frac{r_2}{r_1}\right)\right\}. \tag{51}$$

Here T_{in} is the temperature in the centre of the pellet. The value of T_{in} together with the heat generation rate q may be determined upon knowing the boundary conditions on the outer surface of the cladding, namely the external temperature T_{ex} and effective emissivity coefficient ε.

The boundary condition on the outer surface has the form:

$$-\lambda_3\left.\frac{\partial T_3}{\partial r}\right|_{r=r_3}=\varepsilon\sigma T_{ex}^4 \tag{52}.$$

Hence it follows for the values of T_{in} and q:

$$q = \varepsilon\sigma T_{ex}^4 \frac{2r_3}{r_2^2 - r_1^2}, \tag{53}$$

$$T_{in} = T_{ex} + \varepsilon\sigma T_{ex}^4 \frac{2r_3}{r_2^2 - r_1^2} \cdot \varphi \ , \tag{54}$$

where φ is given by

$$\varphi = \frac{1}{2} q \frac{r_1^2}{\lambda_2} \left\{ \left[\left(\frac{r_2}{r_1} \right)^2 - 1 \right] \left(\frac{\lambda_2}{\lambda_3} ln\left(\frac{r_3}{r_2} \right) + \frac{1}{2} \right) - ln\left(\frac{r_2}{r_1} \right) \right\}. \tag{55}$$

Some results of the calculation in accordance with the formulae (49)-(51) are gathered below. In these calculations the value of ZrO2 thermal conductivity is taken as 2.0 W/m·K, the value of Zr thermal conductivity is taken as 20.0 W/m·K, the emissivity coefficient of ZrO2 is 0.8, the emissivity coefficient of Zr is 0.325.

No preoxidation: $r_1 = 0.465$ cm, $r_2 = 0.5375$ cm, $r_3 = 0.5375$ cm.

T_{ex}, K	T_{in}, K	ΔT_{ox}, K	q, W/cm^3
1873	1877.2	0.0	335.313
1673	1675.7	0.0	213.44
1473	1474.6	0.0	128.26

100 μm preoxidation: $r_1 = 0.465$ cm, $r_2 = 0.5308$ cm, $r_3 = 0.5408$ cm.

T_{ex}, K	T_{in}, K	ΔT_{ox}, K	q, W/cm^3
1873	1910.7	28.16	921.17
1673	1697.0	17.93	586.37
1473	1487.4	10.77	352.37

300 μm preoxidation: $r_1 = 0.465$ cm, $r_2 = 0.5175$ cm, $r_3 = 0.5475$ cm.

T_{ex}, K	T_{in}, K	ΔT_{ox}, K	q, W/cm^3
1873	1967.0	86.1	1184.66
1673	1732.8	54.8	754.10
1473	1508.9	32.93	453.16

Here T_{ex} is the temperature of the rod outer surface, T_{in} is the temperature in the center of the pellet, ΔT_{ox} is the temperature difference across the oxide layer, *q* is the heat generation in the unit of the metal volume, necessary for the surface temperature T_{ex} to be fixed at the corresponding value in the stationary conditions.

The results of the experiments simulation

A set of the experiments simulations has been carried out using the elaborated heat exchange quench module. Some results of these calculations are presented below. Since the experimental results obtained on the non-preoxidized rod elements seem to be more reliable in comparison with that from the preoxidized rods, the main attention was paid for the non-preoxidized ones.

Figures 1-2 present the temperature evolution of the upper, central and low TC for the T2408 experiment (tube filled with ZrO_2 pellets, no preoxidation, initial temperature 1200 C) for the time intervals 0-40 sec. and 0-10 sec.

Figures 3-4 present the temperature evolution of the upper, central and low TC for the T28085 experiment (tube filled with ZrO_2 pellets, no preoxidation, initial temperature 1400 C) for the time intervals 0-30 sec. and 0-10 sec.

Figures 5-6 present the temperature evolution of the upper, central and low TC for the T28095 experiment (tube filled with ZrO_2 pellets, no preoxidation, initial temperature 1400 C) for the time intervals 0-40 sec. and 0-10 sec.

Figures 7-8 present the temperature evolution of the upper and central TC for the T31085 experiment (tube filled with ZrO_2 pellets, no preoxidation, initial temperature 1600 C) for the time intervals 0-40 sec. and 0-10 sec.

In all the above described figures the dots correspond to the experimental data, the lines are the result of simulation.

The experimentally observed temperature oscillations of the upper and central TC at the very beginning of reflooding (first 1-2 sec.) can not be explained by the heat exchange model. These oscillations are not understood yet.

In the conditions, when the heat release due to oxidation is insignificant, the experimentally measured temperature evolutions are adequately reproduced by the calculations. The different portions of the temperature curves (especially clear visible at the upper TC evolutions) are interpreted in these calculations as the heat exchange with the steam (PS region, see above), the heat exchange with steam and water drops (DS region), and heat exchange due to film boiling (IAFB region).

Figures 9-10 present the temperature distribution in the radial direction at the elevations of the lower and central TC for the T31085 experiment at different time instants. Figure 11 presents the temperature distribution in the axial direction on the rod surface for the T31085 experiment at different time instants.

Figure 12 presents the temperature evolution of the upper, central and lower TC for the T0507 experiment (tube filled with ZrO_2 pellets, 100 μm preoxidation, initial temperature 1400 C) for the time interval 0-10 sec.

Figures 13-14 present the temperature distribution in the radial direction at the elevations of the lower and central TC for the T0507 experiment at different time instants. Figure 15 presents the temperature distribution in the axial direction on the rod surface for the T0507 experiment at different time instants.

Figure 16 presents the temperature evolution of the upper and lower TC for the T1107 experiment (tube filled with ZrO_2 pellets, 300 μm preoxidation, initial temperature 1600 C) for the time interval 0-10 sec.

Figure 17 presents the temperature evolution of the upper TC for the T1207 experiment (tube filled with ZrO_2 pellets, 300 μm preoxidation, initial temperature 1400 C) for the time interval 0-10 sec.

Figure 18 presents the temperature distribution in the radial direction at the elevations of the upper TC for the T1207 experiment at different time instants. Here the presence of the gap was taken into account and the large temperature drop in a gap is observed.

Conclusion

The description of the heat exchange process requires simultaneous solution of two problems: heat conduction problem inside the solid body (fuel rod) and heat convection problem in the surrounding two phase water-steam media. For the solution of the heat conduction problem the finite differences numerical scheme with adaptive grid is used in the present work. The heat conduction model takes into account: different thermal properties of the different layers and spatial distribution of the heat sources (due to Zr oxidation and possible residual heat release). The adaptive grid accounts for the layers thicknesses axial variation due to phase transition and thermal expansion, and for the sharp axial temperature gradients in the quench region.

The non-stationary four-region thermo-hydraulic model based on the conservation laws was developed for the description of the heat convection process. The four water-steam regions existing at a time at increasing elevations are: Bubble Boiling region upstream from the quench front; Inverted Annular Film Boiling region, Droplets-Splashes region and, finally Pure Steam region downstream from the quench front. The motion of the interregion boundaries and the heat flows in each region are self-consistently calculated in the model.

The results of the calculation are in satisfactory agreement with the experimentally measured rod surface temperature evolution.

References:

1. *G.Yadigaroglu*, “The Reflooding Phase of the LOCA in the PWRs. PartI: Core Heat Transfer and Fluid Flow,” Nuclear Safety, Vol. 19, No.1(Jan.- Feb. 1978), p. 20.

2. *E.Elias and G.Yadigaroglu*, “The Reflooding Phase of the LOCA in the PWRs. PartII: Rewetting and Liquid Entrainment,” Nuclear Safety, Vol. 19, No.2 (March- April 1978), p. 160.

3. *R.A.Nelson*, “Mechanisms of Quenching Surfaces,” in: Handbook of Heat and mass Transfer, Vol.1, Heat Transfer Operations, pp. 1103-1153; Gulf Publishing Company, Houston, London, Paris, Tokyo, 1986.

4. *E.Oliveri, F.Castiglia, S.Taibi and G.Vella*, “Predicting Quench Front Velocity in the Rewetting of Hot Surfaces,” in: Reactors and Industrial Applications, Ch. 44, pp. 1339-1355.

5. *L.A.Bromley*, “Heat transfer in stable film boiling”, Chem.Engrg.Progr. 46 (1950), p. 221.

6. *Y.Sudo*, “Film boiling heat transfer during the reflooding phase in a postulated PWR loss-of-coolant accident”. J.Nucl.Sci.Technol. 17 (1980), p. 526.

7. *M.K.Denham*, “Inverted annular flow boiling and the Bromley model”. Trans.Instn. Chem.Engrg. 86 (1984), p. 13.

8. *Y.Y.Hsu and J.W.Westwater*, “Approximate theory for film boiling on vertical surfaces”, Chem.Engrg. 30, 56 (1961), p. 15.

9. *A.Ohnuki, H.Akimoto and Y.Murao*, “Effect of liquid flow rate on film boiling heat transfer during reflood on rod bundle”, J.Nucl.Sci.Technol., 27[6] (1990), p. 535.

10. *Y.Barnea, E.Elias and I.Shai*, “Flow and heat transfer regimes during quenching of hot surfaces”, Int.J.Heat Mass Transfer, 37 [10] (1994), p. 1441.

11. *J.C.Y.Koh,* “Analysis of film boiling on vertical surfaces”, Trans. ASME, J. Heat Transfer, 84 (1962), p. 55.

12. *K.Nishikawa and I.Ito*, “Two-phase boundary layer treatment of free-convection film boiling”, Int.J.Heat Mass Transfer, 9 (1966), p. 103.

13.*H.S.Kao, C.D.Morgan, M.Crawford and J.B.Jones*, “Stability analysis of film boiling on vertical surfaces as a two-phase flow problem”, A.I.Ch.E Symposium Series Nr.118, 68 (1972), p. 147.

14. *N.V.Suryanarayana and H.Merte* Jr., “Film boiling on vertical surfaces”, Trans. ASME, J. Heat Transfer, 94 (1972) p. 377.

15. *N.Takenaka, T.Fujii, K.Akagawa and K.Nishida*, “Flow pattern transitions and heat transfer of inverted annular flow”, Int.J.Multiphase Flow 15 [5] (1989), 767.

16. *K.C.Chan and G.Yadigarodlu*, “Calculations of film thickness heat transfer above the quench front during reflooding”, 19th ASME Heat Transfer Conf. Experimental and Analytical Modelling of LWR Safety Experiments (1980), p.65.

17. *G.Th.Analytis and G.Yadigarodlu*, “Analytical modeling of inverted annular film boiling”, Nucl.Eng.& Des. 99 (1987) p. 201.

18. *K.P.Yu*, “An experimental investigation of the reflooding of a bare tubular test section”, Ph.D. Thesis, UC-Berkeley (1978).

19. *R.Seban, R.Greif*, *G.Yadigarodlu, E.Elias, K.Yu, D.Abdollahian and W.Peake,* “UC-B Reflood Program; Experimental Data Report”, EPRI Report NP-743 (1978).

20. *F. de Cachard*, “Development, implementation and assessment of specific, two-fluid closure laws for inverted-annular film boiling”, Proceedings of the 7th International Meeting on Nuclear Reactor Thermal-Hydraulics NURETH-7, Vol.1, p.166 (1995).

21. *J.Dreier, R.Chawla, N.Rouge and S.Yanar*, “The NEPTUN experiments on LOCA thermalhydraulics for tight-lattice PWRs”, Proc. IAEA Technical Committee on Technical and Economic Aspects of High Converters, Nürnberg (1990).

22. *K.K.Fung*, “Subcooled and low quality film boiling of water in vertical flow at atmospheric pressure”, Ph.D. Thesis, University of Ottawa (1981).

23. *J.W.H.Chi and A.M.Vetere*, “Two-phase flow during transient boiling of hydrogen and determination of nonequilibrium vapour fractions”, Adv.Cryogen.Engng. 9 (1964), p. 243.

24. P.*Ottosen*, “Experimental and theoretical investigation of inverse annular flow, important under LOCA conditions”. Riso National Lab. Report No. R-424, Denmark, 1980.

25. *M.Aritomi, A.Inoue, S.Aoki and K.Hanada*, “Thermal and hydraulic behaviour of inverted annular flow”, In Proc. 2nd Int. Top. Mtg on Nuclear Plant Thermal Hydraulics, 1986.

26. *G. de Jarlais and M.Ishii*, “Inverted annular flow experimental study”, Report NUREG/CR-4277, ANL-85-31, 1985.

27. *G. de Jarlais and M.Ishii*, “Hydrodynamics of adiabatic inverted annular flow – an experimental study”, In Proc. 3rd Multiphase Flow and Heat Transfer Symp., Miami, Fla., 1983.

28. *S.S.Kutateladze*, “Heat and Mass Exchange and the Waves in the Gas-Liquid Systems.” Novosibirsk: Nauka, 1984 (in Russian).

29. *S.S.Kutateladze*, “Handbook of Heat Transfer and Hydrodynamic Resistance.” Moscow: Energoatomizdat, 1990 (in Russian).

30. SCDAP/RELAP5/MOD2 Code Manual, Volume 4: MATPRO-A Library of Materials Properties for Light-Water-Reactor Accident Analysis. NUREG/CR-5273 EGG-2555. Vol.4. 1990.

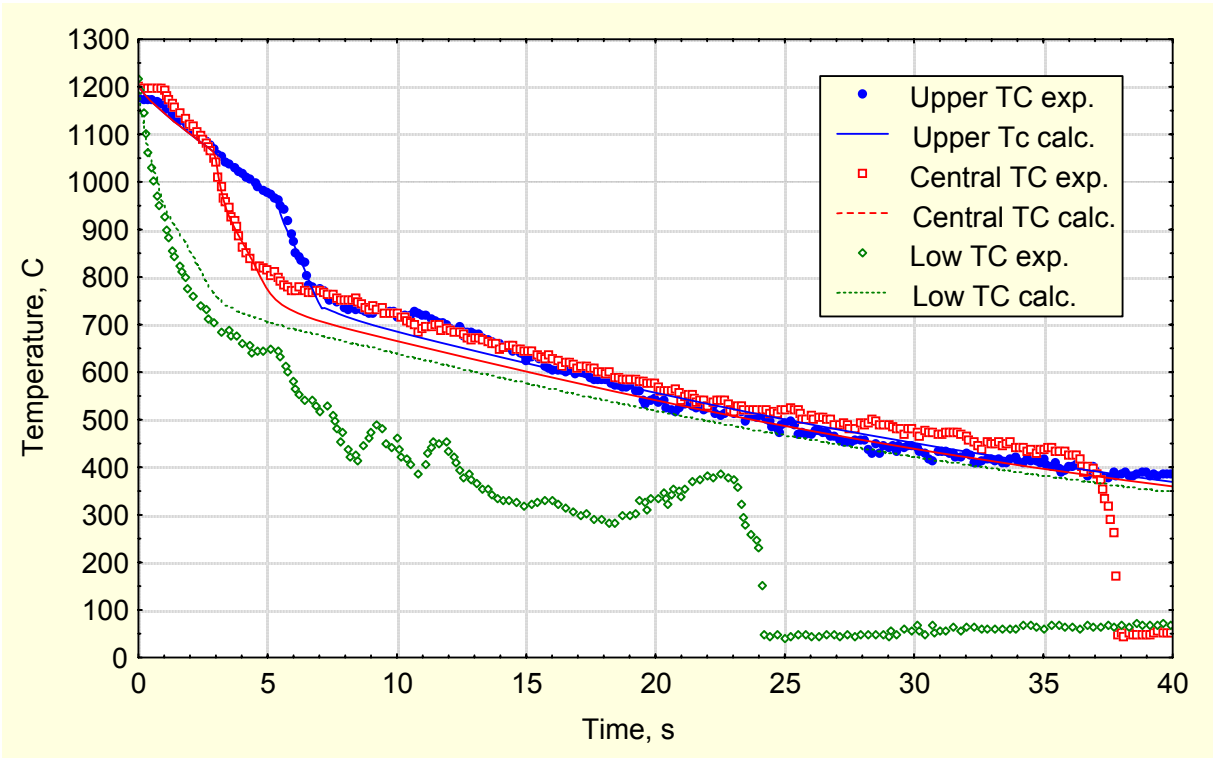

Fig. 1. T2408 experiment data and simulation. Temperature evolution of upper and central TC for the time interval 0 - 40 s.

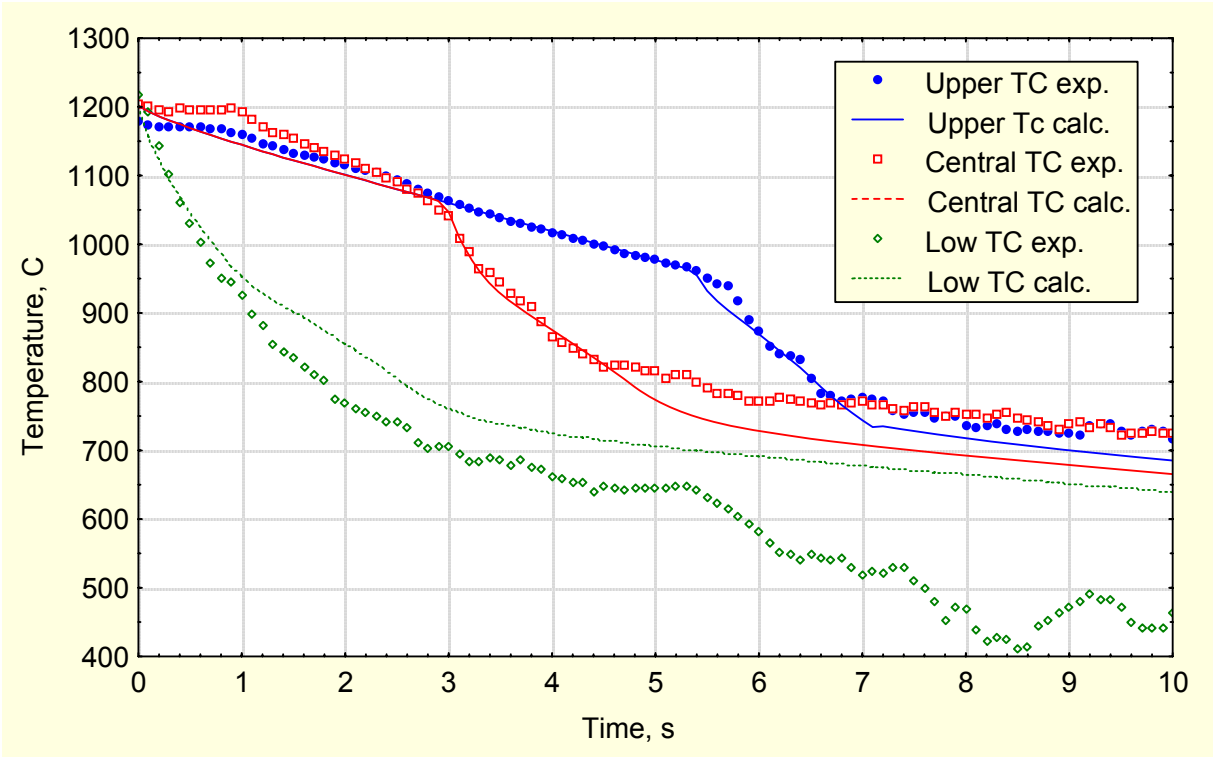

Fig. 2. T2408 experiment data and simulation. Temperature evolution of upper and central TC for the time interval 0 - 10 s.

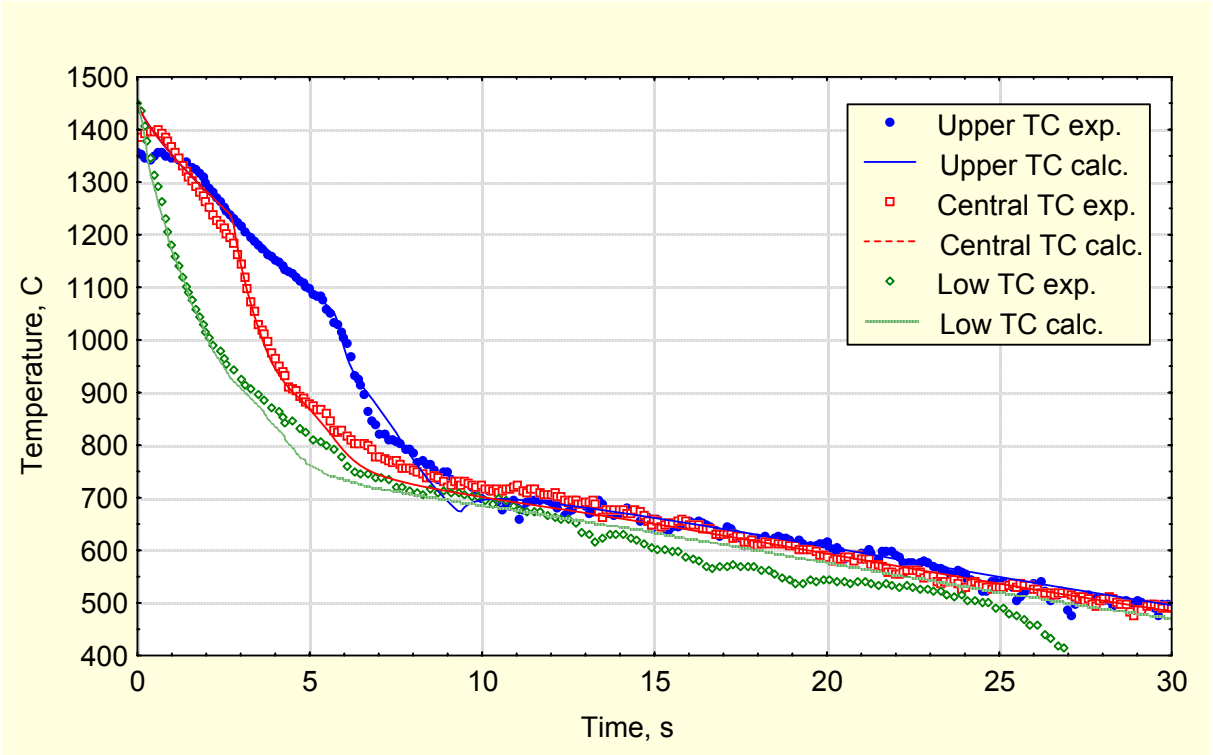

Fig. 3. T28085 experiment data and simulation. Temperature evolution of upper, central and low TC for the time interval 0 - 30 s.

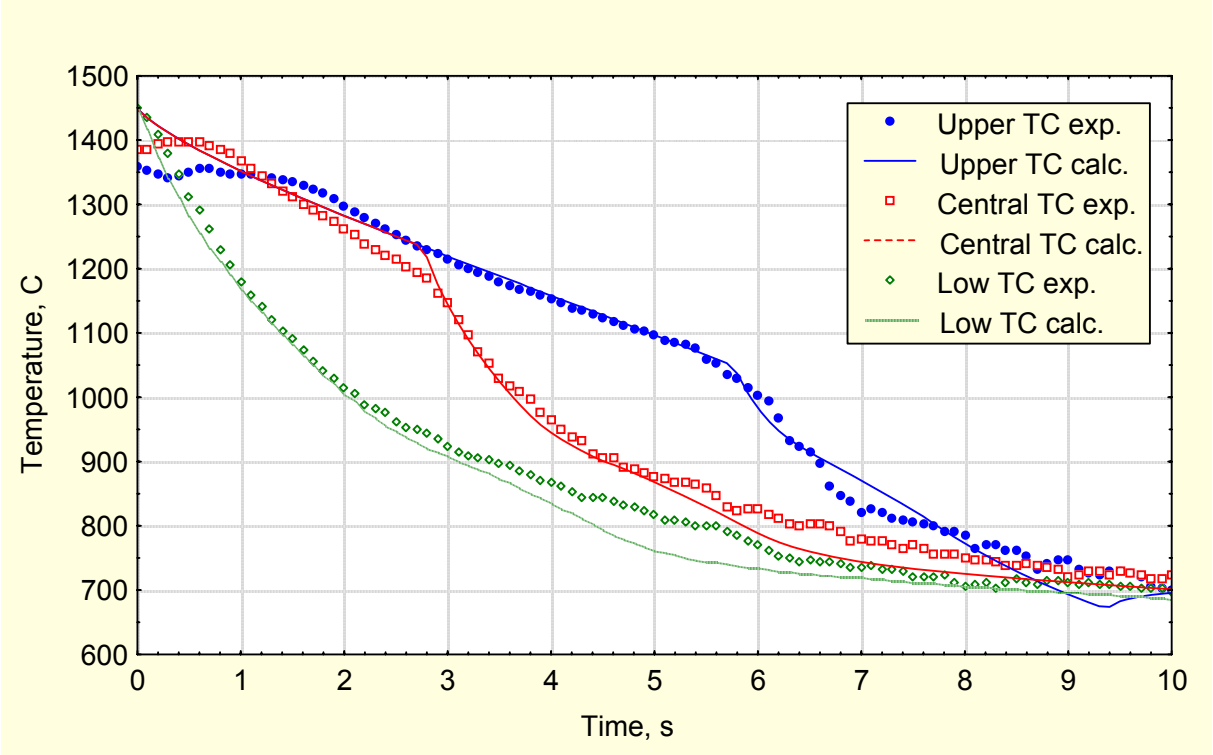

Fig. 4. T28085 experiment data and simulation. Temperature evolution of upper, central and low TC for the time interval 0 - 10 s.

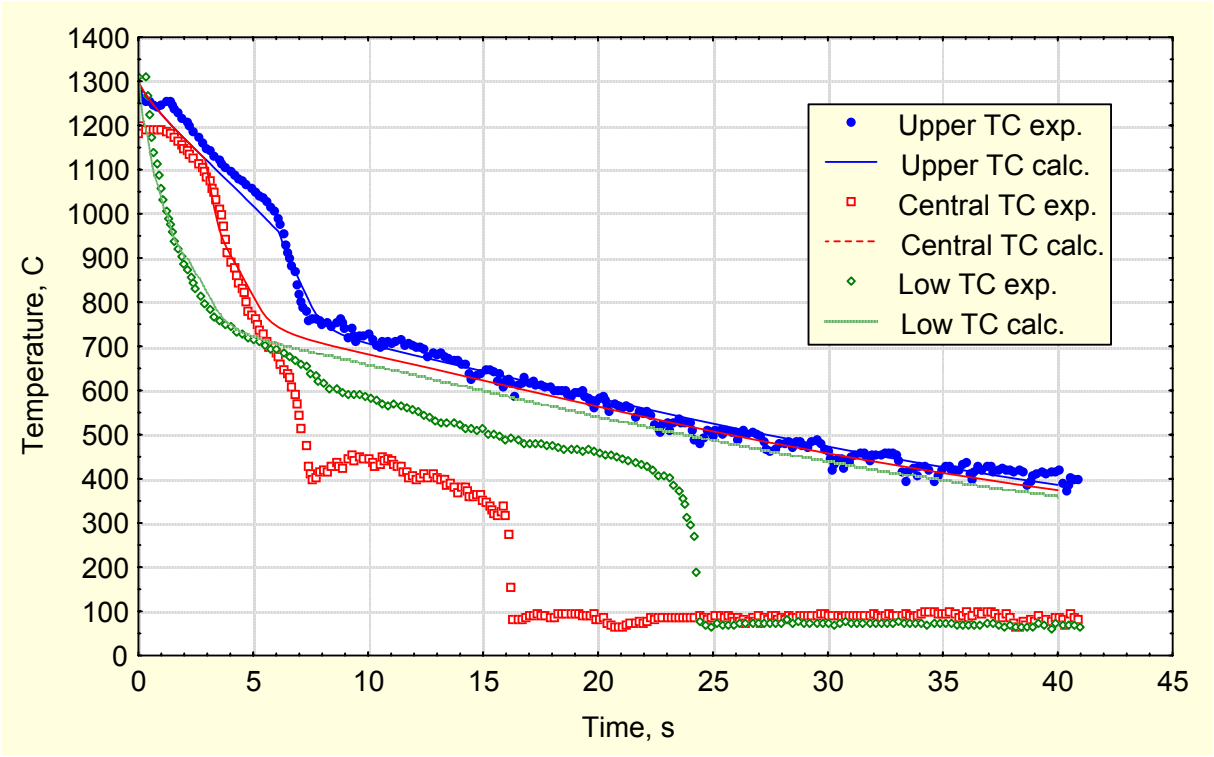

Fig. 5. T28095 experiment data and simulation. Temperature evolution of upper and central TC for the time interval 0 - 40 s.

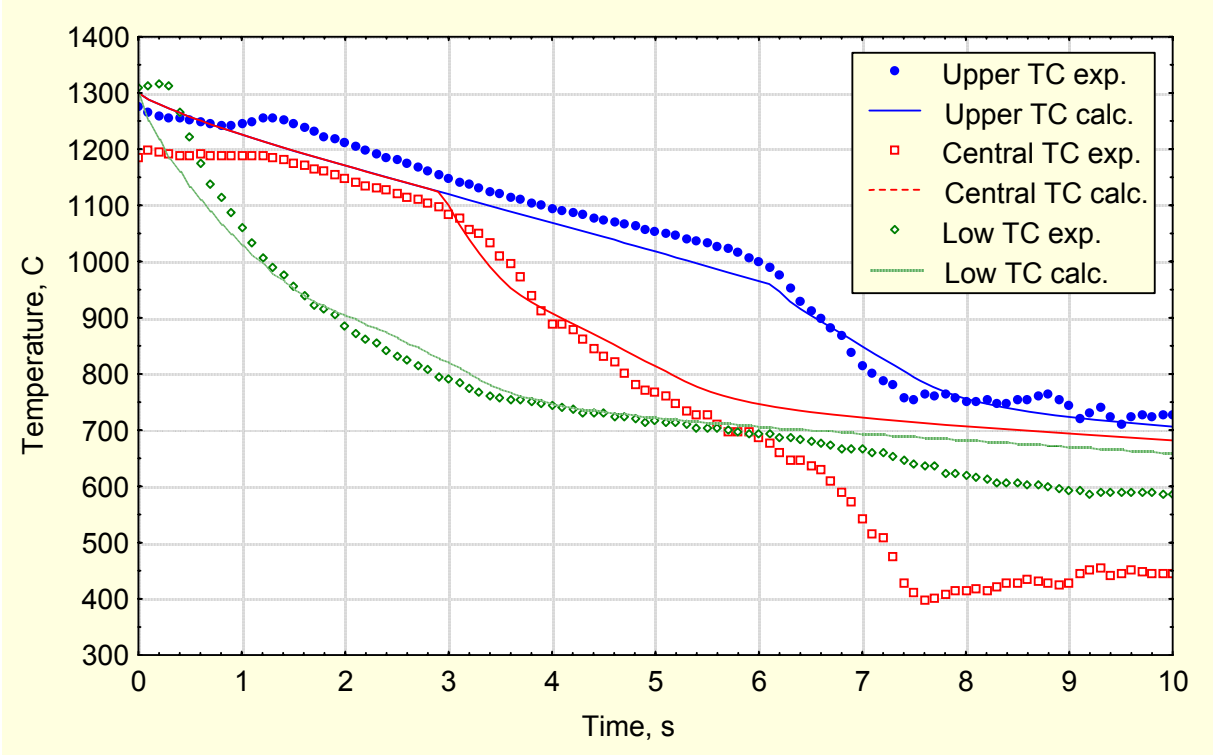

Fig. 6. T28095 experiment data and simulation. Temperature evolution of upper and central TC for the time interval 0 - 10 s.

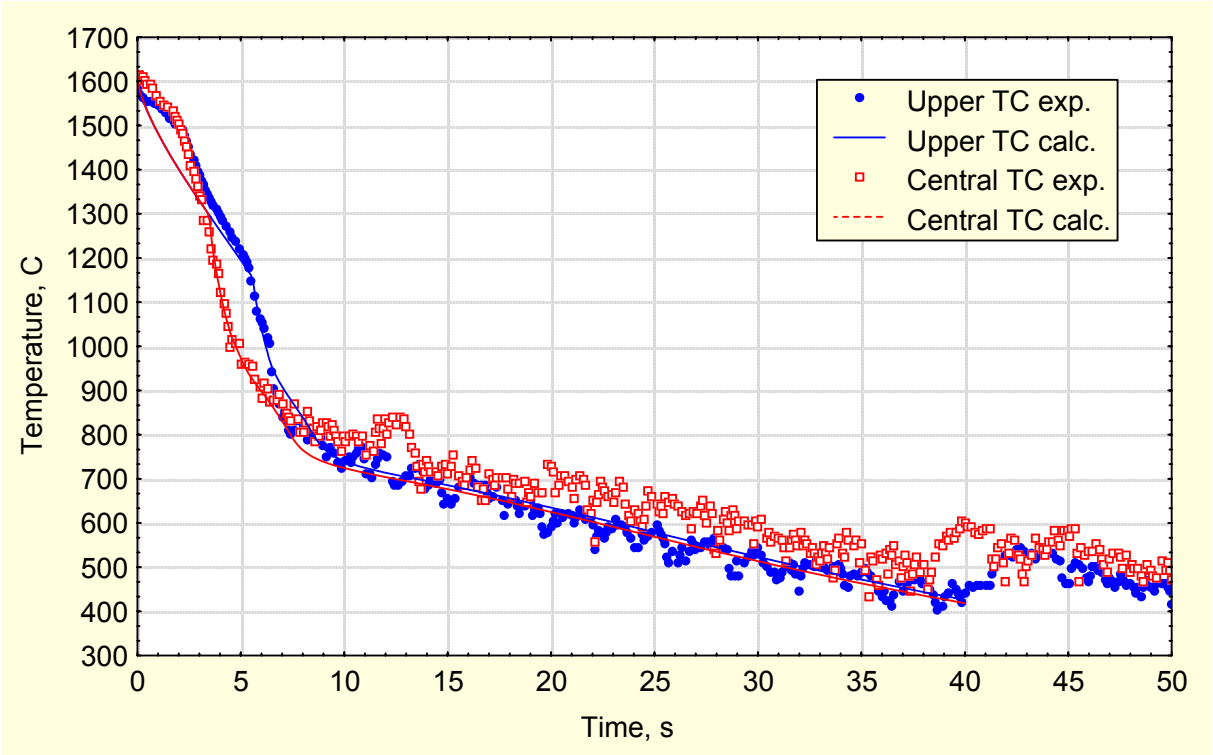

Fig. 7. T31085 experiment data and simulation. Temperature evolution of upper and central TC for the time interval 0 - 40 s.

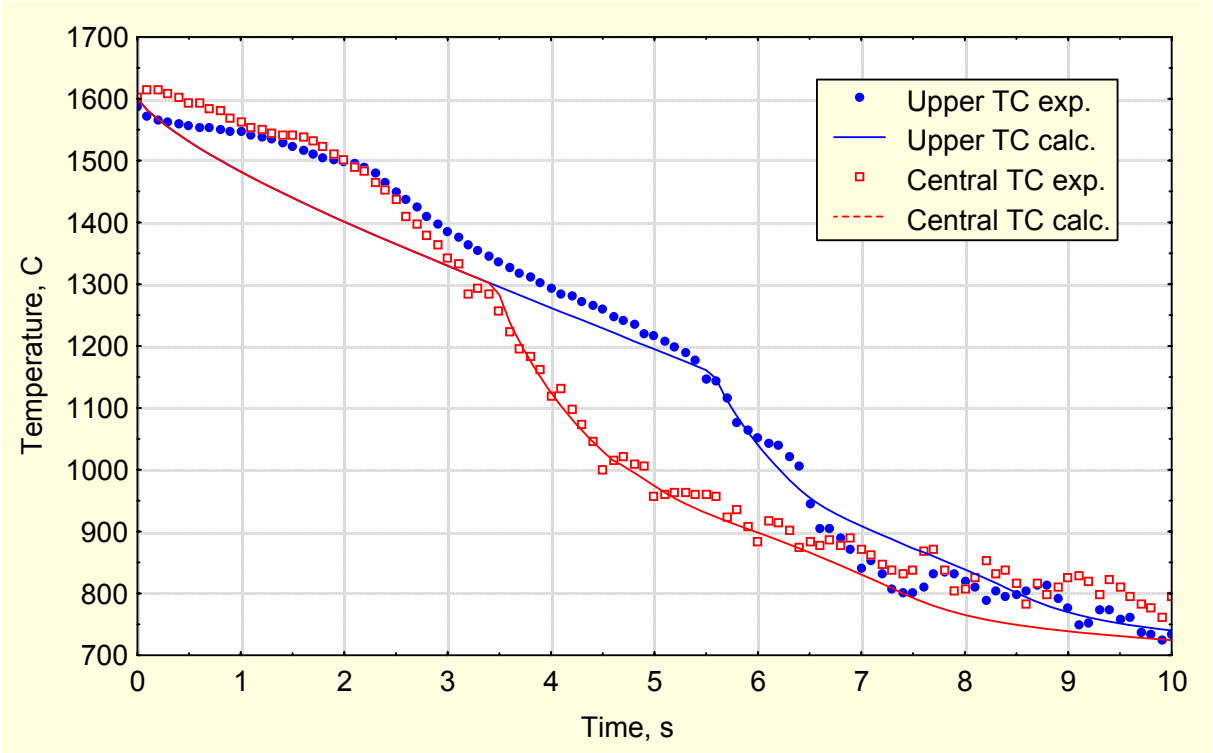

Fig. 8. T31085 experiment data and simulation. Temperature evolution of upper and central TC for the time interval 0 - 10 s.

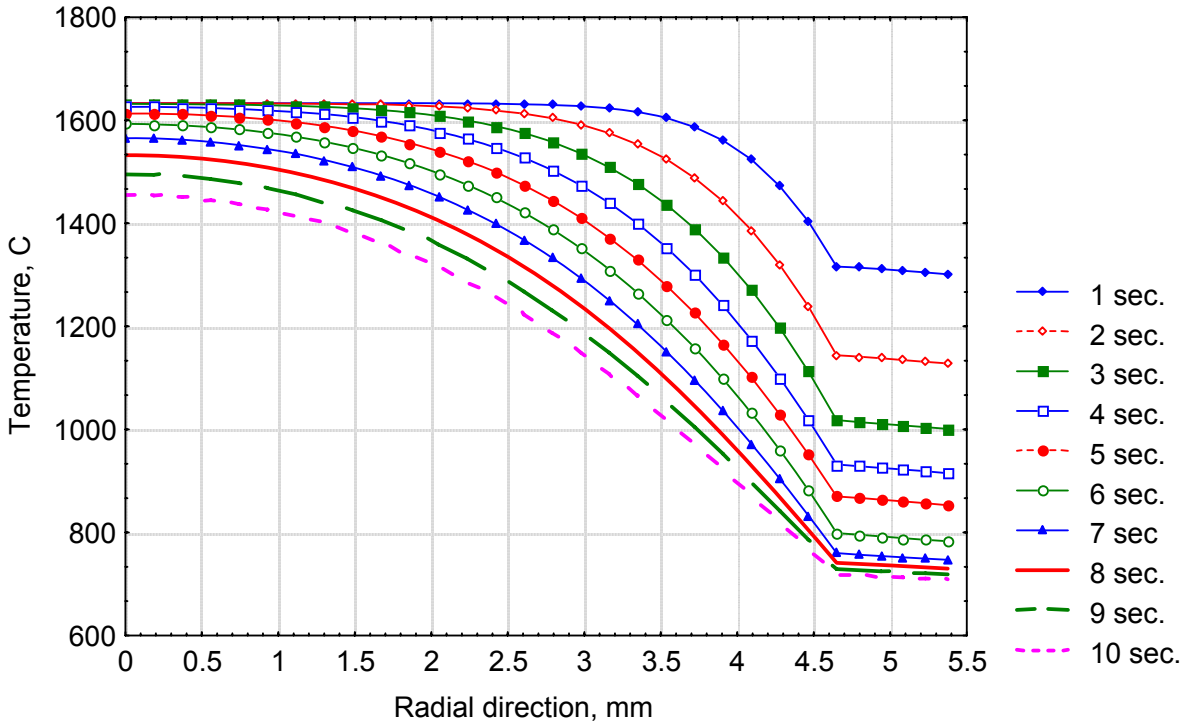

Fig. 9. T31085 experiment simulation. Temperature distribution in the radial direction at the low TC elevation (2 cm from below) at different time instants.

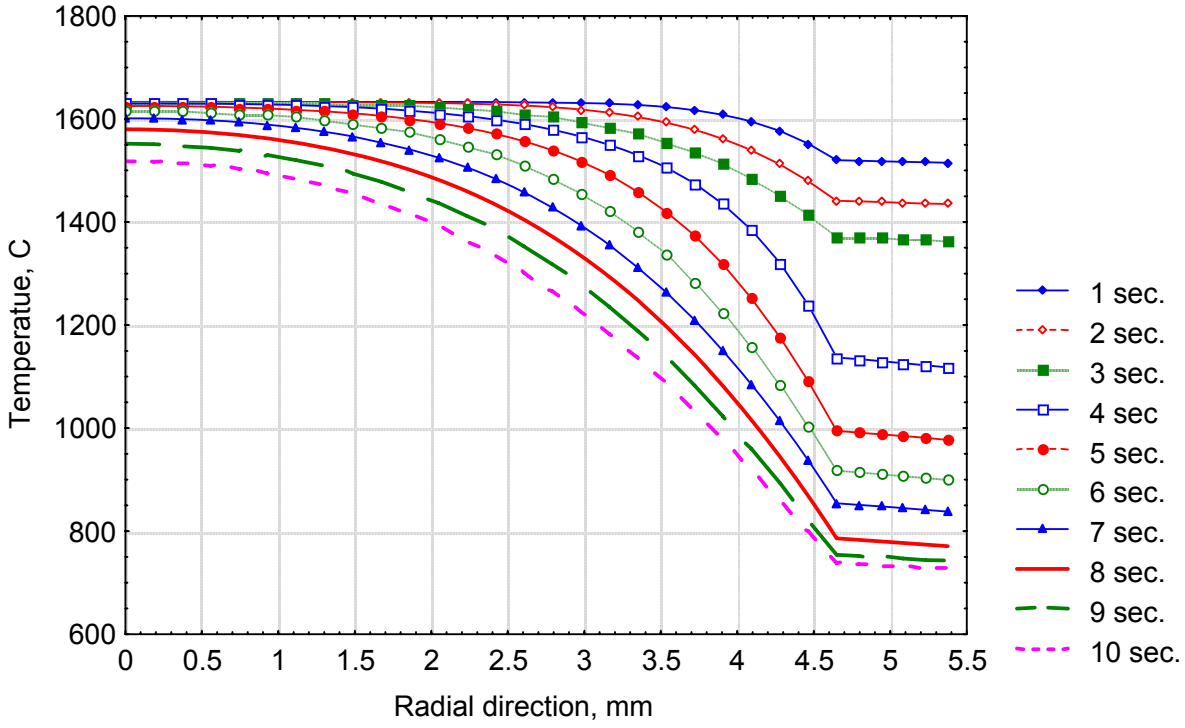

Fig. 10. T31085 experiment simulation. Temperature distribution in the radial direction at the central TC elevation (7.5 cm from below) at different time instants.

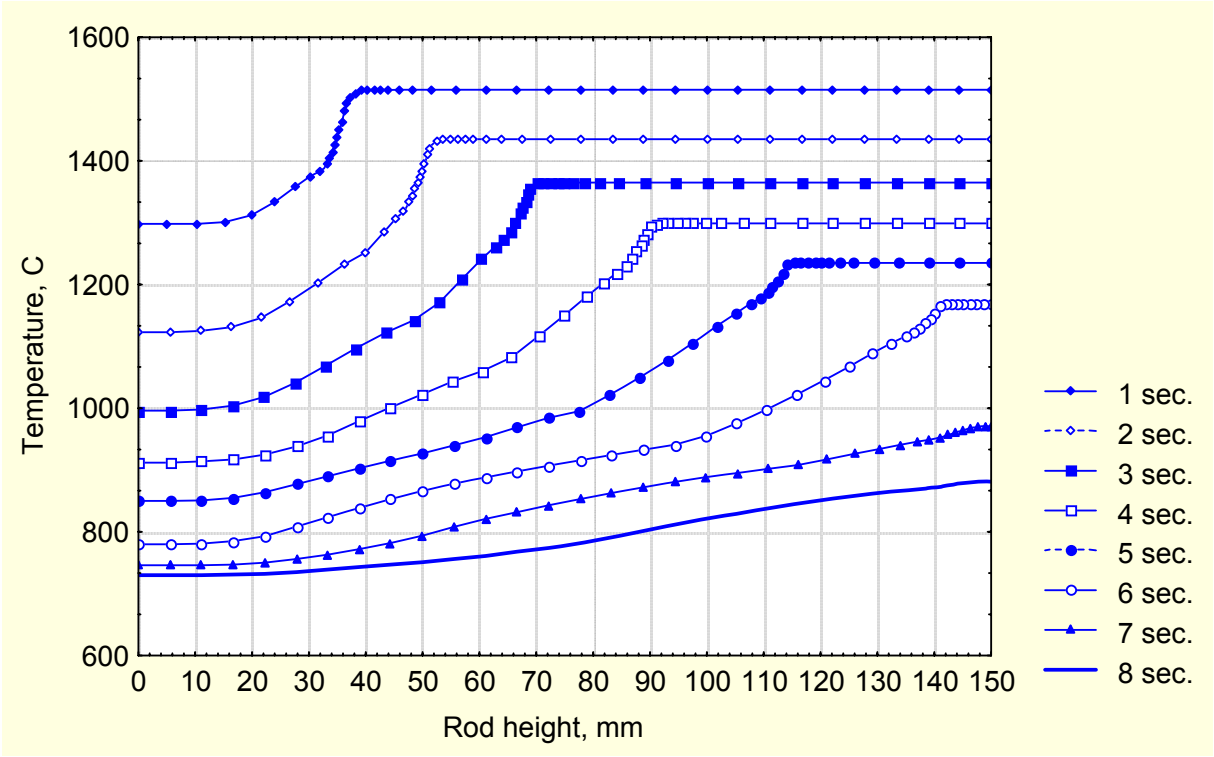

Fig. 11. T31085 experiment simulation. Temperature distribution in the axial direction on the rod surface at different time instants.

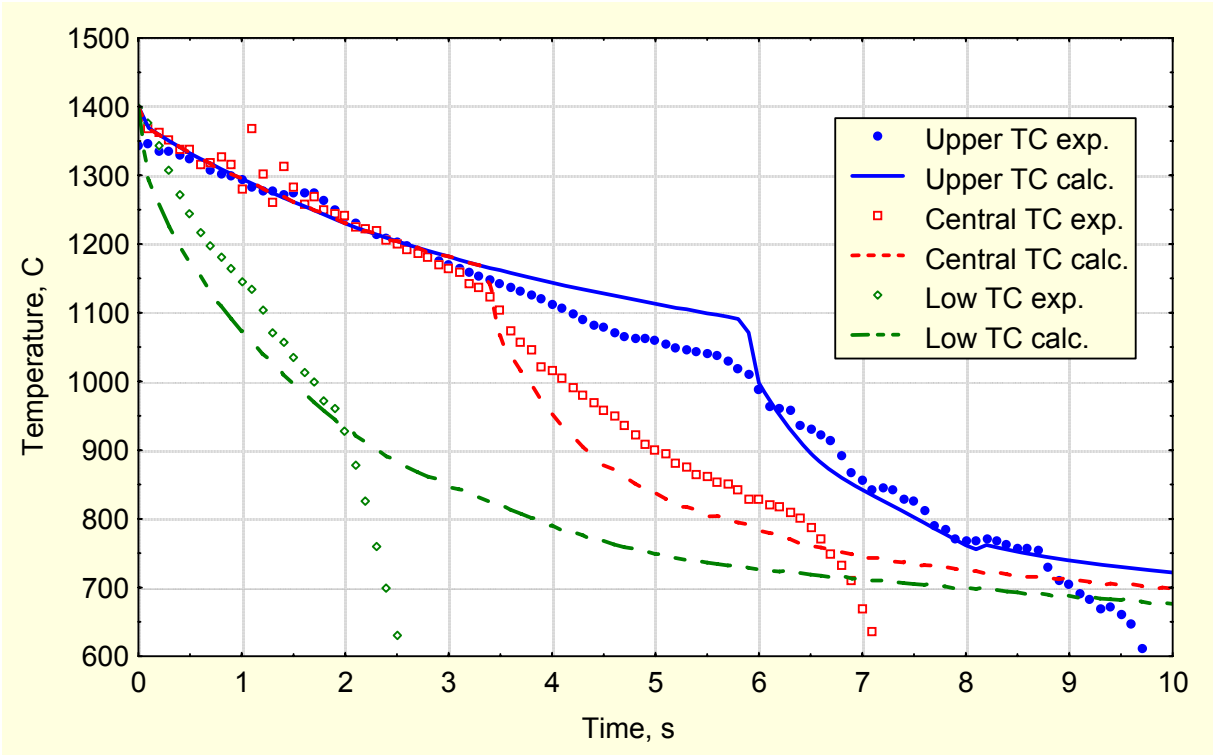

Fig. 12. T0507 experiment data and simulation. Temperature evolution of upper, central and low TC for the time interval 0 - 10 s.

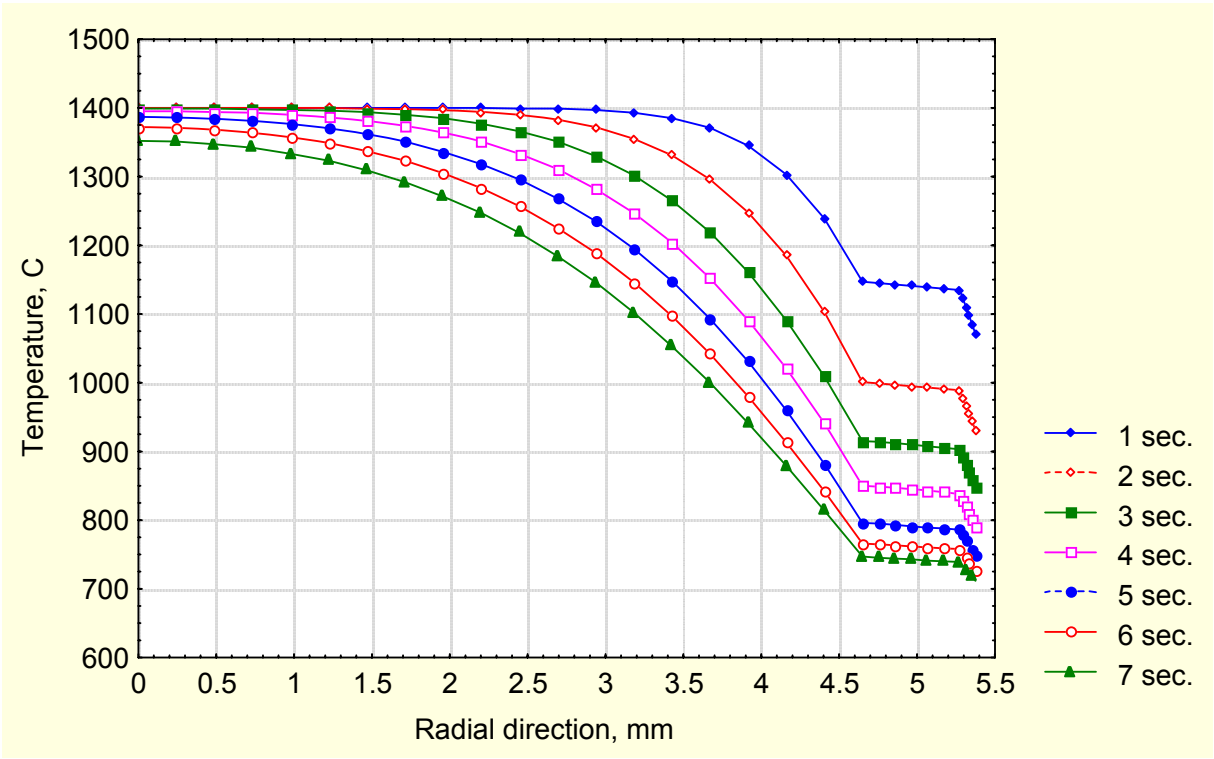

Fig. 13. T0507 experiment simulation. Temperature distribution in the radial direction at the low TC elevation (2 cm from below) at different time instants.

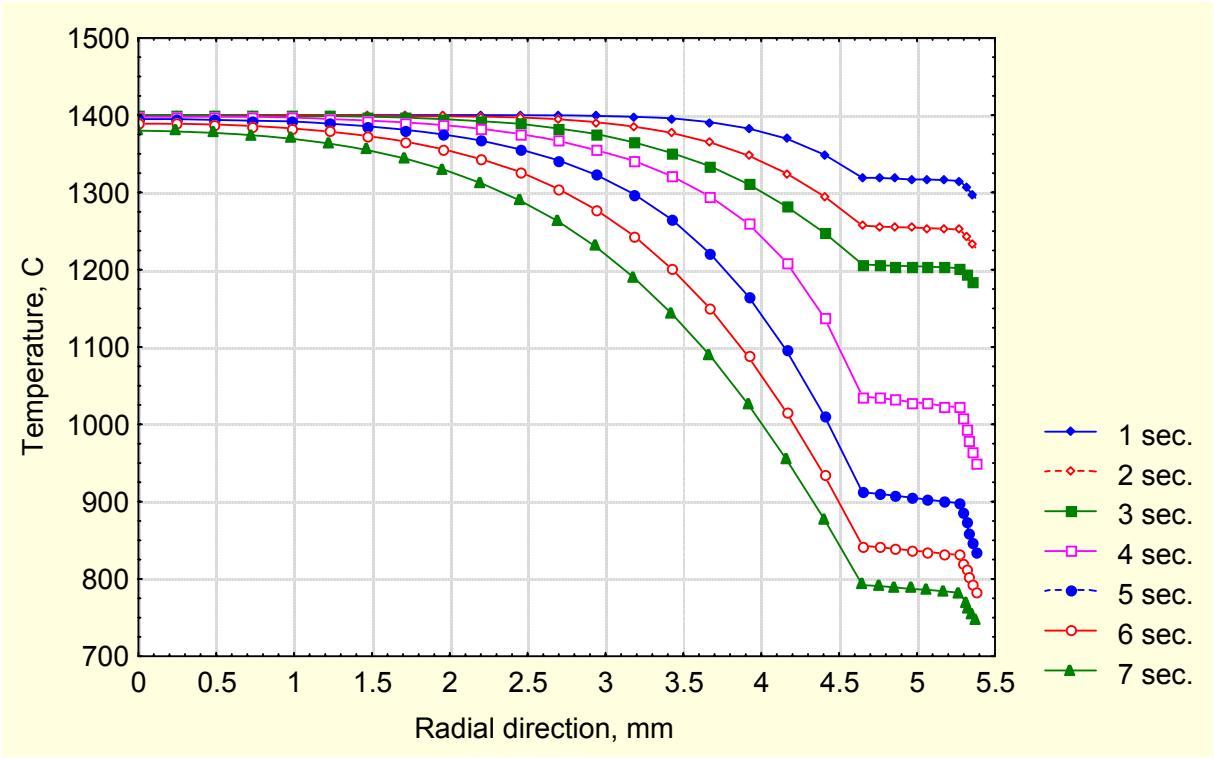

Fig. 14. T0507 experiment simulation. Temperature distribution in the radial direction at the central TC elevation (7.5 cm from below) at different time instants.

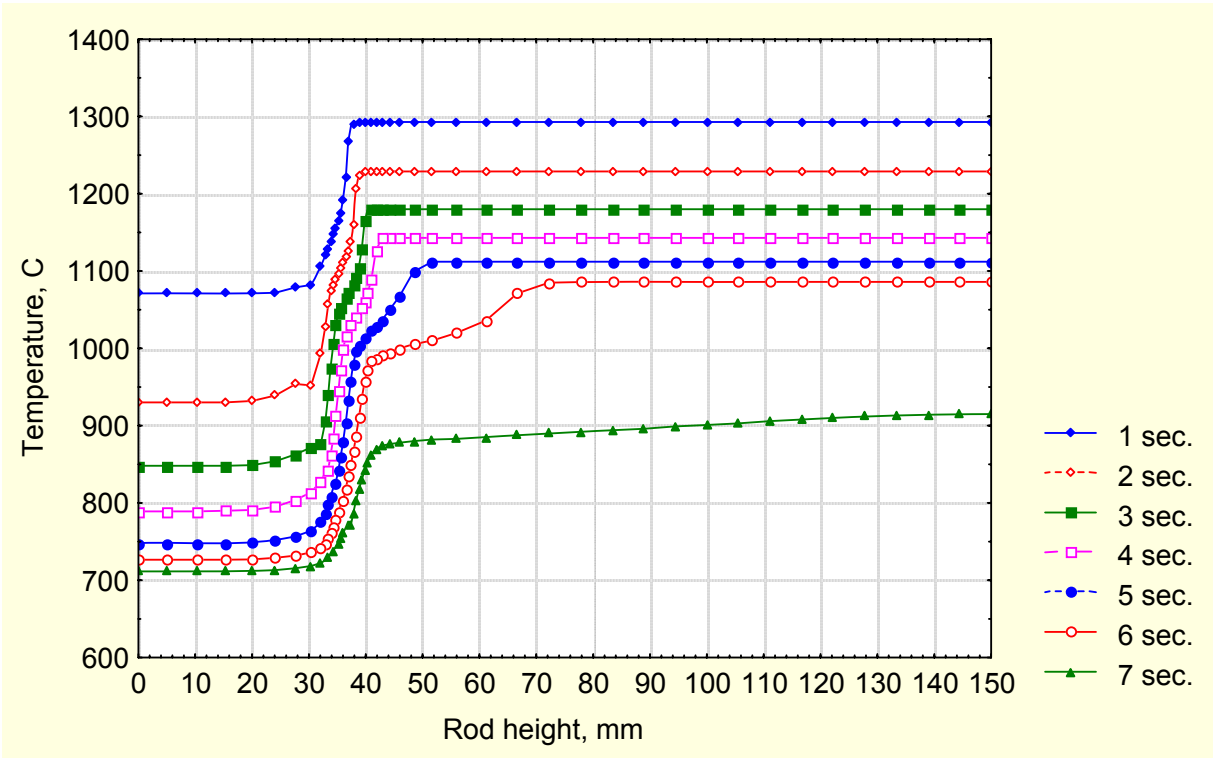

Fig. 15. T0507 experiment simulation. Temperature distribution in the axial direction on the rod surface at different time instants.

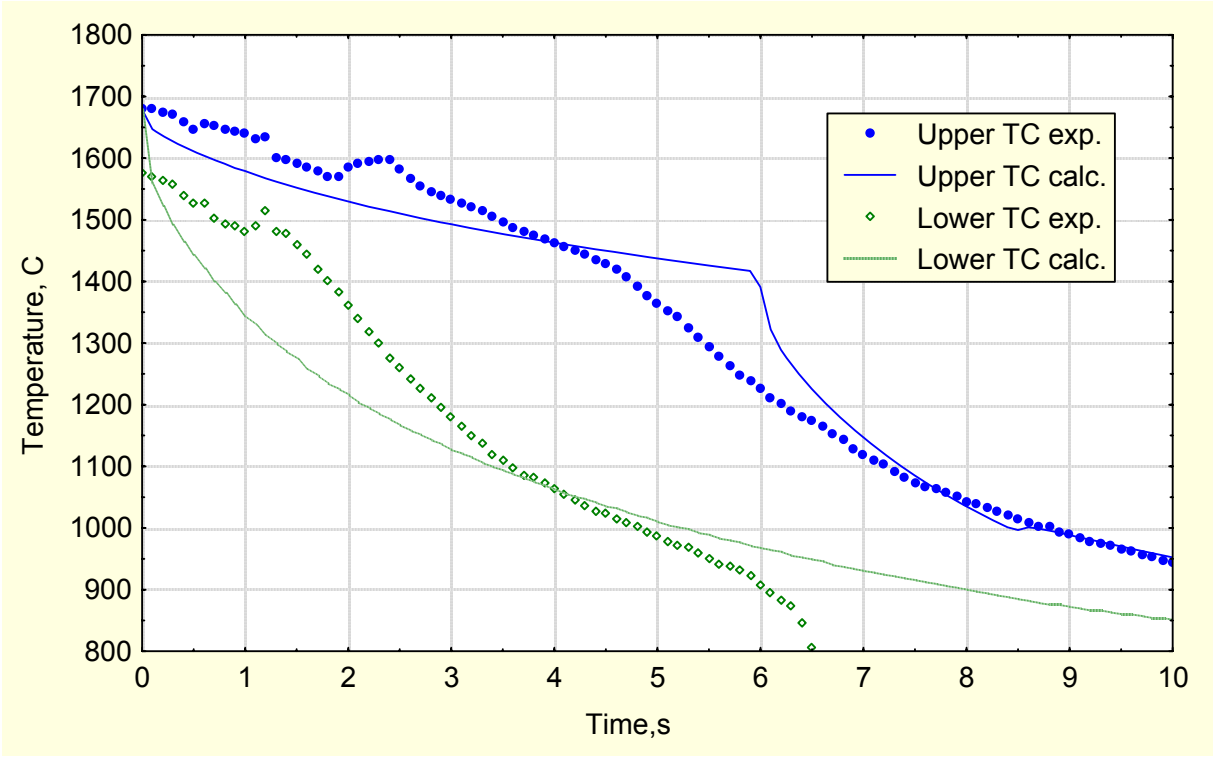

Fig. 16. T1107 experiment data and simulation. Temperature evolution of upper and lower TC for the time interval 0-10 s.

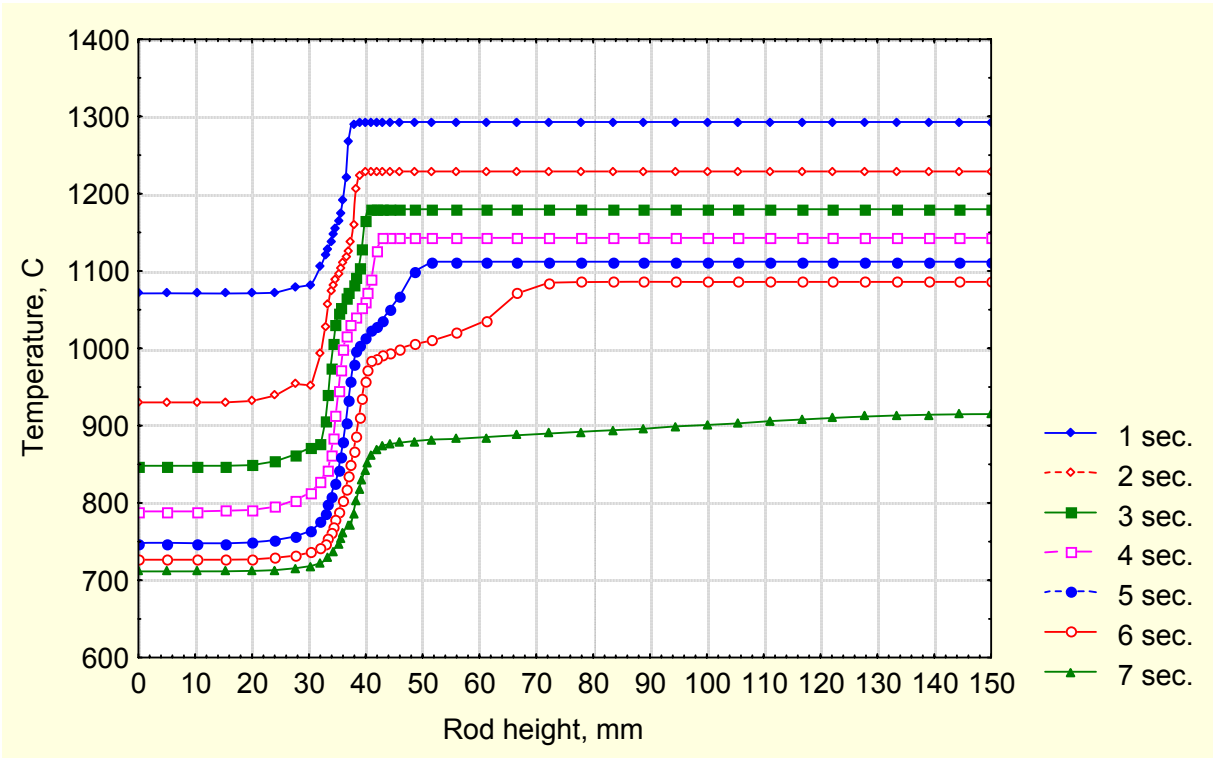

Fig. 15. T0507 experiment simulation. Temperature distribution in the axial direction on the rod surface at different time instants.

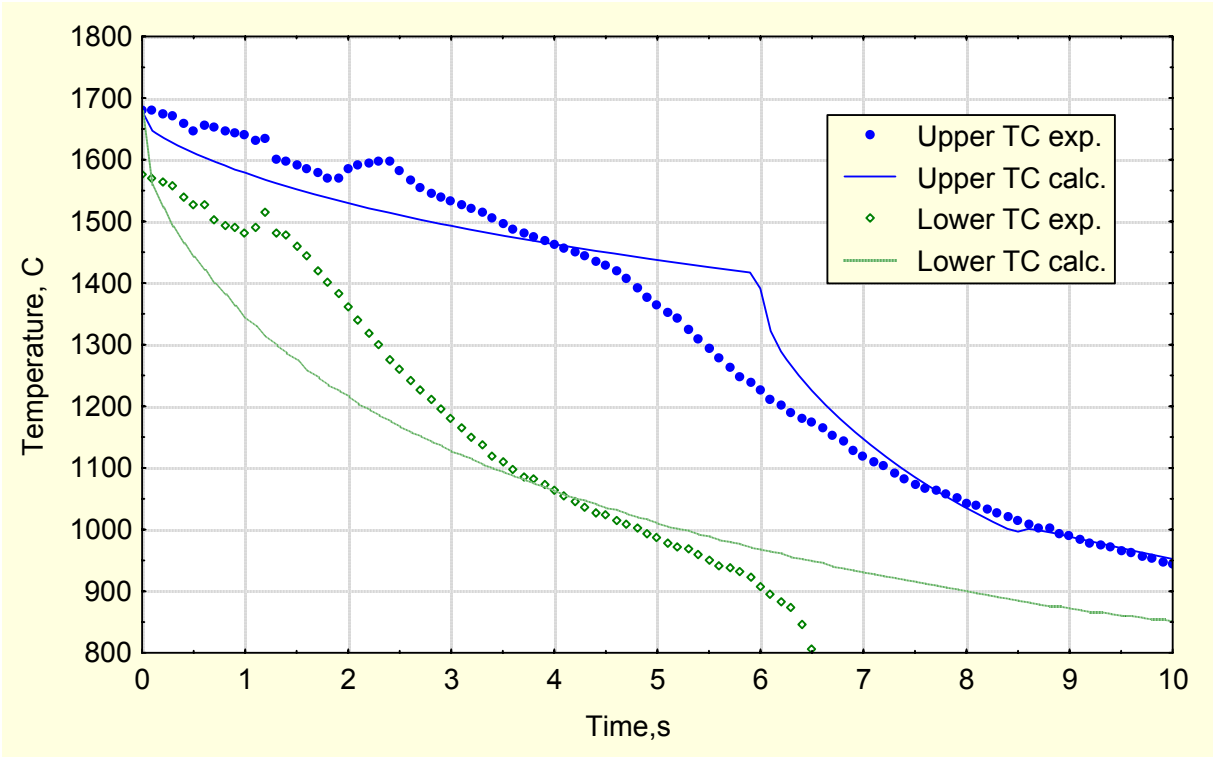

Fig. 16. T1107 experiment data and simulation. Temperature evolution of upper and lower TC for the time interval 0-10 s.

II. Development of the Data Base for the Kinetic Model of the Zircaloy-4 /Steam Oxidation at High Temperatures (1000°C≤T≤1825°C)

1. Introduction.

A series of zirconium-based alloys, known as Zircaloys, has been developed for use as the fuel cladding in light water nuclear reactors. Zircaloy-4 is currently the most generally used alloy of the series.

In the event of a hypothetical Loss of Coolant Accident (LOCA) in which the coolant is drained from the reactor core, the residual and fission product decay heat from the nuclear fuel and the heat generated by the highly exothermic Zircaloy - steam reaction will cause the cladding temperature to increase as the core is refilled with coolant by Emergency Core Cooling System. Steam will be produced, and oxidation steam - Zircaloy reaction will begin when the core is refilled with coolant (borated water). This process determines or influences:

- the extent of hydrogen formation

- the heat generation with the start of the reaction

- the fuel rod - steam transfer coefficient

- the mechanical behavior to the cladding under internal pressure stress, which, in turn, determines the ability of Zircaloy cladding to maintain its integrity and confine the fuel in a geometry amenable to cooling.

Therefore, the precise information on oxidation of these alloys and oxygen diffusion in them is important in determination of safety criteria for light water reactors.

Currently there are different correlations which describe oxidation rate of Zry-4 as function of temperature. They are based on the experimental results of different groups, which will be observed in Sec.2. In spite of rather high accuracy and reproducibility of conducted experiments these correlations give substantially different oxidation rates (thus, for example, the rates of oxygen uptake in [14] and [15] at $T \approx 1000^0$C differ from each other by a factor of two). In such a situation the main objectives of this work were: a) to make a critical review of possible experimental works and to choose those of them which used the mostly grounded methods and experimental procedure, were fulfilled with maximum accuracy and contained minimum systematic errors; b) basing on the results of this experiments to calculate the Arrhenius type dependencies of oxygen diffusion coefficients on temperature in different phases with 95% confidence interval.

To perform this task the following studies were held:

- analysis and comparison of methods and accuracy of various experiments on oxidation kinetics found in literature;

- statistical treatment of the available experimental data in order to determine the presence of possible systematic errors in measurements or treatment of experimental procedures;

- look for possible reasons of the discovered systematic errors and estimation of their values based on the analyses of experimental procedures;

- determination of the most reliable experimental data sets and corresponding kinetic Arrhenius correlations measured in these tests;

- development of final and unique correlation dependencies for oxidation kinetic parameters (diffusion coefficients in various phases of oxidizing Zry) and of confidence intervals for these.

2. Survey of the literature on investigations of the oxidation behavior of Zircaloy in a LOCA.

A great number of papers were published in the past few decades, are interesting in connection with the behavior of Zircaloy in LOCA. Investigations of the oxidation kinetics of zirconium in oxygen and the oxygen diffusion connected with it have been critically reviewed by Rosa [1] and Ritchie et al [2]. Baker and Just investigated the oxidation kinetics of zirconium at its melting point in contact with steam; on the basis of these measurements as well as similar results of Lemmon [3] and Bostrom [4] for Zircaloy at lower temperatures, they formulated a relationship between hydrogen formation under oxidation by steam as a function of reaction temperature and time [5]. This widely used Baker-Just equation gives a straight line in the plot of the logarithm of the parabolic reaction velocity against the reciprocal of the absolute temperature; the slope of this line represents the activation energy. The oft-expressed criticism of Baker-Just equation is the following:

- a uniform activation energy over the whole temperature range is not to be expected because there are three known different crystal structures of zirconium oxide;

- new kinetic data yielded lower oxidation rates, particularly above 1200°C.

Later various correlations have been proposed between oxidation conversion (oxygen uptake, production of hydrogen, equivalent metal conversion) and such parameters as time and temperature (see [6] - [11]). Accuracy of these measurements was significantly lower than in later investigations (described below). On the other hand, availability of these correlations is insufficient for the construction of full oxidation kinetic model, as it will be seen further. As an alternative to [6]-[11] some authors have quantified the growth of the double layer composed with oxygen-rich layers of oxide and α - phase. Holson and Rittenhouse [12] proposed such a relation which fitted measurement results between 927°C and 1371°C. Since then this equation has been the subject of criticism either. The objections were based on a possible shortage of steam under the experimental conditions and on the lack of specimen temperature correct determination. Mallet et al [13] roughly estimated an equation for oxygen dif-

fusion coefficient in the α - phase from experimental results, thus setting up a relation between the thickness of double layer and the expression $\sqrt{D_\alpha t}$ (D_α - oxygen diffusion coefficient in α - phase, t - reaction time). Due to a more complex (three-layer) structure of oxidation zone this estimation is rather simplified.

As it will be shown below, for the development of comprehensive model of Zircaloy oxidation, describing also steam oxidation of Zry during transient temperature regimes, one must know oxygen diffusion coefficient in each phase appeared at a given temperature. These values, in turn, can be obtained from the results of isothermal experiments if growth rates of oxide and α - phase layers were measured separately. For these reasons, experiments in which these values had been measured simultaneously are especially important.

In the experiments of Urbanic and Heidrick [14] reaction kinetics and the growth rates of the oxide and α - phase layers for Zircaloy - 4 in steam have been measured. The parabolic rate constants for oxygen uptake were significantly lower than the constants given by Baker and Just correlation. However, as it was indicated by the authors of Ref. [14], precision of temperature measurements in these experiments was $\pm$25°C. This temperature interval is too large since it allows to strong deviations in measured values ($\approx$50%) at the examined temperatures $T \geq 1000$°C (see below sec.5). In this work methods of oxygen uptake measurements (hydrogen evolution and weight gain methods) are described in some details, however, the description of the layers thicknesses measurements is practically absent; therefor, estimation of the accuracy of these measurements is impossible. Besides Sn content in the samples of [14] was determined with the accuracy of 0.5 wt.%. As it will be shown in sec.5 this uncertainty in the composition may also lead to essential deviations in oxidation rates.

As a part of the Zirconium metal-water oxidation kinetics program at the American Oak Ridge National Laboratory, isothermal oxidation was investigated between 900°C and 1500°C in a 50°C step. In the region of parabolic kinetics above 1000°C velocity constants were formulated for the oxygen uptake and oxide layers thicknesses, α - phase and double (oxide + α - phase) layers as a function of temperature. In addition, the layers' thicknesses were measured metallographically, the oxygen uptake was calculated approximately from these data and compared with direct measurements [15].

Analogous measurements were performed by Leistikow and Schanz [16] in the temperature range up to 1600°C. The results for growth rates of oxide and α - phase layers measurements was in rather good agreement with [15]. But still some discrepancies were observed, and their possible reasons will be discussed below. The influence of preoxidation, steam supply and presence of different gases in steam on oxidation kinetics was also investigated in [16].

The oxidation kinetics of Zircaloy-4 in steam was extended to 2400°C in the experiments of Prater and Courtright [17]. It was shown that oxide and α - phase layers display parabolic growth behavior over the entire temperature range studied. A discontinuity in the oxidation kinetics at 1510°C causes rates to increase above those previously established by the Baker-Just relationship. This increase coincides with the tetragonal-to-cubic phase transformation in oxide in accordance with the equilibrium binary Zr-O phase diagram [21]. No additional discontinuity in the oxide growth

rate was observed when the metal phase melted. Due to the complicated experimental procedure (laser heating) which did not allow an exclusion of significant intrinsic heat generation during oxidation it may be supposed that the precision of temperature measurements was much lower than denoted by the authors (see below in sec.6).

Rather accurate measurements of oxygen diffusion in the β-phase were carried out at 900°C- 1500°C by Perkins [18]. The combination of three different experimental procedures (thin film tracer diffusion, single-phase chemical diffusion couple and phase-boundary-movement chemical diffusion couple) and two methods of oxygen profiling (oxygen-18 radio activation and Auger Electron Spectroscopy) were used to increase the confidence in the results. The use of different analytical methods and evaluation procedures leading to the close results for calculated diffusion coefficients in this investigation allows us to consider these results to be rather reliable, and applicable for further calculations of oxidation kinetics.

In sec.3 experiments [15], [16] and [17] will be described in some details. In sec.4 a theoretical model of isothermal oxidation of Zircaloy is presented. The results of these experiments and discussion for the temperature range from 1000^0C to 1500^0C will be presented in sec.5 and for 1500^0C<T<1823^0C - in sec.6. The conclusions are made in sec.7.

3. Experimental apparatus and technique.

As it was pointed out in sec.2, only few experimental data seem to be reliable and sufficiently complete for self-consistent calculations of diffusion coefficients in various phases of oxidizing Zry. For this reason we will present more detailed description of these experiments.

In [15] an apparatus was used that permits to examine in highly reproducible manner the early stage oxidation behavior of reactive metal specimen at high temperatures. Time duration of heating was 30 sec at maximum temperature 1500°C. In the temperature range considered in this investigation, the isothermal oxidation of Zircaloy results in growth of well-defined product layers in the host beta phase. These layers, the outermost oxide phase and intermediate oxygen-stabilized alpha phase, are generally uniform in thickness and are easily recognized by conventional metallographic procedure. In order to make meaningful measurements of the high temperature, isothermal reaction kinetics for this material, a low thermal inertia apparatus based on a radiant heating furnace was constructed. This apparatus permitted specimen to be subjected to flowing steam during short, precisely documented, temperature excursions.

The multi-specimen technique was used in which a number of samples, oxidized during various periods of time at nominally the same temperature, were examined to determine the layer growth behavior. The specimen consisted of 3 cm of Zircaloy-4 tubing having an inner diameter of about 1 cm and a wall thickness of 0.0635 cm. The nominal composition (weight percent) was: 1.60 Sn, 0.25 Fe, 0.12 Cr, 0.009 C, 0.003 N, 0.0025 H (Sandvik Special Metals Corporation). Each specimen had at its midplane on the inner surface three calibrated Pt *vs*. Pt-10%Rh thermocouples. The hot

junction was formed by a spot welding of the thermocouple beads to small, thin tantalum tabs that were in turn welded to the specimen.

Exhaustive analysis of the magnitude of potential temperature measurement errors in this technique indicates that the maximum probable error for isothermal operation ranged from ±4°C at 900°C to ±6°C at 1500°C. The reactor chamber was a 6 cm OD quartz tube and the specimen was centered along the axis between two smaller quartz tubes. During an experiment, the oxidant flowed over the outer surface of the specimen, while a slight positive pressure of helium was maintained inside the specimen and its support to prevent excessive steam leakage into interior of the tube. For each of 13 temperatures between 900°C and 1500°C being investigated, at least ten specimens were oxidized and examined.

The steam flow rate over the specimen in all cases was about 1 m/sec during oxidation, which was sufficient to avoid steam starvation or gas-phase control of the process. The time temperature cycles used to approximate the isothermal exposures were set into the programmer/controller prior to each experiment. Specimens were heated up to the desired temperature at the rates exceeding of 100°C/sec, then they were held at constant temperature (within ±2°C) for the required time and then cooled at initial rates greater than 200° C/sec. Such cycles comprise accurate approximations of “isothermal” exposures at comparatively low temperatures when exposure time over 100 sec was common,. At higher temperatures when short-time experiments were conducted, the influence of oxidation during heat up and cool down was taken into account in the expression for effective reaction time of oxidation:

$$t_{eff} = \frac{\int_0^t \exp[-Q/RT(t)]dt}{\exp[-Q/RT_{eff}}$$

where t_{eff} - equivalent time in sec at an assigned temperature T_{eff} measured in *K*; *T(t)*- actual temperature as a function of time *t*; *Q* - activation energy which is taken to be 40000 cal/mole; *R*- gas constant; *t* -time. When phase thicknesses were measured at higher temperatures, it was observed that the product layer thickness on each specimen exhibited a circumferential variation implying a similar variation in the reaction temperature. The periodicity of this variation was consistent with the geometry of the radiant heating furnace. The measurements of phase thicknesses were made with a calibrated filar micrometer eyepiece on a small bench metallograph. The average of seven observations made at 5^0 intervals $\pm 15^0$ from each thermocouple position was used.

So it is seen, that experimental measurements and the treatment of the results obtained in [15] have been fulfilled with great accuracy. Thorough comparison of the experimental procedures of the works [15] and [16] is necessary to determine the reason of discrepancy in there results. For this reason a brief overview of the experimental procedure executed by Leistikow, Schanz and Berg [16] should be done. In this work the investigations were carried out on the material Zircaloy-4 supplied by Sandvik Universal Tubes as a tube material for pressurized water reactors (outside diameter 1.075 cm, wall thickness 0.0725 cm). The test equipment for investigating the oxidation in flowing steam consisted primarily of:

- the steam circuit (steam generator, superheater, test run and condenser);

- the heating equipment (tubular furnace or induction coil) to raise the specimen to the desired temperature in the test run;

- the rig for manipulation and positioning of the specimen;

- the inert gas supply for de-aeration of the tube system before the start of the experiment;

- he quenching apparatus for rapid cooling of the specimen at the end of the experiment;

- the measurement and regulation equipment.

The steam circuits and test runs were made of quartz glass. For steam generation the immersion heater principle was used. The steam delivery was suitably adjusted; in the test run it meant a steam velocity of about 1 m/sec. Steam was overheated in the input system by means of electrically heated asbestos strips. Before the start of the experiment the circuits were de-aerated by careful scavenging with highest purity argon. The majority of the experiment was carried out by the method of resistance heating in the thermostatically controlled tubular furnace. The tube specimen then lay in the test run free on a quartz slide with four points of support. The specimen could be edged forward into the hot zone of the furnace by means of hermetically designed quartz rod connected to the slide. At the end of the experiment the specimen was taken out and then dropped into a water-filled receiver. Further experiments were carried out using the induction heating. In this case a high frequency generator was used to which a water-cooled induction coil with several windings was connected. The coil tightly embraced the steam supply tube (3 cm dia.) in the center of which the specimen was carefully located. The centering required for reasons of temperature constancy prevented movement of the specimen during the experiment, and hence it cooling. The specimen temperature was electronically controlled. After switching off the generator the specimen cooled down rapidly in the steam flow.

In the experiments with tubular furnace heating the Pt-Pt10%Rh thermocouple measurement points were placed in touching contact with the tube specimen. Comparison tests with a welded-on thermocouple showed that the touching thermocouple gave a correct indication in the constant-temperature furnace environment; only for the short-time heating up phase of the specimen at the start of the experiment was an indication lag observed. This was taken into account in evaluation of the experiment. The temperature distribution on the specimen lengthwise and peripherally proved practically constant. In the tests with induction heating, because of the cool surroundings, thermocouple contact point was therefore welded to the specimen. A little piece of iridium foil ($2\times2\times0.1$mm) was welded between the specimen and thermocouple measurement bead. The thermocouple did not couple with the high-frequency field. So one may expect a reading error due to heat loss by radiation as well as by conduction through the thermocouple wires and the steam. For this reason in order to fasten the thermocouple a chamfer was milled into the wall of the specimen tube so that the welded-on thermocouple was less exposed to the cooling by steam. This made thermal contact between the thermocouple and the specimen better. In such a way a reliable temperature measurement was achieved. The temperature distribution of the tube specimens in the axial and tangential directions, however, was not entirely satisfactory.

The kinetic assessment of almost isothermal oxidation experiments requires careful study of the heating-up phase during which the reaction gradually starts. For the experiments performed in the tubular furnace the beginning of the reaction period was defined as the moment when 90% of final temperature (90% of temperature range is to be covered) was reached. Because of the indication lag of the laid-on thermocouple the real specimen temperature at this moment was already 95% of the final temperature instead of 90%. In the experiments with induction heating the attainment - measured with welded-on thermocouple - 95% of the final temperature was defined as the start of the reaction. The isothermally performed experiments below 1000°C had no time correction. This time correction is sufficiently accurate and for longer experiment times is small. For current series of experiments the reaction time was 2, 5 and 15 minutes.

Though experimental procedures of the works [15] and [16] were executed with great care, there are some differences in these procedures. It will be shown in sec.5, that these differenciescan explain the discrepancies in the obtained results.

With the escalation of temperature the oxidation rate of Zircaloy by steam increases rapidly, so that standard experimental apparatures used in [15] and [16] becomes unacceptable. For this reason in [17] for the investigation of oxidation kinetics with the temperature up to 2400^0C the system was devised that employed laser energy to heat the sample. Oxidation kinetics was measured by exposing the samples to the flowing steam during various periods of time at the same nominal temperature and then by metallographically examining of each sample to determine the growth behavior of the oxide layers. Experiments were performed on disk specimens (3.8 mm diameter $\times$0.9 mm thick) that had been machined from reactor-grade Zircaloy-4 bar stock obtained from Teledyne Wah Chang. The nominal alloy composition was 1.5 wt.% Sn, 0.20 wt.% Fe, 0.11 wt.% Cr, 0.125 wt.% O, 0.016 wt.% C, 0.004 wt.% N and 0.001 wt.% H. A defocused CO_2 laser beam (λ = 10.6 μm) with a maximum power output of 400 W was used to heat the samples from one side. The surface temperature of the sample was measured with the help of a two-color pyrometer (λ = 0.95 and 1.06 μm) calibrated regularly against an internal radiation source and initially standardized to the melting point of alumina. The temperature measurement was done with the accuracy of $\pm$15°C. The pyrometer was placed to view either the heated or non-heated side of the sample. A computer was coupled to both the pyrometer output and the power control circuit of the CO_2 laser, permitting rapid and reproducible temperature control to a preprogrammed time sequence. Real-time temperature profiles were also recorded.

The critical analysis of the results of oxidation kinetics of Zry-4 by steam will be held in sections 5 and 6 on the basis of the given description of the experimental procedures of [15], [16] and [17].

4. Determination of Oxygen Diffusion coefficients.

4.1 Temperature range $1000^0C \leq T \leq 1500^0C$.

At the temperatures above the α-β phase transition (T_b=960° C), the Zircaloy oxidation is accomplished by the formation of layers of oxide ZrO_2 and oxygen stabilized α-phase, α-Zr(O) . The structure of the layers in case of semi-infinite Zircaloy specimen oxidation is shown in the diagram.

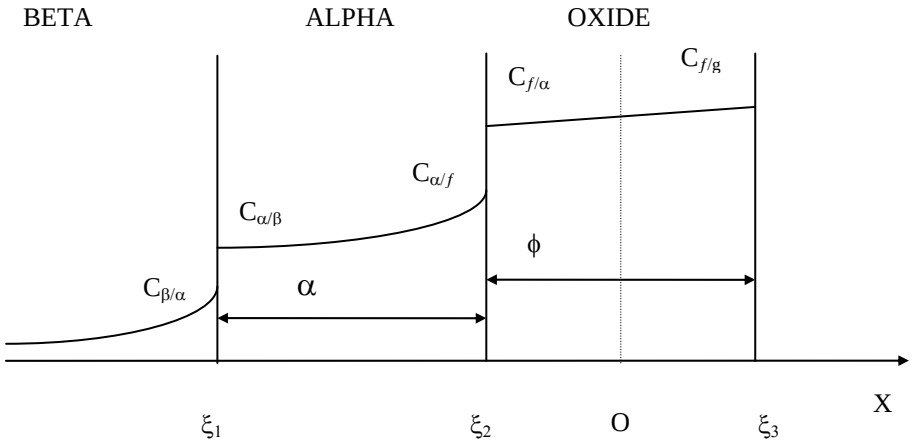

The oxygen concentrations in the phases with various interfaces are assumed to be maintained at the equilibrium values. In each phase the diffusion coefficient is taken independent on oxygen concentration, which is confirmed by the direct experimental measurements for beta and alpha phases[18] and is justified by the small equilibrium oxygen concentration difference $(C_{f/S}-C_{f/\alpha})/C_{f/\alpha}<<1$ for oxide. In such assumptions, the oxidation problem has well known analytical solution (see ref. in [19]). Namely, oxygen concentration distribution in each phase has the form:

$$C = A + B\,erf\,(x / 2\sqrt{Dt}\,), \qquad (1)$$

where constants A and B are defined by the corresponding boundary conditions :

$$\begin{aligned} C(x = x_1, t) &= C_1 \\ C(x = x_2, t) &= C_2 \end{aligned} \qquad (2)$$

As one can see, the solution Eq. (1) determines such a concentration distribution, that the position of the layer with some fixed concentration obeys parabolic time law $\sim\sqrt{t}$, therefore, $x_i = \delta_i\sqrt{t}$ in accordance with Eq. (2). The interface velocity should be obtained from the material balance conditions.

Thus, for each layer of this multiphase system the oxygen concentration distribution is described by the Eq. (1) with constants obtained from corresponding boundary conditions:

$$C_\beta = \frac{C_{\beta/\alpha}(1 + erf\,(x / 2\sqrt{D_\beta t}\,))}{1 + erf\,(\xi_1 / 2\sqrt{D_\beta t}\,)} \qquad (3)$$

$$C_\alpha = C_{\alpha/\beta} + (C_{\alpha/f} - C_{\alpha/\beta})\frac{(erf(\xi_1 / 2\sqrt{D_\alpha t}) - erf(x / 2\sqrt{D_\alpha t}))}{erf(\xi_1 / 2\sqrt{D_\alpha t}) - erf(\xi_2 / 2\sqrt{D_\alpha t})}, \qquad (4)$$

$$C_f = C_{f/\alpha} + (C_{f/g} - C_{f/\alpha})\frac{(erf(\xi_2 / 2\sqrt{D_f t}) - erf(x / 2\sqrt{D_f t}))}{erf(\xi_2 / 2\sqrt{D_f t}) - erf(\xi_3 / 2\sqrt{D_f t})}, \qquad (5)$$

where D_α , D_β and D_f are oxygen diffusion coefficients in α, β phases and in oxide, respectively; $C_{\alpha/\beta}$, $C_{\beta/\alpha}$ are equilibrium oxygen concentrations in the α and β phases at the α/β interface; $C_{\alpha/f}$, $C_{f/\alpha}$ are equilibrium oxygen concentrations in the α phase and oxide at the α/f interface; ξ_1 , ξ_2 and ξ_3 define the α/β , α/f interface positions and specimen surface with respect to the original specimen surface at x=0.

The oxygen flux matches at the α-β and α-f interfaces yields:

$$\frac{d\xi_1}{dt}(C_{\alpha/\beta} - C_{\beta/\alpha}) = D_\beta \left.\frac{\partial C_\beta}{\partial x}\right|_{x=\xi_1} - D_\alpha \left.\frac{\partial C_\alpha}{\partial x}\right|_{x=\xi_1}, \qquad (6)$$

$$\frac{d\xi_2}{dt}(C_{f/\alpha}B - C_{\alpha/f}) = D_\alpha \left.\frac{\partial C_\alpha}{\partial x}\right|_{x=\xi_2} - D_f \left.\frac{\partial C_f}{\partial x}\right|_{x=\xi_2}, \qquad (7)$$

where B≈1.5 is Pilling- Bedworth ratio.

The Zirconium mass balance at the α-f interface and at the specimen surface leads to the relation:

$$\frac{d\xi_3}{dt} = (1 - B)\frac{d\xi_2}{dt}. \qquad (8)$$

The thickness of the individual layer can be easily expressed in terms of the interface positions $\alpha=\xi_2 - \xi_1$, $\phi=\xi_3 - \xi_2$. According to the parabolic time law, $\alpha = \delta\alpha\sqrt{t}$, $\phi = \delta\phi\sqrt{t}$, hence

$$\begin{aligned} \xi_1 &= -(\delta\alpha + \delta\phi / B)\sqrt{t}; \\ \xi_2 &= -(\delta\phi / B)\sqrt{t}; \\ \xi_3 &= (1 - 1/B)\delta\phi\sqrt{t}. \end{aligned} \qquad (9)$$

Thus, equations (3-9) form complete system of equations for determination of oxygen diffusion coefficients.

Equation for diffusion coefficient of oxygen in the α-phase is obtained by substituting of Eqs. (3, 4, 9) into Eq. (6):

$$D_\alpha = \frac{\frac{1}{2}(\delta\alpha + \frac{\delta\phi}{B})\frac{(C_{\alpha/\beta} - C_{\beta/\alpha})}{(C_{\alpha/f} - C_{\alpha/\beta})} + \sqrt{\frac{D_\beta}{\pi}}\frac{C_{\beta/\alpha}}{(C_{\alpha/f} - C_{\alpha/\beta})}\frac{exp(-(\frac{\delta\alpha + \frac{\delta\phi}{B}}{2\sqrt{D_\beta}})^2)}{1 - erf(\frac{\delta\alpha + \frac{\delta\phi}{B}}{2\sqrt{D_\beta}})}}{\frac{1}{\sqrt{\pi D_\alpha}}\frac{exp(-(\frac{\delta\alpha + \delta\phi/B}{2\sqrt{D_\alpha}})^2)}{erf(\frac{\delta\alpha + \delta\phi/B}{2\sqrt{D_\alpha}}) - erf(\frac{\delta\phi/B}{2\sqrt{D_\alpha}})}}. \quad (10)$$

So, the solution of equation (10) gives Dα , assuming knowledge of D_β , appropriate equilibrium oxygen concentrations and the layer growth kinetics.

In analogous way, substitution of Eqs. (4, 5, 9) into Eq. (9) leads to the equation for diffusion coefficient of oxygen in the oxide. However, as shown in [24], concentration profile in the oxide is close to the linear one, which follows from the condition $C_{f/\alpha}$- $C_{\alpha/f}$ >>$C_{f/g}$-$C_{f/\alpha}$. This condition results in a slow movement of the reaction front in compare with a characteristic rate of diffusion process within the layer and, thus, permits a quasistationary approximation for the diffusion problem.

Indeed, the following estimation can be derived from the interface flux matches:

$$V(C_{f/\alpha} - C_{\alpha/f}) \sim D_f (C_{f/g} - C_{f/\alpha})/L,$$

where V is front velocity and $L=\xi_3-\xi_2$ is a reaction layer thickness. The characteristic time for the boundary displacement at the distance L is estimated by: $\tau_b \sim L/V$. A characteristic time for diffusion process in the layer of the L thickness is $\tau_d \sim L^2/D_f$.. Hence, the following relation takes place: $\tau_d/\tau_b \sim VL/D_f \sim (C_{f/g}-C_{f/\alpha})/(C_{f/\alpha}-C_{\alpha/f}) << 1$, which justifies the validity of quasistationary approximation.

In this approximation the solution of one dimensional diffusion problem is represented by a linear function instead of Eq. (1). Such simplification yields an explicit formula for D_f :

$$D_f = \frac{1}{2}\frac{(\delta\phi)^2}{B}\frac{(BC_{f/a} - C_{\alpha/f})}{(C_{f/g} - C_{f/\alpha})} + \delta\phi\sqrt{\frac{D_\alpha}{\pi}}\frac{(C_{\alpha/f} - C_{\alpha/\beta})}{(C_{f/g} - C_{f/\alpha})}\frac{exp(-(\frac{\delta\phi/B}{2\sqrt{D_\alpha}})^2)}{erf(\frac{\delta\alpha + \delta\phi/B}{2\sqrt{D_\alpha}}) - erf(\frac{\delta\phi/B}{2\sqrt{D_\alpha}})} \quad (11)$$

Compare with [19] calculations of D_α and D_f were performed from parabolic rate constants obtained in two independent sets of experiments [15] and [16]. The other necessary data over the temperature range 1273-1773 K where selected in the form:

$$D_\beta = 0.0263 exp(-28200/RT) \text{ cm}^2/\text{sec [18] ;}$$

$$C_{f/g} = 1.511 \text{ g/cm}^3 \text{ [19];}$$

$$C_{f/\alpha} = 1.511(2-x)/2 \text{ g/cm}^3 \text{ ; } x = 0.015 \text{ [21];}$$

$$C_{\alpha/f} = \begin{cases} \dfrac{112}{100-(28.6+exp(-6748/T+4.748)} - 1.12, T < 1487K \\ \dfrac{112}{100-(28.6+exp(-6301/T+4.46)} - 1.12, T > 1487K \end{cases} \text{ g/cm}^3 \text{ [21]}$$

$$C_{\alpha/\beta} = 0.0649(-0.2263 + \sqrt{\frac{T}{63.385} - 16.877}) \text{ g/cm}^3 \text{ [19]}$$

$$C_{\beta/\alpha} = \begin{cases} 0.0649\left(-0.00428 + \sqrt{\dfrac{T}{392.46} - 3.14}\right), T < 1373K \\ 0.0649\dfrac{T-1081.7}{491.159}, T > 1373K \end{cases} \text{ g/cm}^3 \text{ [19]}$$

here [T]= K, R=1.987 cal/mole.

These calculations are similar to [19] which were performed on the basis of kinetic correlations measured in [15] and equilibrium phase diagram [25-29]. Since, the work [19] was published; more accurate data on Zr-O phase diagram become available [21]. The main changes concern the $C_{\alpha/f}$ and $C_{f/\alpha}$ equilibrium lines. The changes in the position of $C_{\alpha/f}$ equilibrium line may be ascribed to the fact that previous experimental results were based on examination quenched samples; thus the equilibrated samples may have been altered by ZrO_{2-x} precipitation. So this boundary should be investigated at equilibrium temperature [21].

The above described approach to determination of the oxygen diffusion coefficients in the alpha Zr and in oxide is based on the knowledge of oxygen diffusion coefficients in the beta Zirconium. Measurements of weight gain of Zirconium samples also were carried out in [16] along with metallographic investigations. This admitted an alternative opportunity of oxygen diffusion coefficient determination. If weight gain $\tau = \delta\tau\sqrt{t}$ is known, one can easily obtain the oxygen diffusion coefficient in oxide:

$$D_f = \frac{\delta\phi\delta\tau}{2(C_{f/g} - C_{f/\alpha})} \text{ .} \qquad (12)$$

The relation (12) is obtained from the oxygen flux matches on the specimen boundary:

$$\frac{d\tau}{dt} = D_f \frac{\partial C_f}{\partial x}\bigg|_{x=\xi_3} = D_f \frac{(C_{f/g} - C_{f/\alpha})}{\delta\phi\sqrt{t}} = \frac{\delta\tau}{2\sqrt{t}} \text{ .}$$

On this basis, the diffusion coefficient D_α can be determined from the equation (11):

$$D_\alpha = \left(\frac{D_f}{\delta\phi} \frac{(C_{f/g} - C_{f/\alpha})}{(C_{\alpha/f} - C_{\alpha/\beta})} - \frac{1}{2} \frac{(\delta\phi)}{B} \frac{(BC_{f/a} - C_{\alpha/f})}{(C_{\alpha/f} - C_{\alpha/\beta})} \right) \Bigg/ \left(\frac{1}{\sqrt{\pi D_\alpha}} \frac{exp(-(\frac{\delta\phi/B}{2\sqrt{D_\alpha}})^2)}{erf(\frac{\delta\alpha + \delta\phi/B}{2\sqrt{D_\alpha}}) - erf(\frac{\delta\phi/B}{2\sqrt{D_\alpha}})} \right)$$

The oxygen diffusion coefficient in beta phase could be determined from equation (10). However, it is straightforward to see that, D_β determined in such a way is a steep function of D_α , so that a small variation in D_α results in large variations in D_β, which make such approach rather inaccurate for D_β determination.

4.2 Temperature range $1525^0C \le T \le 1825^0C$.

The above presented calculations of the three layer oxidation kinetics are valid at temperatures up to the temperature of the phase transformation of the ZrO_2 layer $T^* \approx$ 1525°C. At this temperature formation of an oxide sublayer of cubic structure γ- ZrO_{2-x} takes place. So, the following four layer structure emerges: β-Zr matrix, oxygen stabilized α-Zr(O) layer, cubic structure γ- ZrO_{2-x} scale and tetragonal structure β- ZrO_{2-x} scale. Previously introduced notations of the diffusion coefficient D_f and equilibrium concentrations $C_{f/a}$, $C_{f/g}$ referred to the tetragonal β- ZrO_{2-x} oxide. Since the two oxide phases appear at temperatures above T*, these notations must be specified: $D_f, C_{f/\alpha}, C_{f/g} \rightarrow D_f^\beta, C_l^\beta, C_u^\beta; D_f^\gamma, C_l^\gamma, C_u^\gamma$, where superscripts β and γ designate the β- and γ- ZrO_{2-x} oxides; subscripts *l* and *u* refer to the lower and upper equilibrium oxygen concentrations in each oxide phase.

After introduction of the additional γ- ZrO_{2-x} layer, the flux matching equations (6-8) for oxygen and zirconium have the form form:

$$\frac{d\xi_1}{dt}(C_{\alpha/\beta} - C_{\beta/\alpha}) = D_\beta \left.\frac{\partial C_\beta}{\partial x}\right|_{x=\xi_1} - D_\alpha \left.\frac{\partial C_\alpha}{\partial x}\right|_{x=\xi_1}, \qquad (13)$$

$$\frac{d\xi_2}{dt}(C_l^\gamma B - C_{\alpha/f}) = D_\alpha \left.\frac{\partial C_\alpha}{\partial x}\right|_{x=\xi_2} - D_f^\gamma \left.\frac{\partial C_f^\gamma}{\partial x}\right|_{x=\xi_2}, \qquad (14)$$

$$(\frac{d\xi_4}{dt} - \frac{d\xi_3}{dt})(C_l^\beta - C_u^\gamma) = D_f^\beta \left.\frac{\partial C_f^\beta}{\partial x}\right|_{x=\xi_3} - D_f^\gamma \left.\frac{\partial C_f^\gamma}{\partial x}\right|_{x=\xi_3}, \qquad (15)$$

where ξ_4 is the position of a specimen surface, ξ_3 is γ/β- ZrO_{2-x} interface position. Interface positions ξ_i are connected with layer thicknesses:

$$\xi_1 = -(\alpha + \phi_t / B),$$
$$\xi_2 = -(\phi_t / B), \qquad (16)$$

$$\xi_3 = (1-1/B)\phi_t - \phi_\beta \quad ,$$

$$\xi_4 = (1-1/B)\phi_t \ ,$$

where $\alpha = \delta\alpha\sqrt{t}$, $\phi_\beta = \delta\phi_\beta\sqrt{t}$ and $\phi_t = \delta\phi_t\sqrt{t}$ are thicknesses of α-Zr(O), β- ZrO_{2-x} and total thickness of oxide scale. Substitution of (16) and linear oxygen profiles in oxides into equations (17-19) gives:

$$-\frac{\delta\phi_t}{2B}(C_l^\gamma B - C_{\alpha/f}) = D_\alpha \left.\frac{\partial C_\alpha}{\partial x}\right|_{x=\xi_2} \sqrt{t} - D_f^\gamma \frac{C_u^\gamma - C_l^\gamma}{\delta\phi_t - \delta\phi_\beta}, \qquad (17)$$

$$\frac{\delta\phi_\beta}{2}(C_l^\beta - C_u^\gamma) = D_f^\beta \frac{C_u^\beta - C_l^\beta}{\delta\phi_\beta} - D_f^\gamma \frac{C_u^\gamma - C_l^\gamma}{\delta\phi_t - \delta\phi_\beta}. \qquad (18)$$

These equations could be explicitly solved to determine two unknown values: D_f^γ and $\delta\phi_\beta$. The other values in the equations are known from experiments [17]: $\delta\phi_t$ or obtained by extrapolating of the data derived at relatively low temperatures T<T* to high temperature T>T* region: D^β_f, D_α ,D_β .

The theoretical model used in this section for calculation of diffusion coefficients has three main assumptions that can lead to possible errors and must be discussed:

a). In this model the semi-infinity spatial interval was used when profile of oxygen concentration was calculated. This assumption is valid for the cases when the oxidation front in β-phase does not reach the back side of the sample (the side opposite to one from which oxidation process occurs). This is true for experimental data under consideration, but in the more common case the effect of finite geometry must be taken into account.

b). In our model we suppose that oxygen diffusion coefficients were independent on oxygen concentration. The validity of this was checked by different authors (see ref. [15], [18]).

c). Boundary concentrations used in our model were taken from the equilibrium phase diagram ([21] from our report). This means that boundary kinetics was neglected. The validity of this was checked in the work [30], where it was shown to be true if oxidation time is greater than 5-7 sec for testing temperatures.

5. Analysis of experimental data for $1000^0C \le T \le 1500^0C$.

As it was mentioned above, two uniform product layers (the outermost oxide phase and intermediate oxygen-stabilized alpha phase) were easily recognized by conventional metallographic procedure. Measurements of these layer thicknesses were performed in [15]. In [16] layer thicknesses and oxygen uptake as a function of reaction time for each temperature were investigated. In [15] ten measurements with different time intervals were performed for each temperature (for example, for T = 1250°C measurement duration was in the interval from 50 to 250 seconds, and for T =1500°C - from 10 to 60 sec). For T≥1000°C the growth rates of oxide and α-phase were well

described by parabolic rate law, so that for thicknesses of the layers *L* the following equations were obtained:

$$L^2_{ZrO2} = \delta_\phi{}^2 t$$
$$L^2_{\alpha Zr} = \delta_\alpha^2 t$$

where δ_ϕ and δ_α denote, correspondingly, the growth rates of oxide and α-phase. In the Table IV the mean values of this constants $\delta^2 = \frac{1}{10}\sum_{i=1}^{10}\delta_i^2$ for some temperature are given, which were obtained on the basis of the results [15]. In Ref. [16] layer thickness measurements were made for the reaction time of 2, 5 and 15 minutes. 3-5 measurements were performed for each time-temperature pair, and averaged values of these measurements are also listed in Table IV.

From the comparison of the values listed in Table IV it is easy to conclude (what will be further strictly confirmed by statistical treatment) that there is some systematic discrepancy in the measurements of the layer thicknesses growth rates, especially at low temperatures. These discrepancies cannot be explained by rather small errors of the measurements, which were indicated by the authors of [15], [16]. The growth rate of oxide in [15] is higher than that in [16], and the growth rate of α-phase is higher in [16]. The difference is particularly large at T=1000°C:

$$\delta_{\alpha[1]} \Big/ \delta_{\alpha[2]} \approx 1{,}5$$

For the long-time heating ($t \geq 25$ min at T=1000°C so-called “breakaway”-effect was observed, that led to the great acceleration of the oxidation process, so it should be bear in mind, that the obtained results are applicable only for relatively short times $t < t_{crit}(T)$. For higher temperatures this effect was not observed.

In order to construct the correlation dependencies of oxygen diffusion coefficients in oxide and α-phase it is necessary to perform statistical treatment of the results, obtained in [15] and [16] in the following way. On the bases of values of δ, oxygen diffusion coefficients of D_{ZrO2} and $D_{\alpha Zr}$ were calculated for each temperature-time pair by the model described in sec.3. In Figs.1-2 the set of averaging diffusion coefficient as a function of temperature is represented. For each set of D_{ZrO2} and $D_{\alpha Zr}$ coefficients of linear regression $\ln D = A - BX$ were calculated, where *A* corresponded to $\ln D_0$ and *B* - to the *Q/R* and *X* - to the *1/T* in the linear diffusion model, and the variances of the regressions were determined.

It is necessary to check if one can combine data sets of diffusion coefficients obtained from the two experiments [15] and [16]. For this purpose the statistical comparison of regression dependencies ln*D*(1/T) for these data sets, was performed by F-statistic method, which has the form [18] :

$$F = \frac{\dfrac{SS_C - SS_1 - SS_2}{\nu}}{\dfrac{SS_C}{\nu_C}}$$

where $SS_\alpha = \sum_{i=1}^{N}(observed - predicted)^2$ is the sum of squares of errors of measured values of ln*D* from there regression estimation, SS_1, SS_2 and SS_C correspond to the [15], [16] and combined data set respectively, ν=2 and ν_C=142 are degrees of freedom. The obtained value F=24 appeared to be significantly greater than the critical value for that case: F(2,142)=3 with 2 and 142 degrees of freedom at 10% significant level. This indicates, that the assumption of the absence of systematic errors between two data sets is not valid. This means that systematic errors may exist in the measurements of the two experimental groups, which cannot be determined directly from the data presented in [15] and [16]. But these errors themselves may explain the observed discrepancies between these data. Different averaged values of investigated parameters (i.e. different mathematical expectations) were obtained in [15] and [16] as a result of these errors.

The difference between these two data sets and that sets of data obtained by Urbanic and Heidrick [14] is even more considerable. For this reason let us start the discussion of possible systematic errors in the test [14].

Accuracy of temperature measurements were estimated in [14] as ±25 K. This value for the temperature interval 1000-1500°C is too large in comparison with accuracy of measurements [15], [16] (for example, ±2K for 1000°C in [15]) and may lead to rather large errors (as it will be shown further). In the case when oxidation kinetics was measured by hydrogen evolution method systematic deviation from parabolic law was observed at the initial time intervals (t ≤ 30-40 sec). Systematic error is possible, for example, in the determination of the annealing duration. Besides, the method of hydrogen evolution is rather rough; moreover, as it follows from the comparison of oxidation rate by hydrogen evolution method and weight gain method, the former gives some higher rate of oxidation. This also confirms the inconsistency of methods used in [14]. Another questions, connected with uncertainties in sample composition and vagueness in the layers thicknesses determination procedure were pointed out in sec.2. From all these remarks it can be generally concluded that determination of diffusion coefficients from [14] will contain too large error and so the data set obtained in [14] cannot be included in the combined data set for calculation of the ultimate correlation dependencies.

Let us consider possible sources of systematic errors for experimental procedures used in [15], [16]. As it was pointed out above, using the data from the Table IV for the measured growth rates of oxide and α-phase the following equations can be derived: $\delta_{\phi[1]} > \delta_{\phi[2]}$, $\delta_{\alpha[1]} < \delta_{\alpha[2]}$. The possible reason for these discrepancies could be significant radial temperature gradient detected either in [15], or in [16]. In this connection it should be noted that in [15] tangential temperature gradient exists as a result of heterogeneity of specimen heating. As it is well known from the solution of stationary heat problem, nonuniformity of temperature in one direction (for example, $\propto \sin(qx)$) provokes nonuniformity either in the other direction (with the same wave number $\propto \exp(\pm qy)$. Temperature deviation $\delta T \approx 20$K will disturb the exponential factor for growth rate δ proportionally to

$$\exp\left(\frac{\varepsilon_{act}\delta T}{T^2}\right),$$

thus, at T=1000°C such a disturbance attains approximately 20% for ZrO_2 and ≈30% for α-Zr; at T=1300°C - ≈10% for ZrO_2 and ≈15% for α-Zr. Here activation energies ε_{act} were taken equal to ≈36 kcal/mole for ZrO_2 and ≈48kcal/mole for α-Zry in accordance with values obtained below.

It should be emphasized that in both the experiments the temperature measurements were carried out only on one surface of the specimen (on the inner surface of the tube in [15], and on the outer surface in [16]), therefore, temperature gradients across the specimen was not controlled in these tests.

The systematic errors may also arise from the time measurements, since in [15] and [16] different methods for time corrections due to the heating stage were used (see above). This error can't be estimated directly, since only limited experimental data was presented in [16].

An additional source of errors may be connected with the determination of layers thicknesses. Results of measurements [20] partially presented in the Table V. The conservation of Zr atoms leads to the conclusion that value

$$L = 2\left(\frac{L_{ZrO2}}{B} + L_{\alpha Zr} + L_{0.5\beta Zr}\right)$$

is to be equal to the initial thickness of the tube wall L_0=0,725 mm, where B≈1,5 is the Pilling-Bedworth ratio. It is easy to show that mean thicknesses L calculated from Table V is lower than L_0 by 10-20%. At higher temperatures this discrepancy becomes smaller. It may be connected, for example, with plastic deformations, which could arise as a result of different atomic densities of metal and oxide phases. One should pay attention, that in [15] the specimen was fixed with quartz tube, that restricted axial plastic deformation, while in [16] the specimen was kept free.

As mentioned above, in experiments [15] an essential tangential temperature gradient during annealing was detected. This in turn leads to some heterogeneity in the layer growth rate in various directions. The values of δ indicated in [15] were obtained by averaging of the layer thickness over some area in the vicinity of the point with maximum temperature. Specific measurements and averaging procedure in [15] was not described, but this procedure can apparently introduce the errors of the same order of magnitude as in [16].

The composition of the investigated materials can also provide some differences in oxidation kinetics. In [15] isothermal annealing of different batches of Zry-4, with various composition 1.6 and 1.3 wt% of Sn was performed. At temperature T=1200°C the difference in growth rates of the oxide layers became 20% higher when the content of tin was diminished from 1.6 to 1.3wt.%. The growth rate of the α-phase remained unchanged. Since both batches represent the same material designated by Zry-4, variations of diffusion coefficients determined by these composition uncertainties is to be included in the resulting dispersion as well.

From the above-presented analysis it is seen that ultimate possible error could reach ≈60% for T=1000^{0}C and ≈25% for T=1500^{0}C and can easily cover the discrepancy of the results obtained in [15] and [16] and overcome the systematic errors between the two data sets revealed by the F-statistic analysis.

In this case for determination of oxidation kinetics parameters it is necessary to use both data sets obtained in [15] and [16] (see for example [18]). The procedure of unification of these data sets is not defined unambiguously. One possible way is to consider three data sets:

1) The first set is diffusion coefficients obtained in the result of the experimental data [15] treatment, by consideration for each temperature point of two averaged values of diffusion coefficient (one for ZrO_2 and one for α-phase).

2) The second is the set of diffusion coefficients obtained from the measurements [16] by the "layer thickness" method (see sec.4), in which averaged values of D_{ZrO2} and $D_{\alpha Zr}$ are taken for each temperature point.

3) The third set will consist of the values obtained from [16] by "weight gain" method (see sec.4).

So we distinguish the values of diffusion coefficients obtained from "layers thicknesses" (or "metallographic") and "weight gain" measurements [16], because these two procedures are independent and can have different systematic errors. To conform this fact one can see systematic offset of $D_i(T_k)$ obtained by different treatment of experimental results shown in Figs. 1,2. After combined data set is formed usual regression analysis is used to obtain ultimate Arrenius dependence of ln$D$ on 1/T. The dependence of ln$D$ on $1/T$ for α-Zry and ZrO_2 with 95% confidence interval is shown on Fig.3,4 . The calculated variance for the combined data set appears to lie in the range of summarized possible error determined earlier on the basis of the analysis of experimental procedure.

The final expressions for oxygen diffusion coefficients in the oxide ZrO_2, oxygen stabilized α-Zr(O) and β-Zr have the form

D_{ZrO2}=8.67 exp(-40495/RT)

$D_{\alpha Zr}$=1.54 exp(-48020/RT)

$D_{\beta Zr}$=0.0263 exp (-28200/RT)

where diffusion coefficients are measured in cm^2/s, R is the gas constant, T is the temperature.

6. Analysis of experimental data for $1525^0C \le T \le 1825^0C$.

Oxidation kinetics of Zry changes abruptly at temperatures $\approx$ 1500 ^{0}C, corresponding to the appearance of new (cubic) oxide phase in the equilibrium binary Zr-O phase diagram [21]. In accordance with this phase diagram in the temperature range of 1525<T<2377 ^{0}Ñ oxide layer consists of two sublayers : outer, which corresponds to the tetragonal phase and inner (located between tetragonal ZrO_2 phase and α-Zry) layer, which corresponds to the cubic phase. At 1825 ^{0}C β-phase melts, and at 2377 ^{0}C oxide layer converts into the cubic phase entirely.

Oxidation kinetics at T>1525^{0}C was studied in two series of experiments [17] and [20]. In [20] Leistikow and Schanz extended their lower temperature measurements up to 1600^{0}C. Prater and Courtright [17] performed their measurements in a wide temperature interval 1300 ^{0}C < T < 2400 ^{0}C, but used another experimental methods with lower accuracy (see sec.3).

In [17] oxide and alpha layer thicknesses were measured in 100 ^{0}C intervals for temperatures between 1300 and 2400 ^{0}C. A good correlation of layer thicknesses measurements with ideal parabolic behavior were obtained. Parabolic growth kinetics is applied over the entire temperature range studied and can be described by usual expression: $L_k^2 = \delta_k^2 t$, where $k=\phi,\alpha$ corresponds to oxide and α-phase respectively. Temperature dependence of the growth constants for the ZrO_2 and the combined layer (ZrO_2 + α-Zr(O)) thicknesses are presented in Fig. 5. This figure is reproduced from [17], so that the data points and fits correspond to the results of this work. As one can see, the data measured on the heated and unheated surfaces produced two distinct curves with approximately the same slope and activation energies. The temperature value of each experimental point shown in Fig.5 corresponds to the temperature on the oxide surfaces (heated or unheated). The two curves are offset along the temperature axis by an amount representing the difference between the actual measured temperature at the oxide surface and the effective temperature that characterizes (averages) the diffusion process across the entire oxide layer.

In the interpretation of the results in [17] it is regarded that temperature monotonically drops from left to right (see Fig.5), since for each 100μm of oxide thickness the decrease of temperature is approximately 50 ^{0}C. From this fact it is deduced that the real rate of layers growth lies on the bisectors of two curves shown in the Fig.5.

In such consideration it is implied that the heat source is situated at the irradiated surface of the sample. However in reality the length of absorption of irradiation of CO_2 laser in ZrO_2 may be rather large, and so heat source will be distributed through the hole thickness of oxide layer. This may lead to the temperature distribution in the sample shown on Fig.6. Exact solution of this task is out of the frame of our report.

In the Table VI the comparison of the results obtained in [17] and [20] are represented. In the columns labeled with [20] rate constants of oxide and double layers growth for different temperatures and annealing times are represented, which were obtained on the base of the averaged data of Table I of the work [20]. In columns labled with [17] analogous data of the work [17] are represented. Here the first values in each sell correspond to the lower curve of Fig5, and the second value - to the upper curve.

From the comparison of these two data sets it is seen, that the results of [20], obtained by more accurate methods at two temperature points 1550 and 1600 ^{0}C correspond to the lower curves of [17] much better. This confirms the above -presented assessment of the temperature profile. Moreover, as it follows from the equilibrium binary Zr-O phase diagram [21], a steep increase in the rate constant of the oxide layer growth is to occur at the temperatures above 1525 ^{0}C, when cubic phase layer appears. From Fig.5 it is seen, that following higher curve one obtains that this increase in the rate constant occurs at temperatures $\approx$ 1500 ^{0}C < 1525 ^{0}C, that is qualitatively incorrect.

The set of values presented by the lower curve [17] and the data of [20] listed in Table 1V correspond with each other. Taking into account the given above arguments, we propose to use these data sets for the description of high temperature oxidation kinetics. The results are represented in Fig. 7.

It should be also noticed that the influence of gas content on oxidation kinetics was additionally investigated in [17]. It was shown that the presence of large amount of hydrogen (up to 90 mol%) mixed with steam did not affect oxidation rates. Diffusion through the oxide layer is the rate-controlling factor.

Statistical treatment of experimental results based on the least squares estimation method and for our case described in Appendix A, leads to the following expression for oxygen diffusion coefficients in cubic phase of oxide in the temperature range $1525^0C \leq T \leq 1825^0C$:

$$D_{cub} = 0.047 \exp(-25803/RT)$$

As it follows from Sec.4, oxygen profile in oxide phase can be regarded as linear. In this case it is not necessary to know diffusion coefficient D and boundary concentration difference ΔC in oxide separately, because all equations contain only their product $D\Delta C$. On Fig.8 temperature dependence of this value with 95% confidence level is also presented.

7. Conclusions.

1). Statistical analysis of available experimental data was carried out. As the result it was shown that in these data sets systematic errors exist, which do not allow one to combine these data sets for united correlation to be obtained.

2). Thorough analysis of experimental procedures allows one to choose the works in which the errors of the measurements and treatment of the experimental data was minimum. These are the works [15] and [16] in the temperature range $1000^0C \leq T \leq 1525^0C$ and the works [17] and [20] for $1525^0C \leq T \leq 1825^0C$.

3). It was shown that estimated from these analysis errors can explain the discrepancy in the experimental data sets of these works.

4). The combination of the data sets of [15] and [16] allows one to obtain final expressions for oxygen diffusion coefficients in the temperature range $1000^0C \leq T \leq 1525^0C$, which have the following form:

$$D_{ZrO2} = 8.67 \exp(-40495/RT)$$

$$D_{\alpha Zr} = 1.54 \exp(-48020/RT)$$

$$D_{\beta Zr} = 0.0263 \exp(-28200/RT)$$

5). For the temperature range $1525^0C \leq T \leq 1825^0C$ it was shown that the heat generation during highly exothermic oxidation reaction may significantly change temperature profile in the oxidized sample and hence the rate of oxidation. On the basis of it only part of experimental results [17] were taken to be used in determining of oxidation parameters in this temperature range.

6). As the result for a combined data set taken from [17] and [20] the following correlation dependence for oxygen diffusion coefficient in cubic phase of ZrO_2 in the temperature range $1525^0C \leq T \leq 1825^0C$ was obtained:

$D_{cub} = 0.047 \exp(-25803/RT)$

presented with corresponding 95% confidence intervals in Fig.7.

Appendix A: Statistical treatment of an experimental data

The main purpose of this statistical analysis is quantitative evaluation of the difference between two sets of experimental data [15,16] based on statistical significance level. The conclusion about the statistical significance of between-group difference was made via the F test:

$$F = \frac{(SS_C - SS_1 - SS_2)/\nu}{SS_C/\nu_c} \le F_c \qquad (1.A)$$

where $SS_\alpha = \sum_{i=1}^{N} (observed_i - predicted_i)_\alpha^2$ the sums of squares of deviations of measured values of ln*D* from the regression line, SS_1, SS_2 and SS_C belong to the [15], [16] and combined data set correspondingly, ν=2 and ν_C=*N*-2 are the degrees of freedom(N- the total number of measurements in the experiments [15,16]).

In the course of this work, the problem, which is assumed to be common in published experimental data processing, emerges. As a rule, all measured experimental points are not cited; the mean values, the variances and the number of measurements are represented. The standard regression analysis demands to define all experimental points. However, as it will be shown, it is possible to rearrange standard formulae, so that only the means, the variances and the number of measurements will be used.

Standard equations for the determination of the regression coefficients in the equation $y=\alpha x+\beta$ have the form:

$$\begin{aligned} \sum_{i=1}^{N} y_i x_i - \alpha \sum_{i=1}^{N} x_i^2 - \beta \sum_{i=1}^{N} x_i = 0 \\ \sum_{i=1}^{N} y_i - \alpha \sum_{i=1}^{N} x_i - \beta N = 0 \end{aligned} \quad , \qquad (2.A)$$

where x_i and y_i are measured values of independent and dependent variables, respectively(in the case under consideration $x_i \equiv 1/T_i$ and $y_i \equiv (lnD)_i$). Assume now, that n_k experiments were performed at some fixed value of the independent variable x_i. Such experiments relate to one group. In this case, the experiments can be numerated, so that one index refers to the different experiments belonging to one group (j= 1, n_k) and another index refers to different groups (k=1,n, where n is the number of different groups). The mean and the variance for each group of experiments can be defined by the formulae:

$$\overline{y_k} = \frac{\sum_{j=1}^{n_k} y_{kj}}{n_k}$$

$$\sigma_k = \frac{\sum_{j=1}^{n_k} (y_{kj} - \overline{y_k})^2}{n_k - 1}$$

Correspondingly, the standard formulae (2.A) can be easily reduced to the form:

$$\sum_{k=1}^{n} n_k \overline{y_k} x_k - \alpha \sum_{k=1}^{n} n_k x_k^2 - \beta \sum_{k=1}^{n} n_k x_k = 0$$

$$\sum_{k=1}^{n} n_k \overline{y_k} - \alpha \sum_{k=1}^{n} n_k x_k - \beta N = 0$$

As one can see, these formulae include only means and the number of experiments.

In the same way, the sums of squares in (1.A) can be transformed as:

$$SS = \sum_{i=1}^{N} (y_i - \alpha x_i - \beta)^2 = \sum_{k=1}^{n} \sum_{j=1}^{n_k} (y_{kj} - \overline{y_k} + \overline{y_k} - \alpha x_{k,j} - \beta)^2 =$$

$$= \sum_{k=1}^{n} [\sum_{j=1}^{n_k} (y_{kj} - \overline{y_k})^2 + 2\sum_{j=1}^{n_k} (y_{kj} - \overline{y_k})(\overline{y_k} - \alpha x_{k,j} - \beta) + \sum_{j=1}^{n_k} (\overline{y_k} - \alpha x_{k,j} - \beta)^2] =$$

$$= \sum_{k=1}^{n} [(n_k - 1)\sigma_k^2 + n_k (\overline{y_k} - \alpha x_k - \beta)^2].$$

Thus, even in case when all experimental points are unavailable, and only the mean values, the variances and the number of measurements are given, the regression parameters and F value can be nevertheless calculated.

References

1.*Rosa,C.J.* Jornal of the Less-Common Metals, 16 (1968), p.173-201.

2. *I.G. Ritchie*, A. Atrens, Journ. Nucl. Mat. 67 (1977), p.254.

3. *Lemmon A.W.* Studies relating to the Reaction Between Zirconium and Water at high Temperatures. BMI-1154 (1957).

4. *Bostrom W.A.* The High Temperature Oxidation of Zircaloy in Water. WAPD-104 (1954).

5. *Baker L, Just L.C.* Studies of Metal-Water Reactions at High Temperatures. 111. Experimental and Theoretical Studies of the Zirconium-Water Reaction. ANL-6548 (1962).

6. *Lustman B.* Zirconium-Water Reactions. WAPD-137 (1962).

7. *Douglass D.L.* Atomic Energy Review. Vol.1, No 4, Vienna: International Atomi-cEnergy Agency (1963).

8. *Domagla R.F., Mc Pherson D.J.* Zirconium-Oxygen System. Transactions of the American Institute for Mining Engeneers, 200 (1954), p.238.

9. *Gebhardt E. et al* Journal of Nuclear Materials, 4 (1961), p.255.

10. *Pemsler J.P.* Electrochemical Technology 4 (1966), p.128.

11. *Klepfer H.H*. in: Junni P.W. Metall-Water-Reactions-Effects on Core Cooling and Containment. APED-5454,March 1968.

12. *Hobson D.O., Rittenhouse P.L.* : Embrittlement of Zircaloy-Clad Fuel Rods by Steam During LOCA Transient. ORNL 4758, Jan 1972.

13. *Mallett M.W., Albrecht W.M., Wilson P.R*. Journal of Elektrochemical Society, 106 (1959), p.181.

14. *Urbanic V.F., Heidrick T.R.* Journal of Nuclear Materials 75 (1978),p.251-261.

15. *R.E. Pawel, J.V.Cathcart, R.A.McKee*, J. Electrochem. Soc., 126 (1979), p.1105.

16. *Leistikow S., Schanz G., H.v.Berg* Kinetics and morfology of isotermal steam oxidation of Zrcaloy-4 at 700-1300°C. KfK 2587, March 1978.

17. *Prater J.T., Courtright E.L*. High-Temperature Oxidation of Zircaloy-4 in Steam and Steam-Highdrogen Environments. NUREG/CR-4476, PNL-5558 (1986).

18. *Perkins R.A.* Zirconium Metal-Water Oxidation Kinetics 11. Oxygen-18 diffusion in β-Zircaloy. ORNL/NUREG/TN-19 (1976).

19. *R.E. Pawel*, J. Electrochem. Soc., 126 (1979), p.1111.

S.Leistikow, A.E.Aly, B. Bennek-Kammerichs, H.v.Berg, D.Jennert, G.Schanz. KfK3350 (1983).

Abriata J.P., Garces J., Versaci R., Bull. Alloy Phase Diagrams, 7 (1986), p.116.

22*. Kee-Nam Choo, Su-Il Pyun, Young-Suk Kim*, Journ. Nucl. Mat. 226 (1995), p.9.

23. *D.R.Olander*, J.Electrochem.Soc. 131 (1984), p.2161.

24. *M.Veshchunov, P.Hofmann*, J.Nuc. Mat., 210,(1994),p.11

25. *R.A. Perkins*, J.Nucl. Mater., 68,148(1977)

26. *R.Ruh, H.J.Garrett*, J.Am.Ceram.Soc.,50,257(1967)

27. *E.Gebhardt, H.D.Seghezzi,W.Durrschnabel*, J.Nuc. Mat., 4,(1961),p.255

28. *R.F.Domagala, D.J.McPherson*,Trams.AIME,200,238(1954)

29. *S.Malang*, ANL-75-58(September 1975)

30. *F.C.Iglesias, D.B.Duncan, S.Sagat, H.E.Sills*, J.Nucl.Mat., 130(1985),p.36.

Nomenclature

D_α is oxygen diffusion coefficients in α-Zr(O);

D_β is oxygen diffusion coefficients in β-Zr;

D_f and D_f^β are oxygen diffusion coefficients in tetragonal β- ZrO_{2-x} oxide at temperatures $1000^0C \le T \le 1500^0C$ and $1525^0C \le T \le 1825^0C$ **,** respectively;

D_f^γ is oxygen diffusion coefficient in cubic γ- ZrO_{2-x} oxide;

$C_{\alpha/\beta}$ and $C_{\beta/\alpha}$ are equilibrium oxygen concentrations in the α and β phases of Zry at the α- Zr(O)/ β-Zr interface;

$C_{\alpha/f}$, $C_{f/\alpha}$ are equilibrium oxygen concentrations in the α phase and tetragonal oxide at the α-Zr(O)/ tetragonal ZrO_{2-x} oxide interface at temperatures $1000^0C \le T \le 1500^0C$;

$C_l^\beta, C_u^\beta; C_l^\gamma, C_u^\gamma$ are equilibrium oxygen concentrations in the tetragonal and cubic oxides at temperatures $1525^0C \le T \le 1825^0C$ (superscripts β and γ designate the β- and γ- ZrO_{2-x} oxides; subscripts *l* and *u* refer to the lower and upper equilibrium oxygen concentrations in each oxide phase);

$\delta\phi$ and $\delta\alpha$ are the growth rates of oxide and α-phase at temperatures $1000^0C \le T \le 1500^0C$, correspondingly;

$\delta\phi_\beta$ and $\delta\phi_t$ are thicknesses of β- ZrO_{2-x} and total thickness of oxide scale at temperatures $1525^0C \le T \le 1825^0C$;

$B \approx 1.5$ is Pilling- Bedworth ratio;

R=1.987 cal/mole is the gas constant.

List of Figures

List of Tables

Table I

T,K	Mean D_a, cm^2/s	Max D_a, cm^2/s	Min D_a, cm^2/s
1273	8.79E-09	9.78E-09	7.91E-09
1293	1.18E-08	1.30E-08	1.07E-08
1313	1.57E-08	1.72E-08	1.43E-08
1333	2.07E-08	2.24E-08	1.90E-08
1353	2.70E-08	2.91E-08	2.50E-08
1373	3.50E-08	3.76E-08	3.27E-08
1393	4.51E-08	4.81E-08	4.23E-08
1413	5.77E-08	6.13E-08	5.43E-08
1433	7.32E-08	7.76E-08	6.92E-08
1453	9.24E-08	9.76E-08	8.74E-08
1473	1.16E-07	1.22E-07	1.10E-07
1493	1.44E-07	1.52E-07	1.37E-07
1513	1.79E-07	1.89E-07	1.69E-07
1533	2.20E-07	2.33E-07	2.08E-07
1553	2.70E-07	2.86E-07	2.54E-07
1573	3.29E-07	3.50E-07	3.08E-07
1593	3.98E-07	4.26E-07	3.73E-07
1613	4.81E-07	5.16E-07	4.48E-07
1633	5.78E-07	6.23E-07	5.36E-07
1653	6.91E-07	7.49E-07	6.38E-07
1673	8.23E-07	8.96E-07	7.56E-07
1693	9.76E-07	1.07E-06	8.93E-07
1713	1.15E-06	1.27E-06	1.05E-06
1733	1.36E-06	1.50E-06	1.23E-06
1753	1.59E-06	1.76E-06	1.44E-06
1773	1.86E-06	2.07E-06	1.67E-06
1793	2.16E-06	2.42E-06	1.93E-06
1813	2.51E-06	2.82E-06	2.23E-06
1833	2.90E-06	3.28E-06	2.57E-06
1853	3.35E-06	3.80E-06	2.95E-06
1873	3.85E-06	4.38E-06	3.38E-06
1893	4.41E-06	5.04E-06	3.86E-06
1913	5.04E-06	5.79E-06	4.39E-06
1933	5.74E-06	6.62E-06	4.98E-06
1953	6.53E-06	7.56E-06	5.64E-06
1973	7.40E-06	8.60E-06	6.37E-06
1993	8.37E-06	9.77E-06	7.17E-06
2013	9.44E-06	1.11E-05	8.06E-06
2033	1.06E-05	1.25E-05	9.03E-06
2053	1.19E-05	1.41E-05	1.01E-05
2073	1.34E-05	1.58E-05	1.13E-05
2093	1.49E-05	1.78E-05	1.26E-05
2113	1.67E-05	1.99E-05	1.40E-05
2133	1.86E-05	2.22E-05	1.55E-05
2153	2.06E-05	2.48E-05	1.72E-05
2173	2.29E-05	2.76E-05	1.90E-05
2193	2.53E-05	3.06E-05	2.09E-05
2213	2.79E-05	3.39E-05	2.30E-05
2233	3.08E-05	3.75E-05	2.53E-05
2253	3.39E-05	4.14E-05	2.78E-05
2273	3.73E-05	4.57E-05	3.04E-05

Table II

T,K	Mean D_f, cm^2/s	Max D_f, cm^2/s	Min D_f, cm^2/s
1273	9.73E-07	1.08E-06	8.76E-07
1293	1.25E-06	1.37E-06	1.13E-06
1313	1.59E-06	1.73E-06	1.45E-06
1333	2.00E-06	2.17E-06	1.84E-06
1353	2.51E-06	2.70E-06	2.33E-06
1373	3.12E-06	3.35E-06	2.91E-06
1393	3.87E-06	4.12E-06	3.63E-06
1413	4.76E-06	5.05E-06	4.48E-06
1433	5.82E-06	6.16E-06	5.49E-06
1453	7.07E-06	7.47E-06	6.69E-06
1473	8.56E-06	9.03E-06	8.11E-06
1493	1.03E-05	1.09E-05	9.76E-06
1513	1.23E-05	1.30E-05	1.17E-05
1533	1.47E-05	1.56E-05	1.39E-05
1553	1.75E-05	1.85E-05	1.64E-05
1573	2.06E-05	2.20E-05	1.94E-05
1593	2.43E-05	2.59E-05	2.27E-05
1613	2.84E-05	3.05E-05	2.65E-05
1633	3.32E-05	3.58E-05	3.08E-05
1653	3.86E-05	4.18E-05	3.57E-05
1673	4.47E-05	4.87E-05	4.11E-05
1693	5.17E-05	5.64E-05	4.73E-05
1713	5.95E-05	6.53E-05	5.42E-05
1733	6.82E-05	7.52E-05	6.19E-05
1753	7.80E-05	8.64E-05	7.04E-05
1773	8.89E-05	9.90E-05	7.99E-05
1793	1.01E-04	1.13E-04	9.04E-05
1813	1.15E-04	1.29E-04	1.02E-04
1833	1.30E-04	1.46E-04	1.15E-04
1853	1.46E-04	1.65E-04	1.29E-04
1873	1.64E-04	1.87E-04	1.44E-04
1893	1.84E-04	2.11E-04	1.61E-04
1913	2.06E-04	2.37E-04	1.80E-04
1933	2.30E-04	2.65E-04	2.00E-04
1953	2.57E-04	2.97E-04	2.22E-04
1973	2.85E-04	3.31E-04	2.46E-04
1993	3.16E-04	3.69E-04	2.71E-04
2013	3.50E-04	4.10E-04	2.99E-04
2033	3.87E-04	4.54E-04	3.29E-04
2053	4.26E-04	5.03E-04	3.62E-04
2073	4.69E-04	5.56E-04	3.97E-04
2093	5.16E-04	6.12E-04	4.34E-04
2113	5.65E-04	6.74E-04	4.74E-04
2133	6.19E-04	7.40E-04	5.17E-04
2153	6.76E-04	8.12E-04	5.63E-04
2173	7.38E-04	8.89E-04	6.13E-04
2193	8.04E-04	9.71E-04	6.65E-04
2213	8.74E-04	1.06E-03	7.21E-04
2233	9.49E-04	1.15E-03	7.80E-04
2253	1.03E-03	1.26E-03	8.44E-04
2273	1.11E-03	1.36E-03	9.11E-04

Table III

T,K	Mean D_f, cm^2/s	Max D_f, cm^2/s	Min D_f, cm^2/s
1773	2.97E-05	4.76E-05	1.85E-05
1793	3.22E-05	4.96E-05	2.09E-05
1813	3.49E-05	5.17E-05	2.36E-05
1833	3.78E-05	5.40E-05	2.64E-05
1853	4.08E-05	5.64E-05	2.94E-05
1873	4.39E-05	5.91E-05	3.26E-05
1893	4.73E-05	6.22E-05	3.59E-05
1913	5.08E-05	6.56E-05	3.93E-05
1933	5.45E-05	6.96E-05	4.26E-05
1953	5.83E-05	7.42E-05	4.59E-05
1973	6.24E-05	7.95E-05	4.90E-05
1993	6.67E-05	8.56E-05	5.19E-05
2013	7.11E-05	9.26E-05	5.47E-05
2033	7.58E-05	1.00E-04	5.72E-05
2053	8.07E-05	1.09E-04	5.96E-05
2073	8.57E-05	1.19E-04	6.19E-05
2093	9.10E-05	1.29E-04	6.42E-05
2113	9.65E-05	1.41E-04	6.63E-05
2133	1.02E-04	1.53E-04	6.84E-05
2153	1.08E-04	1.66E-04	7.04E-05
2173	1.14E-04	1.81E-04	7.24E-05
2193	1.21E-04	1.96E-04	7.44E-05
2213	1.27E-04	2.13E-04	7.63E-05
2233	1.34E-04	2.31E-04	7.82E-05
2253	1.41E-04	2.50E-04	8.01E-05
2273	1.49E-04	2.70E-04	8.20E-05

Table IV

T ^{0}C		δ^2_{ZrO2} cm^2/s 10^8				$\delta^2_{\alpha Zr}$ cm^2/s 10^8		
	[15]	[16]			[15]	[16]		
		2min	5min	15min		2min	5min	15min
1000	1.4	0.8	0.8	1.3	0.6	1.6	1.6	1.8
1100	4.3	3	3.6	3.6	3.9	4.8	4.6	4.7
1200	10.8	8.5	9	8.4	11.8	16	17	15.7
1300	22.8	20	21.3	23.4	31.9	49.4	45	45.3

Table V

T, [°C]	t, [min]	ZrO_2 [μm] min	mean	max	α-Zr(O) [μm] min	mean	max	1/2 β-Zr [μm] min	mean	max
1350	1	57	59	60	81	86	90	198	206	218
	2	66	69	72	96	99	105	189	201	216
1400	5	100	105	110	173	184	193	68	80	90
	10	144	152	162	210	218	246	7	14	20
1450	5	110	117	123	210	232	270	15	29	33
	10	168	178	186	198	215	240	15	16	18

Table VI

T° C	ZrO_2 , $\frac{cm}{\sqrt{s}}10^4$			ZrO_2 + α-Zr(O), $\frac{cm}{\sqrt{s}}10^4$		
	t, min	[20]	[17]	t,min	[20]	[17]
1450	5	6.8	7/9.5	5	20	1.5/1.8
	10	7.2		10	16	
1500	5	8.6	8.3/20	5	21	18/35
	10	9.2		10	17	
1550	2	19.5	19/28	2	34	30/42
	5	17		5	24	
1600	2	24.6	23/35	2	38	33/55
	3	28.5		3	---	

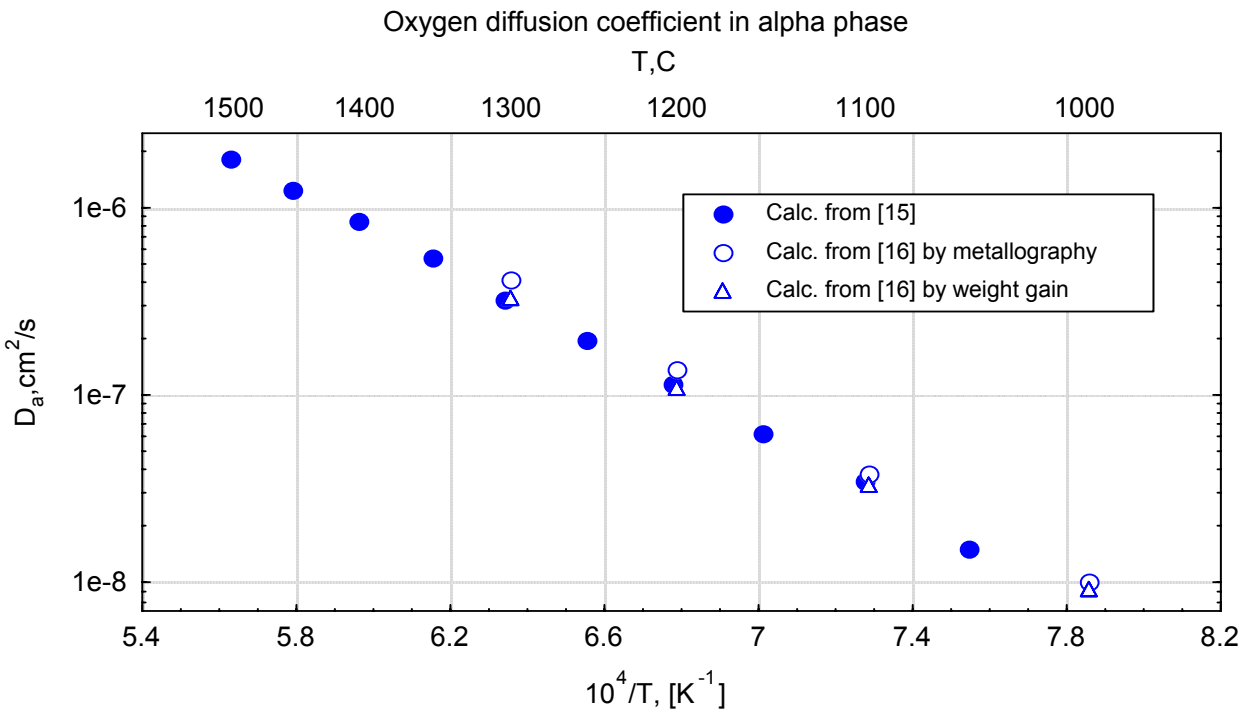
Oxygen diffusion coefficient in alpha phase
T,C
1500
1400
1300
1200
1100
1000
1e-6
1e-7
1e-8
D_a,cm^2/s
Calc. from [15]
Calc. from [16] by metallography
Calc. from [16] by weight gain
5.4
5.8
6.2
6.6
7
7.4
7.8
8.2
10^4/T, [K^{-1}]

Fig.1

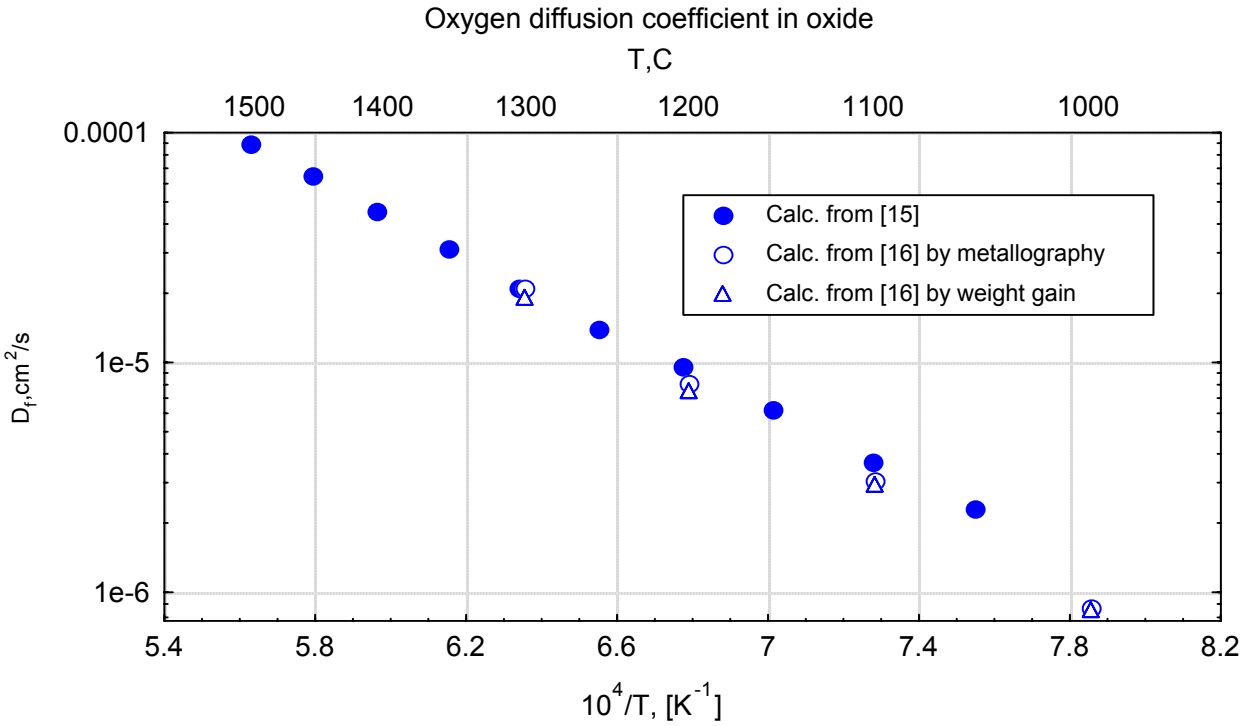
Oxygen diffusion coefficient in oxide
T,C
1500
1400
1300
1200
1100
1000
0.0001
1e-5
1e-6
D_i,cm^2/s
Calc. from [15]
Calc. from [16] by metallography
Calc. from [16] by weight gain
5.4
5.8
6.2
6.6
7
7.4
7.8
8.2
10^4/T, [K^{-1}]

Fig.2

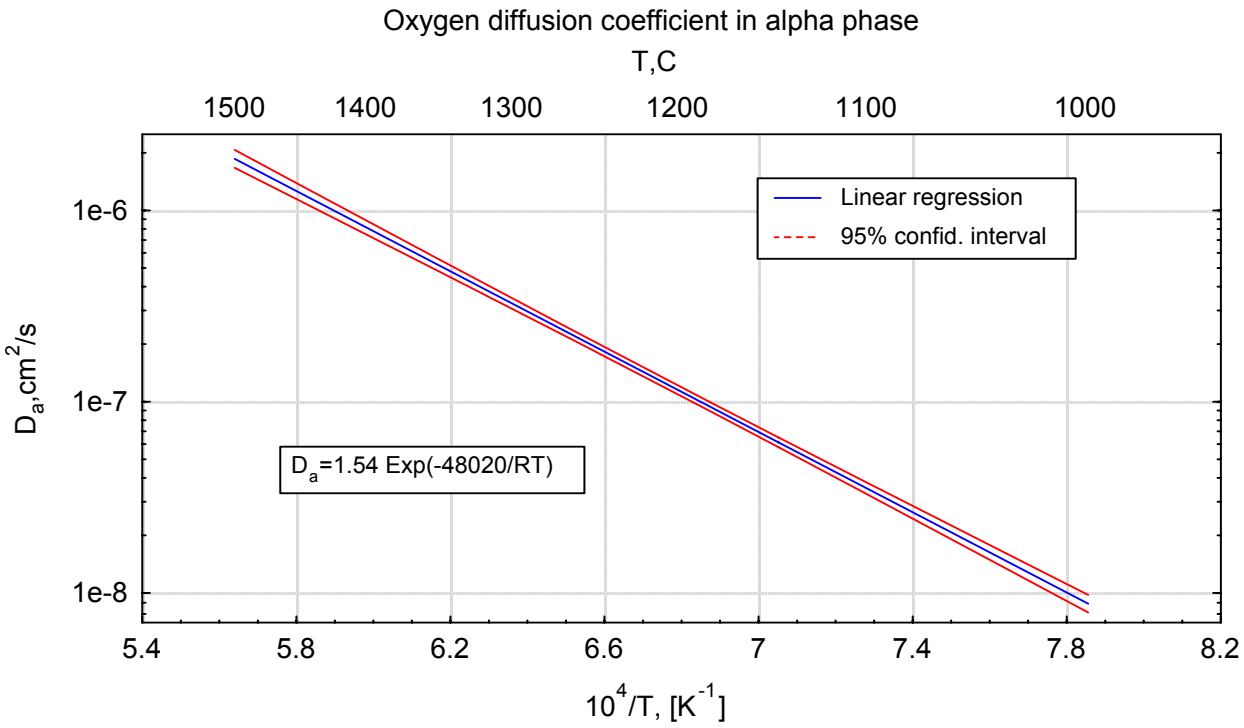
Oxygen diffusion coefficient in alpha phase
T,C
1500
1400
1300
1200
1100
1000
1e-6
1e-7
1e-8
D_a,cm^2/s
Linear regression
95% confid. interval
D_a=1.54 Exp(-48020/RT)
5.4
5.8
6.2
6.6
7
7.4
7.8
8.2
10^4/T, [K^{-1}]

Fig.3

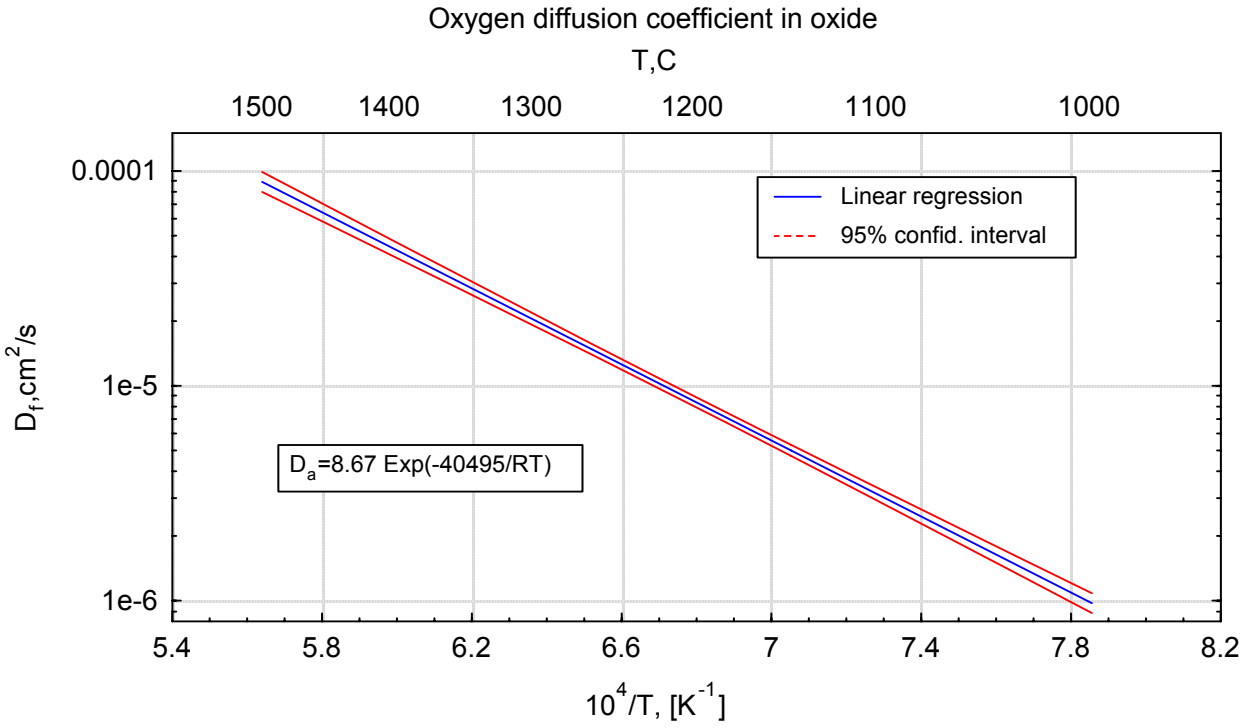
Oxygen diffusion coefficient in oxide
T,C
1500
1400
1300
1200
1100
1000
0.0001
1e-5
1e-6
D_f,cm^2/s
Linear regression
95% confid. interval
D_a=8.67 Exp(-40495/RT)
5.4
5.8
6.2
6.6
7
7.4
7.8
8.2
10^4/T, [K^{-1}]

Fig.4

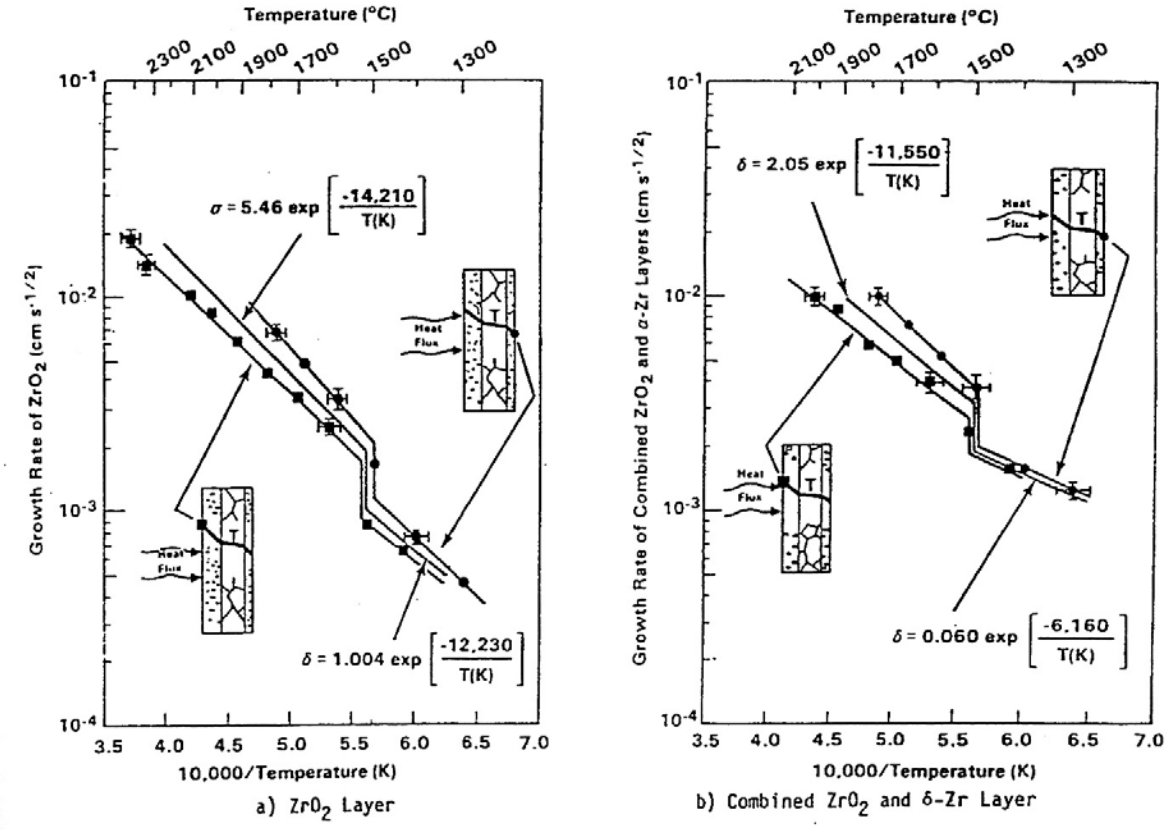
Temperature (°C)
2300
2100
1900
1700
1500
1300
10^{-1}
10^{-2}
10^{-3}
10^{-4}
Growth Rate of ZrO_2 (cm $s^{-1/2}$)
$\sigma = 5.46 \exp\left[\frac{-14,210}{T(K)}\right]$
$\delta = 1.004 \exp\left[\frac{-12,230}{T(K)}\right]$
Heat Flux
T
3.5
4.0
4.5
5.0
5.5
6.0
6.5
7.0
10,000/Temperature (K)
a) ZrO_2 Layer
Temperature (°C)
2100
1900
1700
1500
1300
Growth Rate of Combined ZrO_2 and α-Zr Layers (cm $s^{-1/2}$)
$\delta = 2.05 \exp\left[\frac{-11,550}{T(K)}\right]$
$\delta = 0.060 \exp\left[\frac{-6,160}{T(K)}\right]$
10,000/Temperature (K)
b) Combined ZrO_2 and δ-Zr Layer

Fig. 5

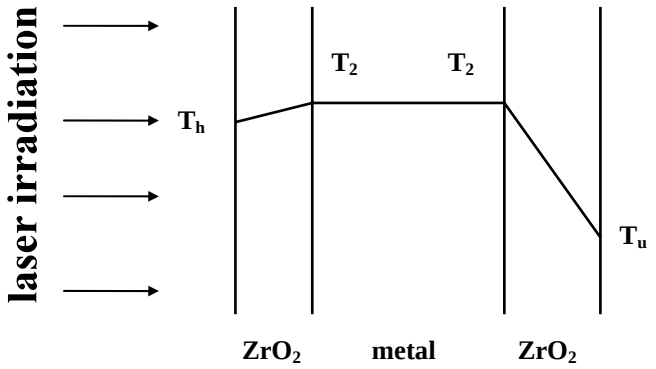
laser irradiation
T_h
T_2
T_2
T_u
ZrO_2
metal
ZrO_2

Fig. 6

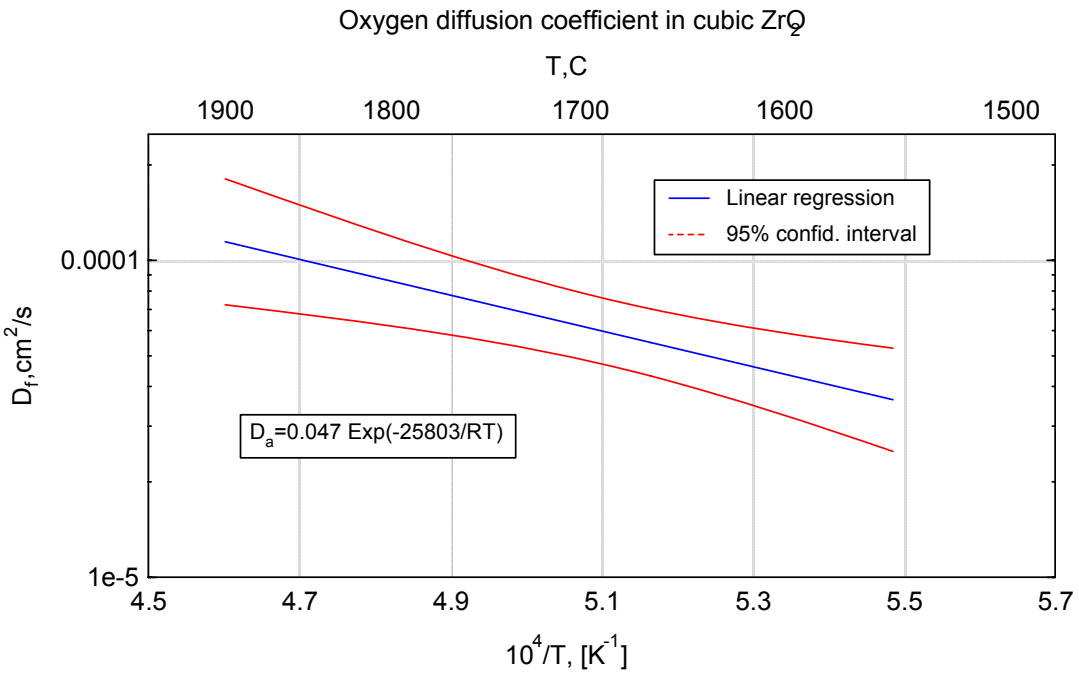
Oxygen diffusion coefficient in cubic ZrO2
T,C
1900
1800
1700
1600
1500
Linear regression
95% confid. interval
0.0001
1e-5
Df,cm2/s
Da=0.047 Exp(-25803/RT)
4.5
4.7
4.9
5.1
5.3
5.5
5.7
10^4/T, [K^-1]

Fig.7

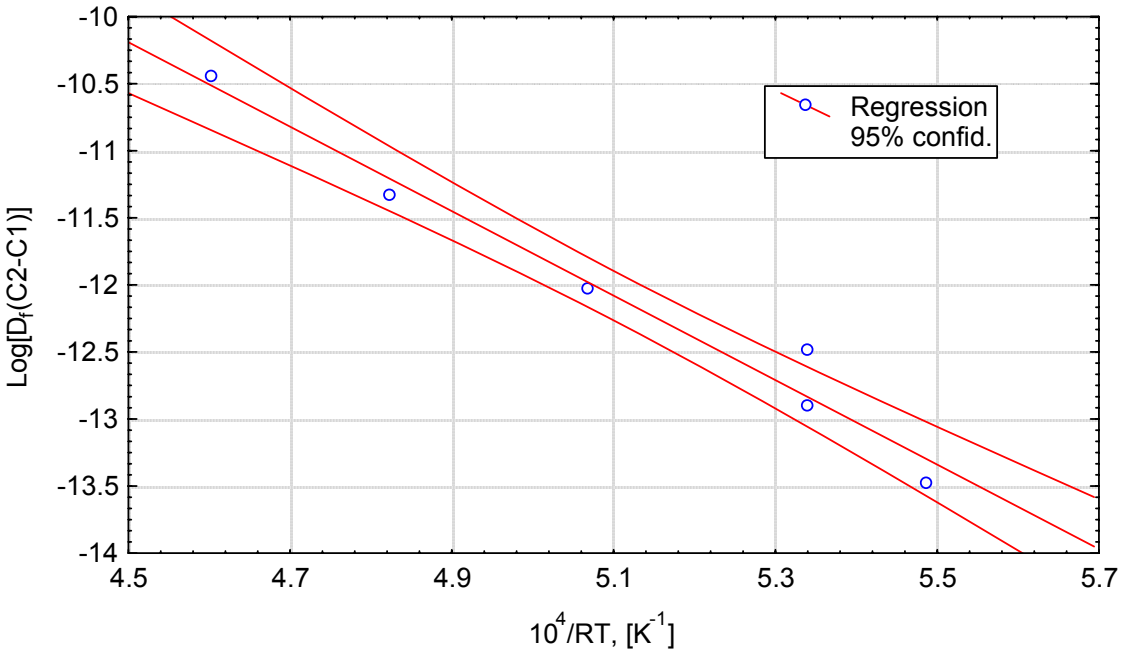
Regression
95% confid.
-10
-10.5
-11
-11.5
-12
-12.5
-13
-13.5
-14
Log[Df(C2-C1)]
4.5
4.7
4.9
5.1
5.3
5.5
5.7
10^4/RT, [K^-1]

Fig.8

III. Deformation Behavior of Zircaloy Fuel Cladding under Quench Conditions

Introduction

The results of CORA test with quenching show that the highest temperatures in the bundle were reached during reflooding. At the reflooding stage of the experiments up to 80 % of the generated hydrogen was produced. Temperature and hydrogen release escalation are the result of intensive oxidation of Zircaloy in steam atmosphere.

High temperature can lead to an increase of internal pressure and, hence, to ballooning of fuel cladding. Clad ballooning influences a heat generation during oxidation by the following way:

- an increase of cladding surface area available for oxidation and heat transfer;
- burst of the cladding allows steam ingression into the gap formed by the fuel pellets and the ballooned cladding and internal oxidation starts;
- oxide cracks and fresh metallic surface becomes available for steam.

After burst of the cladding and equalization of external and internal pressures, the factors that impact the oxide scale rupture are:

- volumetric expansion of Zircaloy due to oxidation;
- steep radial and axial temperature gradients near the quench front leading to the spalling of the oxide scale;
- fuel pellets expansion.

Oxide cracking and spalling decrease the protective power of the oxide scale. Steam reacts with metallic component of the newly formed surface, and as a result of the oxidation, local temperature escalation takes place again.

To take into account the influence of the cladding deformation behavior on the capability of the oxidized cladding to withstand the quench loads the following model is presented.

Model description

1. Structure of the oxidized cladding

Oxidation of Zircaloy at high temperature (> 1200 K) in steam produces a three-layer structure:

- an outer brittle layer of zirconium dioxide ZrO_2,
- an underlying brittle layer of α phase metal stabilized against transformation into β phase by the presence of dissolved oxygen,
- phase core, containing a smaller amount of dissolved oxygen.

2. Effect of oxidation on the cladding deformation behavior

Investigations of deformation behavior of pressurized Zircaloy fuel cladding in steam atmosphere [1-5] show the strengthening effect of oxidation. Oxidation can increase time to rupture due to ballooning in several times or even prevent it.

This can be explained by a decrease of the creep rate of oxygen stabilized α phase. The most strengthening is observed if a layer of oxygen stabilized α phase exists. If the material is heated to produce a duplex structure of α phase dispersed in β phase matrix the creep rate observed is characteristic of the weaker β phase and little strengthening due to oxygen stabilized α phase takes place. The addition of oxygen in solid solution has no effect on the creep behavior of β phase Zircaloy until the $\beta/\alpha + \alpha$ phase boundary is reached. Further addition of oxygen produces an outer layer of stronger α phase and the creep rate is decreased [4].

Another effect of oxidation on cladding deformation is an embrittlement of cladding material. Oxide is assumed to be a brittle material up to its melting. Oxygen in α phase decreases its ductility, especially at low temperatures, besides the cooling rate of cladding through the temperature range of $\beta \rightarrow \alpha$ phase transformation influences the microstructure and extent of oxygen redistribution. Ductile behavior of heavily oxidized Zircaloy cladding depends on oxygen distribution and thickness of β phase [6,7] and influences the capability of cladding to withstand thermal shock loads during quenching as well as loads during handling and transport of fuel assemblies.

3. Effect of irradiation on deformation behavior of oxidized fuel cladding

Because of the strong irradiation of the fuel claddings it is important to know the burst behavior and embrittlement of irradiated claddings in a hypothetical loss-of-coolant accident (LOCA) of LWR.

Results reported in [8] describe transient-heating tube-burst tests of specimens obtained from spent-fuel rods; results published in [9] describe embrittlement under irradiation. These results show that as the burst-behavior as the embrittlement of fuel cladding do not significantly depend on irradiation. The absence of irradiation influence on these properties is not unexpected for the given temperature. The studies of the annealing of irradiation damage indicate complete annealing of irradiation strengthening at temperatures below 973 K during transient heating at rates up to 28 K/s. Increase in ductility due to recrystalization tend to lag behind the strength changes but are beginning at 973 K, even at the highest heating rate of 28 K/s, and

continue to increase as the maximum transient temperature is increased [8]. The elevated temperatures encounted in film boiling operation tend to rapidly anneal irradiation defects [9].

4. Main assumptions of proposed model of deformation behavior of oxidized fuel cladding under quench conditions

Taking into consideration the abovestated features of oxidation and deformation behavior of fuel cladding the next assumptions were used to simulate the cladding behavior under quench conditions:

- The fuel rod is divided into meshes along axial direction. Each mesh consists of fuel pellet and Zircaloy cladding.
- For each mesh the cladding is considered as multilayer cylindrical shell consists of an external oxide layer, an underlying alpha layer, beta layer and the most inner layer that includes the rest of clad wall thickness, Fig.1.
- Material of oxide layer is monoclinic, tetragonal or cubic ZrO_2 phase. It is assumed each oxide phase is stoichiometric ZrO_2 with constant oxygen concentration. Oxide material is assumed to have elastic properties up to melting.
- Material of alpha layer can consist of oxygen stabilized α phase, oxygen reached β phase or mixture of these two phases. Alpha layer material is assumed to have visco-elastic properties up to melting.
- Beta layer is thought to contain a small amount of dissolved oxygen. Material of beta layer can consist of β phase, α phase or mixture of these two phases. Beta layer material is assumed to have visco-elastic properties up to melting.
- The innermost layer includes the materials that are the product of internal oxidation, fuel-cladding interaction or downward relocation of molten material. It is assumed that this layer has no deformation strength and its material is considered as incompressible liquid.
- Fuel pellet is assumed to be a rigid body with radial thermal strain.
- All layers' materials are thought to be isotropic.

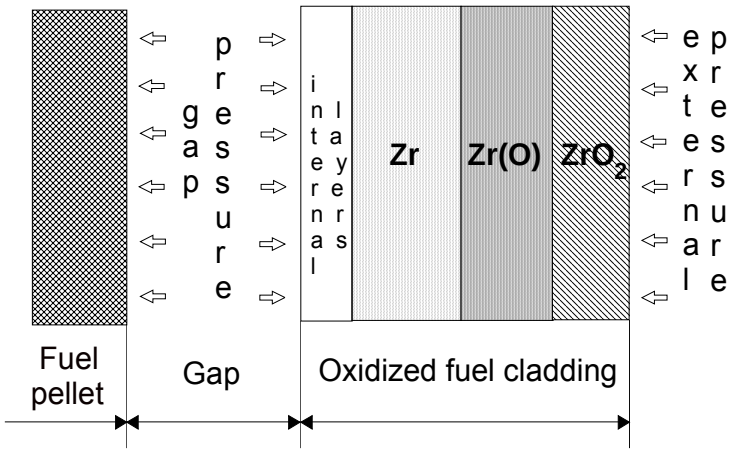

Fig.1. Structure of the mesh of Zircaloy oxidized fuel cladding.

Material of alpha and beta layers is thought to be subjected only creep deformation. Plastic strain which does not depend on time is not included separately, since creep is the dominant deformation mechanism at high temperatures.

All materials are assumed to be isotropic because at the high temperatures, when intensive oxidation occurs, the anisotropy of mechanical properties of Zircaloy is not observed.

5. Constitutive equations

5.1 Stress-strain state of a mesh of oxidized fuel cladding

The factors that impact the mechanical response of the cladding are:

- internal (in the gap between fuel pellets and cladding wall) and external (in the channel of the coolant) pressures;
- volumetric expansion of the material due to oxidation;
- temperature;
- thermal expansion of fuel pellets.

Temperature variation in the radial direction of a mesh is considered, but each layer has an uniform temperature. It is assumed that each layer of a mesh can be described as a thin-walled cylinder. Hence its dimensions can be characterized with the help of a middle radius R, thickness t and height h.

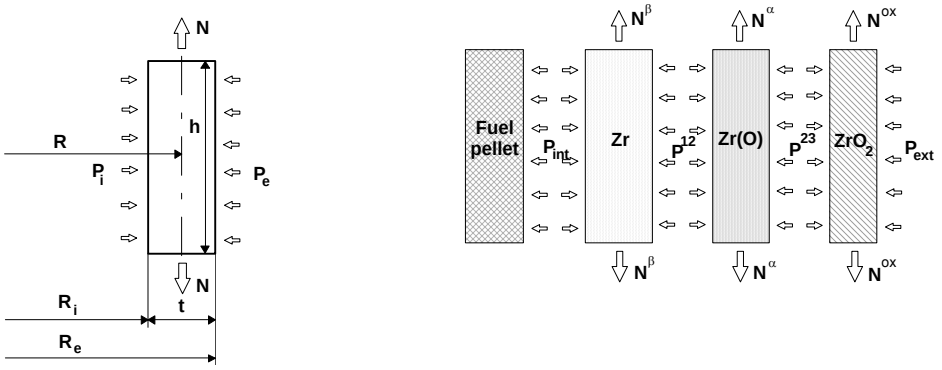

Fig.2 Layer dimensions and calculation diagram of a mesh of oxidized Zircaloy cladding.

The three-dimensional stress state of the thin-walled cylinder can be obtained in the following way:

$$\sigma_r = -\frac{1}{2}(P_i + P_e) \ ;$$

$$\sigma_\theta = P_i \frac{R_i}{t} - P_e \frac{R_e}{t} \ ; \tag{1}$$

$$\sigma_z = \frac{N}{t} \ ,$$

where R_i, R_e - the internal and external layer radii; $t = R_e - R_i$ - the layer thickness; P_i, P_e - the internal and external layer pressures; N - the layer axial force per circumference unit length; r, θ, z - the directions of cylindrical coordinate system. Because of mesh applied loads do not vary along axial and azimuth directions these stress are principle stresses and shearing stress and strain are equal to zero.

The total strain in a given layer is taken to be the sum of elastic, creep and temperature strains:

$$\varepsilon_\chi = \varepsilon_\chi^e + \varepsilon_\chi^{cr} + \varepsilon_\chi^T \ , \tag{2}$$

where $\varepsilon_\chi^e, \varepsilon_\chi^{cr}, \varepsilon_\chi^T$ - elastic, creep and temperature layer strains, correspondingly; index $\chi = r, \theta, z$.

According to Hook's law elastic strains are:

$$\varepsilon_r^e = \frac{1}{E}(\sigma_r - \nu(\sigma_\theta + \sigma_z)) \ ;$$

$$\varepsilon_\theta^e = \frac{1}{E}(\sigma_\theta - \nu(\sigma_r + \sigma_z)) \ , \tag{3}$$

$$\varepsilon_z^e = \frac{1}{E}(\sigma_z - \nu(\sigma_r + \sigma_\theta)) \ ,$$

where E, ν - Young's modulus and Poisson's ratio of a layer material.

Using assumption that stresses do not change significantly due to dimensions changes during time interval *dt*, creep strains increments are given by:

$$d\varepsilon_\chi^{cr} = \frac{3d\varepsilon_{\text{int}}^{cr}}{2\sigma_{\text{int}}}(\sigma_\chi - \sigma_0) \ , \tag{4}$$

where $d\varepsilon_{\text{int}}^{cr}$ - the creep strain intensity increment; $\sigma_0 = (\sigma_r + \sigma_\theta + \sigma_z)/3$; σ_{int} - the stress intensity. Strain and stress intensities can be written as:

$$\varepsilon_{\text{int}} = \frac{\sqrt{2}}{3}\sqrt{(\varepsilon_r - \varepsilon_\theta)^2 + (\varepsilon_\theta - \varepsilon_z)^2 + (\varepsilon_z - \varepsilon_r)^2} \ ; \tag{5}$$

$$\sigma_{\text{int}} = \frac{1}{\sqrt{2}}\sqrt{(\sigma_r - \sigma_\theta)^2 + (\sigma_\theta - \sigma_z)^2 + (\sigma_z - \sigma_r)^2} \ . \tag{6}$$

Zircaloy creep tests data are well-described by a function [10]:

$$\frac{d\varepsilon^{cr}}{dt} = A \cdot \sigma^n \cdot e^{-\frac{Q}{T}} \ , \tag{7}$$

where $d\varepsilon^{cr}/dt$ - the secondary creep velocity; A, n, Q - the creep constants; σ - the applied stress; T - the absolute temperature. Since layer temperature is assumed to be a constant during time interval *dt* , creep strain intensity increment for the case of three-dimensional stress state can be determined in the following way:

$$d\varepsilon_{\text{int}}^{cr} = A \cdot \sigma_{\text{int}}^n \cdot e^{-\frac{Q}{T}} dt \ , \tag{8}$$

Oxygen concentration have an influence on creep rate of oxygen stabilized α phase and it can be taken into account in the following way [4]:

$$\frac{d\varepsilon^{cr,\alpha}(C)}{dt} = \frac{d\varepsilon^{cr,\alpha}(0)}{dt} \cdot e^{-3.42 \cdot C} \ , \tag{9}$$

where $d\varepsilon^{cr,\alpha}(0)/dt$ - the creep rate of α phase with oxygen concentration of as-received cladding; $d\varepsilon^{cr,\alpha}(C)/dt$ - the creep rate of oxygen stabilized α phase with oxygen concentration C; C - the weight fraction of excess oxygen in percents.

Thermal strains can be written as:

$$\varepsilon_r^T = \varepsilon_\theta^T = \varepsilon_z^T = \sqrt[3]{\frac{\rho(T_{ref})}{\rho(T)}} - 1 \ , \tag{10}$$

where $\rho(T_{ref}), \rho(T)$ - the layer material densities at temperatures T_{ref} and T; T_{ref}, T - the initial temperature and the current temperature of the layer, correspondingly.

Finally, if *R,t,h* - the layer dimensions before loading, then under applied loads (temperature, internal and external pressures) layer dimensions are given by:

$$\begin{aligned} R_{def} &= R(1+\varepsilon_\theta) \ , \\ t_{def} &= t(1+\varepsilon_r) \ , \\ h_{def} &= h(1+\varepsilon_z) \ , \\ R_{i,def} &= R(1+\varepsilon_\theta) - \frac{1}{2}t(1+\varepsilon_r) \ , \\ R_{e,def} &= R(1+\varepsilon_\theta) + \frac{1}{2}t(1+\varepsilon_r) \ , \end{aligned} \tag{11}$$

where R_{def} - the middle layer radius under load; t_{def} - the layer thickness under load; h_{def} - the layer height under load; $R_{i,def}, R_{e,def}$ - the internal and external layer radii under load, correspondingly. The strains are considered infinitesimal.

Consideration of the mutual layers displacements under loads (calculation diagram is given in Fig.2) yields the following system of equations:

$$\begin{aligned} R^\beta(1+\varepsilon_\theta^\beta) + \frac{1}{2}t^\beta(1+\varepsilon_r^\beta) - R^\alpha(1+\varepsilon_\theta^\alpha) + \frac{1}{2}t^\alpha(1+\varepsilon_r^\alpha) = 0 \ ; \\ R^\alpha(1+\varepsilon_\theta^\alpha) + \frac{1}{2}t^\alpha(1+\varepsilon_r^\alpha) - R^{ox}(1+\varepsilon_\theta^{ox}) + \frac{1}{2}t^{ox}(1+\varepsilon_r^{ox}) = 0 \ ; \\ h^\beta(1+\varepsilon_z^\beta) - h^\alpha(1+\varepsilon_z^\alpha) = 0 \ ; \\ h^\alpha(1+\varepsilon_z^\alpha) - h^{ox}(1+\varepsilon_z^{ox}) = 0 \ , \end{aligned} \tag{12}$$

where indexes α, β, *ox* denote the beta, alpha and oxide layers, correspondingly. After substitution of (1) - (11) in (12), the system of equations (12) can be written in 5 unknown: $N^\beta, N^\alpha, N^{ox}, P^{\beta,\alpha} = P_e^\beta = P_i^\alpha$ and $P^{\alpha,ox} = P_e^\alpha = P_i^{ox}$.

The fifth equation can be obtained from the consideration of the force balance for the plugged cylinder:

$$N^{\beta} + N^{\alpha} + N^{ox} - N^{\Sigma} = 0 \ , \tag{13}$$

where N^{Σ} - the total axial force, due to internal and external pressures, per unit length.

The total axial force can be written as:

$$N^{\Sigma} = \frac{P_{\text{int}} \cdot R_{\text{int}}^2 - P_{ext} \cdot R_{ext}^2}{R_{\text{int}} + R_{ext}} \ , \tag{14}$$

where R_{int}, R_{ext} - the internal and external cladding mesh radii under loads; P_{int}, P_{ext} - the internal and external cladding mesh pressures.

The considered approach gives solution for the case when the gap between fuel pellet and mesh wall exists. If the internal radius of the mesh is less than external fuel pellet radius, then the internal pressure calculated for cladding as a function of gap volume and temperature is not valid. In this case the obtained solution is not correct and additional equation should be written to determine unknown internal pressure. If fuel pellet is considered as a rigid body and internal cladding layers (besides beta, alpha and external oxide layer) are considered as incompressible liquid then an additional equation can be written in the following way:

$$R^{\beta}(1+\varepsilon_{\theta}^{\beta}) - \frac{1}{2}t^{\beta}(1+\varepsilon_{r}^{\beta}) - R^{pellet}\sqrt{1+\frac{V_{tot}}{\pi h_{def}\,(R^{pellet})^2}} = 0 \ , \tag{15}$$

where R^{pellet} - the external fuel pellet radius; h_{def} - the deformed mesh height at the end of previous time step; V_{tot} - the total volume of the internal layers. The total axial force N^{Σ} is assumed to be equal to zero.

The system of equations (12), (13) is nonlinear in $N^{\beta}, N^{\alpha}, N^{ox}, P^{\beta,\alpha}, P^{\alpha,ox}$, solution method is presented in Appendix A. After solving the system of equations (12), (13) for the unknown $N^{\beta}, N^{\alpha}, N^{ox}, P^{\beta,\alpha}, P^{\alpha,ox}$ one can evaluate the stresses and strains for each mesh layer, and then mesh dimensions. Because of the assumption that changes of layers dimensions during time step are negligible, hence, an intensity of creep strain increments should be checked. If the creep strain increment intensity exceeds the given limit value then time step is reduced and calculations start again.

New mesh dimensions are calculated using (11), creep strains accumulated at the time step lead to irreversible changes of the layer dimensions:

$$R_{new} = R(1+\Delta\varepsilon_\theta^{cr})\ ;$$
$$t_{new} = t(1+\Delta\varepsilon_r^{cr})\ ; \qquad (16)$$
$$h_{new} = h(1+\Delta\varepsilon_z^{cr})\ ,$$

where $\Delta\varepsilon_r^{cr}, \Delta\varepsilon_\theta^{cr}, \Delta\varepsilon_z^{cr}$ - the creep strain increments of the layer at the end of time step Δt.

5.2 Oxide scale cracking.

The oxide layer is assumed to crack and has no deformation strength if the tensile elastic strain in ZrO_2 shell at the end of time step Δt exceeds the ultimate strain limit:

$$\varepsilon_\chi^{e,ox} \geq \frac{\sigma_b^{ox}(T)}{E^{ox}(T)}\ , \qquad (17)$$

where $\sigma_b^{ox}(T), E^{ox}(T)$ - oxide strength limit and Young's modulus at the given temperature. Using (3) the expression (17) may be transformed to the next form:

$$\sigma_1^{ox} - \nu(\sigma_2^{ox} + \sigma_3^{ox}) \geq \sigma_b^{ox}(T)\ , \qquad (18)$$

where σ_i^{ox} is the principle stress in oxide layer (it is assumed that $\sigma_1^{ox} \geq \sigma_2^{ox} \geq \sigma_3^{ox}$).

Microcracks orientation depends on direction of tensile strain that leads to oxide rupture, the direction of maximum elastic strain is perpendicular to crack surfaces :

- $\sigma_\theta^{ox} > \sigma_z^{ox} \geq \sigma_r^{ox}$, if circumferential elastic strain exceeds the strain limit then the axial microcracks appear;

- $\sigma_z^{ox} > \sigma_\theta^{ox} \geq \sigma_r^{ox}$, axial strain leads to circumferential microcracks;

- $\sigma_r^{ox} > \sigma_\theta^{ox} \geq \sigma_z^{ox}$, when radial strains reach the limit value, oxide scale breaks off.

Under quench conditions the last case corresponds to oxide phase transformation at temperature ~ 1500 K, when tetragonal oxide transforms to monoclinic phase. This process is accomplished by the sharp increase of oxide temperature strain ~ 2.5 % and, hence, leads to generation of high stresses in oxide layer and metal sublayers. Break off of oxide scale (the radial cracks) decrease generated stresses in oxidized cladding. This exfoliated oxide may be free of circumferential and axial cracks if the high temperature gradients are absent. Large temperature differences in this scale during quench front movement can lead to oxide cracking in axial and circumferential directions, i.e. so called spalling takes place. Exfoliated oxide scale can be consider

as a part of thin-walled cylinder then the surface stresses generated by radial temperature difference are given by:

$$\sigma_\theta^{ox}(R_e^{ox}) = \sigma_z^{ox}(R_e^{ox}) = \frac{E^{ox}\alpha^{ox}(T_{\text{int}}^{ox} - T_{ext}^{ox})}{2(1-\nu)} ,$$

$$\sigma_\theta^{ox}(R_i^{ox}) = \sigma_z^{ox}(R_i^{ox}) = -\frac{E^{ox}\alpha^{ox}(T_{\text{int}}^{ox} - T_{ext}^{ox})}{2(1-\nu)} , \quad (19)$$

$$\sigma_r^{ox}(R_i^{ox}) = \sigma_r^{ox}(R_e^{ox}) = 0 ,$$

where R_i^{ox}, R_e^{ox} - the internal and external oxide scale radii, α^{ox} - the liner thermal expansion coefficient of oxide, $T_{\text{int}}^{ox}, T_{ext}^{ox}$ - the internal and external temperatures of oxide scale. Using (18), (19) one can predict the spalling of exfoliated oxide due to radial temperature difference.

5.3 Modification of cladding layers dimensions due to oxidation.

After oxide cracking or spalling if oxidation goes on, a new uncracked oxide layer appears. This oxide layer has deformation strength and influences the mesh deformation behavior.

Oxidation leads to change of each layer thickness. Mass of each mesh layer at the end of *k* time step can be obtained in the following way:

$$M_k^\xi = V_k^\xi \rho(T_{ref}) , \quad (20)$$

where M_k^ξ - the mass of layer *x (x=b,a,ox)* at the end of time step *k*; V_k^ξ - the volume of layer *x* for unload state (at the initial temperature T_{ref} , without pressures and axial forces) at the end of time step *k* with account of accumulated creep strains:

$$V_k^\xi = \pi((R_{e,k}^\xi)^2 - (R_{i,k}^\xi)^2)h_k^\xi , \quad (21)$$

where $R_{e,k}^\xi, R_{i,k}^\xi$ - the external and internal radii of layer *x* for unload state at the end of time step *k*; h_k^ξ - the height of layer *x*.

After oxidation during the next time step *k+1* the masses of the layers changed to M_{k+1}^ξ, hence the mass increments can be found. For oxide layer:

$$\Delta M_i^{ox} = M_{k+1}^{ox} - M_k^{ox} \ , \tag{22}$$

It is assumed that this mass change is caused by oxygen stabilized alpha to oxide phase transformation and it occurs at the alpha-oxide surface. The corresponding mass increment of alpha layer at the external surface is given by:

$$\Delta M_e^{\alpha} = -\frac{W^{\alpha}}{W^{ox}} \Delta M_i^{ox} \ , \tag{23}$$

where W^{α}, W^{ox} - the molar mass of alpha layer material and oxide, correspondingly.

The mass increment of alpha layer at the internal surface is given by:

$$\Delta M_i^{\alpha} = M_{k+1}^{\alpha} - M_k^{\alpha} - \Delta M_e^{\alpha} \ , \tag{24}$$

In such way the mass increments of beta layer can be found:

$$\Delta M_e^{\beta} = -\frac{W^{\beta}}{W^{\alpha}} \Delta M_i^{\alpha} \ ;$$

$$\Delta M_i^{\beta} = M_{k+1}^{\beta} - M_k^{\beta} - \Delta M_e^{\beta} \ , \tag{25}$$

where W^{β} - the molar mass of beta layer material.

Dividing these mass increments by the density at the initial temperature T_{ref} one can obtained the volume increments of the layers Fig.3:

$$\Delta V_{\lambda}^{\xi} = \frac{\Delta M_{\lambda}^{\xi}}{\rho(T_{ref})} \ , \tag{26}$$

where ΔV_{λ}^{ξ} - the volume increment of layer *x* at *l* surface, (*l*=*i*,*e*).

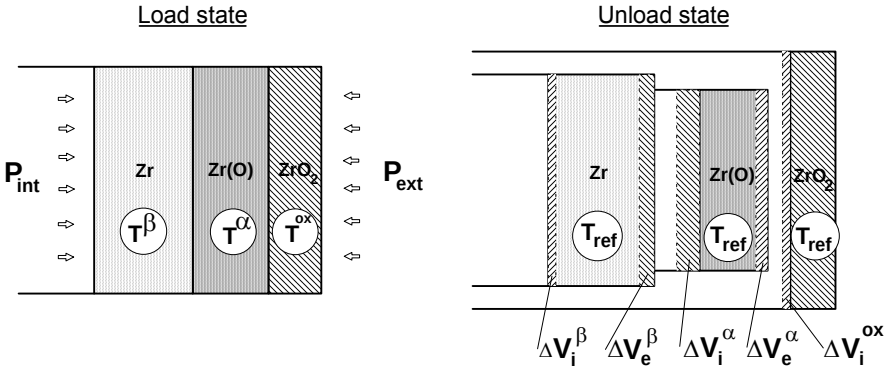

Fig.3. Change of the layers dimensions due to oxidation.

Thus, the new layer radii changed due to oxidation during time step *k+1* are :

$$R^{\xi}_{i,k+1} = \sqrt{(R^{\xi}_{i,k})^2 - \frac{\Delta V_i{}^{\xi}}{\pi h^{\xi}_k}} \; ; \qquad R^{\xi}_{e,k+1} = \sqrt{(R^{\xi}_{e,k})^2 + \frac{\Delta V_e{}^{\xi}}{\pi h^{\xi}_k}} \; . \tag{27}$$

These dimensions are used in the system of equation (12), (13) to simulate the cladding mesh deformation behavior during time step *k+1*. At the end of time step the final alpha and beta layer dimensions are changed due to creep strain (16).

6. Failure of oxidized Zircaloy fuel cladding during quench

Microstructure of oxidized Zircaloy cladding has a great influence on the capability of cladding to withstand thermo-shock loads during quench and the dominant role has β phase layer [6,7]. It is explained by high ductility of β phase which prevents cracks initiation and arrests the propagation of cracks generated in oxide and α phase layers.

The rate of specimen cooling through $\beta \rightarrow \alpha$ phase transformation influences the microstructure of transformed β and, hence, the fracture properties. In general:

- the extent of oxygen distribution and the fraction of the oxygen-depleted zones in the transformed β phase decrease as the cooling rate through the phase transformation increase from ~5 to 100 K/s;

- the effect of cooling rate on oxygen redistribution becomes less significant when the oxygen content of the material exceeds ~0.9 wt %, i.e., for oxidation at $\geq$ 1600 K.

At the oxidation temperatures < 1600 K and slow cooling rates through the phase transformation ~ 5 K/s, a non-uniform oxygen distribution occurs in transformed β phase. Oxygen redistributes between the brittle bar-shape α grains and ductile regions between the grains. Although crack initiation may occur more easily in the oxygen-rich zones, the oxygen-depleted regions are more ductile; consequently, crack propagation through the transformed β phase that exhibits oxygen segregation is more difficult than for relatively homogeneous material, which corresponds to the high oxidation temperatures and cooling rate ~ 100 K/s. This is the reason of the higher thermal-shock resistance of the slower cooled specimens.

Experiment [6] showed that at oxidation temperature $\leq$ 1420 K, the fuel claddings failed primary by propagation of a single circumferential crack; however, at higher oxidation temperatures (e.g. $\geq$ 1520 K) fragmentation of the cladding occurred. Predominantly brittle fracture occurred based upon the observation that pieces of the oxidized cladding could be fit together without appreciable distortion of the macroscopic geometry. A brittle-fracture mode was indicated by scanning-electron microscopy. Intergranular fracture was evident in the stabilized α phase of the specimen. A large number of cracks typically were observed in α phase layer, oxide layer was relatively crack-free. The transformed β phase layer consisted of elongated α grains, which were enriched in oxygen, surrounded by oxygen-depleted regions. The α

grains fractured in a brittle manner, whereas the surrounding material exhibited some evidence of ductile fracture.

The next criteria may be used to predict the capability of oxidized cladding to withstand the quench loads:

- Maximum cladding oxidation. The calculated total oxidation of cladding shall nowhere exceed 0.17 times the total cladding thickness before oxidation. The total oxidation means the total thickness of cladding metal that would be locally converted to oxide if all the oxygen absorbed and reacted with the cladding locally were converted to stoichiometric zirconium oxide. In the case of additional internal oxidation the internal surface of the cladding shall be included into oxidation. Cladding thickness before oxidation means thickness with account of predicted strain due to rupture, deformation or swelling.
- Thickness of β phase layer with the given oxygen concentration. The calculated thickness of the cladding with $\leq$ 0.9 wt % oxygen, based on the average wall thickness at any location, shall be greater than 0.1 mm.

The second criterion is applicable irrespective of the oxidation temperature, initial wall thickness, wall thickness that results from deformation under pressures, and the total oxygen content of the cladding [6]. It takes into account the real oxygen distribution and layers growth kinetics.

The above features of cladding failure during quench give the qualitative explanation of this phenomenon. The proposed failure criteria can predict whether the cladding fails or not. However, the accurate quantitative prediction of the fracture time and reasons of failure is still impossible. One can propose the following factors leading to oxidized cladding failure:

- axial temperatures gradients at the quench front;

- oxide phase transformation;

- pellet-cladding interaction due to different thermal expansion of pellets and cladding wall.

Simulation results

On the base of considered approaches the computer code was worked out. Flowchart of this deformation behavior module is presented in Fig.4. All routines are written in FORTRAN 77. Some tests simulations were performed to evaluate the predictive capability of this code. The results of this simulation are presented below.

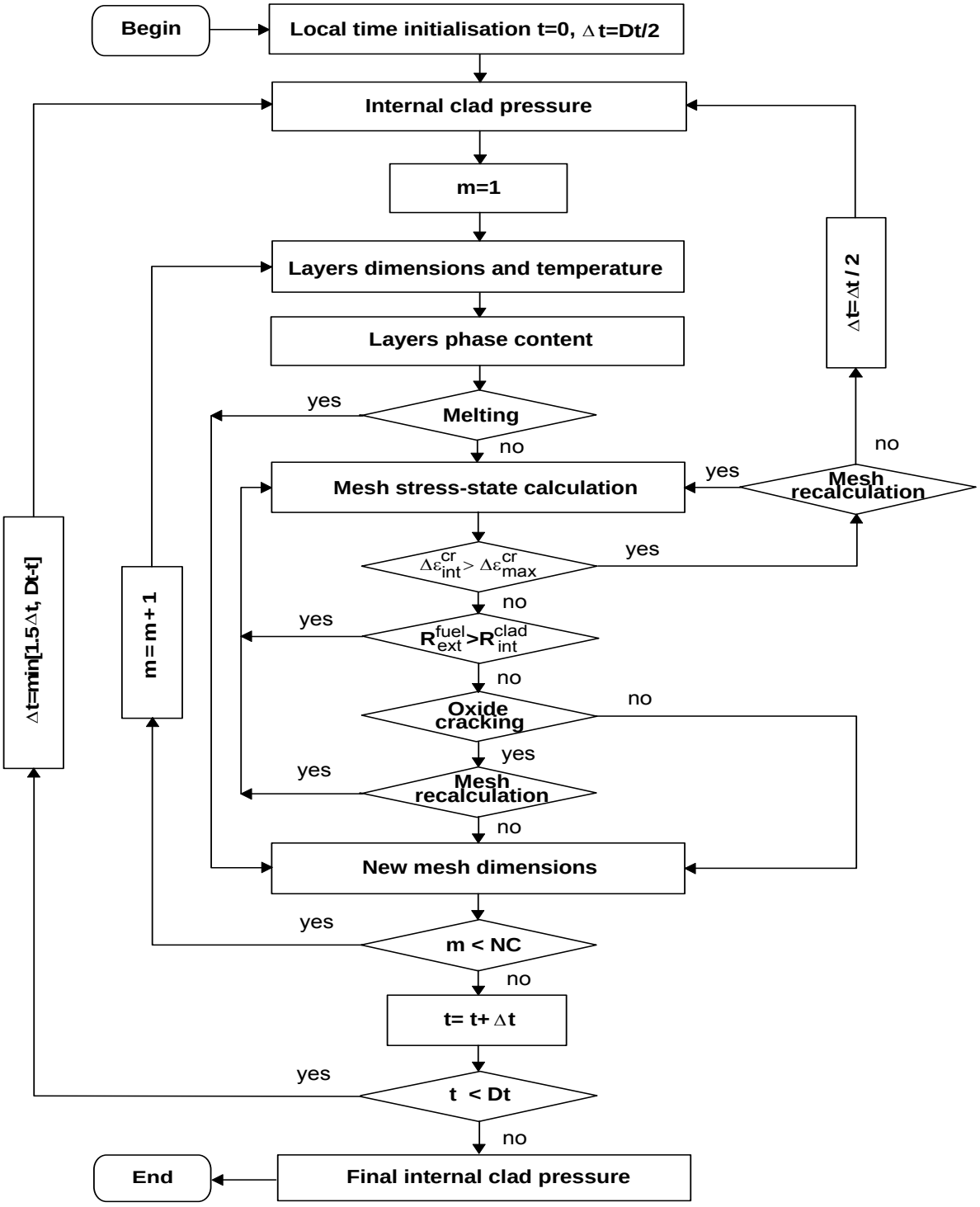

Fig.4. Flowchart of proposed deformation behavior module.

1. Single-rod transient burst test performed within REBEKA project

To verify the prediction of deformation behavior of slightly oxidized fuel cladding the simulations of single-rod burst tests performed within the REBEKA project [5] were carried out. To simulate the oxidation of Zircaloy fuel cladding the worked out oxidation module was used.

Test preparation: The cladding tubes were made of Zircaloy-4 with 10.75 mm outside diameter and 9.30 mm inside diameter.

Test performance: The internal overpressure and the heating rate were kept constant during the deformation process. A heated shroud surrounded the test rod to minimize temperature differences on cladding circumference. Single-rod transient burst test in steam were performed with the following parameters: internal overpressure - 10 - to 140 bar, heating rate - 1 to 30 K/s. Initial temperature - 573 K.

Experimental results: Fig.5 is a plot of burst temperature versus internal overpressure with heating rate as a parameter. With the same heating rate, a higher internal overpressure resultsin a lower burst temperature. The diagram reveals a distinct influence of the heating rate on the burst temperature: increasing of heating rate lead to increasing burst temperature.

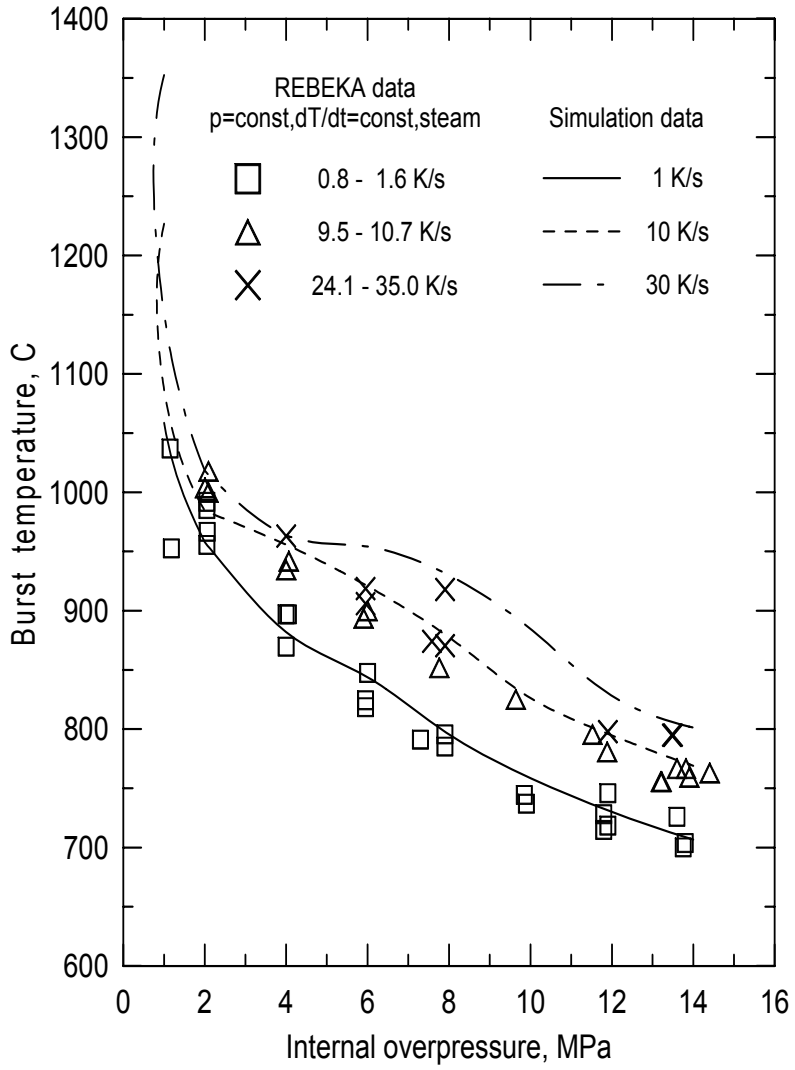

Fig.5. Module predicted and experimental burst temperature versus internal overpressure.

Simulation results: The burst temperatures predicted by fuel cladding deformation behavior module are presented in Fig.5.

2. Sagat at al. experiment

To verify the prediction of oxidation strengthening effect the simulations of single-rod burst tests [5] were carried out. To simulate the oxidation of Zircaloy fuel cladding the carried out oxidation module was used.

Test preparation: The specimens were prepared from Zircaloy-4 cladding 15.25 mm in diameter, 0.45 mm wall thickness, and 489 mm long.

Test performance: Prior to each test, steam was admitted into the test chamber at a flow of about 2~g/s to provide an oxidizing environment on the specimen outside diameter. The apparatus was allowed to stabilize for about 600 s and after then the specimen was internally pressurized with the helium to the test pressure and then the temperature ramped using Joule heating (heating by specimen own resistance) until a predetermined strain was achieved or until the burs occurred. The measured diametral strain were obtained at a heating rate of 5 K/s and at different internal pressures ranging from 0.34 to 1.38 MPa for vacuum and steam environment.

Experimental results: The results showed that at internal pressures greater than or equal to 0.69 MPa (hoop stress of 11.3 MPa) there was little difference between the vacuum and steam data as negligible oxidation occurred during the short test period. The effect of steam oxidation became important at lower pressures where the ramp temperatures exceeded 1300 K, reducing the strain rate of specimens tested in steam. The diametral strains obtained at internal pressures 0.34 and 0.48 MPa in steam are plotted versus temperature in Fig.6 and Fig 7 together with similar data obtained on specimens tested in vacuum.

Simulation results: The diametral strain data predicted by fuel cladding deformation behavior module are presented in Fig.6 and Fig 7.

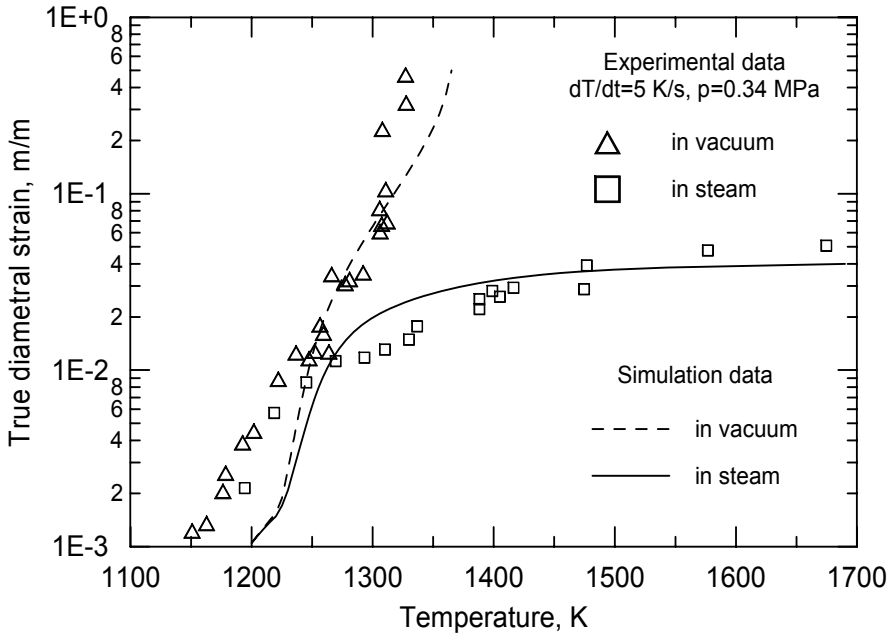

Fig.6 Module predicted and experimental diametral strain data for internal pressure 0.34 MPa.

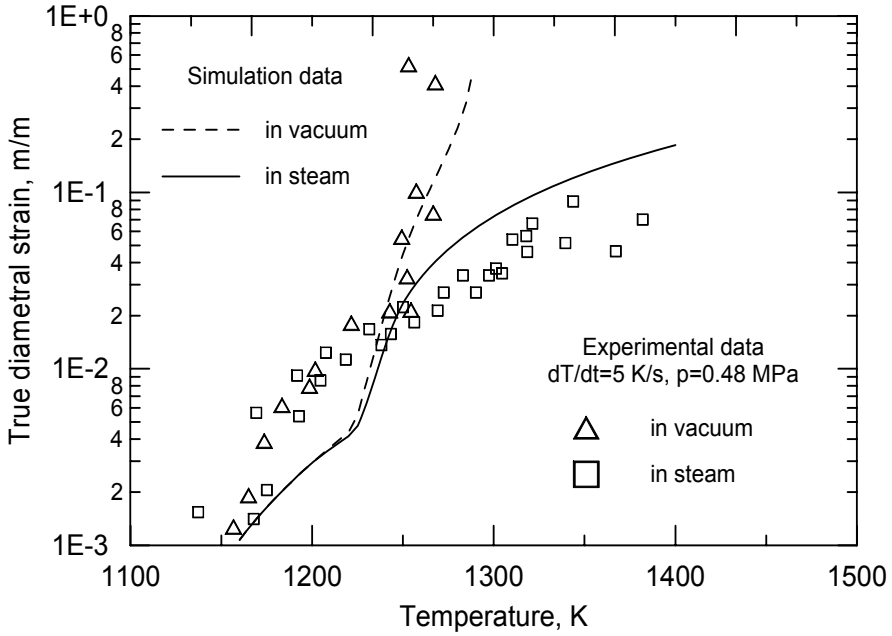

Fig.7 Module predicted and experimental diametral strain data for internal pressure 0.48 MPa.

Others results of deformation behavior simulations are presented in the chapter describing the coupling of deformation, oxidation and heat-exchange modules.

Material properties

1. Zircaloy elastic properties

Zircaloy Young's modulus are based on MATPRO data base [11]:

In α phase:

$$E^{\alpha} = 1.088 \cdot 10^{11} - 5.475 \cdot 10^{7} T + K_1$$

where E^{α} - the α phase Young's modulus, [Pa]; K - the absolute temperature , [K]; K_1 - the modification to account for the effect of oxidation, [Pa]:

$$K_1 = (6.61 \cdot 10^{11} + 5.912 \cdot 10^{8} T) C ,$$

where *C* - the average oxygen concentration minus oxygen concentration of as-received cladding.

In β phase:

$$E^{\beta} = 9.21 \cdot 10^{10} - 4.05 \cdot 10^{7} T ,$$

where E^{β} - the β phase Young's modulus, [Pa]; K - the absolute temperature.

2. Zircaloy creep properties

Creep properties are based on the creep velocity experimental results, which can be expressed as [10]:

$$V(\sigma, T) = A(T) \cdot \sigma^{n} \cdot e^{-\frac{Q}{T}} ,$$

where $V(\sigma, T)$ - the cicumferential creep velocity $\frac{1}{R}\frac{dR}{dt}$, [1/s]; σ - the cicumferential stress, [MPa]; T - the absolute temperature, [K]; $A(T)$ - coefficient, which depends on temperature only for α phase, [1/s(MPa)^n]; n - the stress exponent; Q - the temperature factor, [K].

In α phase:

$$A^{\alpha} = \frac{0.5637}{(1 - 1.1246 \cdot 10^{-3} \cdot (T - 1098))^{5.65}} ,$$

$$n^{\alpha} = 5.65 ,$$

$$Q^{\alpha} = 29640 .$$

The influence of dissolved oxygen on the creep rate of oxygen stabilized α phase is given by [4]:

$$V^{\alpha}(C) = V^{\alpha}(0) \cdot e^{-3.42 \cdot C} ,$$

where *C* - the oxygen content in weight percent; $V^{\alpha}(C)$ and $V^{\alpha}(0)$ - the creep rates of α phases containing zero and *C* weight percent oxygen, respectively.

In β phase:

$$A^{\beta} = 4.067 ,$$
$$n^{\beta} = 3.79 ;$$
$$Q^{\beta} = 17112 .$$

In mixture of α and β phases:

$$A^{\alpha+\beta} = 14.4676 ,$$
$$n^{\alpha+\beta} = 2.97 ,$$
$$Q^{\alpha+\beta} = 20330 .$$

In the case of oxygen free Zircaloy the existence of the mixture depends only on temperature. Since the content of each phase in the mixture varies from 0 to 1 then the temperature interval of α - β transformation is divided into tree interval:

1. 1098 $\leq T <$ 1133 K, content of α phase 0.9 $< F^{\alpha} \leq$ 1. For this temperature interval the creep rate is given by:

$$V^{mix}(\sigma, T) = F^{mix} \cdot V^{\alpha+\beta}(\sigma, T) + \overset{\approx}{F}{}^{\alpha} \cdot V^{\alpha}(\sigma, T) ,$$

where

$$F^{mix} = 10 \cdot (1 - F^{\alpha}) , \qquad \overset{\approx}{F}{}^{\alpha} = 1 - F^{mix} ,$$

where F^{mix} - weight fraction mixture; $\overset{\approx}{F}{}^{\alpha}$ - weight fracture α phase, which is not involved in the mixture.

2. 1133 $\leq T \leq$ 1223 K, content of α phase 0.1 $\leq F^{\alpha} \leq$ 0.9. For this temperature interval the standard procedure of creep rate evaluation is used:

$$V^{mix}(\sigma, T) = V^{\alpha+\beta}(\sigma, T) ,$$

3. 1223 $< T \leq$ 1248 K, content of α phase 0 $\leq F^{\alpha} <$ 0.1. For this temperature interval creep strain increment is given by:

$$V^{mix}(\sigma,T) = F^{mix} \cdot V^{\alpha+\beta}(\sigma,T) + \tilde{\tilde{F}}^{\beta} \cdot V^{\beta}(\sigma,T)$$

where

$$F^{mix} = 10 \cdot F^{\alpha} \ , \quad \tilde{\tilde{F}}^{\beta} = 1 - F^{mix} \ ,$$

where $\tilde{\tilde{F}}^{\beta}$ - weight fracture β phase, which is not involved in the mixture.

The influence of the creep strain and α phase content on the creep rate is given by [10]:

$$V(\sigma,T,\varepsilon,F^{\alpha}) = V(\sigma,T) \cdot \frac{R_0}{R} \cdot K \ ,$$

where R_0 , R - the average initial and current radii, respectively; K - coefficient which is equal to:

$$K = 1 \qquad \text{if } F^{\alpha} < 1 \text{ or } \frac{dT}{dt} < 0 \text{ or } \frac{R - R_0}{R_0} > 0.018 \ ,$$

$$K = 42.5 \cdot e^{-208\left(\frac{R-R_0}{R_0}\right)} \qquad \text{if } 0.005 \le \frac{R - R_0}{R_0} \le 0.018 \ ,$$

$$K = 15 \qquad \text{otherwise.}$$

3. Oxide properties

The oxide properties are based on MATPRO data base [11].

Oxide Young's modulus:

1. $300 \le T < 1478$ K:

$$E^{ox} = 1.637 \cdot 10^{11} - 3.77 \cdot 10^{7} \cdot T \ .$$

2. $1478 \le T < 2810$ K:

$$E^{ox} = 2.255 \cdot 10^{11} - 8.024 \cdot 10^{7} \cdot T \ .$$

3. $T \ge 2810$:

$$E^{ox} = 1 .$$

where E^{ox} - the oxide Young's modulus, [Pa]; K - the absolute temperature , [K].

Oxide strength limit:

1. 300 $\leq T \leq$ 1200 K (monoclinic phase):

$$\sigma_b = 96.28 \cdot 10^6 \ .$$

2. 1200 $< T <$ 1480 K (monoclinic phase):

$$\sigma_b = 1.57 \cdot 10^8 - 5.06 \cdot 10^4 \cdot T \ .$$

3. 1480 $\leq T <$ 1896.4 K (tetragonal and cubic phases):

$$\sigma_b = 3.889 \cdot 10^8 - 2.075 \cdot 10^5 \cdot T \ .$$

4. 1896.4 $\leq T <$ 2810 K :

$$\sigma_b = 1.0 \cdot 10^6 \ .$$

5. $T \geq$ 2810 K :

$$\sigma_b = 1.0 \cdot 10^{10} \ ,$$

where σ_b - the oxide strength limit, [Pa].

4. Thermal expansion

It is assumed that thermal expansion of all fuel rod materials is isotropic and given by:

$$\varepsilon_r^{T,\xi} = \varepsilon_\theta^{T,\xi} = \varepsilon_z^{T,\xi} = \sqrt[3]{\frac{\rho^\xi(T_{ref})}{\rho^\xi(T)}} - 1$$

where T and T_{ref} - the current and the reference temperatures, respectively; $\rho^\xi(T)$ - the density of ξ material of fuel rod as a function of temperature. Evaluation of materials density is based on MATPRO data base [11].

Phase content and state of Zircaloy.

Phase content of oxygen free Zircaloy is assumed to depend only on temperature [10]:

1. $300 \le T \le$ 1098 K:

$$F^{\alpha} = 1 \ .$$

2. $1098 < T \le$ 1123 K:

$$F^{\alpha} = 1 - 2 \cdot 10^{-3} \cdot (T - 1098) \ .$$

3. $1123 < T \le$ 1133 K:

$$F^{\alpha} = 0.95 - 5 \cdot 10^{-3} \cdot (T - 1123) \ .$$

4. $1133 < T \le$ 1173 K:

$$F^{\alpha} = 0.9 - 1 \cdot 10^{-2} \cdot (T - 1133) \ .$$

5. $1173 < T \le$ 1198 K:

$$F^{\alpha} = 0.5 - 1 \cdot 10^{-2} \cdot (T - 1173) \ .$$

6. $1198 < T \le$ 1223 K:

$$F^{\alpha} = 0.25 - 6 \cdot 10^{-3} \cdot (T - 1198) \ .$$

7. $1223 < T \le$ 1248 K:

$$F^{\alpha} = 0.1 - 4 \cdot 10^{-3} \cdot (T - 1223) \ .$$

8. $T >$ 1248 K:

$$F^{\beta} = 1 \ ,$$

where F^{α} and F^{β} - weight fraction oxygen free α and β phases; T - the absolute temperature, [K].

Melting point of oxygen free β phase is 2098 K.

Phase content and melting point of Zircaloy with dissolved oxygen is found from Zry-O phase diagram as a function of the temperature and oxygen content. Zry-O phase diagram is approximated with the help of the simplified MATPRO correlation [11].

The temperature of 2810 K is used as oxide melting point, because above 2810 K the equation for oxide Young's modulus would predict a negative value [11].

Poisson's ratio for all phases and temperatures is a constant of 0.3 for solid state and 0.5 in the case of liquid.

Conclusion

The simulation results of preoxidized specimens quenching show that the additional stresses generated by temperature gradients have some influence on the stress state of the oxidized cladding. However, the main contribution to the high stress state is induced by $\beta \rightarrow \alpha$ phase transformation of Zircaloy and tetragonal-to-monoclinic phase transformation of oxide. Phase transformation in oxide can lead to formation of cracks which penetrate through the wall at the locations above the coolant level. In this case the high cladding temperature and steam environment lead to the beginning

of the inner cladding and cracks surfaces oxidation and increase of hydrogen generation.

Temperature gradient may have an influence on the final spalling (by radial or axial large temperature variation of exfoliated oxide scale) or global cladding failure (through breach formation or cladding fragmentation). The maximum temperature gradients occur near the quench front when film boiling transforms to nucleate boiling, i.e. at the Leidenfrost temperature. At these temperatures there is no oxidation and temperature can not increase due to oxidation. But this low temperature cracking or breach formation can influence the release of hydrogen dissolved in the metal sublayer.

Appendix. Solution of the system of equations (12), (13)

The system of equations (12), (13) is nonlinear in $N^{\beta}, N^{\alpha}, N^{ox}, P^{\beta,\alpha}, P^{\alpha,ox}$, for the solution let's write the layer strains for the unknowns explicitly and then linearize the obtained system of equations.

The elastic strains using (1) and (3) can be written as:

$$\varepsilon_{\chi}^{e} = \sum_{i=1}^{3} G_{\chi,i} F^{i} \ , \tag{A1}$$

where $\chi = r, \theta, z$; F^{i} - the load factor for the layer, index *i*=1 corresponds to the internal pressure P_i , *i*=2 to the external pressure P_e , *i*=3 to the axial force per unit length N; $G_{\chi,i}$ - the coefficients:

$$\begin{aligned}
&G_{r,1} = -\frac{1}{2E} - \frac{\nu R_i}{tE} \ ; \qquad G_{r,2} = -\frac{1}{2E} + \frac{\nu R_e}{tE} \ ; \qquad G_{r,3} = -\frac{\nu}{tE} \ ; \\
&G_{\theta,1} = \frac{\nu}{2E} + \frac{R_i}{tE} \ ; \qquad G_{\theta,2} = \frac{\nu}{2E} - \frac{R_e}{tE} \ ; \qquad G_{\theta,3} = -\frac{\nu}{tE} \ ; \\
&G_{z,1} = \frac{\nu}{2E} - \frac{\nu R_i}{tE} \ ; \qquad G_{z,2} = \frac{\nu}{2E} + \frac{\nu R_e}{tE} \ ; \qquad G_{z,3} = \frac{1}{tE} \ .
\end{aligned} \tag{A2}$$

The creep strain increments during time interval Δt using (4)-(8) can be written as:

$$\Delta\varepsilon_{\chi}^{cr} = \frac{B(T)}{2^{\frac{n-1}{2}}} \cdot \left(\sum_{i=1}^{3} \sum_{j=1}^{3} C_{ij} F^{i} F^{j} \right)^{\frac{n-1}{2}} \cdot \left(\sum_{i=1}^{3} D_{\chi,i} F^{i} \right) \cdot \Delta t \ , \tag{A3}$$

where the coefficients are:

$$B(T) = \frac{3}{2} \cdot A \cdot e^{-\frac{Q}{T}} \ , \tag{A4}$$

$$\begin{aligned}
&C_{12} = C_{21} = \frac{2R_i R_e}{t^2} \ ; \quad C_{13} = C_{31} = \frac{t - 2R_i}{2t^2} \ ; \quad C_{23} = C_{32} = \frac{t + 2R_e}{2t^2} \ ; \\
&C_{11} = \frac{4R_i^2 + 2tR_i + t^2}{2t^2} \ ; \quad C_{22} = \frac{4R_e^2 - 2tR_e + t^2}{2t^2} \ ; \quad C_{33} = \frac{2}{t^2} \ ,
\end{aligned} \tag{A5}$$

$$D_{r,1} = -\frac{R_i}{3t} - \frac{1}{3}\ ; \qquad D_{r,2} = \frac{R_e}{3t} - \frac{1}{3}\ ; \qquad D_{r,3} = -\frac{1}{3t}\ ;$$

$$D_{\theta,1} = \frac{2R_i}{3t} + \frac{1}{6}\ ; \qquad D_{\theta,2} = -\frac{2R_e}{3t} + \frac{1}{6}\ ; \qquad D_{\theta,3} = -\frac{1}{3t}\ ; \qquad \text{(A6)}$$

$$D_{z,1} = -\frac{R_i}{3t} + \frac{1}{6}\ ; \qquad D_{z,2} = \frac{R_e}{3t} + \frac{1}{6}\ ; \qquad D_{z,3} = \frac{2}{3t}\ .$$

Under assumption that the mesh components temperatures and loads do not vary during time step Δt and using their values at the end of the time step, one can linearize the system of equations. The creep strain increments at the time step can be linearized with respect to layer loads increments in the following way:

$$\Delta\varepsilon_\chi^{cr}(F_i + \Delta F_i) \approx \Delta\varepsilon_\chi^{cr}(F_1, F_2, F_3) + \sum_{i=1}^{3}\left[\frac{\partial(\Delta\varepsilon_\chi^{cr})}{\partial F_i}\right]_{(F_1,F_2,F_3)} \cdot \Delta F_i\ , \qquad \text{(A7)}$$

where ΔF_i - the layer loads increments.

Derivatives of creep strain increments (A3) are given by:

$$\frac{\partial(\Delta\varepsilon_\chi^{cr})}{\partial F_i} = \frac{B(T)}{2^{\frac{n-1}{2}}} \cdot \left\{ (n-1)\left(\sum_{i=1}^{3}\sum_{j=1}^{3} C_{ij} F^i F^j\right)^{\frac{n-3}{2}} \cdot \sum_{j=1}^{3} C_{ij} F^j \cdot \sum_{i=1}^{3} D_{\chi,i} F^i + \right.$$

$$\left. \left(\sum_{i=1}^{3}\sum_{j=1}^{3} C_{ij} F^i F^j\right)^{\frac{n-1}{2}} \cdot D_{\chi,i} \right\} \cdot \Delta t\ . \qquad \text{(A8)}$$

After substitution (A1), (A3), (A7) and (A8) the linearized system of equations is solved numerically:

$$f'(X^{m-1}) \cdot \Delta X^m = -f(X^{m-1})\ , \qquad \text{(A8)}$$

where $f(X)$ - the left side of the system of equations (12), (13). The unknowns for the mesh at *m* -th iteration can be written as $X^m = X^{m-1} + \Delta X^m$, where X is the mesh load vector with components of $N^\beta, N^\alpha, N^{ox}, P^{\beta,\alpha}, P^{\alpha,ox}$; ΔX is the load correction vector with components of $\Delta N^\beta, \Delta N^\alpha, \Delta N^{ox}, \Delta P^{\beta,\alpha}, \Delta P^{\alpha,ox}$. As initial approximation an elastic solution (creep strains are equal to zero) of the system (12), (13) is used. The iterations go on up to the moment when the given simulation accuracy will be achieved.

References:

1. *S. Leistikow and G. Schanz*, “Oxidation Kinetics and Related Phenomena of Zircaloy-4 Fuel Cladding Exposed to High Temperature Steam and Hydrogen-Steam Mixtures Under PWR Accident Conditions”, Nuclear Engineering and Design 103 (1987) 65-84, Noth-Holland Amsterdam, pp. 65-84.

2. *S. Sagat, H.E. Sills and J.A. Wolsworth*, “Deformation and Failure of Zircaloy Fuel Sheaths Under LOCA Condition”, Zirconium in the Nuclear Industry: Sixth International Symposium, ASTM STP 824, D. G. Franklin and R. B. Adamson, Eds., American Society for Testing and Materials, 1984, pp. 709-733.

3. *S. Leistikow and R. Kraft*, “Creep-Rupture of Zircaloy Tubing under Superimposed High Temperature Steam Oxidation at 900 C”, EUROCOR'77 6th European Congress on Metallic Corrosion, London 12-13 September 1977, Society of Chemical Industry, pp. 577-584.

4. *B. Burton, A.T. Donaldson and G.L. Reynolds*, “Interaction of Oxidation and Creep in Zircaloy-2”, Zirconium in the Nuclear Industry (Fourth Conference), ASTM STP 681, American Society for Testing and Materials, 1979, pp. 561-585.

5. *F.J. Erbacher, H.J. Neitzel, H. Rosinger and K. Wiehr*, “Burst Criterion of Zircaloy Fuel Claddings in a Loss-of-Coolant Accident”,Zirconium in the Nuclear Industry; Fifth Conference, ASTM STP 754, D.G.Franklin, Ed., American Society for Testing and Materials, 1982, pp. 271-283.

6. *H.M. Chung and T.F. Kassner*, “Embrittlement Criteria for Zircaloy Fuel cladding Applicable to Accident Situations in Light-Water Reactor”,Summary Report, Argonne National Laboratory, Materials Science Division, NUREG/CR-1344, ANL-79-48, January 1980.

7. *A. Sawatzky*, “A Proposed Criterion for the Oxygen Embrittlement of Zircaloy-4 Fuel Cladding”, Zirconium in the Nuclear Industry (Fourth Conference), ASTM STP 681, American Society for Testing and Materials, 1979, pp. 479-496.

8. *A.A. Bauer, L.M. Lowry and W.J. Gallagher*, “Tube-Burst Response of Irradiated Zircaloy Spent-Fuel Cladding”, Zirconium in the Nuclear Industry (Fourth Conference), ASTM STP 681, American Society for Testing and Materials, 1979, pp. 465-476.

9. *R.R. Hobbins, S.L. Seiffert, S.A. Ploger, A.S. Mehner and P.E. MacDonald*, “Embrittlement of Zircaloy-Clad Fuel Rods Irradiated Under Film Boiling Conditions”, Zirconium in the Nuclear Industry (Fourth Conference), ASTM STP 681, American Society for Testing and Materials, 1979, pp. 586-599.

10. NOTE TECHNIQUE DRS/SEMAR 92/24. ICARE2. Version 2.MOD 0 and MOD 0.1. Description of physical models. Institute de Protection et de Surete Nucleaire. CEA-France.

11.SCDAP/RELAP5/MOD2 Code Manual, Volume 4: MATPRO-A Library of Materials Properties for Light-Water-Reactor Accident Analysis. NUREG/CR-5273 EGG-2555. Vol.4., 1990.

IV. Influence of Cracks on the Zircaloy Oxidation Kinetics

Introduction

Such processes as oxidation and deformation of Zircaloy fuel cladding during an accident in a Light Water Reactor (LWR) are strongly connected with each other. Investigations of deformation behavior of pressurized Zircaloy fuel cladding in steam atmosphere show the strengthening effect of oxidation. Oxidation can manifold increase the time to rupture due to ballooning or even prevent it. Another effect of oxidation on cladding deformation is an embrittlement of cladding material [1].

On the other hand, cladding deformation and oxide failure can diminish the protective property of oxide scale, therefore, steam reacts with metallic component much more intensively accelerating the oxidation process. Correct assessment of models describing oxidation and deformation of the cladding against available experimental data is possible when these processes are simulated simultaneously. For this reason, for self-consistent description of the Zircaloy oxidation kinetics under conditions of oxide cracking, coupling of the two developed modules (Oxidation and Mechanical Deformation) should be performed.

Conditions of cracks formation

Deformation behavior module describes the mechanical stress-strain state of the cladding layers. The main sources of stresses in the cladding layers taken into account are the following: internal and external pressure; temperature; volume changes due to phase transformations; thermal expansion of pellet. The cladding is considered as multilayer cylindrical shell, which consists of oxide and metal layers. Under this consideration each layer is exposed to uniform three-dimensional thin-wall cylinder type stress state. Fuel pellet is assumed to be a rigid body with radial thermal strain. Material of metal layers is proposed to be subjected only to elastic and creep deformations.

An external Zircaloy oxide layer is an elastic and brittle material. The strength of the oxide is a function of the layer temperature and decreases with temperature increase from 91.2 MPa at 1030°C to 12.7 MPa at 1540°C [2]. It is assumed that oxide layer fails when the maximum principal tensile stress exceeds the limit value. If oxide is cracked, it looses load resistance. Cracks' orientation depends on direction of tensile stress. The direction of maximum stress is perpendicular to crack surface. Usually circumferential stress is the maximum principal tensile stress. In this case axial cracks formation takes place. After oxide cracking a new uncracked oxide sub-layer appears. This oxide sub-layer has deformation strength and influences the cladding deformation behavior. Zircaloy oxide is hardly deformed material and its failure occurs under very small elastic deformations.

It is supposed that cracks penetration depth is equal to the thickness of previously uncracked oxide scale. The estimation of a characteristic distance between axial cracks gives the value of the order of cracks penetration depth. If the cracks are open, they provide short circuits for oxygen transport through the cracked part of the

oxide. Such a state of open cracks can be attained when the metal cladding layers are exposed to tensile hoop strain.

Model for accounting of cracks influence on the oxidation kinetics

The Zircaloy oxidation kinetics module is based on the solution of one dimensional diffusion equation in the layered cylindrical rod. Thus, an accurate mechanistic description of oxygen transport through the oxide layer via two-dimensional network of cracks turns to be beyond the accepted one-dimensional approximation. For this reason, a simplified model can be proposed for modification of the oxidation kinetics by cracking of the oxide layer.

It is assumed within the framework of this model that cracking renormalizes an effective thickness of the oxide layer in the oxygen diffusion problem, namely, that a certain part of the cracked oxide sub-layer becomes transparent for the oxygen. With the lack of any systematic experimental data on the oxygen diffusion through the cracked oxide, the ratio between the transparent part of the oxide and the cracked part is an undefined parameter. In order to clarify a physical meaning of this parameter, two limiting cases can be considered. If parameter is equal to zero, it means the absence of any transparent part of oxide layer for the oxygen penetration, i.e. usual diffusion transport through the oxide. In the opposite case when parameter is equal to unit, the whole cracked part of the oxide becomes transparent for the oxygen penetration. Therefore, it can be logically proposed that in reality a certain intermediate value (between 0 and 1) of this parameter should be determined.

For simulation of cracking influence on oxidation kinetics, improved and modified data base for the oxygen diffusion coefficients and phase boundary oxygen concentrations was developed and implemented in the Oxidation module. Diffusion coefficients of various oxidized cladding layers were calculated by physically grounded procedure using the results of precise isothermal oxidation experiments [3], [4]. Modified equilibrium Zr-O phase diagram from [5] was used for the phase boundary concentrations. After this, modified oxidation model was validated against various isothermal and transient tests performed at temperatures above 1233 K.

Oxidation-deformation stand alone module

Fuel cladding deformation behavior module CROX and cladding oxidation module PROF was coupled into the oxidation-deformation stand alone module. Integrated program proceeds in particular the preparation and the interchange of data between subroutines CROX and PROF. Coupling of modules was performed on a global time step by such values as follows: layers structure radii; the oxygen mass content in alpha-Zr(O) layer; the ratio between the transparent part of the oxide and the cracked part of this layer (relative transparent depth). Cladding layers dimensions change in both modules. At first, PROF program calculates oxygen content in the cladding layers and layers radii for the end of present global time step. Values of oxygen mass in the ZrO_2 layer both for the end of previous and present time steps and new layers radii are used for determination of the input parameters for CROX program. Deformation module calculates the new modified layers radii and the thickness of cracked oxide for the end of present time step. Transparent oxide depth is calculated by multiplication of the cracked oxide thickness by the user defined parameter (relative transparent depth). The relative depth of transparent oxide and modified layers radii are the input parameters for PROF program at the following global time step.

Assessment of oxidation-deformation module against experimental data

1. Isothermal and transient temperature experiments of S.Leistikow and G.Schanz [6]

Test preparation. The tested specimens were Zircaloy-4 hole short tube sections of 10.75 mm external diameter and 0.725 mm wall thickness. The specimens' lengths were 30 mm.

Test performance. Oxidation reactions were performed by double-side exposure of specimens to atmospheric pressure steam in tubular furnace. In the case of low-temperature 600°C-1300°C isothermal tests, the specimens were held at the actual reaction temperature. In contrast, during the high-temperature oxidation tests at 1350°C-1600°C the specimens under flowing steam were inserted into a slightly cooler part of the furnace and suitably moved into the final hot position. Specimens reach their predetermined temperature within less than 1 min. and the commence of test time was defined after reaching 95% of the desired temperature. In temperature transient tests tube specimens were inductively heated under appropriately programmed temperature control while exposed to steam. Thus, a variety of different LOCA-typical transients could be simulated (Fig. 1). Metallographic investigations of cross sections of specimens were performed for determination of growth of the oxygen-rich layers.

Experimental results. Results of long-term double-side steam oxidation isothermal tests in temperature range 1000°C-1600°C are shown in Fig. 2. At temperatures 1050°C and above parabolic oxidation kinetics was observed. At lower temperatures at long times of exposure the breakaway effect in oxidation kinetics occurred.

In all cases of transient exposure (Table 1) the extent of oxidation was lower than under isothermal conditions.

Simulation results. The conditions of double-side oxidation in isothermal and transient experiments were modeled in calculations.

A rather good agreement was attained between measured and simulated values of outer oxide thickness in temperature range from 1100°C to 1500°C under isothermal conditions (see Fig. 2). At temperature 1000°C the breakaway effect occurs at long times of exposure which is beyond the scope of present consideration.

For the experiments performed under transient conditions with maximum temperature from 1000°C to 1300°C (see Fig.1) all calculations of outer oxide layer thickness demonstrate an excellent agreement with experimental data (see Table 1).

In these experiments cladding was not exposed to any mechanical loads, perhaps, with the exception of volume expansion due to oxidation. The calculations show that cladding oxide scale periodically cracks during oxidation. However, with the lack of external mechanical loads, generated cracks may be characterized as microcracks (not opened). For these reasons, cracking was not taken into account in the oxidation kinetics (compare with the following section 4.2). Due to a rather good agreement of calculation results with experimental data, one can conclude that under conditions of isothermal and LOCA-similar transient experiments without pressure and mechanical interactions with pellet, open cracks do not appear in the oxide scale and, therefore, influence of cracking on the oxidation kinetics turns to be negligible.

2. Transient temperature experiments of P. Hofmann [7]

Test preparation. The tests [7] were performed using short Zircaloy-4 cladding tube specimens filled with stoichiometric high-density uranium dioxide pellets. The specimens were 100 mm long with an outside diameter of 10.75 mm and a wall thickness of 0.725 mm.

Test performance. Experiments were performed in an argon + 25% vol. oxygen gas mixture in the high-temperature and high-pressure autoclave apparatus. The specimen was contained in a high-pressure vessel and inductively heated with equal heat up and cool down rates of 0.25, 1, 5 and 10 K/s. The maximum temperature varied between 1000°C and 2000°C. The initial temperature was the same (650°C) for all experiments. The holding time at the maximum temperature was 10 s. The external overpressure was about 40 Bar. The reaction layers thickness was determined metallographically after experiment in dependence of the maximum temperature.

Experimental results. The results showed, that the slower are the heat up and cool down rate, the larger is the extent of oxidation of the cladding. The temperature of the cladding complete oxidation, depending on heating rate, was between 1800°C and 2000°C. Formation of Zircaloy oxide results in a diameter increase of the fuel rod segments. No oxide spalling could be noticed. The experimental thickness of oxide layer is plotted versus maximum cladding temperature in Fig. 3.

Simulation results. At the present moment, conditions of temperature transient experiments with maximum temperature below 1525°C were simulated in calculations. Results of simulations of high temperature tests (above 1525°C) in which a new oxide layer (cubic phase) appeared in accordance with the equilibrium binary Zr-O phase diagram [5], will be presented in the final report in December, 1996.

Under conditions of these low temperature tests chemical interactions between cladding and uranium dioxide pellet practically do not influence the Zr oxidation kinetics and, for this reason, were not taken into account.

The first series of calculations in which cracking influence was ignored (Fig. 3), showed a good agreement with experimental results but not in all cases, mainly for temperatures above 1400°C and for heating rates from 1 to 10 K/s. When cracking was taken into account in the oxidation module (ratio of the oxide “transparency” was varied and finally chosen equal to 0.4, the same for all simulations!), the calculation results (Fig. 4) were in a better agreement with experiments for all rates and for all considered temperatures.

An important difference exists between this series of experiments and one described in the previous section 3.1. Owing to the thermally expanding pellet inside the Zircaloy tube in [7], cladding was exposed to strong tensile loads and deformed. As a result, cracks appeared in the oxide as open ones providing short circuits for oxygen penetration inside the oxide layer, thus, noticeably influencing the oxidation kinetics.

Conclusion

Assessment of different sets of experimental data shows that the developed coupled oxidation-deformation module gives an opportunity to account for the cracks influence on the oxidation kinetics at temperatures above 1000°C.

In the cases when Zircaloy oxidized cladding is not exposed to large tensile deformations [6], there is no necessity to use special procedure for the oxide effective thickness modification. Under conditions of cladding deformation [7], the proposed method of the two modules coupling (oxidation module PROF and mechanical deformation module CROX) allows an account of oxide cracking influence on the oxidation kinetics and significantly improves the results of simulations.

References:

N.Yamshchicov, A.Boldirev, O.Komarov, The Modelling of Fuel Cladding Deformation Behavior under Severe Accident, Preprint NSI-2-93, Nuclear Safety Institute, Russian Academy of Sciences, Moscow 1993.

SCDAP/RELAP5/MOD2 Code Manual, Volume 4: MATPRO - A Library of Materials Properties for Light-Water-Reactor Accident Analysis, NUREG/CR-5273 EGG-2555, 1990.

R.E. Pawel, J.V. Cathcart, R.A. McKee, J. Electrochem. Soc., 126 (1979), p.1105.

S. Leistikow, G. Schanz, H.V. Berg, Kinetics and Morphology of Isothermal Steam Oxidation of Zircaloy-4 at 700-.P. 1300°C, KfK 2587 March 1978.

J Abriata, J. Garces, R. Versaci, The O-Zr (Oxygen-Zirconium) System, Bull. of Alloy Phase Diagrams, 7, No 2 (1986), p.116.

S. Leistikow, G. Schanz, The Oxidation Behavior of Zircaloy-4 in Steam between 600 and 1600°C, Werkstoffe und Korrosion, 36 (1985), p.105.

P. Hofmann, Chemical Interactions of Zircaloy-4 Tubing with UO2 Fuel and Oxygen at Temperatures between 900 and 2000°C (Experiments and PECLOX Code), Part 1: Experimental Results, KfK 4422, Kernforschungszentrum Karlsruhe, 1988.

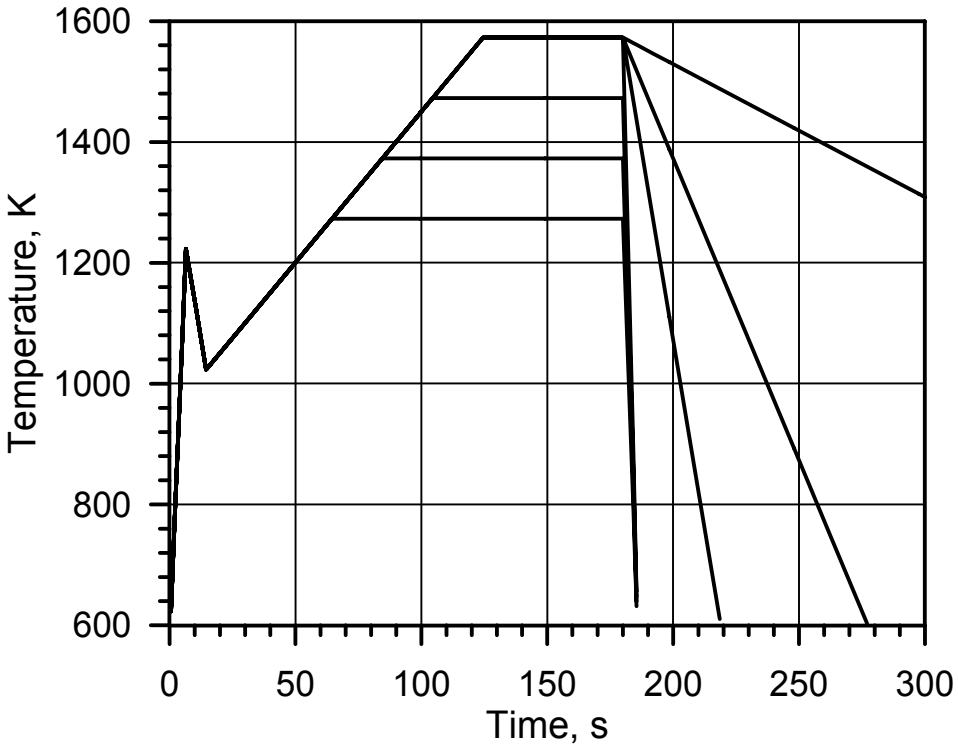

Fig. 1 Temperature conditions of LOCA-similar Zircaloy-4 tubes steam oxidation experiments of S. Leistikow, G. Schanz [6]. Temperature of the cladding as a function of time.

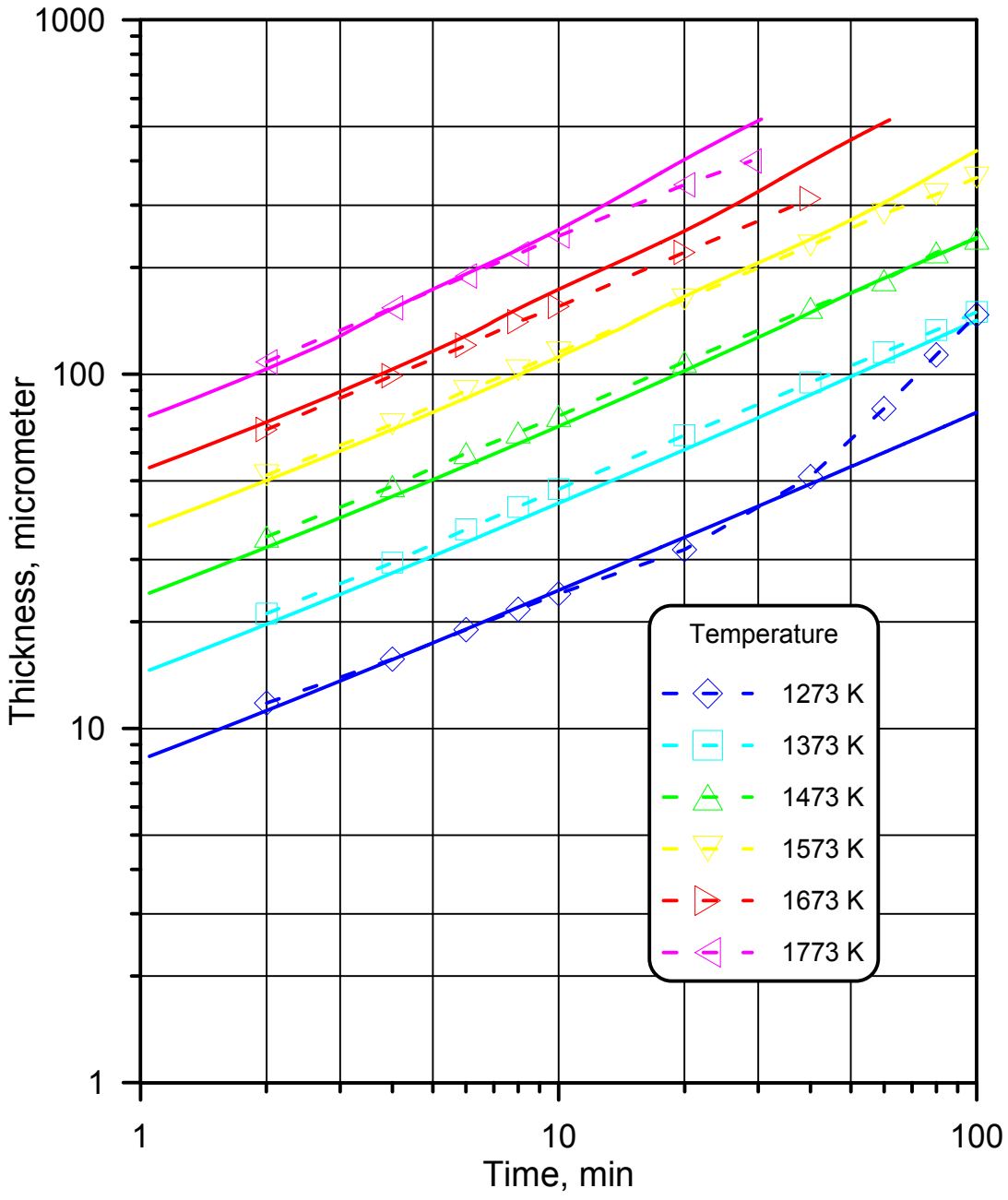

Fig. 2. Comparison of oxidation kinetics calculation results (solid lines) and experimental results (dashed lines) of S. Leistikow, G. Schanz [4] under isothermal conditions. Thickness of outer oxide layer versus time of exposure. Double side oxidation.

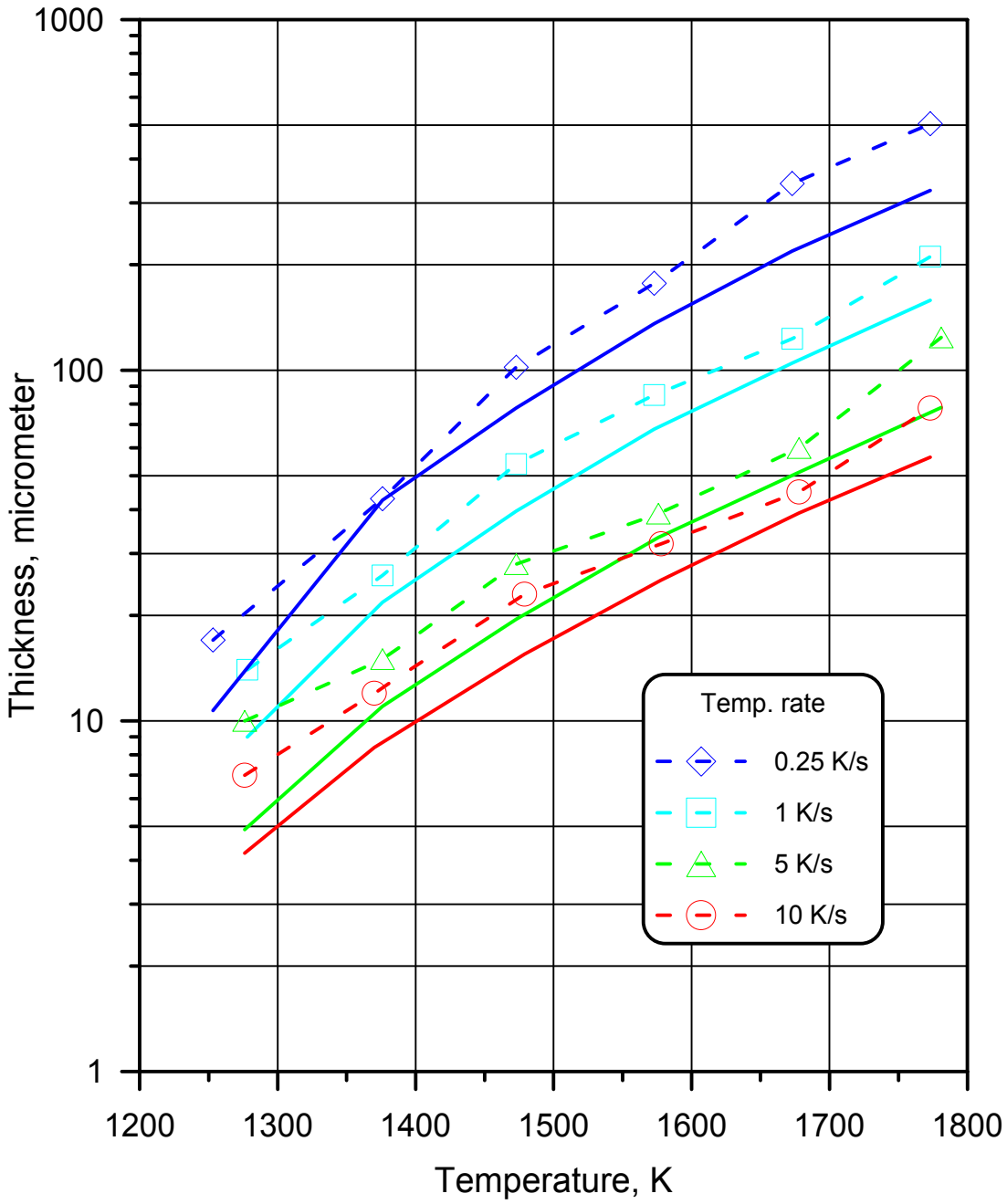

Fig. 3. Comparison of oxidation kinetics calculation results (solid lines) and experimental results (dashed lines) of P. Hofmann [7] under transient temperature conditions. Thickness of outer oxide layer versus maximum temperature. Cracking is not taken into account.

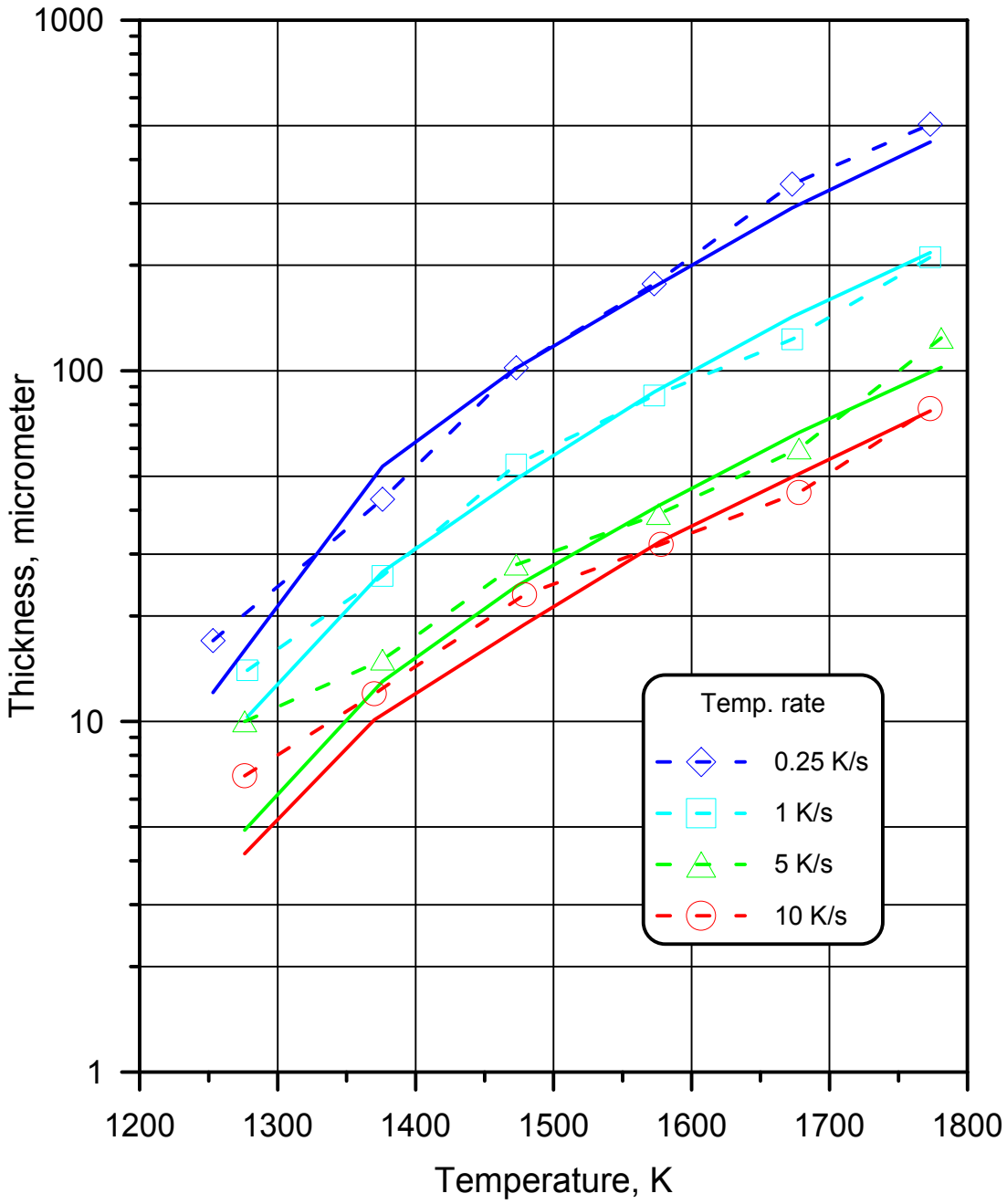

Fig. 4. Comparison of oxidation kinetics calculation results (solid lines) and experimental results (dashed lines) of P. Hofmann [7] under transient temperature conditions. Thickness of outer oxide layer versus maximum temperature. Cracking is taken into account.

Table 1. Comparison of the results of calculations with experimental data

(S. Leistikow, G. Schanz [6]) for the temperature-transient double-side oxidation behavior of Zircaloy-4 tubing in steam

Conditions of experiment	Thickness of external ZrO2 layer (in micrometers)	
	experiment	calculation
Time of experim. - 3 min., maximum temperature:		
1273 K	11	11
1373 K	17	18
1473 K	32	28
1573 K	37	40
Time of experim. - 5 min., maximum temperature:		
1273 K	12	14
1373 K	24	24
1473 K	41	38
Time of experim. - 3 min., 25 K/s cooling, maximum temperature		
1573 K	39	41
Time of experim. - 3 min., 10 K/s cooling, maximum temperature		
1573 K	42	42
Time of experim. - 3 min., 2 K/s cooling, maximum temperature		
1573 K	50	51

Experimental data scattering is approximately equal to 3 micrometer.

V. Coupling of the Deformation, Oxidation and Heat Exchange Modules.

Introduction

To take into account the interaction of oxidation kinetics, deformation behavior and cladding temperature evolution of Zircaloy fuel cladding during quenching the coupling of the described above stand alone modules were performed.

The main features of the integral module are:

- a fuel rod is divided into meshes along axial direction, each mesh is assumed to be a multilayer structure, which is a result of mesh wall oxidation;
- deformation behavior of a cladding mesh is simulated with account of oxidation influence on the mechanical properties of layer materials;
- temperature distribution of a cladding mesh is simulated by heat exchange module with account of multilayer mesh structure, the obtained temperature distribution is used for simulation of oxidation kinetics and mechanical behavior;
- oxidation of a cladding mesh is simulated by using the dimensions of multilayer structure which is a result of deformation behavior;
- to take into consideration oxide scale cracking it is assumed that the part of cracked oxide thickness is quite transparent for oxygen and does not take part in oxidation kinetics;
- computation process is the set of the global time steps, for each module the global time step is the same; global time step calculation is the set of local time sub-steps, the sub-step values are found by each module.

To realize the coupling of stand alone modules the special driver was worked out. This driver includes the routines to provide the following main functions:

- creation, initialization and updating of the database for each module and the generalized database;

- preparation input data for the modules;

- interpretation of the modules output date;

- processing and recording of user specified output information.

All routines are written in FORTRAN 77.

Simulations of some experiments were carried out with the help of the integral module to test the interaction of the modules and evaluate the directions of further developments.

Simulation of preoxidation kinetics of the quench specimens

In order to simulate oxidation kinetics of the specimens in the preoxidation stage, both oxidation and mechanical modules were used. To take into account the oxide scale cracking it is assumed that 40 % of cracked scale thickness is quite transparent for the oxygen (see chapter IV). Simulation of the preoxidation without cracking influence were also carried out.

1. Preoxidation of 100 μm - test 1603_1.95

Test preparation. The Zircaloy-4 cladding tubes had 10.75 mm outside diameter, 0.725 mm wall thickness, and 150 mm length.

Test performance. The temperature of the specimen was increased during 10 min from 600°C to 1350 °C in gas flow of 120 l/h argon and 20 l/h oxygen, then kept constant at 1350°C during 5 min under the same gas flow, then the temperature was increased up to 1500 °C and reflooding started.

Experimental results. The following values of layer thicknesses were measured after the test:

Elevation * mm	Oxide thickness μm	Zr(O) thickness μm
125	125-135	180
80	115-125	180

* distance from the bottom end of specimen.

Simulation results. Preoxidation was simulated up to the moment of the temperature increase from 1350 °C to 1500 °C. Uniform temperature distribution of cladding was assumed. Calculated thicknesses of the cladding layers are presented in the table:

Oxide cracking influence	Oxide thickness μm	Zr(O) thickness μm
no influence	98	181
with influence	129	173

Evolution of layers thickness and stresses generated by volumetric expansion under oxidation are presented in Fig.1, 2 (with cracking influence on oxidation).

To evaluate the capability of oxidized up to 100 μm-oxide Zircaloy cladding to withstand the quench loads the two parameter were calculated:

- the equivalent-cladding reacted (ECR) ,

- the thickness of the cladding with $\leq$ 0.9 wt % oxygen.

For the case of preoxidation of 129 μm-oxide ECR=16.5 %, this value is less than critical value of 17 %, hence, according to this criterion cladding does not fail under quench condition. Nevertheless small exceeding of this value of preoxidation can lead to cladding failure.

The second parameter may be evaluated using the average oxygen concentration in beta layer which is calculated by oxidation module. For this temperature regime the calculated average oxygen concentration in beta layer is 0.84 wt %. From the Zircaloy-oxygen quazi-binary phase diagram the equilibrium oxygen concentration at temperature 1350 °C is $\sim$ 1.0 wt %. The oxygen concentration profile is unknown. Under conservative assumption that it may be similar to linear distribution inside cladding wall with $\leq$ 0.9 wt % oxygen the value of 0.3 mm can be obtained. Hence, according to the second criterion the cladding does not fail during quenching.

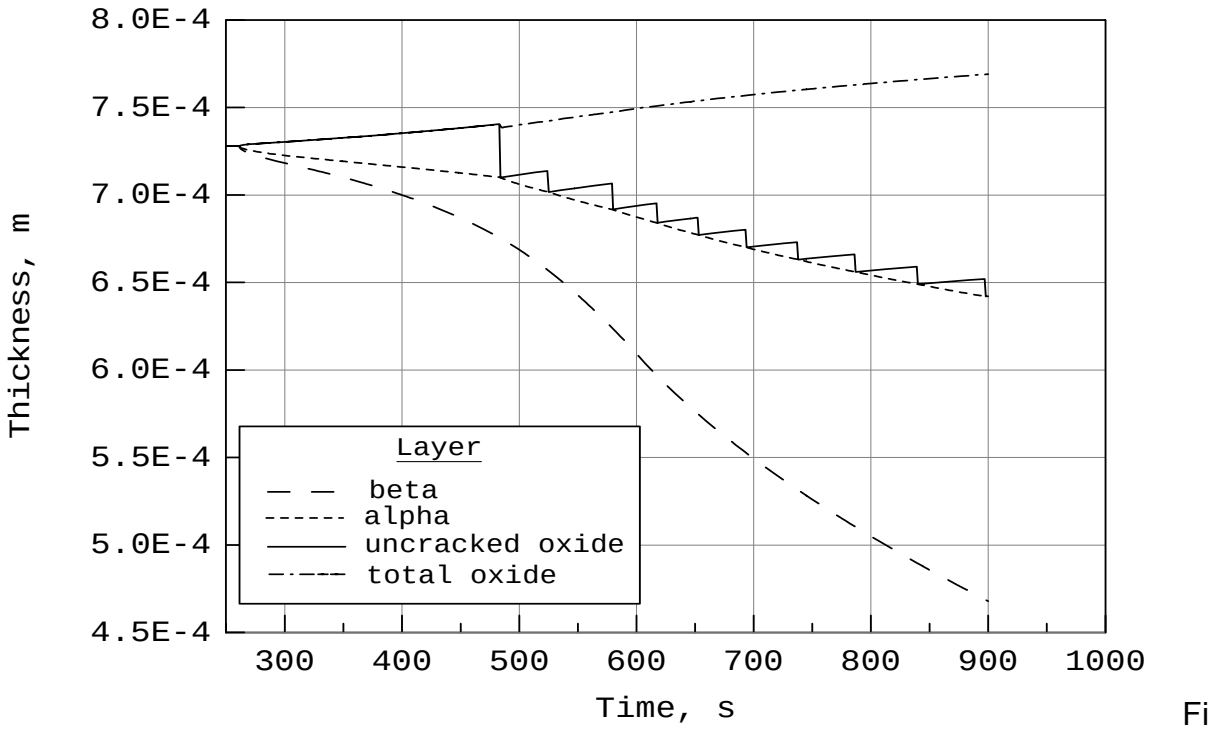

Fi

g. 1 Evolution of cladding layers thickness during preoxidation up to 100 μm of oxide thickness.

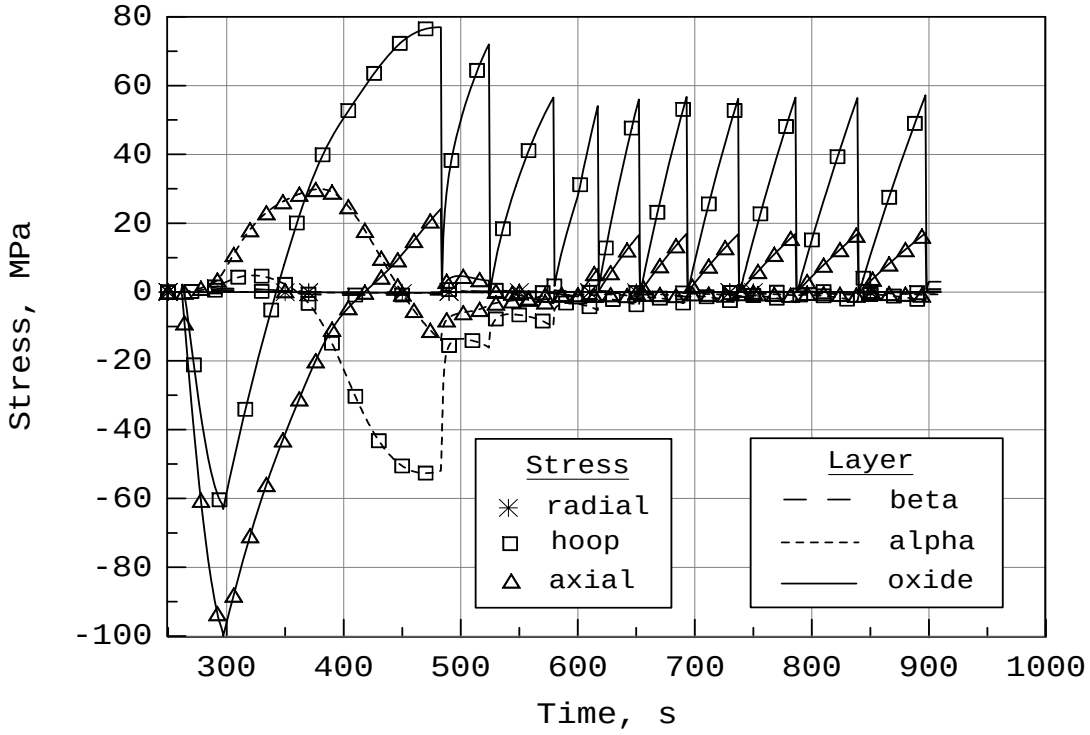

Fig. 2 Evolution of stresses in cladding layers during preoxidation up to 100 μm of oxide thickness.

2. Preoxidation of 200 μm - test 2203_1.95

Test preparation. The Zircaloy-4 cladding tubes had 10.75 mm outside diameter, 0.725 mm wall thickness, and 150 mm length.

Test performance. The temperature of specimen was increased during 10 min from 600°C to 1350 °C in gas flow of 120 l/h argon and 20 l/h oxygen, then kept constant at 1350°C during 15 min and increased up to 1500 °C during 2 min under the same gas flow conditions, then quench started in gas flow of 40 l/h argon.

Experimental results. The following values of layer thicknesses were measured after the test:

Elevation mm	Oxide thickness μm	Zr(O) thickness μm
125	210-225	250-300
70	200-225	300
20	160-170	250

After the test through breaches penetrating through the cladding wall were observed.

Simulation results. Preoxidation was simulated up to the moment of the temperature increase up to 1500 °C. Uniform temperature distribution of cladding was assumed. Calculated thicknesses of the cladding layers are presented in the table:

Oxide cracking influence	Oxide thickness μm	Zr(O) thickness μm
no influence	172	356
with influence	231	345

Evolution of layers thicknesses and stresses is similar to the case of 100 μm-oxide preoxidation.

Both criteria of cladding failure predict the cladding rupture: ECR=29 %, the average oxygen concentration in beta layer is 1.7 wt %

3. Preoxidation of 300 μm - test 0604_1.95

Test preparation. The Zircaloy-4 cladding tubes had 10.75 mm outside diameter, 0.725 mm wall thickness, and 150 mm length.

Test performance. The temperature of specimen was increased during 10 min from 600°C to 1350°C in gas flow of 120 l/h argon and 20 l/h oxygen, then kept constant at 1350°C during 30 min under the same gas flow conditions, then temperature was increased up to 1500°C during 2 min, the first minute in atmosphere with oxygen and the second in pure argon, then quench started in gas flow of 40 l/h Argon.

Experimental results. The following values of layer thicknesses were measured after the test:

Elevation mm	Oxide thickness μm	Zr(O) thickness μm
125	280-320	max 500
80	260-290	max 500
30	250-275	460-500

After the test breaches penetrating through the cladding wall were observed.

Simulation results. Preoxidation was simulated up to the moment when oxygen flow was interrupted. Uniform temperature distribution of cladding was assumed. Calculated thicknesses of the cladding layers are presented in the table:

Oxide cracking influence	Oxide thickness μm	Zr(O) thickness μm
no influence	266	549
with influence	362	486

Evolution of layers thicknesses and stresses is similar to the case of 100 μm-oxide preoxidation.

Both criteria of cladding failure predict the cladding rupture owing to the absence of the beta layer.

From the comparison of calculated and experimental results one can see that cracking influence on oxidation kinetics increases for long time oxidation experiment and heavily oxidized cladding.

Simulation of quenching of nonoxidized specimens

Quench experiments with non-oxidized specimens were simulated. Oxidation, mechanical and heat exchange modules were used. To take into account the oxide scale cracking it was assumed that 40 % of cracked scale thickness is quite transparent for oxygen. Hydrogen release was calculated assuming that two g-atoms of hydrogen were generated for each g-atom of oxygen consumed in the reaction of Zr oxidation.

1. Quenching from the temperature 1600 °C- test 3108_1.95

Test preparation. The Zircaloy-4 cladding tubes had 10.75 mm outside diameter, 0.725 mm wall thickness, and 150 mm length. Cladding was filled with oxide pellets.

Test performance. Temperature of specimen was increased during 10 min from 600°C to 1590 °C in gas flow of 40 l/h, then quench started.

Experimental results. The following values of oxide layer thicknesses were measured after the test:

Elevation mm	Oxide thickness μm
120	14
78	16
40	30
0-15	30

The amount of generated hydrogen was 13.62 mg. The amount of hydrogen stored in the specimen was 9.45 mg. Hence, the total amount of hydrogen production due to Zr oxidation was 23.07 mg.

Simulation results. Initial uniform temperature distribution of cladding and pellets was assumed. Calculated thicknesses of the cladding layers are presented in the table:

Elevation mm	Oxide thickness μm
130	25
75	23
20	14

The total amount of hydrogen production due to Zr oxidation is 27.88 mg.

Evolution of layers thicknesses, temperature distribution and stress-state of the cladding at different locations are presented in Fig.3-14.

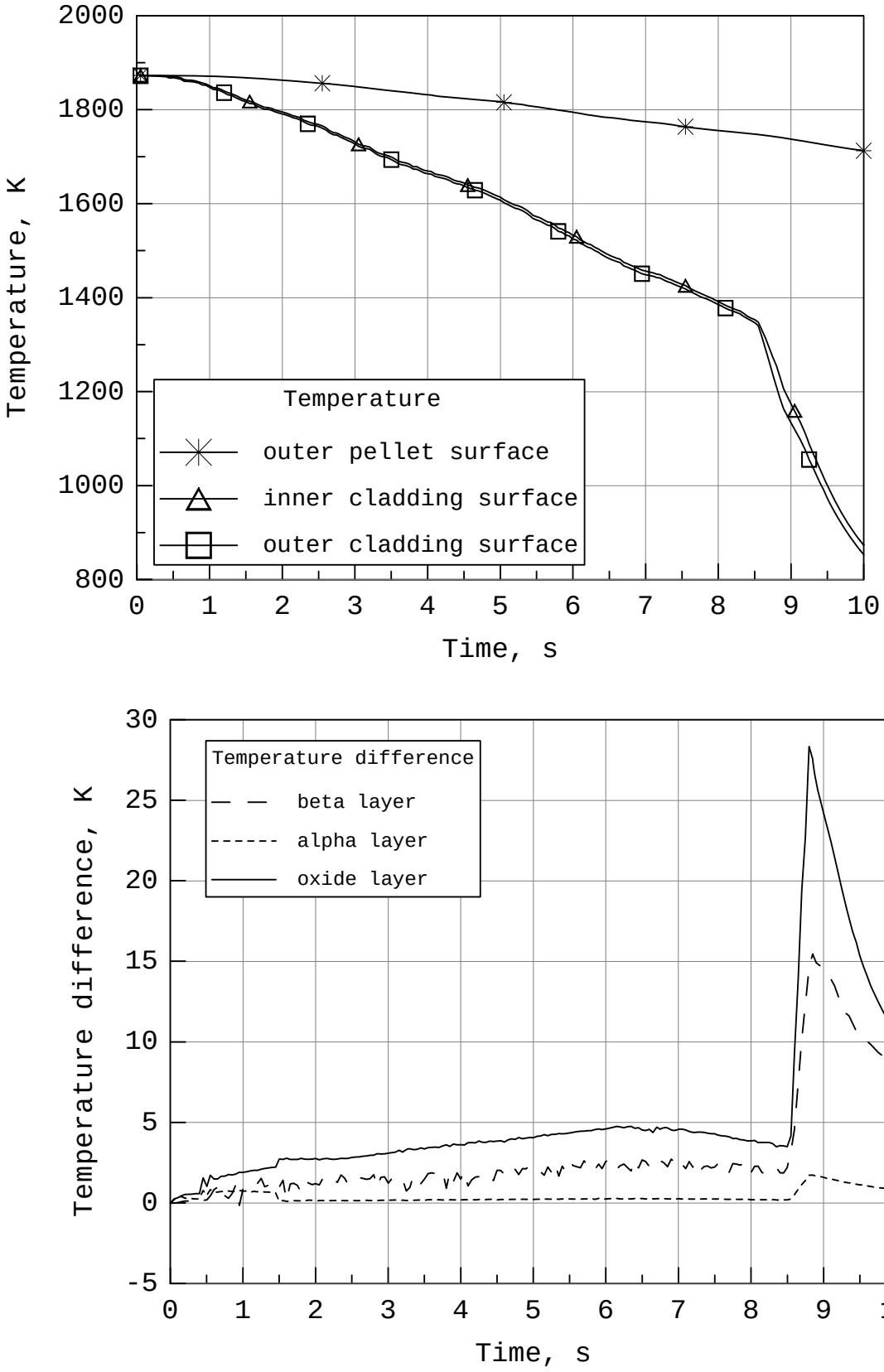

Fig.3-4. Temperature history of the cladding layers during quenching. No pre-oxidation. To=1873 K. Elevation 130 mm.

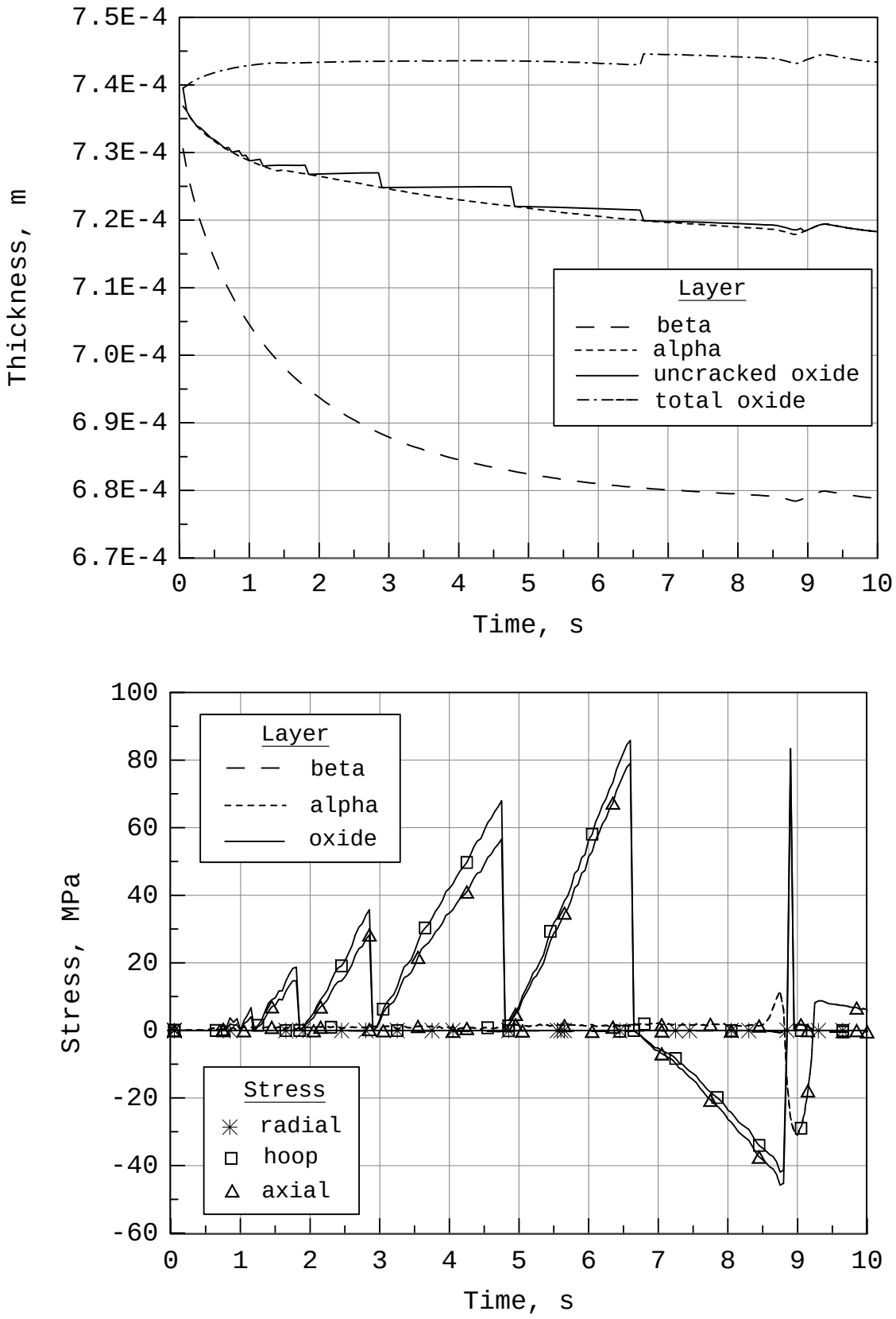

Fig.5-6. Evolution of thickness and stresses of the cladding layers during quenching. No preoxidation. To=1873 K. Elevation 130 mm.

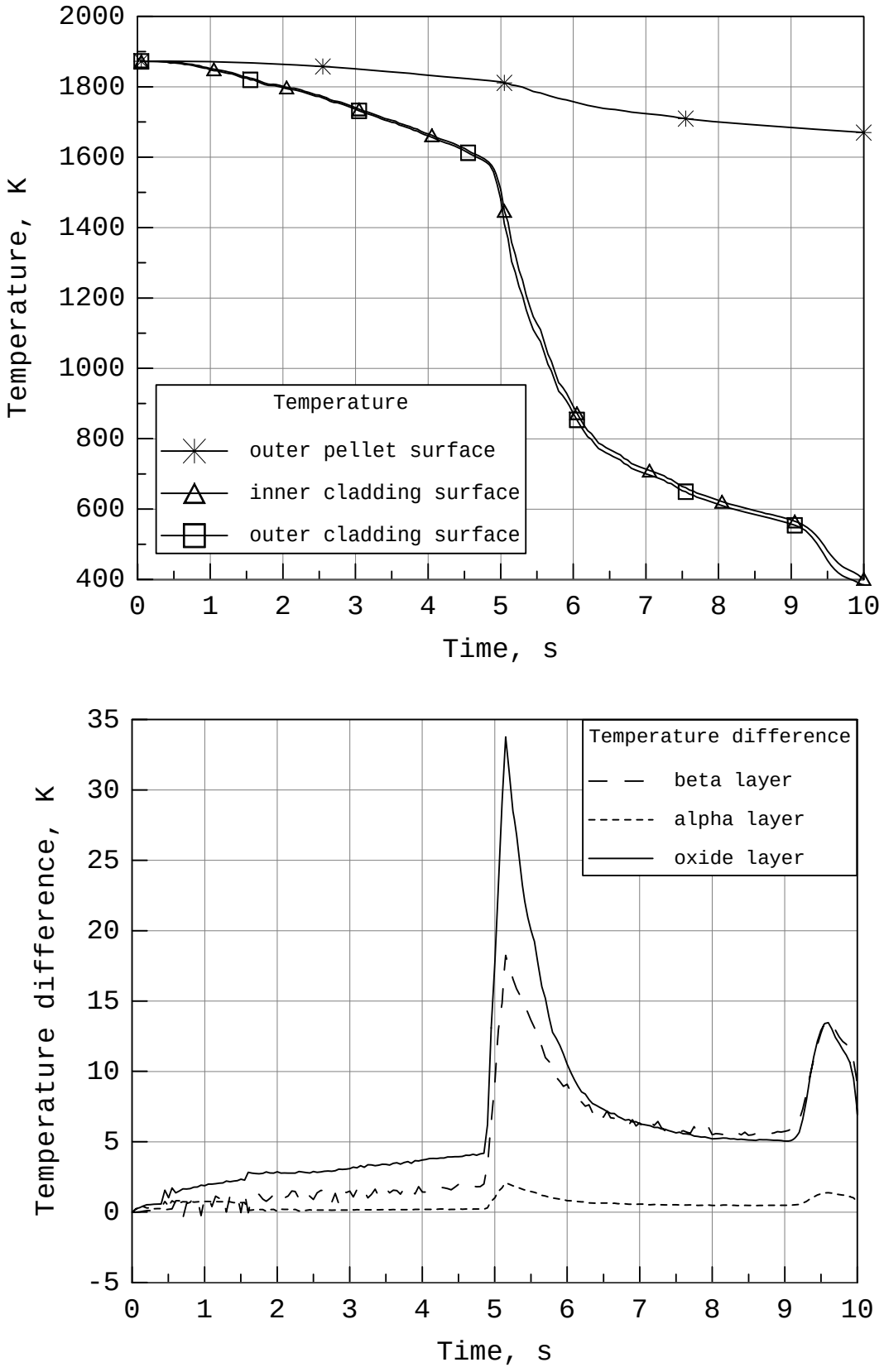

Fig.7-8. Temperature history of the cladding layers during quenching. No pre-oxidation. To=1873 K. Elevation 75 mm.

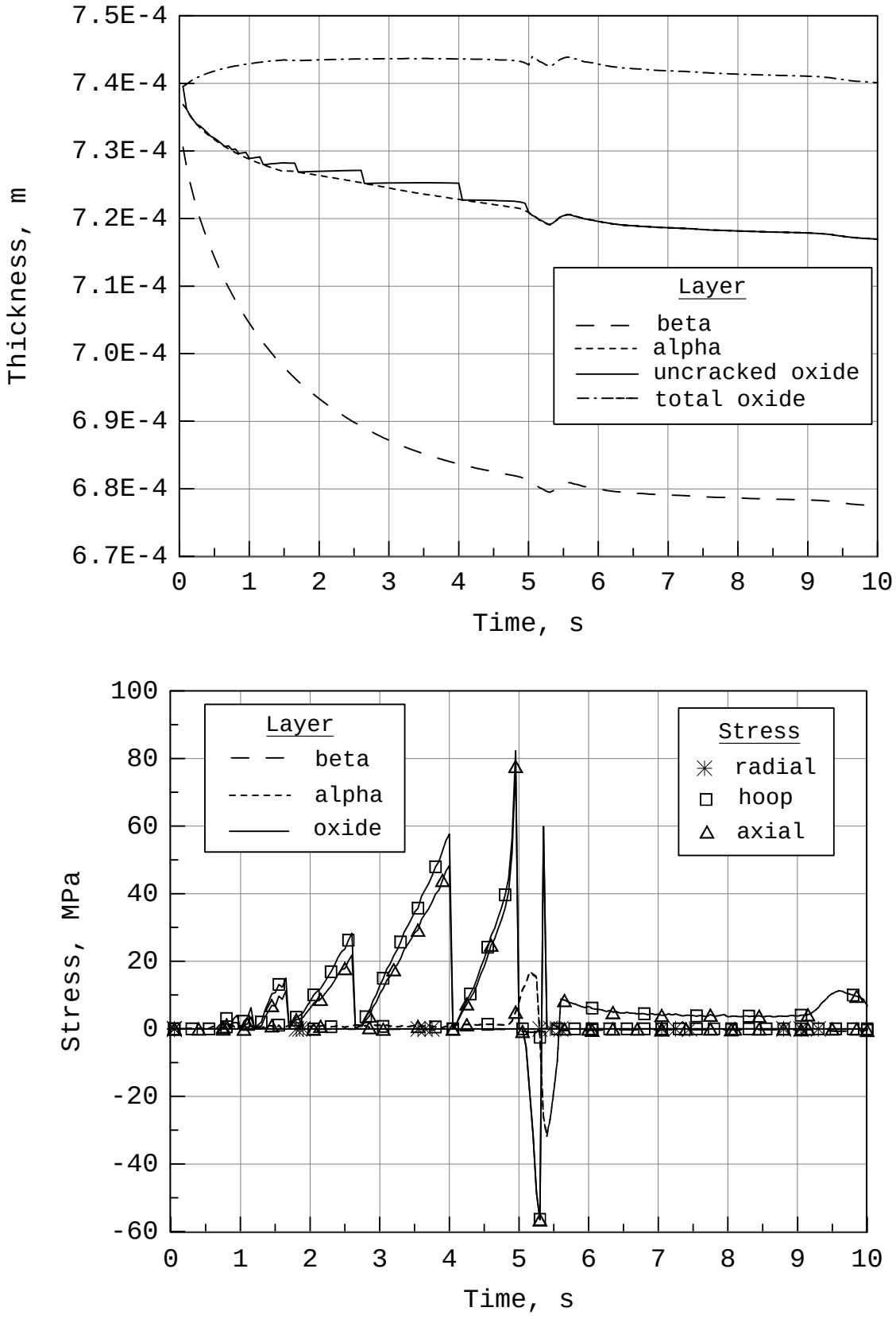

Fig.9-10. Evolution of thickness and stresses of the cladding layers during quenching. No preoxidation. To=1873 K. Elevation 75 mm.

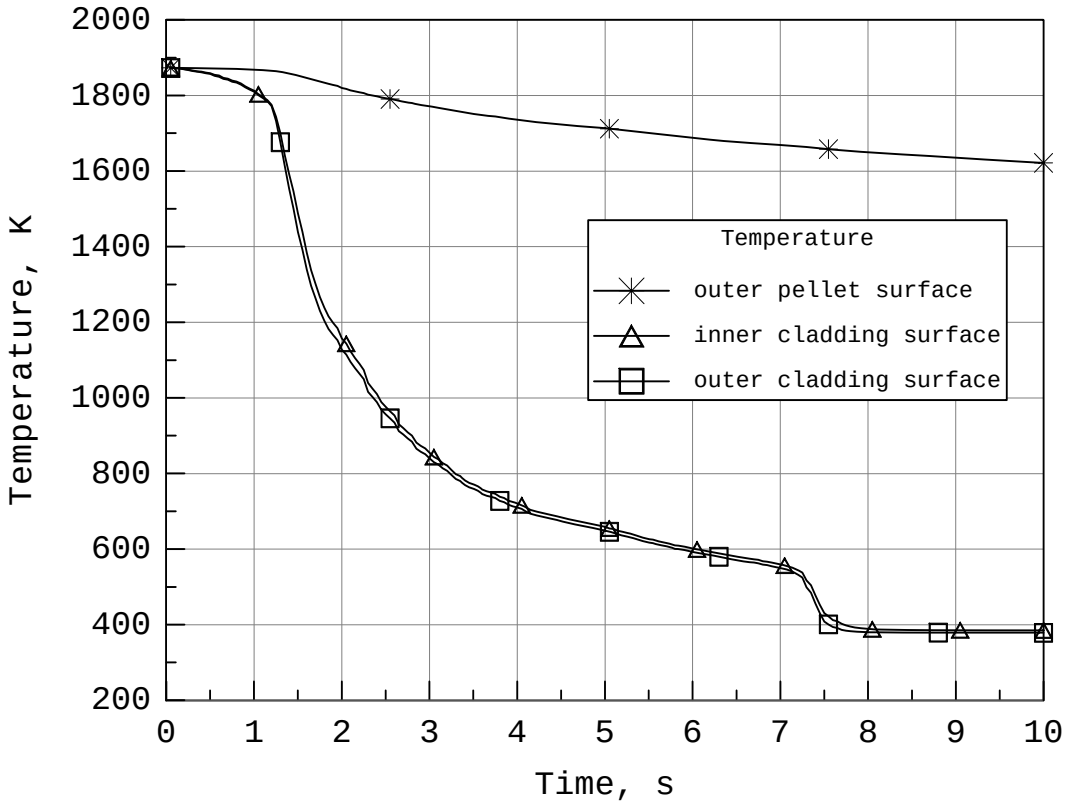

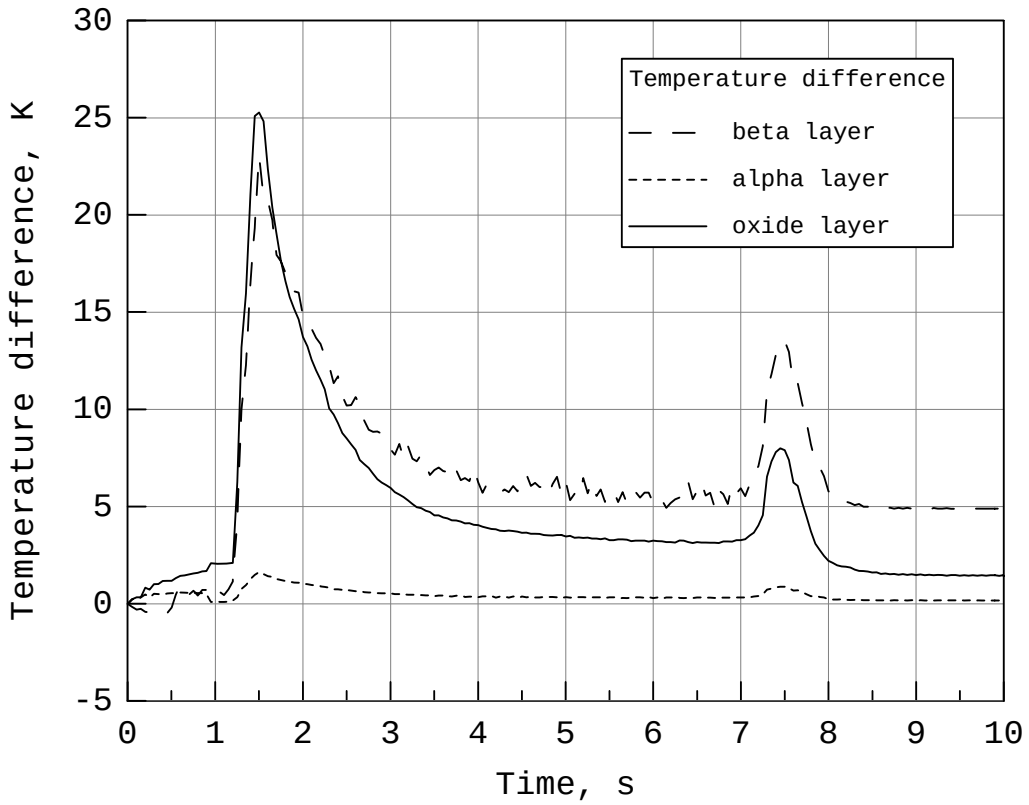

Fig.11-12. Temperature history of the cladding layers during quenching. No pre-oxidation. To=1873 K. Elevation 20 mm.

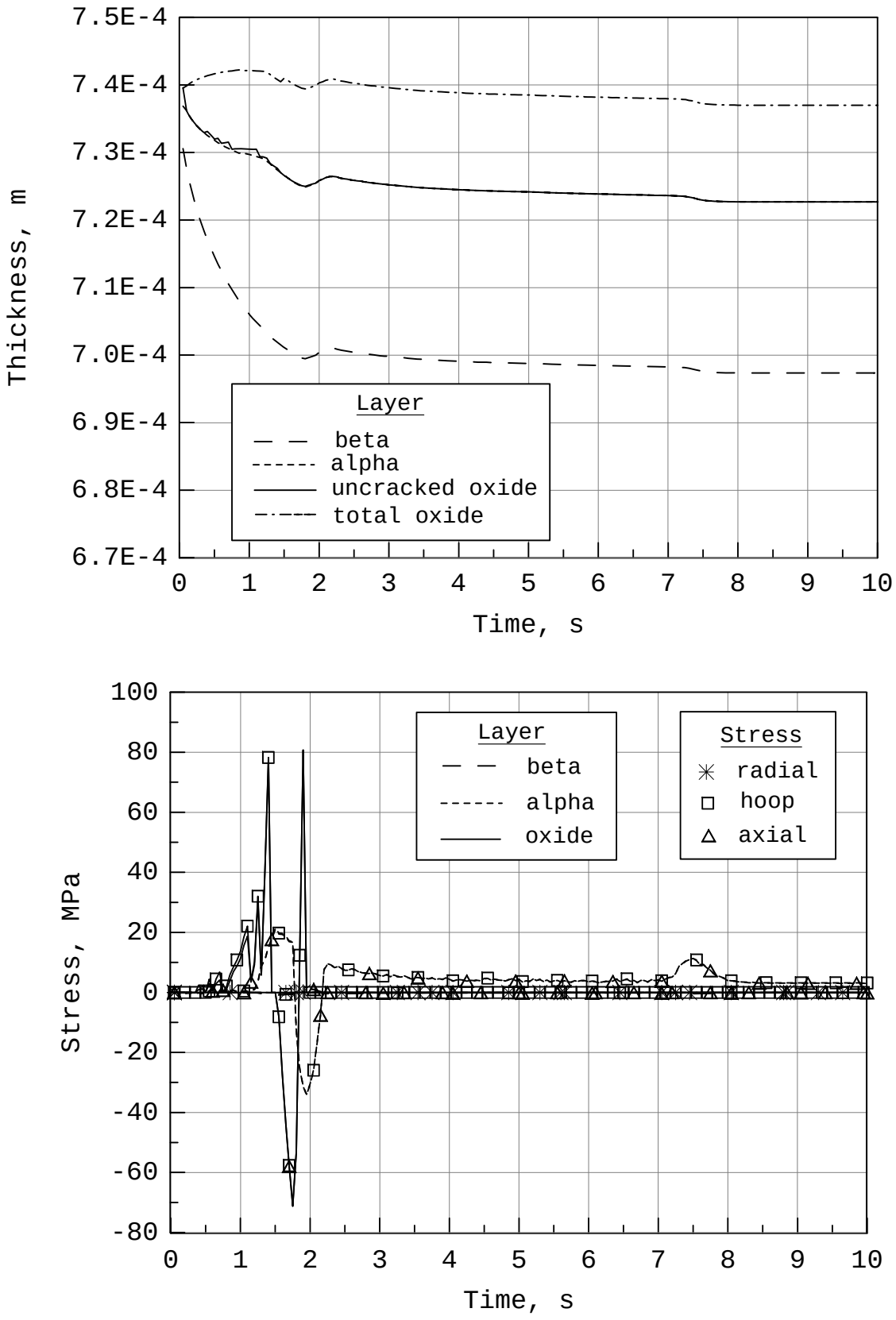

Fig.13-14. Evolution of thickness and stresses of the cladding layers during quenching. No preoxidation. To=1873 K. Elevation 20 mm.

2. Quenching from the temperature 1400 °C- test 2808_1.95

Test preparation. The Zircaloy-4 cladding tubes had 10.75 mm outside diameter, 0.725 mm wall thickness, and 150 mm length. Cladding was filled with oxide pellets.

Test performance. The temperature of the specimen was increased during 10 min from 600°C to 1400 °C in gas flow of 40 l/h, kept constant at 1400 °C during 2 min, then quench started.

Experimental results. The following values of oxide layer thicknesses were measured after the test:

Elevation mm	Oxide thickness μm
120	7.5
78	10
28	13
18	19

The amount of generated hydrogen was 7.72 mg. The amount of hydrogen stored in specimen is unknown. Assuming that this value is the average between the hydrogen storage at the temperature 1200 °C (4.5 mg) and 1600 °C (9.45 mg), this value is estimated as 7 mg. Hence, the total amount of hydrogen production due to Zr oxidation is 14.72 mg.

Simulation results. Initial uniform temperature distribution of cladding and pellets is assumed. Calculated thicknesses of the cladding layers are presented in the table:

Elevation mm	Oxide thickness μm
130	14
75	13
20	7

The total amount of hydrogen production due to Zr oxidation is 12.45 mg.

Evolution of layers thickness, temperature distribution and stress-state of the cladding is similar to the one presented above.

3. Quenching from the temperature 1200 °C- test 2408_1.95

Test preparation. The Zircaloy-4 cladding tubes had 10.75 mm outside diameter, 0.725 mm wall thickness, and 150 mm length. Cladding was filled with oxide pellets.

Test performance. The temperature of specimen was increased during 10 min from 600°C to 1200 °C in gas flow of 40 l/h, kept constant at 1200 °C during 2 min, then quench started.

Experimental results. The following values of oxide layer thicknesses were measured after the test:

Elevation mm	Oxide thickness μm
120	5
78	5.5
28	7.5

The amount of generated hydrogen was 3.21 mg. The amount of hydrogen stored in the specimen was 4.5. The total amount of hydrogen production due to Zr oxidation was 7.71 mg.

Simulation results. Initial uniform temperature distribution of cladding and pellets is assumed. Calculated thicknesses of the cladding layers are presented in the table:

Elevation mm	Oxide thickness μm
130	7.1
75	6.2
20	3.8

The total amount of hydrogen production due to Zr oxidation is 5.67 mg.

Evolution of layers thickness, temperature distribution and stress-state of the cladding is similar to the one presented above.

From the comparison of the calculated and experimental data one can see that the hydrogen production values have the following tendency: at higher temperatures the hydrogen production is also higher. However, oxide thickness profile along the cladding height has the opposite tendency: in calculations at higher elevations the oxide is thicker; in experiments at higher elevations the oxide is thinner. The reasons of this disagreement are not clear yet, since at lower elevations the temperature more rapidly decreases and cladding oxidation ceases.

Simulation of quenching of preoxidized specimens

Quench experiments with preoxidation 100 μm were simulated for the case of initial quench temperature of 1200 °C and 1600 °C, in order to find the influence of initial temperature on the stress-strain state of the cladding under quench conditions. Oxidation, mechanical and heat exchange modules were used. It was assumed that after preoxidation before quenching the cladding was free from stresses.

1. Preoxidation 100 μm . Quenching from the temperature 1200 °C- test 0607_1.95

Test preparation. The Zircaloy-4 cladding tubes had 10.75 mm outside diameter, 0.725 mm wall thickness, and 150 mm length. Cladding was filled with oxide pellets.

Test performance. Temperature of the specimen was increased during 10 min from 600°C to 1350 °C in gas flow of 120 l/h argon and 20 l/h oxygen, then kept constant at 1350°C during 6 min under the same gas flow conditions, then temperature was decreased up to 1200 °C and quench started.

Simulation results. Evolution of the layers temperature distribution and stress-state of the cladding at central location are presented in Fig.15-18.

2. Preoxidation 100 μm . Quenching from the temperature 1600 °C- test 1007_1.95

Test preparation. The Zircaloy-4 cladding tubes had 10.75 mm outside diameter, 0.725 mm wall thickness, and 150 mm length. Cladding was filled with oxide pellets.

Test performance. Temperature of the specimen was increased during 10 min from 600°C to 1350 °C in gas flow of 120 l/h argon and 20 l/h oxygen, then kept constant at 1350°C during 6 min under the same gas flow conditions, then temperature was increased up to 1600 °C and quench started.

Simulation results. Evolution of the layers temperature distribution and stress-state of the cladding at central location are presented in Fig.19-21.

3. Preoxidation 300 μm . Quenching from the temperature 1600 °C- test 1107_1.95

Test preparation. The Zircaloy-4 cladding tubes had 10.75 mm outside diameter, 0.725 mm wall thickness, and 150 mm length. Cladding was filled with oxide pellets.

Test performance. Temperature of the specimen was increased during 10 min from 600°C to 1350 °C in gas flow of 120 l/h argon and 20 l/h oxygen, then kept constant at 1350°C during 30 min under the same gas flow conditions, then temperature was increased up to 1600 °C and quench started.

Simulation results. Evolution of the layers temperature distribution and stress-state of the cladding at central location are presented in Fig.23-26.

Simulation results of preoxidized specimens under quenching show that additional stresses generated by temperature gradients have an influence on the stress-strain state of the oxidized cladding, but the main contribution to the high stress state is induced by $\beta \rightarrow \alpha$ phase transformation of Zircaloy and tetragonal-to-monoclinic phase transformation of oxide. Radial or axial temperature gradients may have some influence on final spalling of exfoliated oxide scale or global cladding failure (through breach formation or cladding fragmentation). One can suppose that the maximum temperature gradients occur near the quench front when film boiling transforms to nucleate boiling, i.e. at the Leidenfrost temperature. At these temperatures no oxidation occurs and temperature can not increase due to oxidation. However, this low temperature cracking or breach formation can influence the release of hydrogen dissolved in the metal sub-layer.

Conclusion

The integral Quench module worked out by coupling of the heat exchange, oxidation and mechanical stand alone modules was used for the simulation of the FZK quench experiments. The main aim of this work was the description of the mutual influence of the oxidation kinetics, deformation behavior and temperature evolution. The presented module also allows to study the above phenomena separately and in pairs (for example, interaction of oxidation and deformation behavior, temperature history in this case is given; or interaction of the temperature evolution and deformation behavior without oxidation).

The results of the calculations are in good qualitative agreement and in some cases in good quantitative agreement with the experimental data To improve the predictive capability of the integral Quench module the systematic analysis of the full set of the quench experiments should be done to find the quantitative criteria describing the most important features of the cladding behavior under quenching conditions.

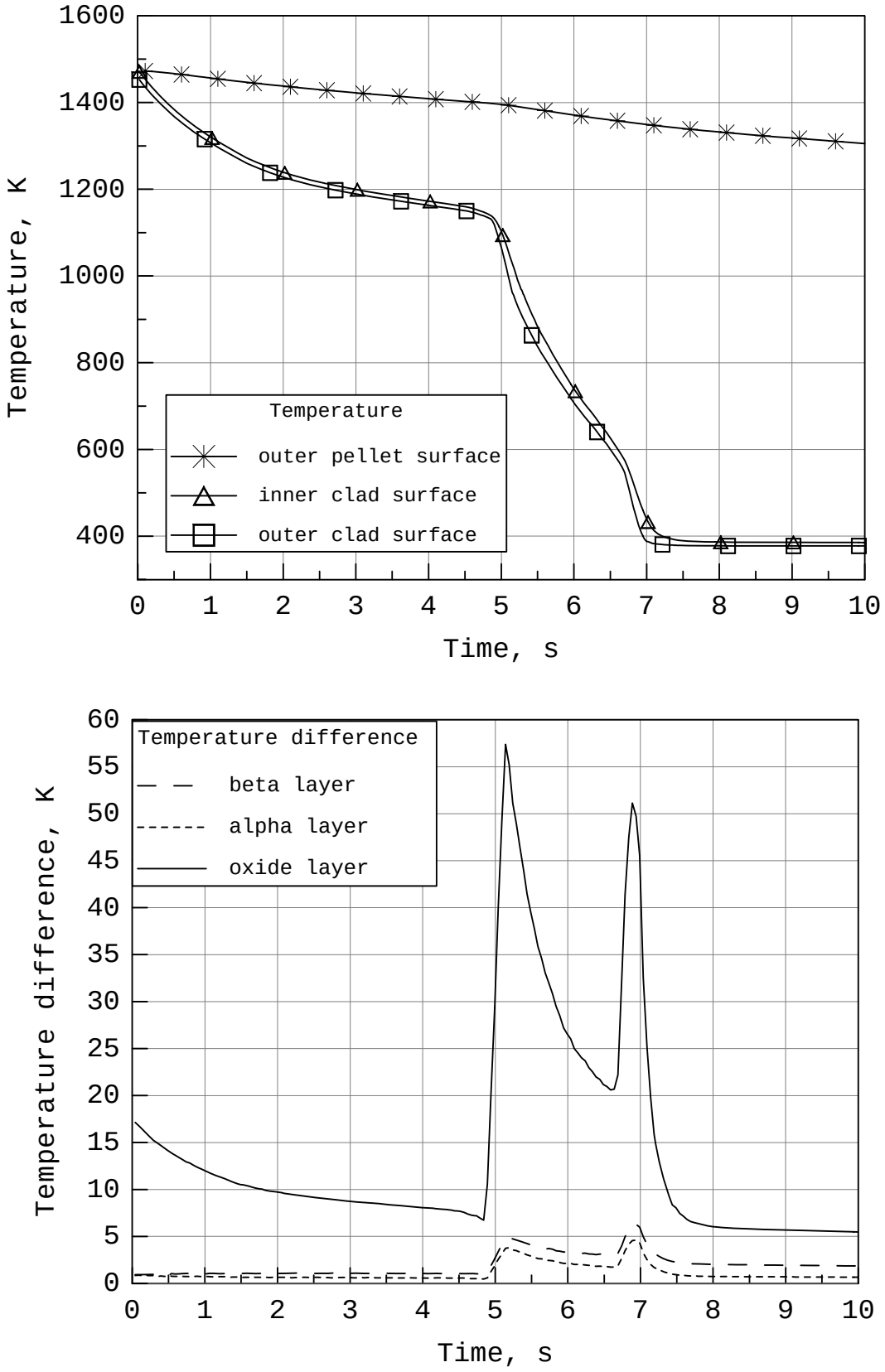

Fig.15-16. Temperature history of the cladding layers during quenching. Preoxidation 100 μm. To=1473 K. Elevation 75 mm.

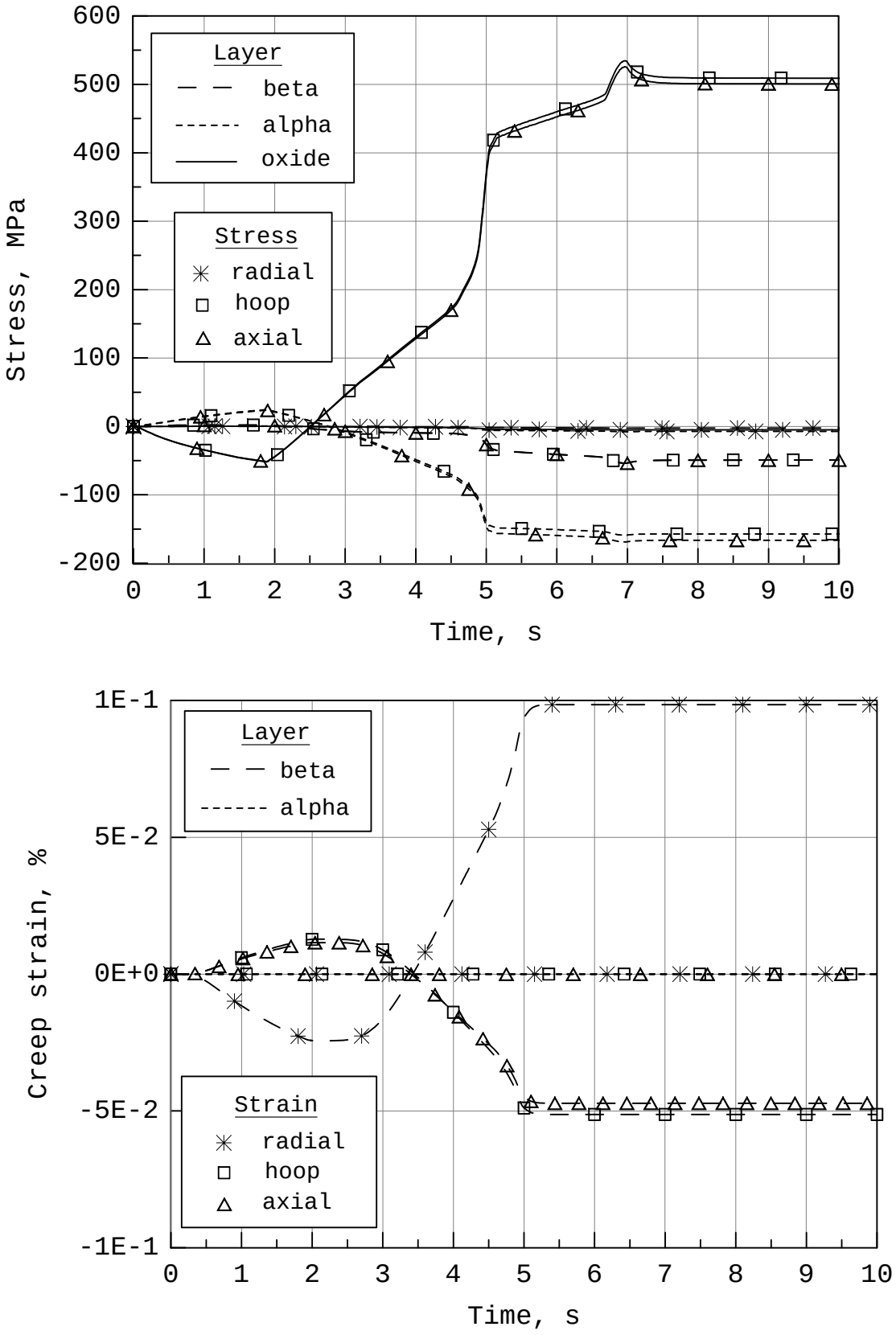

Fig.17-18. Evolution of stresses and creep strains of the cladding layers during quenching. Preoxidation 100 μm. To=1473 K. Elevation 75 mm.

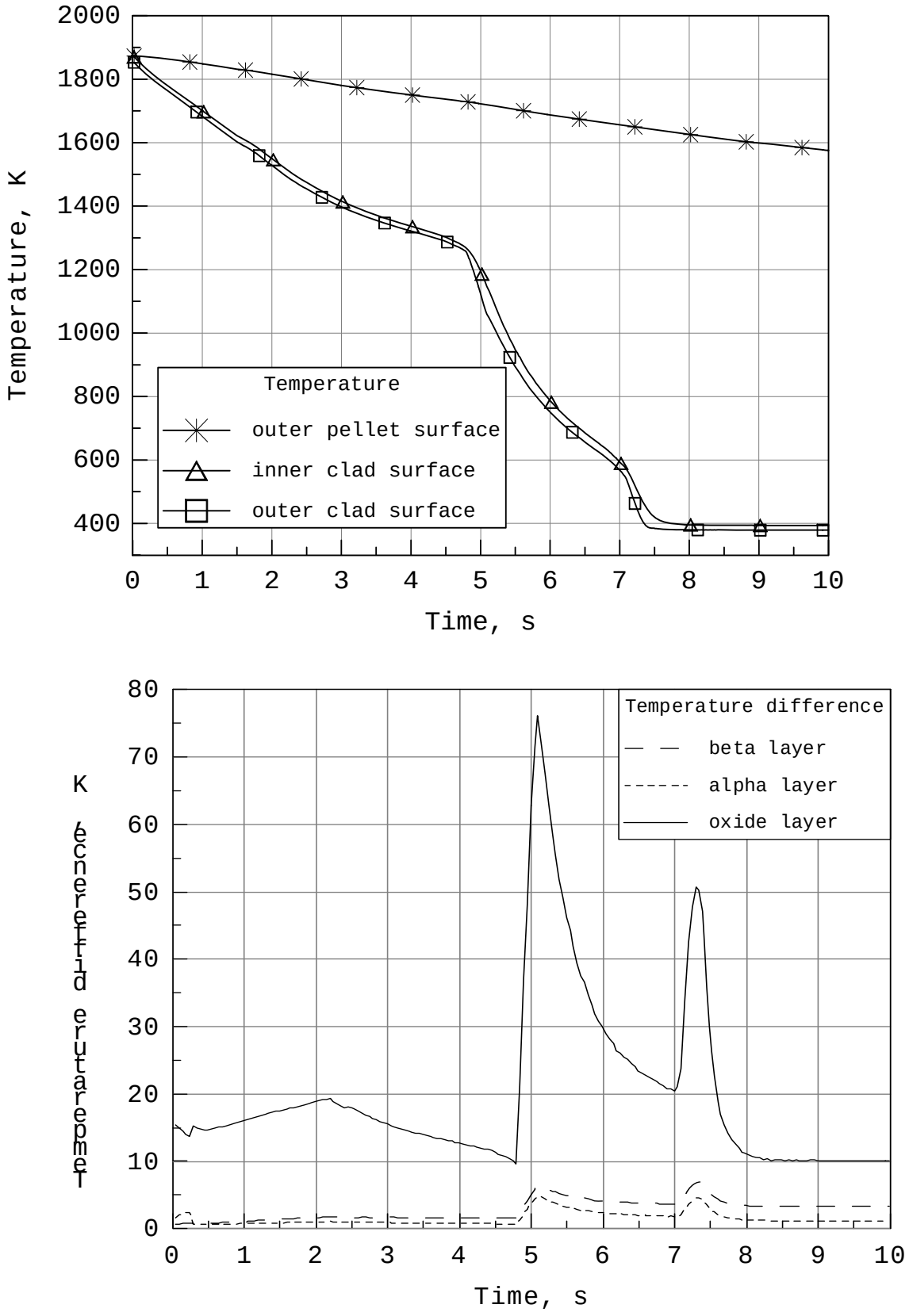

Fig.19-20. Temperature history of the cladding layers during quenching. Preoxidation 100 μm. To=1873 K. Elevation 75 mm.

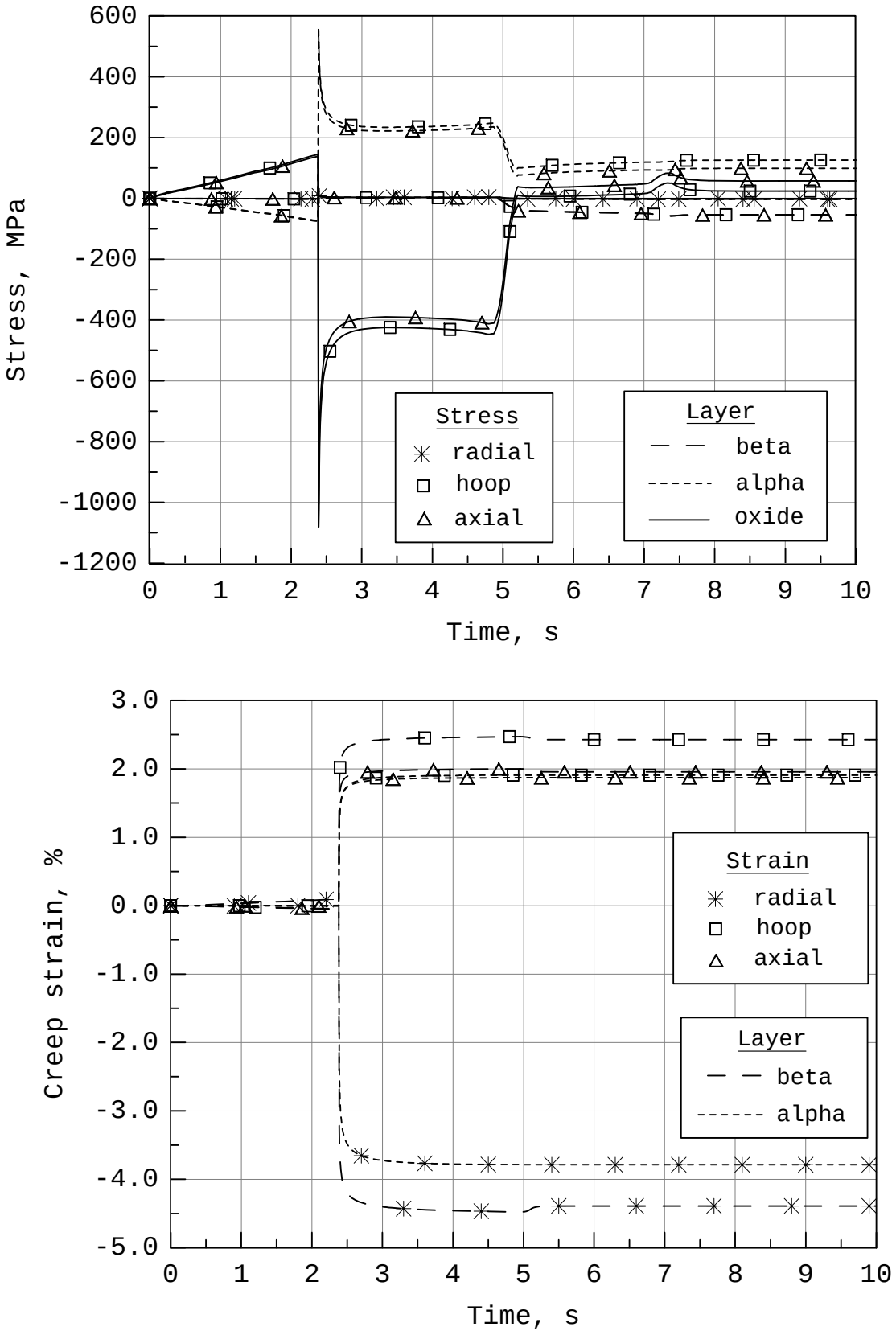

Fig.21-22. Evolution of stresses and creep strains of the cladding layers during quenching. Preoxidation 100 μm. To=1873 K. Elevation 75 mm.

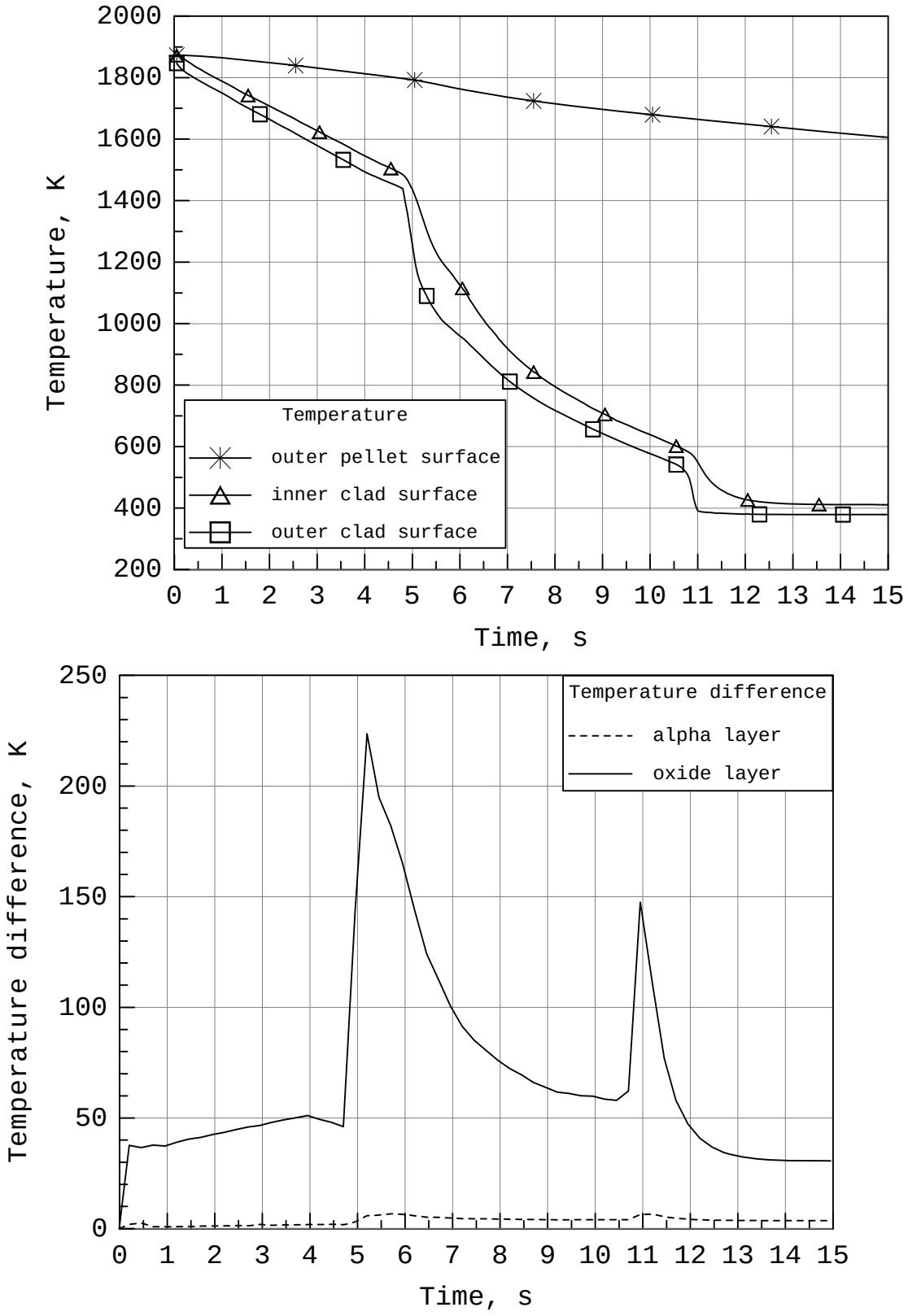

Fig.23-24. Temperature history of the cladding layers during quenching. Preoxidation 300 μm. To=1873 K. Elevation 75 mm.

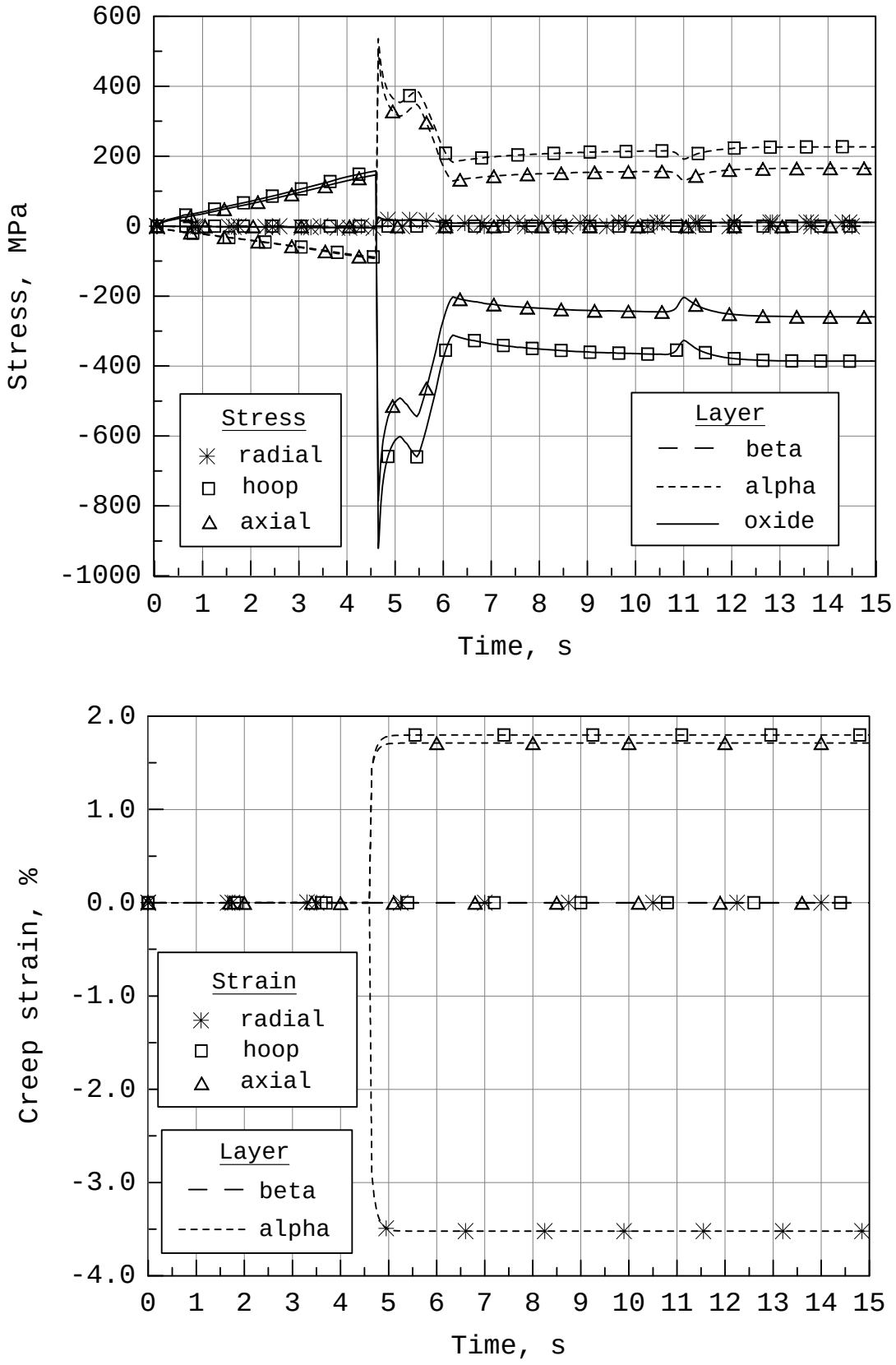

Fig.25-26. Evolution of stresses and creep strains of the cladding layers during quenching. Preoxidation 300 μm. To=1873 K. Elevation 75 mm.